Shape Evolution of Nanostructures by Thermal and Ion Beam Processing

– Modeling & Atomistic Simulations –

von der
Fakultät Mathematik und Naturwissenschaften
der Technischen Universität Dresden
genehmigte

Dissertation

zur Erlangung des akademischen Grades
doctor rerum naturalium
(Dr. rer. nat.)

von
Diplom-Physiker Lars Röntzsch
geboren am 09.09.1977 in Dresden

Parabase

Freudig war vor vielen Jahren
Eifrig so der Geist bestrebt,
Zu erforschen, zu erfahren,
Wie Natur im Schaffen lebt.

Und es ist das ewig Eine,
Das sich vielfach offenbart;
Klein das Große, groß das Kleine,
Alles nach der eignen Art.
Immer wechselnd, fest sich haltend,
Nah und fern und fern und nah;
So gestaltend, umgestaltend -
Zum Erstaunen bin ich da.

Johann Wolfgang von Goethe

Contents

Abbreviations

The following acronyms are used in order to avoid frequently occurring and space consuming expressions. Naturally, common scientific and technological terms are taken into account.

a.u.	arbitrary units
b.b.	broken bonds
BC	binary collision
b.c.c.	body-centered cubic
BOX	buried oxide
CMOS	complementary metal-oxide-semiconductor
CM	center of mass
CNT	carbon nanotube
DIC	differential image contrast
dpa	displacements per atom
ECS	equilibrium crystal shape
ESS	empty-space-in-silicon
f.c.c.	face-centered cubic
FET	field effect transistor
FIB	focused ion beam
FWHM	full width at half maximum
FZD	Forschungszentrum Dresden-Rossendorf
GIF	graphics interchange format
IBS	ion beam synthesis
KMC	kinetic Monte Carlo
l.h.s.	left hand side
LSA	linear stability analysis
MC	Monte Carlo

MCS	Monte Carlo step per particle
MD	Molecular Dynamics
MOS	metal-oxide-semiconductor
NC	nanocluster
NW	nanowire
NN	nearest neighbor
NNN	next-nearest neighbor
PMMA	polymethyl methacrylate
r.h.s.	right hand side
RT	room temperature
s.c.	simple cubic
s.hc.	simple hypercubic
SET	single electron transistor
SEM	scanning electron microscopy
SIMOX	separation by implantation of oxygen
SOI	silicon-on-insulator
SON	silicon-on-nothing
SPP	surface plasmon polariton
TEM	transmission electron microscopy
TM	transverse magnetic
TRIM	transport and range of ions in matter
ULSI	ultra-large-scale integration
1D	one-dimensional
2D	two-dimensional
3D	three-dimensional
4D	four-dimensional

Chapter 1

Introduction

1.1 Nanotechnology and Capillarity

In the course of miniaturization of functional structures, capillary phenomena have become increasingly important because of the growing surface-to-volume ratio with shrinking structure dimensions. Various nanoscale structures exhibit surfaces with mean curvature gradients which can have emerged, for example, during structure growth, during fabrication processes or by thermal fluctuations. If such structures evolve freely, the system-inherent capillary force tends to level off such curvature gradients (free energy minimization), i.e. the structures undergo shape transformations which require redistribution of material. These shape transformations can destroy the structure integrity which goes along with the failure of functionality. On the contrary, capillarity-driven processes may be of practical use in view of non-conventional nanostructure fabrication methods based on self-organization mechanisms.

Shape evolution proceeds as long as the kinetics in the system is fast enough to allow substantial mass transport at finite times. The dynamics of the shape evolution depends on various global and/or local process parameters like temperature, chemical potential, geometrical constraints, externally applied force fields etc. If a finite condensed phase is left to itself, the capillary force leads to the minimization of the free energy that is associated with the phase boundary (surface/interface). This principle applies equally to systems in the solid [1, 2, 3, 4, 5, 6] and in the liquid state [7, 8, 9]. The difference lies in the kinetics of the material redistribution processes: atomic diffusion along a concentration gradient on the one hand, hydrodynamic flow along a pressure gradient on the other hand. In crystalline solids, where various diffusion channels are simultaneously open (surface diffusion, bulk diffusion, and volume diffusion through the surrounding medium), capillary processes can be highly anisotropic due to the symmetry of the underlying lattice structure. Hence, crystalline structures with similar macroscopic shape but with different crystallographic orientation may show diverse behavior under the action of the capillary force. Important examples of capillarity-driven material redistribution processes in solid-state systems are the coarsening of cluster ensembles (Ostwald ripening) after phase separation of supersaturated solid solutions [10, 11], the breakup of wires or cylindrical trenches into chains of spherical particles (Plateau-Rayleigh instability) [1, 2], and the dewetting of ultra-thin films into complex patterns of wires and clusters [3, 4]. There are particular cases where the capillary force transforms one characteristic nanostructure into another one which for

itself is suitable for functional purposes, e.g. in this work the disintegration of metal NW structures into chains of nanoparticles is discussed that can be employed for SPP waveguiding [12, 13].

In general, functional nanostructures must be regular, long-range-ordered, and producible with high reliability. However, capillary processes are shown to be subject to thermal fluctuations at the nanoscale. Consequently, capillarity-induced shape transformations often lead to nanostructure morphologies with reduced regularity. Hence, the applicability of these self-organization or "bottom-up" processes is limited in view of technological exploitation. To overcome this inherent fluctuation problem, this work demonstrates that capillarity-driven reaction pathways can be controlled and unwanted fluctuations can be suppressed to a certain extent by weak external force fields. Periodic temperature fields, for instance, give rise to thermocapillary effects. Under the action of locally uncompensated surface forces, a system is "guided" along a desired reaction pathway resulting in regular and long-range-ordered structures, e.g. regular nanoparticle chains or regular surface ripples and hillock arrays on thin films [14].

In contrast to the hitherto outlined scenarios, a system's evolution can indeed be directed and the formation of a particular structure can thereby be forced if the system is exposed to strong external fields or forces. Hence, it can be driven to a state farther away from thermodynamic equilibrium than its initial state. The irradiation of phase boundaries (surfaces, interfaces) with energetic ions is a very prominent example for such non-equilibrium processes [15, 16, 17, 18, 19]. Atoms can be displaced ballistically during collisions with energetic particles [20]. Thereby, the detailed balance of thermally activated defect formation and annihilation is locally violated, thus, atomic configurations are achieved which are not or very unlikely obtained by thermally activated atomic migration alone. Hence, the action of the capillary force can be suppressed, retarded, or even accelerated depending on the ballistic displacement rate. Structures with steady-state shapes not to be found in the case of a freely evolving system may result. In short, the competition of driving forces like the action of the capillary force under simultaneous energetic particle irradiation has a high potential to become the fundament of novel nanostructure fabrication processes.

With these challenges and prospects at hand, formation and transformation of nanostructures in the solid state driven by the system-inherent capillary force and external forces are being investigated in the frame of this work. The main emphasis is put on nanostructures which have a cylindrical geometry, e.g. wires, rods, tubes etc. The kinetics along the corresponding reaction pathways, its dependence on physical parameters and thereby its potential controllability are examined by means of atomistic computer simulations (kinetic Monte Carlo). Although the results being presented here are outcomes of "computer experiments", which are performed under artificial and idealized conditions, they allow to reproduce and thereby help to further understand the physical mechanisms and possible control parameters of the processes observed in real systems. In various cases, these computer experiments can even predict reaction pathways of particular morphological transformations from which new processes of nanostructure fabrication may arise. These topics are closely related to the targets of the DFG Project "Theoretical Studies of Growth, Stability and Functionality of Nanowires" (contract no. HE 2137/2-1, part of the DFG Priority Program 1165 "Nanowires and Nanotubes: From Controlled Synthesis to Function") the author has been working on.

This dissertation is organized as follows: The introductory chapter continues with fundamental physical aspects of capillarity at the nanoscale, particularly in view of single-crystalline materials. Later, non-conventional routes of nanostructure formation and modification are portrayed which are relevant for the subsequent chapters. This introduction closes with a concise overview over the field of computational materials science. The second chapter portrays the 3D lattice KMC method as the principal simulation method applied in the frame of this work. In the third chapter, reaction pathways are presented which describe how NW structures can be fabricated in a controlled manner by FIB-based IBS, i.e. by phase separation and coarsening of supersaturated solid systems which are characterized by high supersaturation gradients. In chapter 4, the capillary instability of single-crystalline nanostructures is investigated most of which have cylindrical geometry, e.g. NWs, rods, tubes, tori etc. It is shown how the capillary instability can be used to fabricate and manipulate functional nanostructures based on self-organization. The subsequent chapter deals with the non-equilibrium processing in view of nanostructure shape evolution. It is demonstrated that thermal fluctuations, which are inherent in capillary processes at the nanoscale, can be suppressed by periodic temperature field gradients (guided evolution). Furthermore, the role of collisional mixing on the shape evolution of nanoscale structures will be examined. It is shown that ballistic displacements as they occur for example during ion irradiation can drive nanoscale structures to far-from-equilibrium shapes, thereby suggesting new routes of structure formation and modification. The last chapter summarizes the results and outlines perspectives, particularly in view of non-conventional processes in which equilibrium and non-equilibrium driving forces act simultaneously.

1.2 Fundamentals and Examples of Nanoscale Capillarity

Capillary phenomena occur in finite systems of condensed matter, thus, they play a ubiquitous role in nature and technology. Capillarity arises conceptually from the fact that atoms which are located at a surface or an interface have a lower number of neighboring atoms of the same species than those in the bulk [21]. In other words, they miss approximately one half-space of interatomic attraction. Surface atoms have therefore a higher potential energy since they are more weakly bound than bulk atoms. In addition, the number of possible atomic configurations at the surface is larger than that in the bulk which gives rise to an entropic contribution to the free energy. The change in the system's free energy F that goes along with a change in its surface area A is defined as the surface tension γ:

$$\gamma = \left. \frac{\partial F}{\partial A} \right|_{T,N,V} , \tag{1.1}$$

where T, N and V denote temperature, particle number and total volume, respectively. The surface tension can alternatively be perceived as a temperature-dependent force acting on a line element in the surface plane[1]. In the case of an infinite and flat surface the surface tension acts at each surface line element equally into the two directions

---

[1] γ is measured in Jm^{-2} or Nm^{-1}

orthogonal to the line element, i.e. these two surface tension contributions are antiparallel, thus, they compensate each other and the net force is zero. However, if the surface is curved with a mean curvature, κ, the vectorial summation of the two forces results in a net inbound/outbound force for a convex/concave surface. This net force is antiparallel/parallel to the surface normal. The net force results in an increase/decrease of pressure $p - p_0 = \Delta p$ beneath the surface which is called "capillary pressure" or "Laplace pressure". It is given by the Young-Laplace equation as the product between the surface mean curvature and the surface tension [21]:

$$p - p_0 = \Delta p = \gamma \times \kappa \ . \tag{1.2}$$

For example, the pressure increase in spherical and cylindrical entities with radius R amounts to

$$\Delta p = \gamma \times \kappa = \left\{ \begin{array}{l} 2\gamma/R_{\text{sphere}} \\ \gamma/R_{\text{cylinder}} \ . \end{array} \right. \tag{1.3}$$

Capillary phenomena have a venerable history. They were originally discussed in the framework of hydrodynamics because under standard conditions[2] there is sufficient kinetics in most liquids[3] resulting in shape transformations on length and time scales that are observable with the naked eye. Thus, it is not surprising that the scientific foundations of capillarity have already been established in the 19th century by Laplace, Young, Plateau, Taylor, Rayleigh, Marangoni and many others for liquid systems [21, 22, 23, 24].

However, capillary phenomena are also observed in solid-state systems. The difference lies in the microscopic kinetics of the material redistribution processes involved: hydrodynamic flow in liquids on the one hand, atomic diffusion in solids on the other hand. In general, the driving force of capillarity is a gradient of chemical potential which corresponds in liquids to a pressure gradient and in solids to a gradient of atomic concentration. The change in chemical potential per atom is given by [25]:

$$\mu = \left\{ \begin{array}{lll} kT \ln[p/p_0] & \simeq & kT[(p - p_0)/p_0] \quad \text{or rather} \\ kT \ln[c/c_0] & \simeq & kT[(c - c_0)/c_0] \quad . \end{array} \right. \tag{1.4}$$

In crystalline solids, there exist manifold diffusion mechanisms. In the case of surface diffusion the material flux along the surface reads [25]:

$$j_s = -\frac{c_s D_s}{k_B T} \times \frac{\partial \mu}{\partial s} \ , \tag{1.5}$$

where $\partial/\partial s$ denotes the derivative along the surface, c_s is areal concentration of species participating in the diffusion (ad-atoms, surface vacancies), and D_s denotes the surface diffusion coefficient. The chemical potential at a given surface point P is a function of the mean curvature of P. According to Herring [25, 26], the excess of μ at the point P on a curved surface of a crystalline structure reads

$$\mu\left(P\right) = \Omega \left[\left(\gamma_0 + \frac{\mathrm{d}^2\gamma}{\mathrm{d}\theta_1^2} \right) K_1 + \left(\gamma_0 + \frac{\mathrm{d}^2\gamma}{\mathrm{d}\theta_2^2} \right) K_2 \right] \ , \tag{1.6}$$

---

[2]$T = 273.15\,\text{K}; \ p = 101\,325\,\text{Pa}$

[3]Under standard conditions the intrinsic diffusion coefficients of liquids are on average three orders of magnitude higher compared to solids.

$d\,(\mathrm{nm})$	N_{atoms}	$N_{\mathrm{surface\ at.}}$	$N_{\mathrm{surf.\ at.}}/N_{\mathrm{at.}}$
100	3.09×10^7	4.85×10^5	0.016
50	3.86×10^6	1.21×10^5	0.031
20	2.47×10^5	1.90×10^4	0.077
10	3.08×10^4	4.63×10^3	0.150
5	3.85×10^3	1.09×10^3	0.285
2	2.53×10^2	1.45×10^2	0.572

Table (1.1): The growing surface-to-volume ratio with shrinking structure size illustrated for a spherical Au cluster with diameter d in the sub-100 nm range.

where K_1 and K_2 are the principal curvatures at P; θ_1 and θ_2 are the angles between the surface plane in P and the two principal directions; γ_0 is the surface tension of a planar surface; Ω is the atomic volume. Obviously, the analytical treatment of capillary effects in crystalline solids is very complicated due to surface tension anisotropy compared to liquids or amorphous solids with isotropic surface tension where

$$\mu(P) = \Omega\gamma\,(K_1 + K_2) = \Omega\gamma\kappa. \qquad (1.7)$$

If surface diffusion dominates the system's kinetics, the capillarity-driven shape evolution can be even more complicated due to contributions of different species like ad-atoms and surface vacancies.

Capillary phenomena in solid-state systems were brought into focus of materials science with the advent of powder metallurgy in the first half of the 20th century [27]. Various metallurgical processes involve the capillarity-driven reduction of surface free energy, for example, contact sintering [28] or thermal faceting [29]. The Plateau-Rayleigh instability was observed for the first time in the solid state during the sintering of wire compacts (cf. Fig. 9 in Ref. [30]). The authors did not recognize this renown surface instability of a cylindrical object and called it "erratic pore closure" at that time. The theoretical foundations of capillary phenomena in solid-state systems and the corresponding material transport processes, with a strong emphasis on metals, were established by Herring, Mullins, Sekerka and others from the 1950's onward [25, 26, 31, 32, 33, 34]. The aim was to describe capillary phenomena in the micrometer range with analytical continuum equations. Already in 1963, Mullins pointed out that capillary driving forces are seemingly small but they become dominant on a sufficiently small scale corresponding to a large surface-to-volume ratio [25]. In the micrometer range, capillary phenomena in solid metals are observed during thermal treatments at temperatures close to the melting temperatures for time spans from several hours to days [27]. Due to the characteristics of the diffusion length (Einstein relation), the thermal budget required to obtain a capillarity-driven morphological change scales inversely with the surface-to-volume ratio of the structures. For illustration, Tab. 1.1 lists the surface-to-volume ratio with shrinking structure size of an ideal Au cluster of spherical geometry given by the ratio between the number of surface atoms $N_{\mathrm{surf.\ at.}}$ and the total number of atoms $N_{\mathrm{at.}}$

At present, where the miniaturization of functional structures – particularly in modern information technology – has reached the sub-100 nm range [35], capillarity-driven morphological transformations will occur at much lower thermal budgets compared to metallurgical situations, i.e. for lower temperatures and/or for shorter durations of thermal processing. It is expected that this tendency of the miniaturization of func-

tional structures (often called "Moore's Law"[4]) will continue, thereby, reaching even higher integration densities. In order to avoid capillarity-induced device failure during high-temperature processes or during high-temperature device operation it is therefore of vital importance to examine how nanoscale solid-state systems behave under the action of the capillary force, particulary from the atomistic point of view.

   Two representative examples of capillarity-driven transformations of sub-100 nm solid-state structures are

  1. the Plateau-Rayleigh instability of single-crystalline NWs and

  2. the dewetting of ultra-thin films

which are depicted in Fig. 1.1 (real experiments) and for comparison Fig. 1.2 ("computer experiments" using the lattice KMC method). In these cases, the corresponding thermal budgets are comparable with those applied in ULSI fabrication processes of integrated circuits [35] which indicates the technological challenges arising from capillary instabilities.
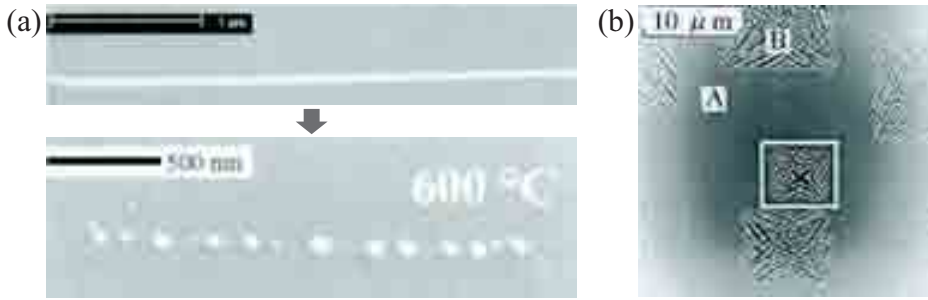

Figure (1.1): Two representative examples of capillary instabilities in sub-100 nm solid-state systems. (a) Plateau-Rayleigh instability of a single-crystalline, [011]-oriented Cu NW with an initial diameter of 38 nm and a length of 1.7 μm which transforms and thereby disintegrates during a thermal treatment at 600 °C within 10 min into a chain of Cu NCs (from Ref. [1]); (b) Dewetting of an ultra-thin (001)-SOI layer (top view; initially 10 nm in thickness) into complex patterns of Si NCs and nanorods during a thermal treatment at 950 °C for 10 s indicating that crystallographic anisotropy can play an important role in solid-state capillary processes (from Ref. [37]).
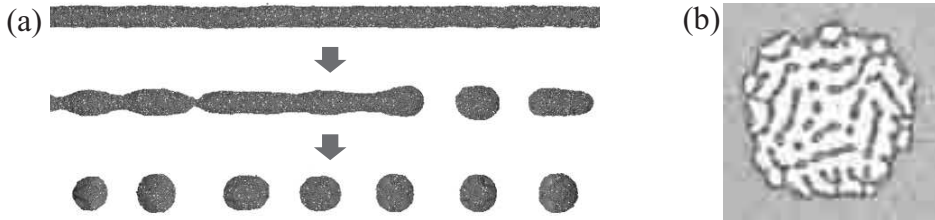
Figure (1.2): Examples of KMC simulations (a) on the Plateau-Rayleigh instability of a cylindrical structure (cf. chapter 4 for details) and (b) on the dewetting of a thin layer (top view). The comparison with Fig. 1.1 reveals that the reaction pathways obtained from 3D lattice KMC modeling have a lot in common with those of real nanoscale systems.

---

   [4]Named after Gordon Moore who found empirically that the number of transistors on integrated circuits doubles approximately every 24 months [36].

1.3 Non-Conventional Methods of Nanostructure Fabrication and Modification

There are two conceptually different approaches to fabricate functional structures in the sub-100 nm range [38]. At first, the extension of the conventional technology, where structure generation is achieved by "sculpting" bulk material (e.g. by photo lithography and chemical etching) towards smaller feature sizes by reducing the lithographic wavelength ("top-down" approach). The other approach is based on self-organization and self-assembly processes where individual structures grow from atomistic processes and later arrange themselves forming an ensemble of structures ("bottom-up" approach). The latter approach, however, suffers severe difficulties due to thermal fluctuations which usually prevent the formation of long-range-ordered and regular nanostructure ensembles (cf. Fig. 1.1 (a)). There are various strategies to circumvent this inherent nanoscale fluctuation problem. In the following, three of them are briefly portrayed since they come into focus again in the subsequent chapters.

1.3.1 Combined Top-Down/Bottom-Up Approach

It is widely expected that the combination of conventional lithographic methods (top-down) with self-organization processes (bottom-up) can solve many problems to produce complex structures with a minimum feature size below 50 nm [39]. Nonetheless, it will be difficult to implement combined approaches into device production due to high technological barriers. These combined processes must in any case be fast, reliable and cheap. An important example of a combined approach is the lateral pre-structuring of thin films (e.g. thin SOI) and the subsequent self-organized formation of nanostructure patterns which arrange in a regular manner due to an initial geometrical constraint (cf. Fig. 1.3 and subsection 4.6.2). In chapter 3, a further combined top-down/bottom-up processes is presented where the laterally confined implantation of energetic ions using a FIB leads to the formation of self-organized NW structures during a subsequent phase separation process at elevated temperatures.

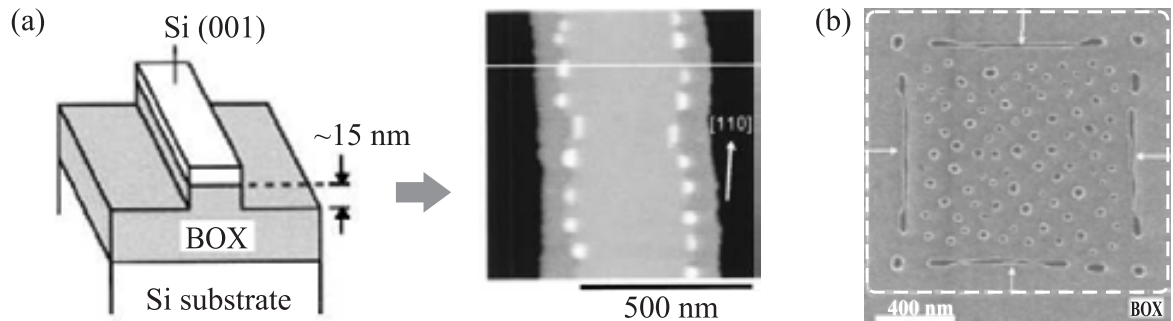**Figure (1.3):** Two examples of combined top-down/bottom-up processes to form ordered Si nanostructures atop SiO_2 by self-organized dewetting of pre-structured SOI: (a) Dewetting of a SOI stripe into chains of Si NCs parallel to the edges of the stripe (taken from Ref. [40]; cf. Fig. 4.37); (b) Dewetting of a pre-structured SOI square into a complex pattern of peripheric Si NWs and a central Si NC pattern (taken from Ref. [41]).

1.3.2 Guided Self-Organization by External Forces Fields

Free evolution (self-organization) of structures is accompanied with thermal fluctuations, particular at the nanoscale. These fluctuations have to be suppressed for a technological exploitation of bottom-up processes if one aims at nanostructure formation. In this connection, non-equilibrium processing during the self-organized evolution can result in regular and long-range-ordered structures. In other words, if external fields are applied on a system the self-organization of that system can be influenced and thereby the self-assembly of nanostructures can be "guided" into a wanted direction. For example, temperature fields, which are periodic in space, induce periodic temperature gradients which bias the material transport processes in the system. In subsection 5.1.1, it will be demonstrated that periodic thermal gradients suppress self-organization-inherent fluctuations during the Plateau-Rayleigh instability of cylindrical NW structures leading to the formation of long-rang-ordered chains of regular NCs (cf. Fig. 1.1 and Fig. 5.1). Moreover, it is shown that in-plane periodic temperature fields cause the formation of regular surface patterns (ripples or hillock arrays) on thin films (cf. subsection 5.1.2).

1.3.3 Nanostructure Shape Evolution Driven by Collisional Mixing

Collisions with energetic ions can cause ballistic displacements of atoms in a solid. Thereby, atomic configurations are obtained which would not be achieved by thermally activated mass transport. The morphology of nanostructures under ion bombardment can therefore change in puzzling ways depending on the balance between thermal and "ballistic" forces, i.e. on the ratio between the rates of thermally activated and ballistic displacements [15, 17, 19, 42]. In view of the capillarity-induced transformation of crystalline NWs it will be demonstrated in section 5.2 that the Plateau-Rayleigh instability of single-crystalline NWs can be either accelerated or retarded depending on the crystal orientation of the NW and on the balance between capillary force and collisional mixing. Moreover, periodicity and shape of the emerging NCs are controlled by the strength of collision mixing.

1.4 Computer Simulations: A Virtual Reality

During the past two decades, computer simulations have become significant in the fields of solid-state physics and materials research [43, 44, 45, 46]. Computer simulations are capable to deliver detailed insight into complex physical and chemical processes, thereby, improving our understanding of these processes. Therefore, it is legitimate to state that computer simulations span the bridge between analytical theory and experiment (cf. Fig. 1.4).

Besides the scientific and technological benefits, computer simulations have also gained economic importance. The globalization of markets puts enormous pressure on the industry to reduce the time span between fundamental materials research, development of devices and production in order to bring new products fabricated with advanced materials onto the market as quickly as possible [48]. This has led to the intensified use of computer simulations during recent years. In computer experiments one
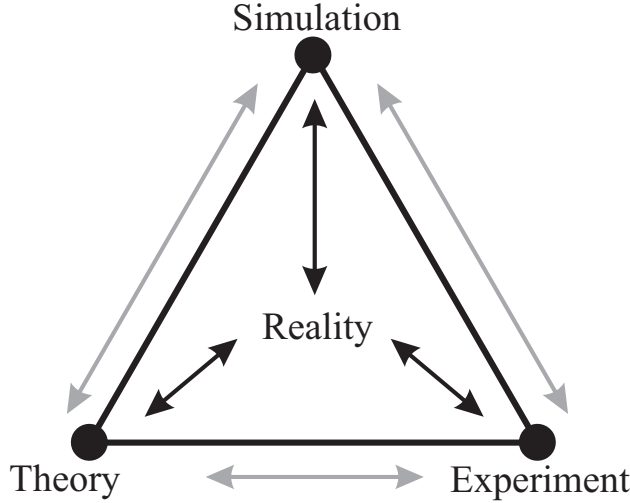
Simulation

Reality

Theory   Experiment

Figure (1.4): A schematic representation of the interdependence of theory, simulation, and experiment (after Ref. [47]).

aims at reliable, quick and inexpensive predictions on fabrication methods of functional device structures and of the operation modi of such devices.

Performing computer simulations can be considered as the two sides of one medal: developing physical models and conducting experiments. Uzi Landman famously said that "computer simulations can be used as a source of physical information which is not accessible to laboratory experiments, and in some instances the computer experiment itself serves as a testing ground for theoretical concepts" [49]. In the computer model one can "switch off" or "switch on" effects and thereby examine their physical significance for the behavior of the system. Therefore, one often speaks about the "third path" [46]. If the results of a computer simulation reproduce the experimental findings the computer simulation becomes trustworthy and it can be concluded that the underlying theoretical models are correct. In that case, the input parameters of the simulation can be adjusted even in ranges which have not been accessed in real experiments. Thus, computer modeling becomes predictive, and in some cases real experiments may indeed be substituted. Besides the predictive power, the importance of computer simulations in materials science is to quantify and to visualize the energetics as well as the dynamics of physical processes *in-situ* with atomistic resolution which can hardly be realized by experimental means.

Today, numerous simulation methods are available to examine the physical behavior of solid-state systems. Every simulation model has a characteristic domain in which it can be applied appropriately (cf. Fig. 1.5). All simulation methods vary with regard to the size of the system, the number of atoms involved, and the time scale of the processes of interest. As rule of thumb for computer modeling it can be stated that the more detailed the requirements for the knowledge of the atomistic kinetics are the more complex the underlying model needs to be and the bigger the computational effort becomes.

Ground state properties of many-atom systems, for example, can be examined with very high accuracy using first-principle ab-initio methods. Here, electronic and atomic structures are calculated which arise from the interaction of wave functions, i.e. quantum mechanical approaches are used which try to solve the system's Schrödinger equation,

$$\mathcal{H}\Phi\left(\vec{r}\right)_k = E_k \Phi\left(\vec{r}\right)_k \ , \tag{1.8}$$

in a self-consistent manner. Here, $\mathcal{H}$, $\Phi\left(\vec{r}\right)_k$, and E_k denote the system's Hamiltoni-
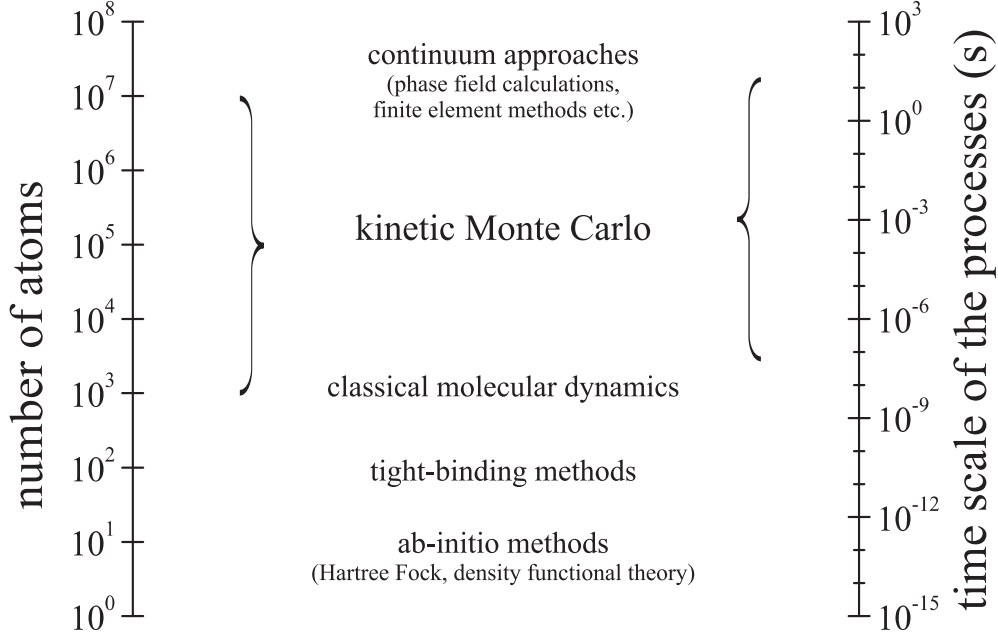
Figure (1.5): A schematic representation of computer simulation methods for solid-state systems with typically accessible system sizes and time scales.

an, its kth eigenfunction (wavefunction), and the energy eigenvalue of the kth state, respectively. The accurate computation of electronic levels of systems that contain many atoms is a highly complex task which has lead to the development of sophisticated approximative techniques like density functional methods [46]. Despite the loss of accuracy, even in this case the computational effort for a system with N electrons scales approximately with the third power of N [45]. Thus, systems with maximally a few hundred atoms can be studied in this manner on modern high-performance computers [46]. To circumvent these computational restrictions other simulation methods were developed that are based on semi-empirical techniques, e.g. tight binding methods [45]. However, all these simulation methods are far too slow for the modeling of the evolution of structures at the micro- and nanoscale. Their domain of application is the investigation and prediction of fundamental materials properties such as the structures of crystalline solids in the ground state.

For the examination of the dynamics of systems with thousands or even millions of atoms empirical models have to be applied with interaction functions that contain only few parameters. For such atomistic models the computational effort scales linearly with the number of particles. In order to perform atomistic simulations on the dynamics/kinetics of a system there are basically two options. Indeed, the dynamics of a system of classical particles that interact via a potential $V_{ij} = V_{ij}(\vec{r}_{ij})$, where $\vec{r}_{ij}$ is the distance vector between the ith and the jth particle, can be described by solving Newton's classical equations of motion numerically:

$$m_i \ddot{\vec{r}}_i = -\vec{\nabla} \sum_j V_{ij} \ . \tag{1.9}$$

For simplicity, only a pair potential V_{ij} is written here, however, the atomic interaction in condensed matter is a many-body phenomenon, in general. This procedure is the so-called molecular dynamics (MD) method [50, 51]. Thereby, starting from a given point in phase space $\{\vec{r}_i, \vec{p}_i\}$, where $\vec{r}_i$ and $\vec{p}_i$ denote the position and the momentum

vector of the ith particle, respectively, the evolution of a system is calculated deterministically. The limitation of MD simulations lies in the fact that the time scale of atomic motion is in the range of 10^{-12} s. Thus, atomic positions and momenta have to be determined in infinitesimal time steps in the range of 10^{-15} s which is correlated with the highest characteristic frequency in the system. This time step has an intrinsic limitation, i.e. if it becomes too large the numerical solution becomes unstable. Therefore, MD simulations are applied up to the nanosecond range in general (for small systems up to a few microseconds), e.g. to study diffusion pathways of single defects in crystalline silicon [52]. On the other hand, in the case of sub-nanosecond processes like the shock-induced melting of metals, systems that contain several million atoms can be simulated with MD [53]. However, for these leading-edge large-scale simulations, up to two hundred thousand (!) micro processor units are needed in parallel operation [54].

Compared to individual diffusion pathways or the spreading of shock waves, phase separation and capillary phenomena of solid phases proceed on time scales which are several orders of magnitude larger [1, 3, 55]. Thus, treating the motion of millions of atoms with MD over a range of seconds or longer is not practicable with modern computers.

Instead of solving Newton's equations of motion it can alternatively be assumed that the motion of atoms results in positional changes which happen with a well-defined probability. In other words, the physical view on the system's dynamics is shifted from a deterministic to a stochastic (or statistic) description. In this stochastic picture, the system's atomic configuration $\mathcal{C}$ corresponds to a defined energy E. Coupled to an external heat bath, positional changes of individual atoms (e.g. diffusional jumps) may consequently change the energetic state of the whole system. Such transitions $\mathcal{C}(E) \rightarrow \mathcal{C}'(E')$ take place with an exact probability that is determined by the interaction between neighboring atoms in a close neighborhood and relevant system parameters such as temperature T. The transition probability P_{if} is usually of Boltzmann-type, i.e.

$$P_{if} \propto \exp\left(-\frac{E_{\text{ final state}} - E_{\text{ initial state}}}{k_B T}\right) \ . \tag{1.10}$$

Here, k_B is Boltzmann's constant. Because of this probabilistic approach of atomic migration a vast number of random numbers is required on the basis of which the decision whether an atom moves or not is made. Therefore, this method is named "Monte Carlo" (MC) after the gambling resort in Monaco. In MC simulations, only the energetic difference between the initial and the final state is of relevance for the calculation of the transition probability. However, the detailed energy landscape in-between these states does not play a role, in general. MC models provide therefore a simplified atomistic dynamics compared to MD simulations. Thereby, it is possible to very effectively scan through the phase space of the system. Several phase space sampling methods are available. For thermally activated processes such as atomic migration the dynamics of Metropolis [56] or Glauber [57] are mainly used. The great advantage compared to MD simulations is that the frequency in a MC simulation is not the vibration frequency of atoms around their equilibrium position but the frequency with which the atoms undertake jumps to neighboring sites. The series of configurational states that the system goes through during a MC simulation is the so-called "reaction pathway" which reflects the kinetics of the system's evolution. Therefore, this specific MC simulation method is

called *kinetic* MC (KMC). It can also perceived as a realization of a Markovian chain of states in view of the transition probability [58, 59]. Usually, KMC methods rely on the discretization of time and also of space, i.e. atoms are bound to the nodes of a lattice. Such lattice KMC methods are special realizations of cellular automata which are of stochastic[5] and probabilistic[6] nature [60, 61].

Yet, there are other simulation methods by means of which the shape evolution of nano- and micro-sized systems can be studied [62]. These are continuum approaches like finite element methods or phase field calculations that are usually employed if the physical quantities of interest vary spatially over distances that reach much further than the interatomic spacing (e.g. stress effects) [63]. Phase field methods can even be used to examine phenomena that are due to crystallographic anisotropy, e.g. dendritic growth at liquid-solid interfaces [64, 65, 66] or stress-induced self-assembly of surface patterns [67]. However, local phenomena that are due to atomic-scale effects like nucleation, dissociation, grain boundary segregation, or single diffusion events can hardly be described by these methods – in other words, the physical picture is less detailed [68].

In recent years, much progress has been made regarding the combination of various simulation methods which is known as "multi-scale modeling". Here, the aim is to merge the advantages of different methods, e.g. to be able to consider short-term and short-range processes that give rise to the long-term and long-range evolution of a system, where one simulation method alone would not be able to deliver reasonable results. One example from the realm of ion-solid interaction is the combination of MD and KMC simulations for the investigation of compositional pattering of immiscible alloys. Here, MD simulations deliver detailed distributions of the relocated atoms produced during energetic particle collisions which in a second step are input for a lattice KMC model to simulate the long-term evolution of the long-range compositional patterns in the binary alloy [69].

In conclusion, there is a variety of computer models aiming at the calculation and prediction of the properties and the dynamic behavior of solid-state systems. Among these methods, KMC models have the main advantage to be able to consider local atomistic processes in a realistic manner on experimentally relevant time scales [70]. The diffusion-controlled transformation of the macroscopic shape of nano- and micro-sized solid-state systems is a long-term process based on atomistic events which renders the KMC method the simulation method of choice. Despite the ongoing growth of computer power, that is going to shift the domain boundaries of each simulation method (cf. Fig. 1.5), the KMC method will certainly keep its role in this particular field of computational materials science.

Despite the foregoing argumentation, one has to keep always in mind that "physical models are caricatures of reality" [71, 72], i.e. they are simplifications and abstractions of the real world.

---

[5]stochastic: the atom that is given the chance to migrate at a certain time is chosen randomly from all atoms in the system.

[6]probabilistic: the transition from one state to another occurs with the defined probability P_{if}.

Chapter 2

Lattice KMC Simulations for Nanostructure Shape Evolution

In this chapter, the lattice KMC method is presented with emphasis on characteristics that are relevant for this work: phase separation, diffusion-mediated capillary phenomena, non-equilibrium processes due to external field gradients or collisional mixing. For a detailed survey of the realm of KMC methods in computational physics the interested reader is referred to the works of Binder & Heermann[73], Landau & Binder[47], Newman & Barkema [59], or Voter [74].

2.1 KMC in Materials Research

In many areas of materials science lattice KMC methods have been applied for a description of discrete atomic-level, molecular-level, or spin-level processes, e.g.

- phase separation [75, 76, 77, 78, 79],

- bulk or surface diffusion phenomena [80, 81, 82, 83],

- the growth or erosion of thin films [84, 85, 86, 87, 88, 89, 90, 91, 92, 93, 94],

- the chemical ordering of metal alloys [95, 96, 97, 98, 99, 100, 101, 102, 103],

- ion-irradiation-induced effects [98, 104, 105, 106, 107],

- magnetic phase transitions [108, 109],

- strain-induced effects on nucleation [110, 111],

- formation of ordered polymer structures [112] etc.

In the past decade, the lattice KMC code used in the frame of this work was developed at FZD [11, 113, 114, 115]. It has been mainly employed for the modeling of phase separation phenomena during thermal treatments of supersaturated solid solutions that were usually achieved by surface-near implantation/irradiation of energetic ions into/of thin layers, of the coarsening of NC ensembles (Ostwald ripening), and of NC self-alignment processes at interfaces [11, 17, 115, 116, 117, 118, 119, 120, 121, 122].

Additionally, this lattice KMC model was applied for the description of ion-beam-driven systems, i.e. systems in which atoms change their site due to thermal activation but also due to collisions with energetic particles. Such ballistic displacements have

been studied during the irradiation of NCs or thin films with energetic ions [17, 98, 115, 123, 124].

In continuation and extension of these former studies, the present work focuses on the description and the prediction of reaction pathways of

- the FIB-based IBS of NW structures,

- capillary instabilities of nanostructures (mainly cylindrical ones), and

- the influence of applied temperature fields and collisional mixing on the capillary-driven nanostructure evolution.

Behind this spectrum of topics there are three physical principles. At first, the self-organized relaxation of a solid-state system from a non-equilibrium to the equilibrium state driven by the diffusion-mediated capillary force. These investigations had been partly motivated by preliminary results on FIB-based IBS and the Plateau-Rayleigh instability of NWs [125, 126]. Secondly, applied temperature fields which control the system's relaxation pathway towards equilibrium ("guided" self-organization), thus, suppressing thermal fluctuations which leads to long-range-ordered nanostructures. Thirdly, non-thermal processes like ballistic displacements of atoms which occur during energetic particle collisions which can literally "drive" a system from a quasi-equilibrium to a non-equilibrium steady state.

2.2   Conserved-Order-Parameter Ising Model

In section 1.4, it was pointed out that a lattice KMC simulation is a statistical method to describe the spatio-temporal development of a many-particle system in which the particles are positioned on the nodes of a rigid grid. In this work, physical processes are described which occur in solid-state systems, thus, the particles are interpreted as atoms whose spatial positions are discretized and coincide with lattice nodes (crystal). The system's energetic state is determined by the atomic configuration and the interatomic potential. In order to provide a control parameter, the system is embedded into an external heat bath[1] of temperature T, i.e. in the nomenclature of thermodynamics a canonical ensemble is given if the volume of the system and the number of atoms is constant.

Atomic interaction in the solid phase is a very complex phenomenon which is strongly characterized by the electronic structure of the material of interest expressed by the different types of bonding [49, 127, 128]. In order to run a KMC simulation for systems with millions of atoms efficiently on a computer, energetics and dynamics of such an artificial microworld has to be simple [60]. Therefore, the present like many other lattice KMC methods are based on an Ising-like model[2] [43, 47, 59, 73, 96, 129, 130], where atomic interaction is based on a simple pair-potential, i.e. a bond energy of certain strength is assigned to each pair of NN atoms. Nonetheless, more complex interatomic interactions (e.g. many-body interactions) would not directly lead to an increase

---

[1]In other words, there is no condensation or evaporation heat considered, i.e. the heat locally released or consumed does not change the local temperature. All these processes are coupled to the heat bath.

[2]In the literature, the Ising model is considered as the "drosophila" of interaction models [115].

of computation speed because of the cellular automaton concept of the present KMC code.

The Ising model was originally developed by Ernst Ising in the 1920's to account for the magnetic phase transition from a paramagnetic to a ferromagnetic state [131]. In the Ising-picture of magnetism, single spins are considered which can either point up or down. If the system is quenched below the critical temperature, the system approaches a ferromagnetically ordered state, i.e. domains are formed in which neighboring spins point into the same direction. Throughout this process, the overall magnetization changes, i.e. the number of up- and down-spins varies with time (spin flips). In the present case, however, atomic particles of one or more sorts are considered that can occupy the vertices of a rigid lattice. These atoms are allowed to change their positions, i.e. in case of migration they exchange their positions with neighboring vacancies or with atoms of different sort. Consequently, the number of particles is conserved, i.e. in the language of magnetics this model allows no spin flips, but only spin exchanges. Thus, the overall "magnetization", i.e the number of particles is invariant (conserved order parameter). This model is named after Kawasaki [57].

The kinetics of the many-particle system is described by transitions of configurational states which may cause a change of the systems internal energy (ΔE). Those state transitions are thermally activated and occur with a defined Boltzmann-like[3] probability ($\propto \exp(-\Delta E/(k_B T))$) at a certain attempt frequency (definition of the time scale). The state transition probability provides therefore a weighting of all possible atomic configurations in the system (importance sampling), thus, preserving ergodicity while aiming at the minimization of the system's free energy. The series of states the system runs through is called the "reaction pathway". Starting from a non-equilibrium state, it reflects the system's free evolution (i.e. relaxation) in an approximate manner because of the simplified atomistic dynamics (discrete degrees of freedom due to the rigid lattice; no surface relaxation; all atomic jump configurations have to be known prior to each jump; reduced variety of diffusion events etc.).

Energetics. In the classical Ising model, a coupling between NN spins is considered, thus, the system's Hamiltonian at zero external magnetic field reads [59]:

$$H = - J_{NN} \sum_{\langle i,j \rangle_{NN}} s_i \, s_j \; , \tag{2.1}$$

where J_{NN} is the interaction energy[4]. The notation $\langle i, j \rangle_{NN}$ expresses that i and j are NN lattice sites. The sum has to be taken over all NN lattice sites. The spin variables s_i can take two values: $+1$ (spin up) or -1 (spin down).

In the atomic picture, however, the above Ising-Hamiltonian has to be modified. The spin variables have to be redefined as variables which give the occupation state of a single lattice site [59]:

$$c_i = \frac{(s_i + 1)}{2} \; , \tag{2.2}$$

---

[3]Maxwell-Boltzmann statistics apply because localized atoms are considered that are distinguishable.

[4]$J_{NN} > 0$: ferromagnetic coupling; $J_{NN} < 0$: anti-ferromagnetic coupling

thus,

$$
c_i = \begin{cases} 1 & \text{if the lattice site is occupied or} \\ 0 & \text{if the lattice site is empty.} \end{cases} \tag{2.3}
$$

Defining a NN bond energy ε_{NN}, the new Hamiltonian reads:

$$
H = - \varepsilon_{NN} \sum_{\langle i,j \rangle_{NN}} c_i\, c_j \; + \; \text{constant}. \tag{2.4}
$$

with

$$
\varepsilon_{NN} = 4 J_{NN} \; . \tag{2.5}
$$

In the frame of this work, only attractive NN interactions are considered, i.e. $\varepsilon_{NN} > 0$. Repulsive NN interactions between particles, i.e. $\varepsilon_{NN} < 0$, would be used to study antiferromagnetic-like and ferri-like ordering of particles which occurs e.g. in chemically-ordered intermetallic alloys such as FePt [97] or in intercalated compounds such as Ag-TiS$_2$ [132].

Since two atoms share one NN bond, the binding energy E_b of a fully coordinated atom (i.e. the bulk binding energy or the sublimation energy) for a lattice with η NN lattice sites is given by

$$
E_b = \tfrac{1}{2}\, \eta\, \varepsilon_{NN} \; . \tag{2.6}
$$

Atomic interactions in solids are of very complex nature due to the electron structure of the materials [49, 127, 128]. In general, atoms interact over a range that exceeds the NN distance. Moreover, atomic interaction in solids is usually not a two-body phenomenon, but may involve the correlative interaction of several atoms [5]. In this regard, the Hamiltonian given in Eqn. 2.4 may be extended towards many-body interaction terms and interaction terms that exceed the NN distance:

$$
\begin{aligned}
H = \;&- \; \varepsilon_{NN} \sum_{\langle i,j \rangle_{NN}} c_i\, c_j \; - \; \zeta_{NN} \sum_{\langle r,s,t \rangle_{NN}} c_r\, c_s\, c_t \; - \; ... \\
&- \; \varepsilon_{NNN} \sum_{\langle i,j \rangle_{NNN}} c_i\, c_j \; - \; ... \\
&- \; ...
\end{aligned} \tag{2.7}
$$

Here, ζ_{NN} denotes the three-body interaction energy between NN lattice sites; ε_{NNN} stands for the two-body interaction energy between NNN lattice sites (cf. section 2.5). Likewise, many-body interactions and/or neighborhoods of even higher rank can be considered. Note that in the case of many-body interaction terms the prefactor of the contribution to the binding energy (cf. Eqn. 2.6) changes with the rank of the interaction, e.g. for a three-body interaction it amounts to 1/6.

---

[5]In metals, for example, the bond strength typically increases if the coordination number is reduced which originates in the quantum mechanical bond formation [133].

Dynamics. In many studies, MC simulations are applied to calculate static properties like critical exponents. In that case, the Hamiltonian completely describes the situation, i.e. the rules of a state transition can almost be arbitrary since the correct equilibrium distribution of states is needed only, i.e. detailed balance must be fulfilled [58]. On the contrary, if one aims at the examination of dynamical properties of a far-from-equilibrium system in which thermally activated atomic processes like diffusion or aggregation phenomena occur, the situation becomes more difficult since the dynamics of the transition from one state to another can not be deduced from the Hamiltonian alone. The dynamics is expressed by transition probabilities. Thus, the evolution in lattice KMC can be interpreted by a master equation [73]. An arbitrary configuration of a system can be characterized by a set of probabilities $W(\varphi)$ to find the system in the state φ. The time evolution of a state is expressed by the master equation for $W(\varphi, t)$ [57, 134]:

$$\frac{\partial}{\partial t} W(\varphi, t) = \sum_{\psi} \left\{ P(\varphi|\psi) W(\psi, t) - P(\psi|\varphi) W(\varphi, t) \right\} , \tag{2.8}$$

where $P(\varphi|\psi)$ is the transition probability per unit time from state ψ to state φ.

If an atom jumps from a lattice site i to a vacant NN site f the configuration of the system is changed which goes along with a change in internal energy:

$$\Delta H = (n_i - n_f)\, \varepsilon_{NN} , \tag{2.9}$$

where n_i and n_f represent the numbers of occupied NN lattice sites of the two neighboring sites i and f, respectively. It is emphasized that the two-body interaction ε_{NN} is constant throughout the entire system, thus, the binding energy of an atom scales linearly with its number of NNs.

In this work, the probability P_{if} for such a NN jump is calculated according to the Metropolis algorithm [56, 135]:

$$P_{if} = \begin{cases} \Gamma_0 \exp\left\{-E_m \beta\right\} & , \quad n_f \geq n_i \\ \Gamma_0 \exp\left\{-\left(E_m + \Delta H\right)\beta\right\} & , \quad n_f < n_i , \end{cases} \tag{2.10}$$

where Γ_0 is the attempt frequency for atomic jumps referring to the Debye frequency which is in the THz range $(10^{12}\,\text{s}^{-1})$, i.e. it contains dynamical information. In solids it is easy to understand the attempt frequency: it is the vibration frequency of the atom. It can often be predicted to fair accuracy when the atom vibration properties of the lattice (elastic and sound) are known. As a good approximation, Γ_0 is T-independent, at least in solids, because the elastic constants are almost T-independent. In Eqn. 2.10, E_m denotes the migration energy barrier (cf. Fig. 2.1) and $\beta = 1/(k_B T)$ bears common meaning.

In a simplifying manner it is assumed that the migration energy barrier E_m is equal throughout the entire potential energy landscape of the virtual KMC crystal. Thus, Eqn. 2.10 can be rewritten in a reduced form (cf. Fig. 2.2):

$$\tilde{P}_{if} = \frac{P_{if}}{\Gamma_0 \exp\left\{-E_m \beta\right\}} = \begin{cases} 1 & , \quad n_f \geq n_i \\ \exp\left\{-\Delta H \beta\right\} & , \quad n_f < n_i . \end{cases} \tag{2.11}$$

The term $1/(\Gamma_0 \exp\left\{-E_m \beta\right\})$ is then a measure for the time scale [115]. In most of the KMC simulations presented in this work, only the ratio between bond energy and
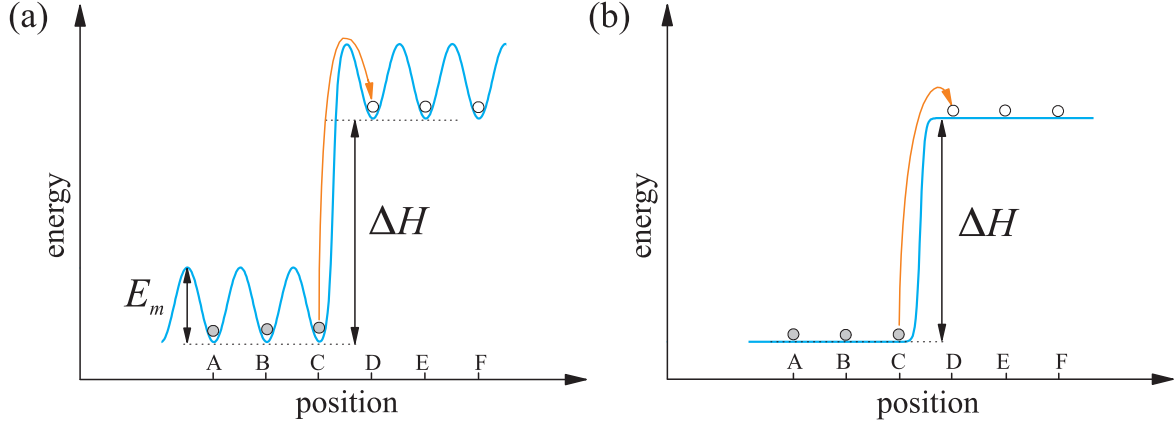
Figure (2.1): A simplified schematic representation of diffusion in the KMC model using the concept of energetic barriers. In (a), between each lattice site there is an energy barrier E_m accounting for the activation of migration on the lattice. Additionally, there is an energy barrier ΔH which has to be overcome during a state transition which changes the system's internal energy, e.g. during the evaporation of an atom from a cluster of atoms (solid circles, pos. A-C), i.e. during the jump to an empty NN lattice site (open circles, pos. D-F). In (b), the energy landscape of the lattice is reduced according to Eqn. 2.11.

temperature is of interest (reduced variable), thus,

$$\tilde{P}_{if} = \begin{cases} 1 & , & n_f \geq n_i \\ \exp\left\{-(n_i - n_f)\tilde{\varepsilon}_{NN}\right\} & , & n_f < n_i , \end{cases} \tag{2.12}$$

where

$$\tilde{\varepsilon}_{NN} = \frac{\varepsilon_{NN}}{k_B T} . \tag{2.13}$$

The acceptance of transitions from low to high energy states refers to the fact that the Helmholtz free energy F,

$$F = U - TS , \tag{2.14}$$

is minimized where U and S denote internal energy and entropy, respectively. The internal energy U can directly and exactly be determined from any configurational state of the system by counting the NN bonds (Hamiltonian). However, the correct determination of entropy for a given configurational state of a many(million)-particle
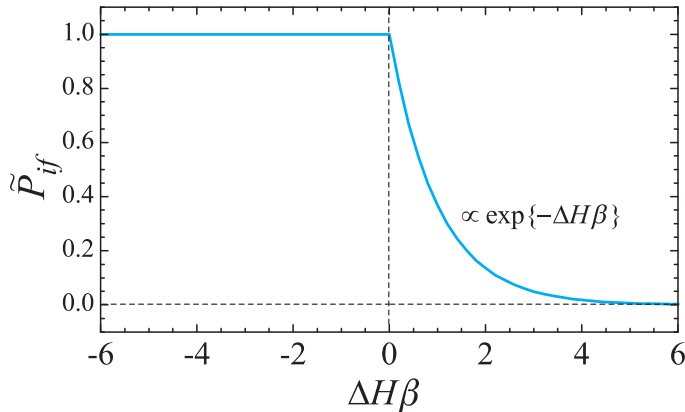

Figure (2.2): The Metropolis transition probability $\tilde{P}_{if}$ [56, 59].

system is a very difficult task since it requires the calculation of the system's partition sum. Moreover, in the frame of this work, non-equilibrium states with spatial inhomogeneities (separated phases) are mostly considered; for such systems the computation of entropy is still subject to scientific debate although some approximations do exist in the literature [136, 137, 138].

If one assumes that F converges to its minimum monotonically from its initial value, one finds for its time derivative [138]:

$$\frac{\partial F}{\partial t} = \frac{\partial U}{\partial t} - T\frac{\partial S}{\partial t} \leqslant 0 \ . \tag{2.15}$$

This leads to the constraint

$$\frac{\partial U}{\partial t} \leqslant T\frac{\partial S}{\partial t} \ . \tag{2.16}$$

In a closed system, entropy can only increase according to the second law of thermodynamics, i.e. $T\frac{\partial S}{\partial t} \geq 0$ ($\frac{\partial S}{\partial t} > 0$ in irreversible processes; $\frac{\partial S}{\partial t} = 0$ in equilibrium). In chapters 3 and 4 it will be seen that the time derivative of the internal energy, $\frac{\partial U}{\partial t}$, is always negative during the capillarity-driven free evolution of nanostructures (relaxation), thus, Eqn. 2.15 is fulfilled. The KMC simulations performed in this work always assume temperatures which are lower than the critical temperature (cf. section 2.3), thus, the contribution of entropy to the free energy is assumed to be small compared to the contribution of internal energy. Consequently, the minimization of free energy during the free relaxation from a non-equilibrium to a quasi-equilibrium state can be described approximately by $U = U(t)$.

Time Scale and MC Loop.   Like the spatial coordinates, the time scale is also divided into discrete intervals, the so-called MC steps (MCS). During a single MCS every active atom in the simulation cell performs one jump attempt on average. In a system with N active atoms, a MCS consists of N MC loops whose computational implementation is schematically outlined in Fig. 2.3. The random selection of atoms has to be used since not only static equilibrium properties but also dynamic correlations are of interest [47]. Thus, a lattice KMC simulation can also be regarded as cellular automaton whose elements (atoms) are chosen randomly (stochastic cellular automaton) and the transition from one to another configuration of the system is probability-dependent (probabilistic cellular automaton) [61, 113, 139]. The cellular automaton concept offers the possibility to include many-body interactions without a penalty in computational speed.

A thorough discussion about the time scale of the present KMC method is given in Refs. [11, 115]. Accordingly, the KMC time scale is linear, however, is becomes temperature-dependent due to the reduced form of the jump probability. Moreover, it is dependent on the employed transition probability algorithm. Consequently, the gauging of the simulation time scale to the time scale of real experiments is a very difficult task (cf. subsection 4.2.1 in Ref. [116]).

The present KMC model relies on a bit-representation of the virtual lattice which enables a bit-encoding of the configurational state transitions. In appendix A, an illustration of important bit-encoding principles is given. Besides the use of bitwise operations, the use of look-up tables for the transition probabilities enhances the simulation
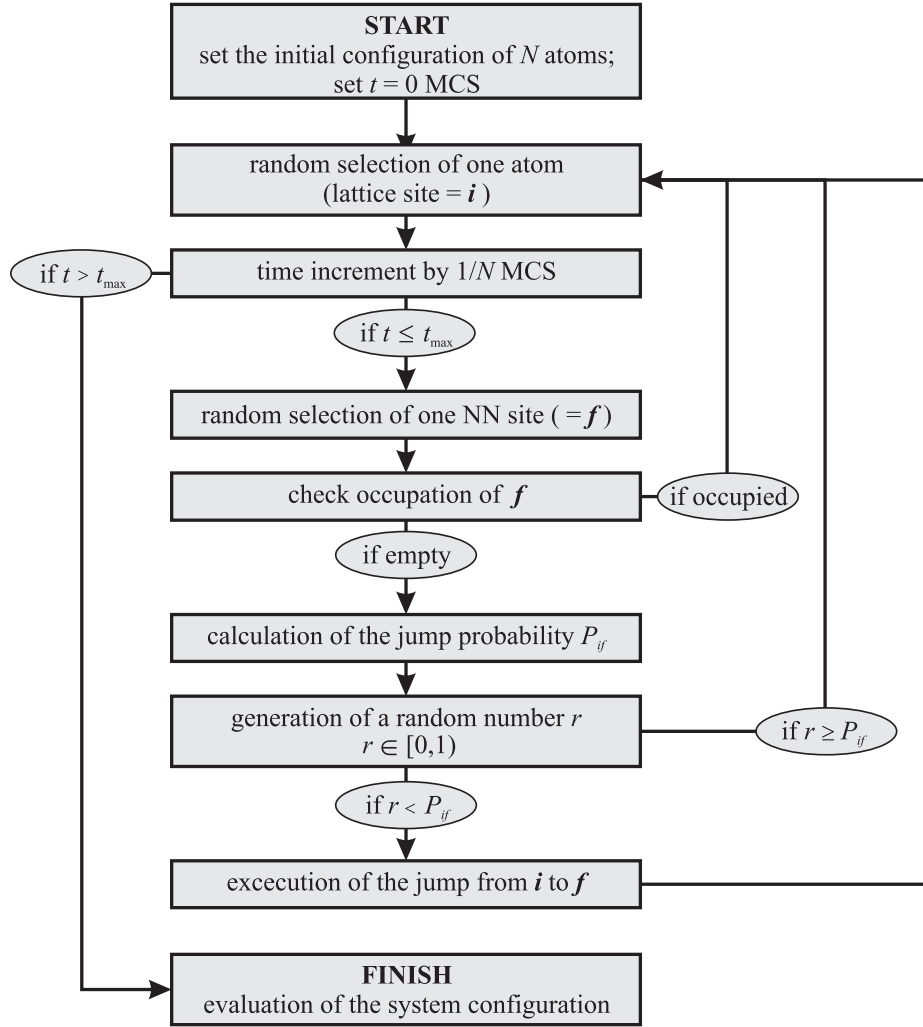
Figure (2.3): A schematic representation of the computational implementation of a MC loop referring to a time interval of $1/N$ MCS.

speed further. For instance, the number of possible NN configurations for two neighboring lattice sites i and f for the f.c.c. lattice is $2^{18} = 262\,144$. Hence it is advantageous to store the corresponding transition probabilities P_{if} in a look-up table so that the exponential function needs not to be calculated for each single jump attempt.

According to Fig. 2.3, unsuccessful jump attempts occur if the chosen NN site is already occupied (so-called "null" events). Moreover, at low temperatures the transition probability is much smaller than one making a jump unlikely which again results in a loss of computation time because no configurational state transition is performed. Therefore, other KMC methods (sometimes called "time-dependent KMC") have been developed which rely on a different procedure by which all possible jump configurations, the corresponding jump probabilities and thereby the time scale are computed prior to each jump [58, 140]. Due to the weighting of all transition probabilities the individual time increment of a MCS differs from jump to jump. This has the advantage that all jumps are successful events, thus, changing the configuration of the system. However, the computational effort to determine all possible jump configurations and their probabilities and to weight those probabilities consumes much computation time (compensation of the benefits) which becomes the longer the larger the number of NNs

is. Thus, these alternative KMC procedures have been mostly employed for 2D system or (2+1)D systems (so-called "solid-on-solid" models) where the number of NN is small [141, 142]. For more complex lattices like the f.c.c. lattice, which has been mainly used in this work, or for systems, in which many different jump processes are possible depending on the environment of each particle, the advantage of time-dependent KMC methods is lost [58].

2.3 Binary Phase Diagram and Phase Separation

In chapter 3, the FIB-based IBS of NW structures is investigated where a supersaturated solid solution with a particular supersaturation gradient evolves via phase separation and coarsening towards a NW structure. Thus, the basic properties of the present lattice KMC method in view of the modi of phase separation are of interest.

A binary system of particles of one sort and vacancies is considered. The KMC lattice is homogeneously occupied with atoms expressed by the particle concentration c. This initial state is quenched at time zero to a finite and positive value of $\tilde{\varepsilon}_{NN} = \varepsilon_{NN}/(k_B T)$. During the free evolution, the system tries to minimize its free energy. Above a critical value $\tilde{\varepsilon}_{NN,c} = \varepsilon_{NN}/(k_B T_c)$ any system with $0 < c < 1$ exhibits a stable homogeneous phase. At $T > T_c$, entropy dominates the interaction energy and although NNs tend to agglomerate, this is a small perturbation on the random configuration.

On the contrary, if the system is quenched below a distinct temperature (coexistence curve in Fig. 2.4) the homogeneous phase loses its stability, i.e. it decomposes and coexisting phases appear. This process can be described by a first-order phase transition [143]. A schematic binary phase diagram and the corresponding free energy as function of c are depicted in Fig. 2.4. Apparently, there are two different modi of phase separation (separated by the spinodal curve): On the one hand the system is quenched into the metastable state for the phase decomposition of which an energy barrier must be overcome (by thermal activation) causing precipitates to nucleate
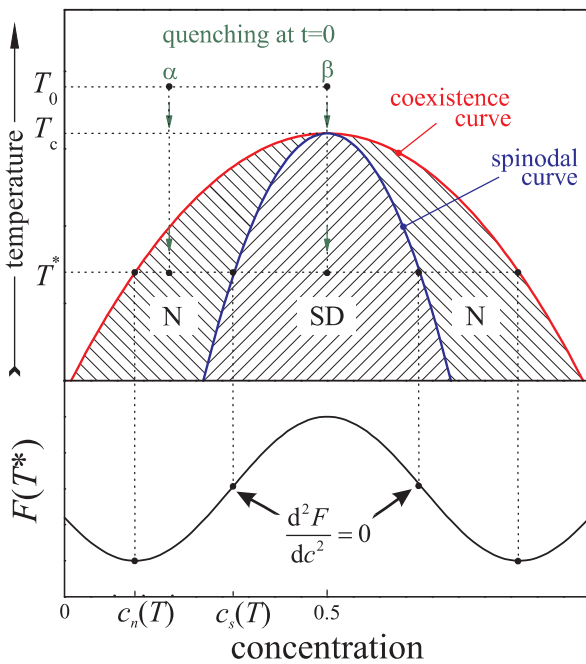

Figure (2.4): A schematic representation of a binary phase diagram (after Ref. [143]) and the corresponding free energy curve. The hatched areas indicate the regions of two coexisting phases (N: nucleation; SD: spinodal decomposition), whereas in the non-hatched area there exists only one homogeneous phase.
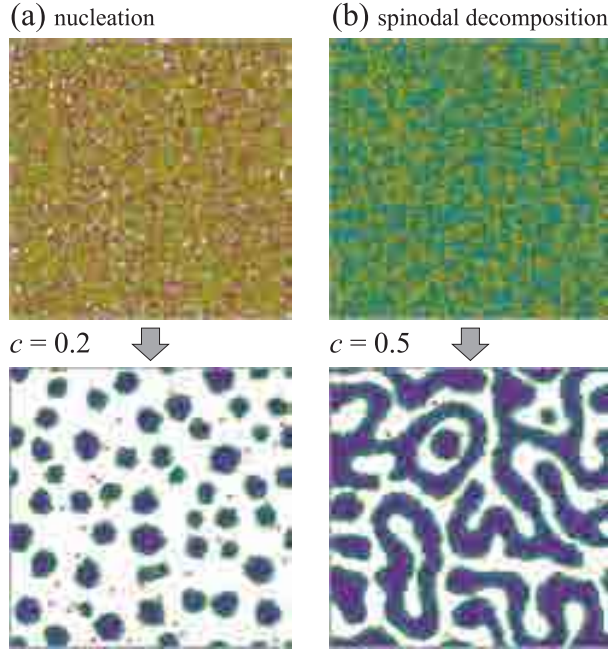
(a) nucleation

(b) spinodal decomposition

Figure (2.5): The two regimes of phase separation prior to (upper row) and shortly after quenching (lower row): (a) nucleation and (b) spinodal decomposition (cf. text for details).

$c = 0.2$

$c = 0.5$

$(\mathrm{d}^2 F/\mathrm{d}c^2 > 0)$. One the other hand the system is quenched into an unstable state which spontaneously decomposes via spinodal decomposition, i.e. interconnected domains of the two phases appear which intertwine each other in a meander-like manner $(\mathrm{d}^2 F/\mathrm{d}c^2 < 0)$. For a thorough discussion of the decomposition mechanisms the reader is referred to Refs. [143, 144, 145, 146]. According to Binder, the differentiation between nucleation and spinodal decomposition is only meaningful in the early stage of phase separation because both the spinodal structure and the precipitate ensemble undergo ageing processes leading to morphological transformations [144]. For illustration, the two modi of phase separation on a f.c.c. lattice are depicted in Fig. 2.5. The lattice sites are randomly occupied with atoms: $c = 0.2$ (Fig. 2.5 (a): nucleation) and $c = 0.5$ (Fig. 2.5 (b): spinodal decomposition). At $t = 0$, both systems are quenched at $\tilde{\varepsilon}_{NN} = 1.3$ and their configurations shortly after quenching ($t = 2 \times 10^4 \, \mathrm{MCS}$) are depicted (cross-sections).

no.	dimension	lattice type	number of NNs	$J_{NN}/k_B T_c$
1	2	square	4	0.4406867935^a
2	3	diamond	4	0.3698
3	3	s.c.	6	0.22165
4	3	b.c.c.	8	0.1574
5	3	f.c.c.	12	0.1021
6	4	s.hc.^{b}	8	0.1497
7	5	s.hc.	10	0.1139

^{a}Exact value $= \mathrm{arcsinh}(1)/2$ according to Lars Onsager's "tour-de-force" [147].
^{b}cf. appendix B

Table (2.1): Inverse critical temperatures (in units of k_B/J_{NN}) of the Ising model with NN interactions J_{NN} for different dimensions and lattices types. The values are taken from Ref. [129] and given references therein.
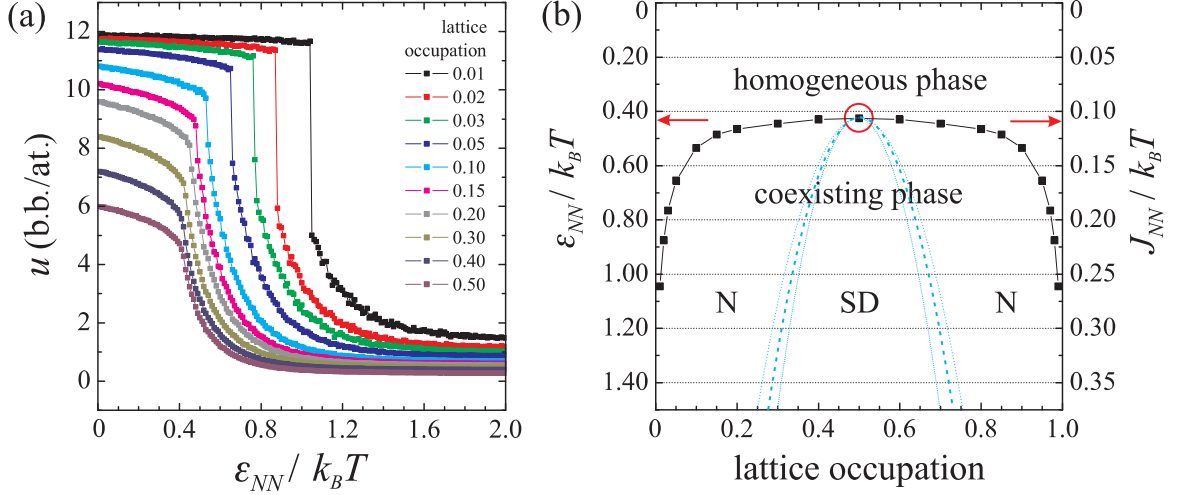
Figure (2.6): (a) Internal energy density u vs. $\varepsilon_{NN}/(k_BT)$ for different f.c.c. lattice occupations. (b) Corresponding binary phase diagram from KMC simulations (N: nucleation; SD: spinodal decomposition). The red arrows indicate the critical temperature.

For various values of lattice occupation, Fig. 2.6 (a) shows the internal energy density curve vs. temperature. Apparently, there are discontinuities (jumps) in the internal energy curve which account for first-order phase transitions. The respective transition temperatures were used to plot the coexistence curve in Fig. 2.6 (b). These simulations started with the given lattice occupation at infinite temperature (i.e. $\tilde{\varepsilon}_{NN} = 0$; $\varepsilon_{NN}=$ const.) and where cooled down adiabatically in infinitesimal steps. For $c = 0.5$, the transition temperature coincides with the critical temperature (cf. Fig. 2.4) which amounts to about $\tilde{\varepsilon}_{NN,c} = \varepsilon_{NN}/(k_BT_c) = 0.41$ for the f.c.c. lattice. This value very nicely coincides with the literature value. For various lattice types the critical temperatures of the NN Ising model are listed in Tab. 2.1. In Fig. 2.6 (b), only the coexistence curve is drawn (please note Eqn. 2.5). The spinodal curve is rather difficult to determine. Previous investigations indicate that the transition between nucleation and spinodal decomposition occurs in the interval $0.25 < c_s < 0.3$ for $\tilde{\varepsilon}_{NN} < 1.0$ [120, 121]. The corresponding blue curve in Fig. 2.6 (b) is an approximation for the spinodal curve, therefore.

2.4 Diffusion Channels

Diffusion is the thermally activated migration of particles from regions with higher to regions with lower chemical potential [148]. In the case of a material consisting of one sort of atoms, the present KMC model allows diffusive material redistribution by various channels (cf. Fig. 2.7):

1. surface diffusion:

   (a) by ad-atoms,
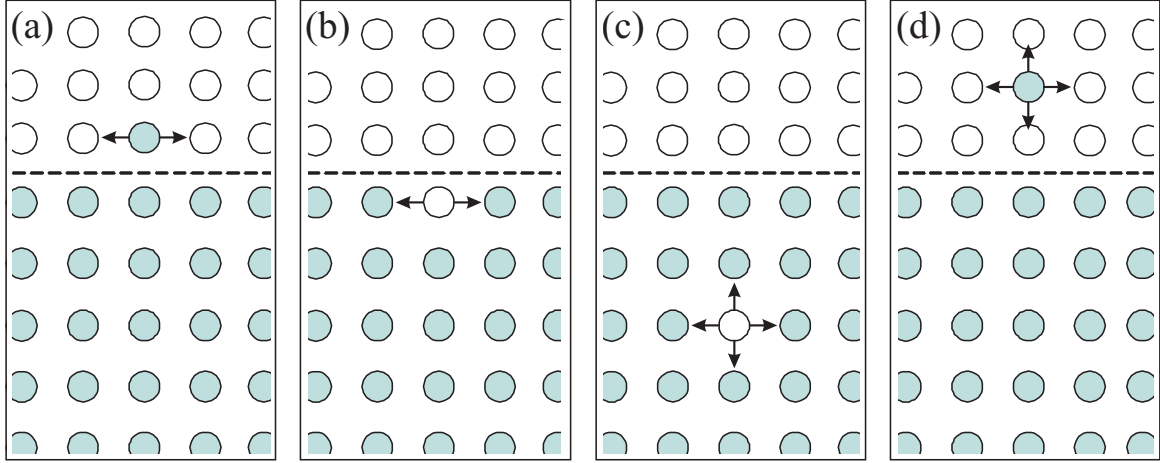   (b) by surface vacancies

   and

Figure (2.7): A schematic representation of the lattice KMC diffusion channels: (a) ad-atom diffusion, (b) surface vacancy diffusion, (c) bulk vacancy diffusion, and (d) volume diffusion through the vapor.

    2. volume diffusion:

        (a) by vacancies through the bulk,

        (b) by atoms through the vapor.

Obviously, these diffusion channels represent a simplification compared to real materials. In the present KMC model, for example, bulk interstitials are explicitly not considered. Consequently, interstitial-related events like Frenkel pair formation/annihilation do not occur. Thus, vacancies can merely be generated by diffusion of surface vacancies into the bulk ("evaporation" of vacancies into the material; vacancies can be interpreted as anti-particles because of the symmetry of the Hamiltonian). Moreover, complex diffusion mechanisms like multiple exchanges or concerted movements involving a large number of atoms are not taken into account [149]. Furthermore, only diffusional jumps to NN lattice sites are considered. However, in MD simulations it was found that for example ad-atoms on Ag(110) can also perform "long jumps", i.e. far-distance jumps over more than one NN distance [58]. Despite these simplifications, atomic events on surfaces like edge diffusion, terrace diffusion, edge descent (including an Ehrlich-Schwoebel barrier effect [150, 151]), nucleation, aggregation, or dissociation do occur based on the intrinsic dynamics of the NN Ising model.

    The diffusion coefficients for the respective diffusion channels are given as intrinsic properties of the lattice KMC model. They are given in units of a^2/MCS (a is the KMC lattice constant; cf. Fig. A.3) and are related to the jump attempt frequency Γ_0, the migration energy barrier E_m, and the number of NN lattice sites [115, 148]. One has also to keep in mind that the results for the diffusion coefficients depend on the choice of the transition algorithm [58]. In Ref. [115] it is demonstrated for a dilute system how the intrinsic volume diffusion coefficient is related to experimental values. In the present work, the surface diffusion coefficient D_s is examined more closely in view of surface-diffusion-dominated capillary phenomena.

    The scenario of a single ad-atom which performs thermally activated jumps between adjacent lattice sites is conceptually a simple picture for surface diffusion. The classical method to determine the surface diffusion coefficient experimentally is field ion microscopy [88, 152]. More recent experiments are performed by scanning tunneling
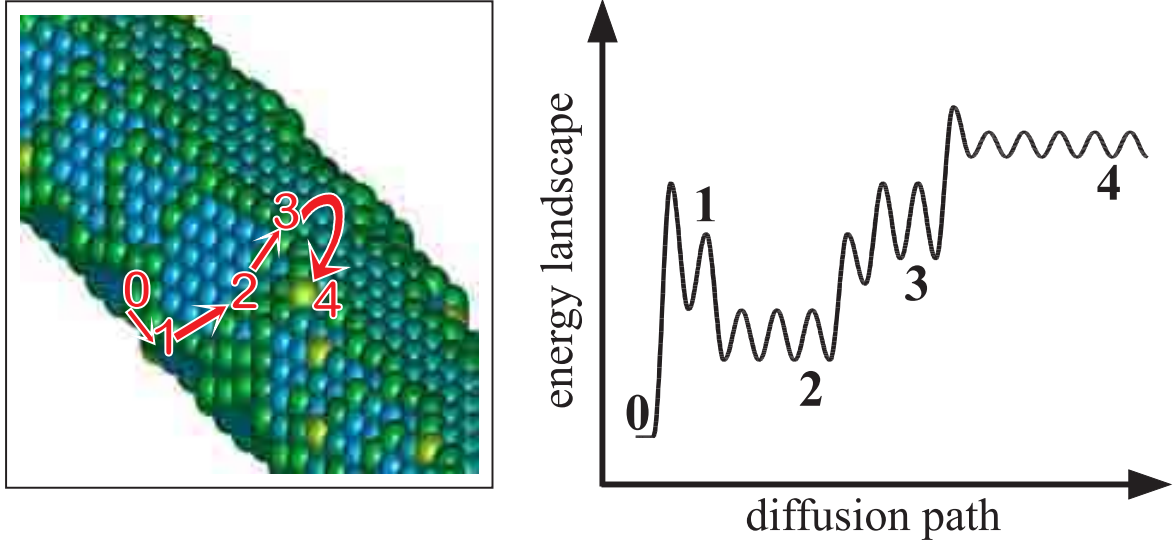
Figure (2.8): A schematic representation diffusion path of an ad-atom migrating over the surface of a NW with an underlying f.c.c. lattice (perspective view) and the corresponding qualitative representation of the surface "energy landscape" the atom is wandering over.

microscopy [153, 154]. The diffusion coefficient of such a single atom (tracer atom) is defined as the mean square displacement of the atom at asymptotically long times. In the case of low surface coverage, i.e. for isolated ad-atoms, subsequent jumps are not correlated, hence, they are statistically independent. The situation becomes much more complicated when the jumps are correlated which is the case at finite coverage [58]. This is the case for most of the present KMC simulations where shape transformations of curved surfaces of nanoscale structures at elevated temperatures are investigated. In these cases there is no single well-defined energy barrier. Due to the interaction among ad-atoms the actual activation barrier depends on the local configuration of all other NN ad-atoms. Moreover, lattice site blocking effects may occur. The effective energy barrier that controls the diffusion results from a complicated average over all the occurring configurations. In Fig. 2.8, this situation is schematically depicted for the diffusion of an ad-atom along the surface of a cylindrical structure (NW). As pointed out by Ala-Nissila and coworkers [58], in addition to the single particle diffusion there is also a collective surface diffusion coefficient D_s which measures the rate at which deviations from the equilibrium density spread out in the long time limit. It is an average which weights different surface diffusion events.

In a KMC computer experiment, the collective diffusion coefficient D_s can be directly measured. A surface with a small harmonic undulation of the surface height in one direction is considered (cf. Fig. 2.9 (a); surface with (001)-orientation), i.e. the surface profile reads

$$s(x,t) = h(t)\sin(\omega x). \tag{2.17}$$

The free energy minimization during evolution causes a smoothing of that undulation (Fig. 2.9 (b-d)), i.e. material migrates along the gradient of chemical potential (cf. Eqn. 1.6) from the crest to the trough of the surface profile. Based on Eqn. 1.5 and Eqn. 1.6 one finds for pure surface diffusion (cf. the complete derivation in Ref. [25]):

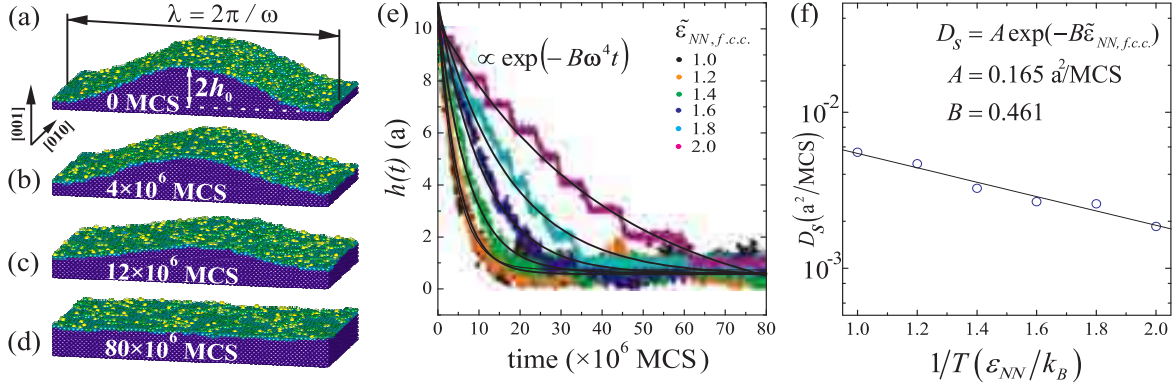$$s(x,t) = h_0 \exp(-B\omega^4 t)\sin(\omega x) \tag{2.18}$$

Figure (2.9): (a)-(d) Capillarity-driven morphological change of a sinusoidal surface profile which flattens out (here: $\tilde{\varepsilon}_{NN,f.c.c.}$=1.6). (e) Exponential decay of the amplitude of the sinusoidal surface profile for different values of $\tilde{\varepsilon}_{NN,f.c.c.}$. The cascade-like shape of the purple and light-blue curve indicates the layer-by-layer surface smoothing at low temperatures. (f) Collective surface diffusion coefficient measured by the amplitude decay showing Arrhenius behavior.

with

$$B = \frac{c_s D_s \gamma \Omega^2}{k_B T} \ . \tag{2.19}$$

Here c_s is the areal density of the diffusing species (ad-atoms and surface vacancies), γ is the surface tension, and Ω is the atomic volume. The exponential decay of the undulation amplitude $h(t)$ can directly be measured for different values of $\tilde{\varepsilon}_{NN}$ from which the collective surface diffusion coefficient D_s is fitted (cf. Fig. 2.9 (e, f)). Apparently, the collective surface diffusion in the present lattice KMC model shows Arrhenius-like behavior [155].

So far, isothermal systems have been considered where the diffusional flux j involves the gradient of chemical potential caused by surface curvature gradients. However, externally applied fields can give rise to additional contributions to the diffusional flux, e.g. temperature fields: "thermo-migration" (cf. subsection 5.1.1) or electric fields: "electro-migration". According to [148], the T-gradient-induced material flux at quasi-equilibrium (i.e. for small T-gradients) for an interstitial solute reads

$$j_T = -\frac{D\,c\,\Delta H^m}{k_B T^2} \frac{\mathrm{d}T}{\mathrm{d}x} \ , \tag{2.20}$$

where D is the isothermal diffusion coefficient, c is the concentration of the solute, and ΔH^m is the heat of transport. The temperature gradient changes neither the jump mechanism nor the jump attempt frequency at any given temperature; it does merely bias the direction of jumps [156]. For a thorough discussion of the sign of the heat of transport consult Refs. [148, 156]. The sign of ΔH^m determines the direction of biasing: For example, in the case of self-thermo-migration in bulk metal is was found that the material flux is directed towards the cold region [148].

In view of the surface-diffusion mediated capillary phenomena discussed in the present work, the implementation of temperature gradients into the lattice KMC code requires an alteration of the jump probability normalization introduced in Eqn. 2.11. Since the exponential prefactor containing the energy barrier is T-dependent, defined

values for the surface atom migration energy barrier E_m and the diatomic bond energy ε_{NN} have to be introduced in order to calculate the respective jump probabilities correct. In the studies of section 5.1, where periodic T-field at the surface along the longitudinal axis z of a cylindrical structures were applied, both values were set to a constant value of $0.2\,\mathrm{eV}$. The respective reduced jump probability reads:

$$\tilde{P}_{if}(\vec{r}) = \frac{1}{\Gamma_0 \exp\left\{\frac{-E_m}{k_B T_{\max}}\right\}} \left\{ \begin{array}{ll} \exp\left\{-E_m/(k_B T(\vec{r}))\right\} & , \quad n_f \geq n_i \\ \exp\left\{-\left(E_m + \Delta H\right)/(k_B T(\vec{r}))\right\} & , \quad n_f < n_i \ . \end{array} \right. \tag{2.21}$$

In the present KMC model, thermocapillary phenomena based on material transport along a T-gradient can alternatively be understood by the fact that the concentration (solubility) of the migrating species is T-dependent: $c(T) \propto \exp(-E_a/(k_b T))$ which applies for the solubility of atoms in the vapor phase above a surface, for the solubility (areal concentration) of ad-atoms and surface vacancies, or for the solubility of vacancies in bulk material. Thus, a temperature gradient induces gradients in concentration of the respective species which gives rise to a net flux down the T-gradient from hot ($=$ high concentration) to cold ($=$ low concentration) regions. Consequently, depending on the species which dominates j, material can be driven either from cold to hot regions (vacancy-dominated case) or from hot to cold regions (atom-dominated case). In the steady state, i.e. $j_{\text{tot}} = 0$, it can be deduced from Eqn. 1.5, Eqn. 1.6, and Eqn. 2.20 that a given temperature gradient gives rise to a surface curvature gradient. The chemical potential μ which is proportional to the product of curvature κ and surface tension γ (cf. Eqn. 1.6 and Eqn. 1.7) has to be the same everywhere on the surface in the stationary case:

$$\frac{\mathrm{d}\mu(\vec{r})}{\mathrm{d}\vec{r}} = \frac{\mathrm{d}\kappa(\vec{r})}{\mathrm{d}\vec{r}}\gamma(\vec{r}) + \kappa(\vec{r})\frac{\mathrm{d}\gamma(\vec{r})}{\mathrm{d}\vec{r}} = 0 \ . \tag{2.22}$$

Consequently, the mean curvature (i.e. the surface profile) of structures changes under the action of a temperature field along the surface: hot surface regions become concave; cold surface regions become convex (cf. section 5.1).

2.5 Surface Tension Anisotropy

In chapter 1, it is was outlined that capillary effects in crystalline materials can be strongly anisotropic due to the symmetry of the respective lattice structure. Thus, the manner in which surface tension anisotropy is described by the present lattice KMC model deserves closer consideration.

According to the Wulff-theorem, a crystal is in thermodynamic equilibrium if the distances of its facets from its center are proportional to their specific surface free energies ("Wulff-plot") [157, 158]. The ECS of a crystalline cluster of a fixed volume takes that shape which minimizes the surface free energy:

$$F_s = \oint \gamma(\vec{s})\,\mathrm{d}A \ . \tag{2.23}$$

Here $\gamma(\vec{s})$ is the surface free energy per unit surface area (surface tension) that depends on the orientation $\vec{s}$ of the surface element $\mathrm{d}A$ relative to the crystal axes.
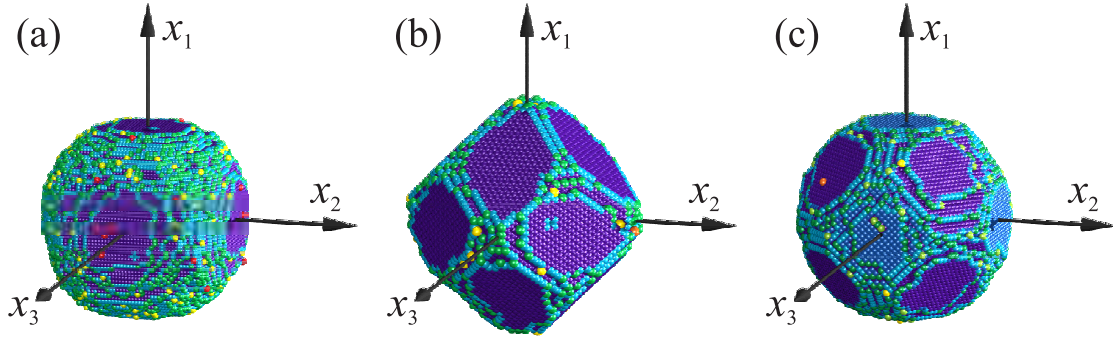
Figure (2.10): Quasi-ECSs for the three different lattice types: (a) s.c. ($\tilde{\varepsilon}_{NN,s.c.}$=3.0), (b) b.c.c. ($\tilde{\varepsilon}_{\mathrm{NN,b.c.c.}}$=3.0), and (c) f.c.c. ($\tilde{\varepsilon}_{\mathrm{NN,f.c.c.}}$=2.5). The initial configuration was a cluster of spherical geometry in each case with R_0=30 a.

It has been pointed out recently that atomic discreteness may influence the morphology of nanostructures, i.e. in extension of the above equation not only facets but also surface steps, edges between facets, and corners contribute to an increasing amount to the surface free energy if the structure dimensions decrease [159, 160]. The results presented here, however, indicate that the classical treatment of considering merely the free energy of facets delivers very good results compared to lattice KMC simulations which include contributions of all surface atoms, naturally.

In Fig. 2.10, for illustration, ECSs are depicted for the three cubic lattices at low temperatures (cf. Tab. 2.1). Apparently, those quasi-ECSs are dominated by flat surfaces with low surface energies (cf. Tab. 2.2). These shapes were obtained from lattice KMC simulations by relaxing a cluster of spherical shape (R_0=30 a) for a duration of 10^7 MCS in each case. "Quasi"-ECS means that after t=10^7 MCS the system is supposed to have reached the equilibrium state approximately, although it reaches the true equilibrium state theoretically only in the ($t\rightarrow\infty$)-limit because the driving forces become steadily smaller as the system approaches equilibrium.

These quasi-ECSs exhibit cusps between facets of different orientation due to discontinuities of the angular derivatives of the surface free energy. The tendency of faceting is reduced as the temperature rises. In other words, facets indicate order which is increasingly destroyed by entropy if the temperature rises, i.e. the cusps blunt because the step free energies are reduced and the facets shrink, therefore. A given facet will finally disappear at the roughening transition temperature of the corresponding infinite planar surface, thus, above the roughening transition temperature the corresponding region of the ECS becomes smoothly rounded [161, 162, 163]. Lattice KMC simulations confirm this development which is shown for the f.c.c. ECS in Fig. 2.11.

In the rigid-lattice Ising-model considering two-body NN and NNN interaction energies (cf. Eqn. 2.7), the surface tension γ at $T = 0$ for an arbitrary (hkl)-oriented facet
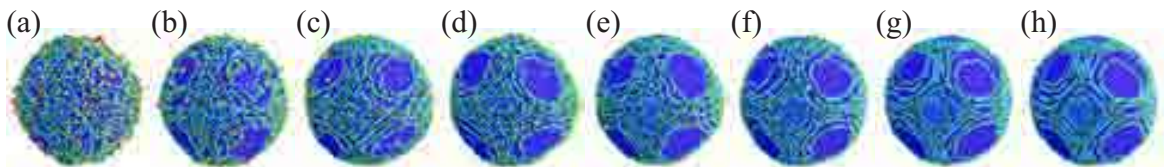

Figure (2.11): Quasi-ECSs of a f.c.c. NC for different temperatures (decreasing T from left to right): (a) $\tilde{\varepsilon}_{NN}$=1.0, (b) $\tilde{\varepsilon}_{NN}$=1.3, (c) $\tilde{\varepsilon}_{NN}$=1.5, (d) $\tilde{\varepsilon}_{NN}$=1.7, (e) $\tilde{\varepsilon}_{NN}$=2.0, (f) $\tilde{\varepsilon}_{NN}$=2.5, (g) $\tilde{\varepsilon}_{NN}$=5.0, and (h) $\tilde{\varepsilon}_{NN}$=10.0.

surface orientation	lattice structure		
	s.c.	b.c.c.	f.c.c.
(100)	$(2+8\kappa)$	$(8+4\kappa)$	$(16+8\kappa)$
(110)	$\sqrt{2}(2+6\kappa)$	$\sqrt{2}(4+4\kappa)$	$\sqrt{2}(12+8\kappa)$
(111)	$\sqrt{3}(2+4\kappa)$	$\sqrt{3}(4+4\kappa)$	$\sqrt{3}(\ 8+8\kappa)$

Table (2.2): Normalized surface energies for flat, low-index surfaces for the Ising model of three cubic Bravais lattices considering NN and NNN interactions [164].

surface orientation	$\kappa = \varepsilon_{NNN}/\varepsilon_{NN}$						
	-3/5	-2/5	-1/5	0	1/5	2/5	3/5
(100)	2.021	1.540	1.300	1.155	1.058	0.990	0.938
(110)	1.837	1.497	1.327	1.225	1.157	1.108	1.072
(111)	1	1	1	1	1	1	1

Table (2.3): Surface energies of the f.c.c. lattice Ising model normalized to the (111)-surface energy for different values of κ referring to the ECSs of Fig. 2.12 (c) and Figs. 2.13 (f-k).
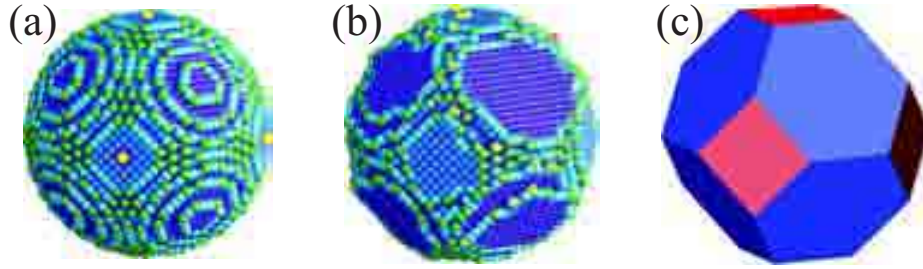
Figure (2.12): Shape of a NC with f.c.c. lattice structure: (a) initial spherical shape before quenching, (b) after quenching and 10^7 MCS of relaxation (here: $\tilde{\varepsilon}_{NN} = 2.5$, $\kappa = 0$), and (c) its corresponding ECS according to a 3D Wulff construction (truncated octahedron).
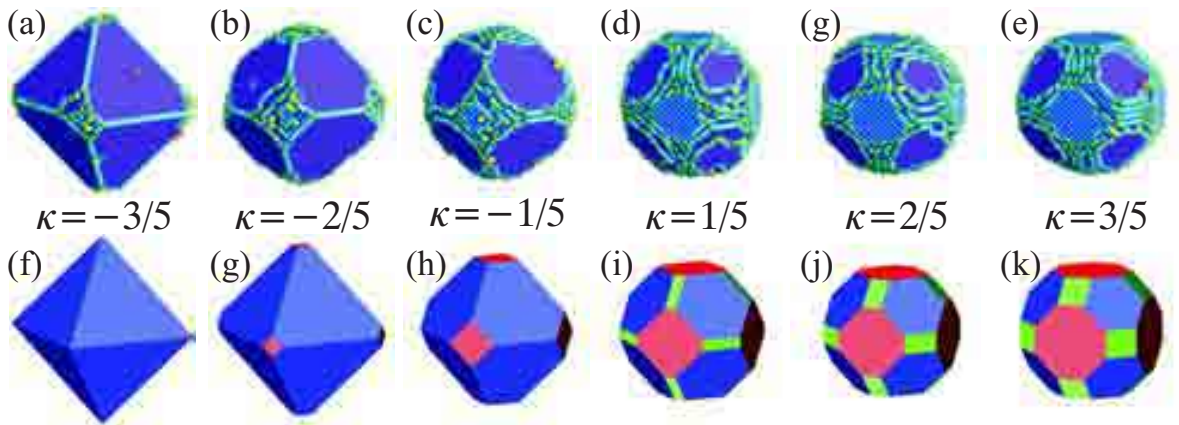
Figure (2.13): Upper row: quasi-ECSs of f.c.c.-type NCs for different values of κ after 10^7 MCS of relaxation starting from a spherical shape ($\tilde{\varepsilon}_{NN} = 2.5$ in each case). Lower row: The respective theoretical ECSs according to 3D Wulff constructions ($T=0$).

is simply given by

$$\gamma(hkl) \;=\; \frac{\varepsilon_{NN}}{2}\, n_1(hkl) \;+\; \frac{\varepsilon_{NNN}}{2}\, n_2(hkl) \;, \tag{2.24}$$

where n_1 and n_2 denote the areal density of NN and NNN broken bonds of the (hkl)-oriented facet, respectively. Defining κ as the ratio between NN and NNN interaction energy, i.e.

$$\kappa = \frac{\varepsilon_{NNN}}{\varepsilon_{NN}} \;, \tag{2.25}$$

Eqn. 2.24 transforms into

$$\gamma(hkl) \;=\; \frac{\varepsilon_{NN}}{2}\, \left[n_1(hkl) + \kappa n_2(hkl) \right] \;. \tag{2.26}$$

In Tab. 2.2, the corresponding normalized surface energies are listed for the three cubic lattice types. The influence of NN and NNN interaction energies on the ECS is analytically discussed in Ref. [164] (cf. Tab. 2.3). For various values of κ, quasi-ECSs for the f.c.c. lattice at low temperatures are shown in Fig. 2.12 (b) and Fig. 2.13. The KMC simulations started from a spherical cluster ($R_0 = 30$ a, cf. Fig. 2.12 (a)) and lasted 10^7 MCS in each case. The KMC results are compared to the ideal ECS at $T = 0$ given by 3D Wulff constructions using the surface tensions given in Tab. 2.3. Apparently, there is good agreement between the quasi-ECSs obtained by lattice KMC simulations at low temperatures and the theoretical ECSs deduced from 3D Wulff constructions for $T = 0$.

In the case of the f.c.c. lattice, the dominant {111}-facets will play an important role in chapter 4 in view of the Plateau-Rayleigh instability of single-crystalline f.c.c. NWs since they stabilize those NWs whose crystal orientations along the longitudinal axis lie in {111}-planes, namely [011]- and [112]-oriented NWs (cf. subsection 4.2.6). For the f.c.c. lattice, the surface-tension-hierarchy of low-index surfaces reads $\gamma_{111} < \gamma_{100} < \gamma_{110}$ (cf. Tab. 2.3, $\kappa{=}0$). This tendency agrees with literature results on various f.c.c. metals [165, 166]. Also for A-type precipitates of $CoSi_2$ in c-Si the typical truncated octahedron ECS was found (cf. Fig. 6 in Ref. [167]) which indicates that the f.c.c. lattice KMC simulations reflect the surface tension relations for $CoSi_2$ in c-Si in good approximation due to the fact that the Co atoms occupy a f.c.c. sublattice in c-$CoSi_2$ (cf. Fig. 3.6 (b))[6]. Moreover, this tendency is even correct for c-Si although its crystal lattice structure is that of diamond. It has been shown experimentally in TEM studies that voids within c-Si exhibit dominant {111} and {100} facets (cf. Fig. 1 in Ref. [169]; $\gamma_{100} : \gamma_{111} = 1.1 : 1$).

---

[6]During phase separation of Co-supersaturated c-Si a c-$CoSi_2$ phase forms (cf. chapter 3) which from a crystallographic point of view can be embedded coherently (A-type precipitates) or semi-coherently (B-type precipitates; two twinned opposite {111}-interfaces) in the c-Si matrix [168]. The latter type is not considered in the present KMC model for which anisotropic {111}-interface energies would be required.

2.6 Gibbs-Thomson Equation

If a solid phase is in direct contact with another condensed phase (solution or solid matrix) it has a non-zero solubility in that neighboring phase. This equilibrium solubility scales with temperature obeying Arrhenius-behavior: $c(T) \propto \exp[-E_a/(k_B T)]$. The lattice KMC method reproduces this characteristic equation over a large temperature range for the Ising model on all three cubic lattices [115].

Moreover, the solubility is affected by the curvature of the phase boundary [115, 170]. This scenario is equivalent to the case where a condensed phase is in contact with its vapor pressure which was originally examined by William Thomson (*alias* Baron Kelvin) in 1871 who famously stated that

> "the pressure of saturated vapor in contact with a liquid differs according to the curvature of the bounding surface, being less when the liquid is concave and greater when it is convex" [171].

The mathematical expression – the so-called Gibbs-Thomson equation (also known as Kelvin equation) for a spherical cluster of radius r reads

$$\ln \frac{p(r)}{p_0} = \frac{2\gamma\Omega}{rRT} \ , \tag{2.27}$$

where $p(r)$ is the actual vapor pressure, p_o is the vapor pressure over a planar surface, γ is the surface tension, Ω is the molar volume, R is the universal gas constant and T is the absolute temperature. The mathematical derivation can be found for instance in Ref. [172].

Later in 1900, Wilhelm Ostwald was the first to transfer the relation between curvature and vapor pressure to the dependence of the equilibrium solubility of a condensed-phase cluster in the surrounding solution on the cluster's curvature:

> "da nach bekannten Prinzipien ein feines Pulver löslicher sein muss als ein grobes, ebenso wie kleine Tröpfchen einen grösseren Dampfdruck haben als grosse" [173].

Providing that c_0 is the solubility over a planar surface, the equilibrium solubility $c(r)$ of a condensed-phase cluster with radius r in the surrounding solution is given by the Ostwald formula [170, 173] in analogy to the Gibbs-Thomson equation (cf. Fig. 2.14):

$$\ln \frac{c(r)}{c_0} = \frac{2\gamma\Omega}{rk_B T} = \frac{R_c}{r} \ , \tag{2.28}$$

where

$$R_c = \frac{2\gamma\Omega}{k_B T} \tag{2.29}$$

denotes the capillary length of a sphere. For arbitrarily curved phase boundaries with local mean curvature K the local solubility reads

$$\ln \frac{c(r)}{c_0} = \frac{K\gamma\Omega}{k_B T} \ . \tag{2.30}$$
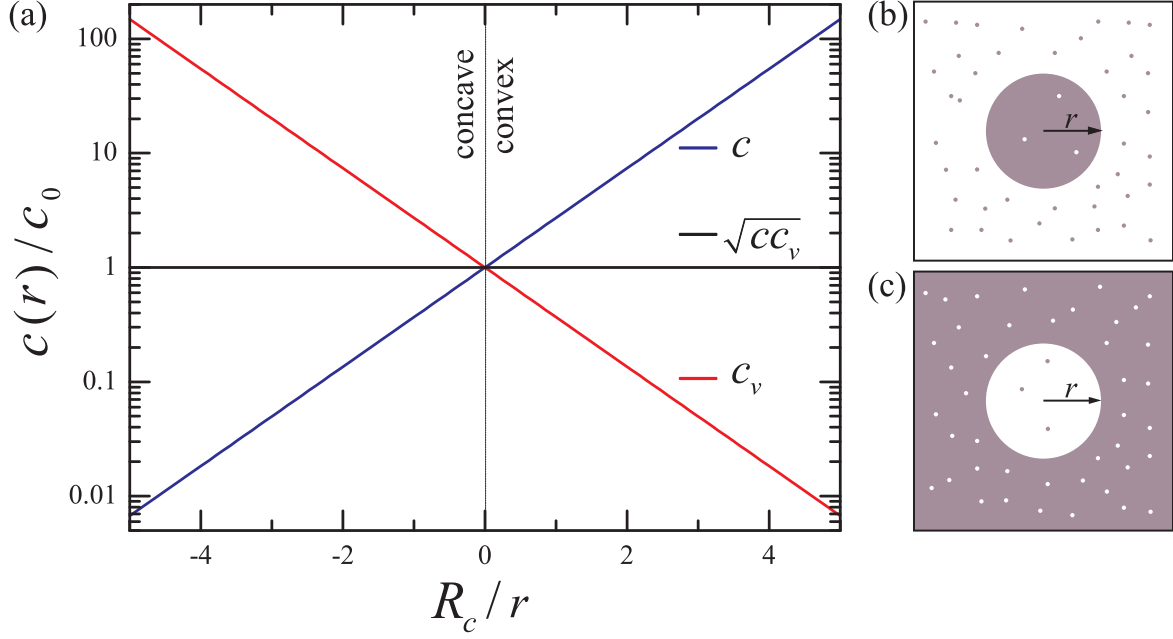
Figure (2.14): (a) Generalized Gibbs-Thomson relation of the NN Ising model relating the equilibrium monomer concentration c and the vacancy concentration c_v to convex and concave phase boundaries, respectively (cf. Eqn. 2.28; after Ref. [115]). (b) A schematic representation of a spherical particle embedded in its vapor phase (convex phase boundary). (c) A schematic representation of a spherical void embedded in bulk material (concave phase boundary).

The validity of the Gibbs-Thomson equation in the case of highly curved interfaces with mean radii of curvature in the nanometer range has been tested by direct experiment and could be validated [174]. Moreover, it was found that the Gibbs-Thomson equation delivers correct results within an error of only a few percent for temperatures approaching the critical temperature [175]. As for the Ostwald formula it was found by the present lattice KMC method based on the Ising model that it is also valid in the low nanometer range [11].

According to Fick's first law, the diffusional flux which causes redistribution of material scales with the concentration gradient of the diffusing species. Consequently, if a phase-separated system exhibits a gradient of phase boundary curvature then there is a concentration gradient of the solute above the phase boundary which gives rise to mass transfer by volume diffusion of the solute. This principle applies equally for single-domain (e.g. spinodal structures) or multi-domain (e.g. cluster ensembles) phase-separated systems. In both cases the overall surface free energy is reduced by volume diffusion through the neighboring phase. In the first case the curved phase boundary of the single domain is smoothed; in the latter case high-curvature domains evaporate and the material condenses onto domains with lower curvature.

2.6.1   Example I: Ostwald Ripening

Due to the curvature-dependent solubility an ensemble of clusters in a phase-separated solid system undergoes a capillary-driven coarsening process, the so-called Ostwald ripening [173]. In the frame of this work, a similar process occurs during the FIB-based IBS of NW structures where due to an initial supersaturation gradient a spinodal structure with lower average surface curvature than the surrounding cluster ensemble
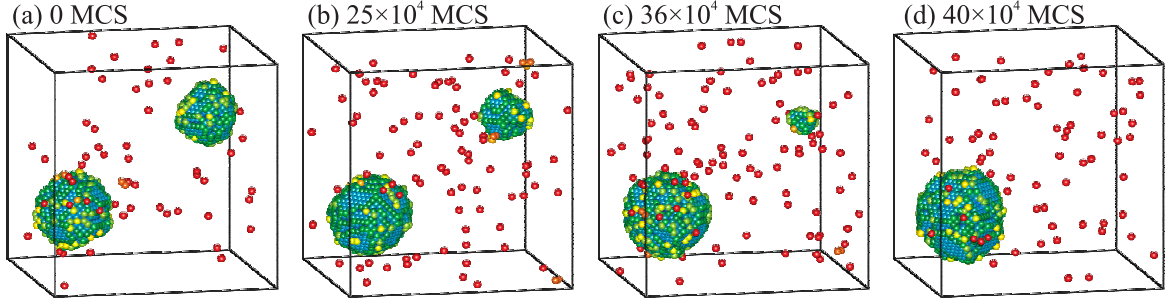
Figure (2.15): (a-d) Lattice KMC simulation demonstrating the coarsening or Ostwald ripening of an ensemble of two f.c.c. clusters ($\tilde{\varepsilon}_{NN,f.c.c}$=1.3; R_1=10 a; R_2=8 a).

consumes all phase-separated material in the system (cf. chapter 3).

The theoretical foundations of Ostwald ripening were established in 1956 by G. W. Greenwood [176]. Later on, further theories on the dynamics of that process were developed (most prominent the Lifshitz-Slyozov-Wagner theory) [10, 177, 178, 179, 180]. Ostwald ripening was also thoroughly examined using the lattice KMC method used in the frame of this work [11, 115]. Thus, this process is only briefly illustrated here (cf. Fig. 2.15 and a similar GIF animation[7]): According to Eqn. 2.28 small clusters (high curvature) have a higher solubility than large clusters (low curvature) which gives rise to a diffusive flux from small to large clusters through the matrix in which the cluster ensemble is embedded. While small clusters shrink they become subcritical at a certain moment and they finally evaporate. This thermodynamic instability of a small cluster that is dissolved during Ostwald ripening is the so-called *Kelvin instability* [181]. Consequently, the number of clusters in the system decreases with time, however, the mean size of the clusters $\overline{R}$ increases because of volume conservation (cluster coarsening): $\overline{R}(t) \propto t^{1/3}$ in the diffusion-controlled regime [115, 177, 178].

2.6.2   Example II: Shrinkage of Hollow-Core Particles

Similar to the coarsening of a cluster ensemble is the capillary-driven shrinkage of a particle with a hollow core [182]. In the former case of Ostwald ripening material redistribution is achieved by atoms which diffuse through the vapor – in the case of a hollow-core particle, however, vacancies are the diffusing species that cause material redistribution (cf. Fig. 2.14).

Boris Yakovlevich Pines was the first who extended the validity of the Gibbs-Thomson equation to vacancies in crystalline systems. In his seminal work "О спекании в твердой фазе" (On sintering in the solid state) he interpreted vacancies as virtual particles which diffuse through a crystalline matrix. Their concentration beneath a curved surface is also described by Eqn. 2.30 [183]. This fact has been validated formerly by the present KMC model [115]. Picturing vacancies as particles obeying the Gibbs-Thomson equation helps to understand the shrinkage of a spherical cluster that possesses a hollow core (cf. Fig. 2.16(a)). The inner surface is from the point of view of vacancies a convex surface with a vacancy concentration in the bulk higher than that of a flat surface. On the contrary, the outer surface of the cluster is concave in the vacancy picture with a vacancy concentration in the bulk material that is lower than that of a flat surface. This gradient in vacancy concentration causes a diffusional flux

---

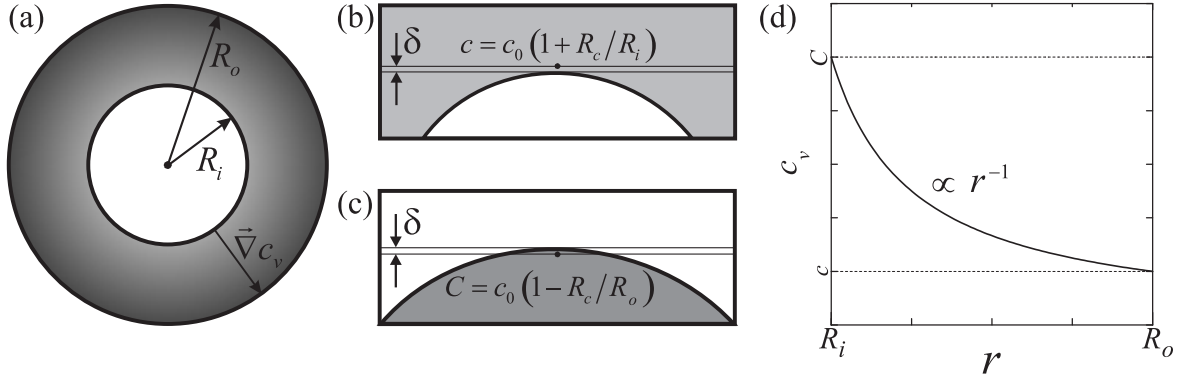[7]The GIF animation is located at: `http://www.roentzsch.org/OR/index.html`

Figure (2.16): (a) A schematic representation of a spherical cluster with outer radius R_o containing a void at its center with radius R_i. (b,c) The vacancy concentration c_v above the inner surface is higher than beneath the outer surface which gives rise to an outbound vacancy flux causing the cluster to shrink. (d) c_v is inverse proportional to the radius.

of vacancies in outward radial direction. Consequently, bulk material of the cluster is moving in the reverse direction, i.e. towards the center of the cluster. Consequently, the spherical void shrinks. Under the constraint of material conservation, the outer radius of the cluster is reduced as well. The process stops when the entire core of vacancies is dissolved and has diffused out of the cluster. Then, there remains merely the constant vacancy equilibrium concentration in the cluster.

In Fig. 2.17, the evolution of such a process is depicted as a series of KMC snapshots. In this case, the outer and inner radii amount to $R_o{=}50\,\mathrm{a}$ and $R_i{=}30\,\mathrm{a}$; $\tilde{\varepsilon}_{NN,f.c.c.} = 1.2$.

The dynamics of the shrinkage of a hollow cluster can analytically be treated as follows: A spherical cluster of outer radius R_o is considered which contains at its center a spherical void of radius R_i where $R_i < R_o$ (cf. Fig. 2.16(a)). The vacancy concentrations beneath the respective surfaces read according to the linearized Gibbs-Thomson equation for $\delta \ll 1$:

$$c = c_v(R_i + \delta) = c_0 \left(1 + \frac{R_c}{R_i} \right) \tag{2.31a}$$

$$C = c_v(R_o - \delta) = c_0 \left(1 - \frac{R_c}{R_o} \right) \tag{2.31b}$$

Here, R_c denotes the capillary length of a sphere (cf. Eqn. 2.29). In the steady state, the diffusion equation in spherical coordinated reads:

$$\frac{\mathrm{d}}{\mathrm{d}r} \left(r^2 \frac{\mathrm{d}c_v}{\mathrm{d}r} \right) = 0 \ . \tag{2.32}$$

With the given boundary conditions $c_v(R_i) = c$ and $c_v(R_o) = C$ its solution reads (cf. Fig. 2.16(d))

$$c_v(r) = \frac{cR_i(R_o - r) + CR_o(r - R_i)}{r(R_o - R_i)} \ . \tag{2.33}$$

The radial vacancy concentration gradient in the bulk of the cluster gives rise to a diffusive vacancy flux j_v from the inner to the outer surface. To calculate the shrinkage
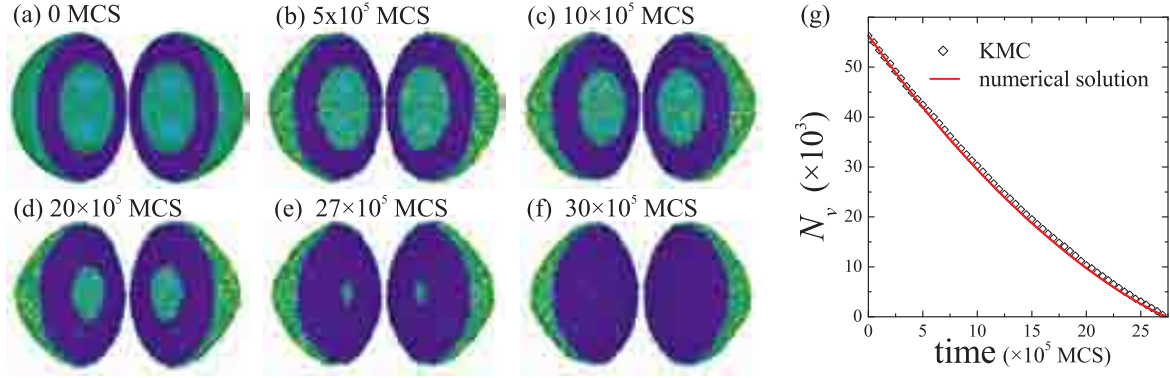
Figure (2.17): (a-f) Series of KMC snapshots describing the vacancy-diffusion-mediated shrinkage of a spherical cluster containing a void (here: N_a=205000; $N_v(t=0)$=56321). Just for illustration, the hollow cluster is cut into two halves which are opened up in order to reveal the interior. (g) The decrease of the void volume measured during a KMC simulation and calculated numerically demonstrating very good agreement between experiment and theory.

of the void the total flux of vacancies arriving per unit time at the outer surface is considered:

$$j_v = \frac{\mathrm{d}N_v}{\mathrm{d}t} = 4\pi R_o^2 \times D_v \times \left(\frac{\mathrm{d}c_v}{\mathrm{d}r}\right)_{r=R_o} = 4\pi R_o^2 \times D_v \times \frac{R_i}{R_o}\frac{(C-c)}{(R_o-R_i)} \ , \qquad (2.34)$$

where D_v is the vacancy diffusion coefficient. In the beginning, the void contains a number of vacancies $N_v(t=0) = \frac{4}{3}\pi\rho R_i^3(t=0)$, where ρ denotes the density of vacant lattice sites[8]. Inserting Eqn. 2.31(a) and Eqn. 2.31(b) into Eqn. 2.35 yields

$$\frac{\mathrm{d}N_v}{\mathrm{d}t} = -4\pi D_v c_0 R_c \times \frac{(R_o+R_i)}{(R_o-R_i)} \ . \qquad (2.35)$$

In order to solve Eqn. 2.35, $R_o(t)$ and $R_i(t)$ can be expressed in terms of the number of vacancies in the void $N_v(t)$ and the total number of atoms N_a which is constant throughout the process due to the conservation of bulk material:

$$R_o(t) = \sqrt[3]{\frac{3}{4\pi\rho}(N_a + N_v(t))} \qquad (2.36\mathrm{a})$$

$$R_i(t) = \sqrt[3]{\frac{3N_v(t)}{4\pi\rho}} \ . \qquad (2.36\mathrm{b})$$

Thus, Eqn. 2.35 can be rewritten as

$$\frac{\mathrm{d}N_v(t)}{\mathrm{d}t} = -4\pi D_v c_0 R_c \times \frac{\sqrt[3]{(N_a + N_v(t))} + \sqrt[3]{N_v(t)}}{\sqrt[3]{(N_a + N_v(t))} - \sqrt[3]{N_v(t)}} \ . \qquad (2.37)$$

Since the only time-dependent variable in this equation is $N_v(t)$ the solution can be obtained numerically in a straightforward manner. Here, the commercial program FlexPDE (“**Flex**ible Solution System for **P**artial **D**ifferential **E**quations”) was used. The numerical result for $N_v(t)$ is plotted in Fig. 2.17(g) where it is compared with the measured time-development of N_v during the KMC run. Accordingly, there is a very good agreement between computer experiment and the theoretical treatment presented above – even though the linearized Gibbs-Thomson equation has been employed.

---

[8]For the f.c.c. lattice, $\rho = 0.5\,\mathrm{a}^{-3}$.

2.7   Substrate Wetting

In view of chapter 4, where capillary instabilities are discussed, it is of interest how a supporting substrate influences the dynamics of these processes (cf. Fig. 1.1 (a) where the Plateau-Rayleigh instability is depicted for a Cu NW supported by SiO_2).

In extension to the Ising model portrayed in section 2.2, the energetics of a system with only NN interactions consisting of three phases (wetting phase (A), substrate (B), and vapor) is described as

$$H = -\varepsilon_{AA} \sum_{\langle i,j \rangle_{AA}} c_i\, c_j - \varepsilon_{AB} \sum_{\langle m,n \rangle_{AB}} c_m\, c_n - \varepsilon_{BB} \sum_{\langle k,l \rangle_{BB}} c_k\, c_l \ . \tag{2.38}$$

In the frame of this work, the substrate is always assumed to be passive, i.e. the substrate atoms do not change their lattice sites ($\varepsilon_{BB} \to +\infty$, i.e. the last term in Eqn. 2.38 is constant and can be neglected). In Fig. 2.18, a series of lattice KMC simulations is shown (f.c.c. lattice) for different $\tilde{\varepsilon}_{AB}$ values keeping the other parameters constant ($\tilde{\varepsilon}_{AA} = 1.3$). In the spirit of a relaxation process the simulations started with spherical clusters of equal size slightly touching the substrate ($R = 40\,a$). The pictures show the quasi-ECSs after 10^7 MCS of relaxation.

Apparently, the contact angle between the wetting phase and the substrate is anisotropic due to the underlying crystal structure, i.e. it varies with the direction of view (cf. upper and lower row of Fig. 2.18). In this case of a f.c.c. lattice for both wetting phase and substrate, the contact angles differ between the {111}-facets of the NC and the (001)-oriented substrate surface and between the {110}-facets of the NC and the substrate surface. With increasing $\tilde{\varepsilon}_{AB}$ the {111}-facets of the wetting NC that are in touch with the substrate reduce their area at constant contact angle.

With increasing attractive interaction ($0 < \tilde{\varepsilon}_{AB} < \tilde{\varepsilon}_{AA}$) between the substrate and the wetting phase the equilibrium shape of the wetting NC, i.e. the contact angle decreases (partial wetting). For $\tilde{\varepsilon}_{AB} = \tilde{\varepsilon}_{AA}$ total wetting (zero contact angle) is anticipated.

In view of capillary instabilities, the minimization of the interface energy between wetting phase and substrate as well as of the surface energy of the wetting phase become the driving principles, thus, a retardation of capillarity-driven morphological transformations can be expected for increasing $\tilde{\varepsilon}_{AB}$ with $0 < \tilde{\varepsilon}_{AB} < \tilde{\varepsilon}_{AA}$ (cf. subsection 4.2.8).
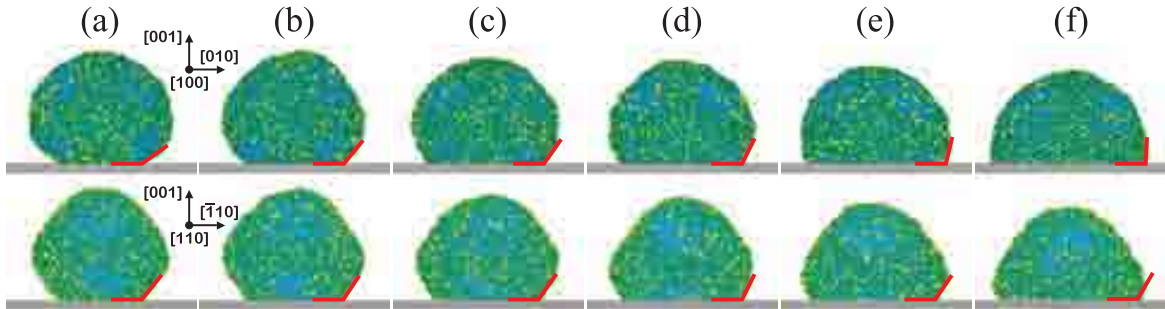
Figure (2.18):   (a)-(f) Wetting of a substrate by a NC with f.c.c. lattice structure for increasing cluster-substrate interaction strength ($\tilde{\varepsilon}_{AA} = 1.3$ and from (a) to (f) $\tilde{\varepsilon}_{AB} = \{0.0; 0.1; 0.2; 0.3; 0.4; 0.5\}$). The upper and the lower row differ in the direction of view indicating the contact angle anisotropy.

2.8 Ballistic Displacements

Very fascinating effects are observed if a solid-state system is exposed to energetic particle bombardment (irradiation) during its evolution at elevated temperature. As energetic particles (e.g. ions, neutrons, electrons) penetrate a solid system they can introduce microscopic perturbations to the atomic configuration, e.g. collisional mixing, displacements, replacements etc. (cf. subsection 3.1.1). Schmitmann and coworkers stated that systems which are driven by external fields or forces into non-equilibrium steady-states demonstrate non-trivial singular behavior [20]. They pointed out that the system gains energy from the external field. Thus, ballistic displacements of atoms can be understood as a coupling of the system to a second thermal reservoir with higher (i.e. infinite) temperature. Martin emphasized that such far-from-equilibrium processes are suitable for the synthesis of unstable and metastable structures [184]. Various phenomena can occur during ion-irradiation ranging from inverse Ostwald ripening [17, 19, 115, 124], to the shrinkage of nanocavities [185], to irradiation-induced phase transformations [98, 186, 187], to segregation effects [107], to ECS modifications [42], to ripple formation by ion erosion [94, 188, 189, 190] etc.

In the frame of this work, it is of great interest how the irradiation of cylindrical nanostructures with energetic ions influences the surface-diffusion-dominated capillary instabilities of such systems (non-equilibrium dynamics).

The implementation of ballistic displacements into the present KMC model is realized following the procedure of Heinig and Strobel [17, 115]. It is assumed that atoms can be displaced isotropically to free NN lattice sites[9] with a defined frequency ("ballistic jumps"). The value ρ defines the ratio between ballistic jump attempts and thermally activated jump attempts, i.e. it is at constant $\tilde{\varepsilon}_{NN}$ a direct measure for the ion flux. In other words, ρ indicates the strength of the competition between ballistic (predominantly excitation) and thermal (predominantly relaxation) driving forces. Using this definition, $\rho=0$ denotes the case of purely thermally activated jumps which cause the relaxation of the system towards thermodynamic equilibrium. On the contrary, for $\rho=\infty$ the system would be transformed (excited) into a random solid solution. In the present work, only those atomic displacements are permitted which keep the atoms bound to the surface, i.e. sputtering into the surrounding matrix is suppressed. This situation would account for the low-energy ion bombardment of nanostructure surfaces where ad-atoms are generated but sputtering does practically not occur [113]. Thus, the number of atoms of a simulated nanostructure is constant (volume conservation).

According to Eqn. 1.5 the material flux along a surface scales with solubility and diffusivity of ad-atoms. At $\rho=0$, these values are given for different crystallographic surface orientations due to the intrinsic properties of the Ising model (cf. section 2.4, section 2.5, and Refs. [11, 115]). At equilibrium, all facets of a crystal are in a detailed balance with one another, i.e. the net diffusive flux of ad-atoms is zero between individual facets. Thus, regular ECSs are found in agreement with respective 3D Wulff constructions (cf. section 2.5).

However, both solubility and diffusivity of ad-atoms are modified under ion-irradiation: non-equilibrium ad-atom generation and radiation-enhanced surface diffusion. Those changes cause the ratios between the effective surface free energies to change, too [42]. Thus, under ion irradiation steady-state crystal shapes are anticipated

---

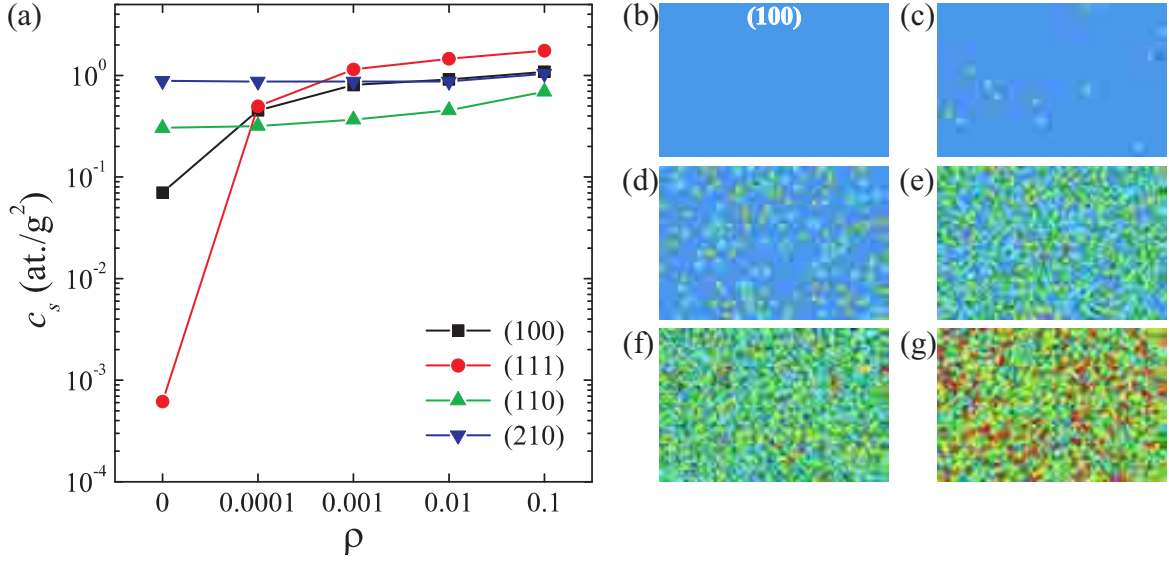[9]Thus, neglecting the long-range tails of the displacement distribution.

Figure (2.19): (a) Surface atom concentration c_s on low-index surfaces of the f.c.c. lattice for different ratios ρ between ballistic and thermal jump attempts. In all cases, $\tilde{\varepsilon}_{NN,f.c.c.}$=2.5 (cf. Fig. 2.21). Please note the logarithmic scale. (b)-(g) Image series of the (100) surface (top view) for the corresponding ρ-values: (b) pristine state at and for the stationary states ($\tilde{\varepsilon}_{NN,f.c.c.}$=2.5) at (c) $\rho = 0$, (d) $\rho = 0.0001$, (e) $\rho = 0.001$, (f) $\rho = 0.01$, and (g) $\rho = 0.1$.

which do not match the Wulff-ECS. The term "ballistic crystal shape" is suggested here in analogy to the kinetic Wulff shape that emerges during the growth of a crystal [66]. A similar situation was observed by Bellon who found a change in the steady-state crystal shape for ballistic atom exchanges with nearby vacancies in the bulk of a f.c.c. crystal, i.e. for a typical volume diffusion situation [42].

In Fig. 2.19 (a), the concentration of ad-atoms (surface solubility) in the steady-state is plotted for different values of ρ and for different low-index surfaces of the f.c.c. lattice. For ρ=0, the respective values reflect qualitatively the ECS characteristics of a truncated octahedron which is dominated by {111}- and {100}-facets (cf. Fig. 2.20 (2,1) and Fig. 2.20 (4,1)). For non-zero ρ the solubilities change dramatically, thus, the hierarchy of effective surface energies (broken bonds per unit area) alters so that facets dominate the steady-state crystal shape at $\rho > 0$ that do not appear at ρ=0.

For illustration, Figs. 2.19 (b-g) exhibit the steady-state configuration of a {100}-surface for different values of ρ at low temperature ($\tilde{\varepsilon}_{NN,f.c.c.}$=2.5). Accordingly, at low ballistic displacement rate (ρ={0.0001;0.001}) the ad-atom concentration is increased but the surface itself remains flat. With increasing ballistic displacement rate (ρ={0.01;0.1}), however, the surface roughens as well.

Fig. 2.20 shows steady-state ballistic crystal shapes (f.c.c. lattice) at different temperatures and at different ρ-values. Apparently, {210}-facets are dominant at low (ρ=0.001) and moderate (ρ=0.01) ballistic displacement frequencies. For high ballistic displacement rates (ρ=0.1), {100}-facets become the dominating ones. In accordance with Fig. 2.19 (a), {111}-facets do not appear since they are less favorable for the system (high effective surface energy).

The influence of temperature (assuming that $\varepsilon_{NN,f.c.c.}$ = const.) on these ballistic crystal shapes appears to be the same like for ECSs at ρ=0 (cf. Fig. 2.11), i.e. roughening of facets at high temperatures and sharpening of facets at low temperatures. However, the crystal orientation of the facets which appear under irradiation is ob-
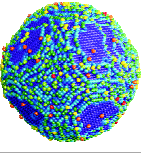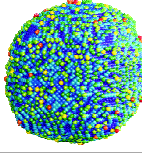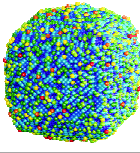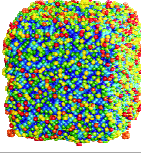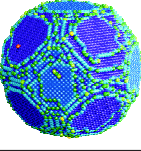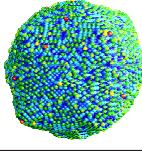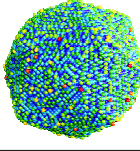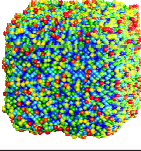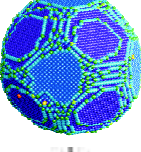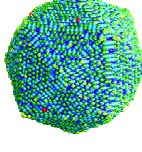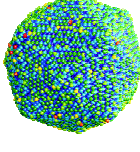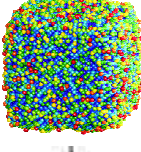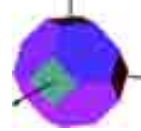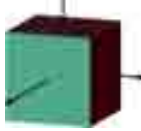
(a,b)	(a,1) $\rho = 0$	(a,2) $\rho = 0.001$	(a,3) $\rho = 0.01$	(a,4) $\rho = 0.1$
(1,b) $\widetilde{\varepsilon}_{NN,f.c.c.} = 1.3$				
(2,b) $\widetilde{\varepsilon}_{NN,f.c.c.} = 2.5$				
(3,b) $\widetilde{\varepsilon}_{NN,f.c.c.} = 4.0$				
(4,b) polyhedral shape				

Figure (2.20): (1-3,1) Quasi-ECSs (ρ=0) for different temperatures for the f.c.c. lattice after relaxation from a spherical geometry with initial radius R_0=30 a in each case. (1-3,2-4) Ballistic crystal shapes in the steady-state for the f.c.c. lattice for the same temperatures but varying strength of the ballistic force expressed by ρ. (4,b) Corresponding polyhedral shapes: (4,1) truncated octahedron (Wulff shape for f.c.c. Ising), (4,2) and (4,3) (210)-polyhedron, and (4,4) cube.
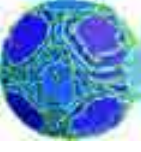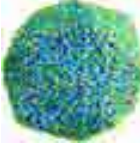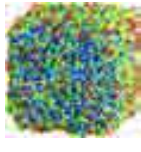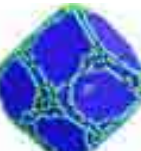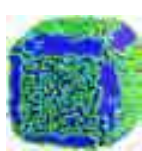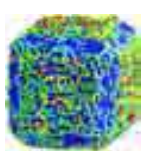
(a,b)	(a,1) $\rho = 0$	(a,2) $\rho = 0.001$	(a,3) $\rho = 0.01$	(a,4) $\rho = 0.1$
(1,b) $\widetilde{\varepsilon}_{NN,f.c.c.} = 2.5$				
(2,b) $\widetilde{\varepsilon}_{NN,b.c.c.} = 3.0$				
(3,b) $\widetilde{\varepsilon}_{NN,s.c.} = 3.0$				

Figure (2.21): (a,1) Quasi-ECSs (ρ=0) in agreement with the Wulff theorem for (1,1) the f.c.c. lattice, (2,1) the b.c.c. lattice, and (3,1) the s.c. lattice after relaxation from a spherical geometry with initial radius R_0=30 a in each case. (a,2-4) Ballistic crystal shapes in the steady-state for the three lattice types with increasing strength of the ballistic force expressed by ρ.

Figure (2.22): Specific internal energy u vs. the strength of the ballistic force ρ for the transformation of a f.c.c. NC sta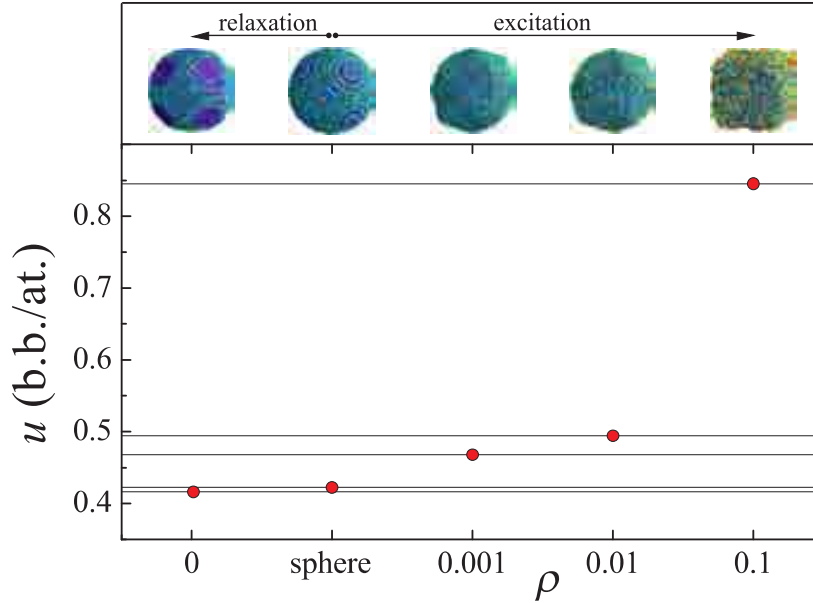rting from a spherical shape: at $\rho = 0$ the system relaxes to a lower energetic state; for $\rho > 0$ the system is excited (driven) to higher energetic states.

viously not influenced by temperature. Consequently, the appearance of those facets is merely controlled by ρ.

In Fig. 2.21, for all three cubic lattices the ECSs are compared with the ballistic crystal shapes. Apparently, b.c.c. crystals which are dominated by {110}-facets at $\rho=0$ turn into crystals with dominating {100}-facets and minor {110}-facets. For the s.c. lattice, which is characterized by strong {100}-facets at $\rho=0$ evolve under irradiation into nearly ideal octahedra, i.e. they exhibit strong {111}-facets. However, in the investigated range of ρ for b.c.c. and s.c. crystals there is no change in the ballistic crystal shape observed for increasing ρ like for f.c.c. crystals.

In order to underline the fact that ballistic displacements drive the system away from equilibrium, i.e. excite the system to an energetically higher state, in Fig. 2.22 the specific internal energy u of a f.c.c. crystal is plotted vs. ρ. The initial spherical state (u_0) relaxes at $\rho=0$ to a lower energetic state ($u(\rho=0) < u_0$). For $\rho > 0$ the system is steadily driven (excited) to higher energetic states.

The fact that ballistic displacements in addition to thermally activated atomic jumps alter the hierarchy of surface energies of low-index surfaces will have significant impact on the capillary-driven instability of crystalline nanostructures where surface free energy anisotropy can lead to an anisotropic action of the capillary force (cf. section 5.2). Thus, those nanostructures at which the action of the capillary force is retarded due to stabilizing facets at $\rho=0$ can lose their stable character under energetic particle bombardment and vice versa.

Chapter 3

FIB-based Ion Beam Synthesis of Nanowire Structures

In view of the atomistic modeling of the FIB-based NW synthesis, the KMC method provides the unique advantage to study how elementary atomistic processes like nucleation and dissociation of precipitates or discrete diffusion events lead to the formation of cylindrical nanostructures by a series of complex processes. Thereby, the evolution of a system containing several million atoms is examined the time scale of which extends over several orders of magnitude.

Starting from a 3D FIB line scan implantation profile the supersaturated system undergoes

1. *phase separation* via nucleation or spinodal decomposition,

2. *coarsening* (Ostwald ripening-like), and

3. an *interface smoothing* procedure.

The two latter processes are driven by the capillary force because of interface curvature gradients.

The synthesis of NW structures using FIBs (cf. Fig. 3.1) originates at first in the advent of liquid metal alloy ion sources making a variety of elements other than Ga available for FIB implantation. Secondly, FIB line scans can result in implantation profiles of particular shape from which elongated nanoscale structures like wires or rods can emerge in a self-organizing manner during phase separation. Therefore, this non-conventional method of controlled nanostructure synthesis represents a combination of a top-down with a bottom-up approach (cf. subsection 1.3.1): on the one hand the implantation of energetic ions with an ion beam that is laterally focused down to a few tens of nanometers, on the other hand the self-organized phase separation of a supersaturated solid solution in the course of which elementary atomistic processes cause the formation of mesoscopic structures.

The laterally confined implantation of energetic ions into a solid matrix may cause a surface-near concentration profile of the implanted species in the host matrix with a maximum concentration of implanted impurities well above the solid solubility limit, i.e. the system is locally driven to an extreme non-equilibrium state due to the compulsory incorporation of impurity atoms and ballistic displacements of atoms as
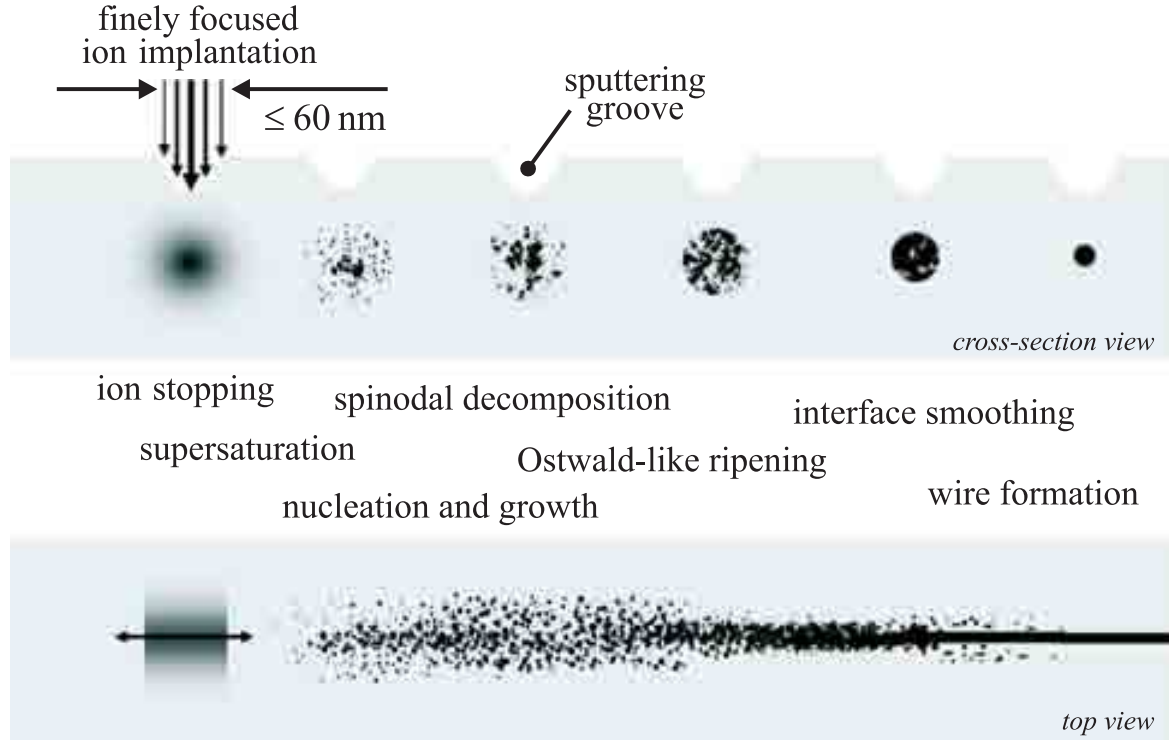
Figure (3.1): A schematic representation of the processes which contribute to the evolution of the FIB-based IBS of NW structures.

a result of collisions with energetic particles. For the synthesis of NW structures, the 3D distribution of implanted atoms in the host matrix ought to obey approximately a cylindrical symmetry where the longitudinal axis is parallel to the scanning direction of the FIB.

In order to escape the non-equilibrium state, the system tends to relax locally after (or already during) the generation of that supersaturation. In other words, the system reduces its free energy in the implanted region by phase separation, i.e. by transforming into a heterogeneous mixture of solid phases. Thus, a complex pattern of precipitates emerges in the implanted region which are fully embedded in the target. In order to relax the system must have a fast enough kinetics for the manifold processes of thermally activated mass transport by which material redistribution and thereby nanostructure formation are mediated. At RT, the kinetics is too slow in most systems for a relaxation on a mesoscopic scale for technologically reasonable times. Therefore, a thermal treatment is usually performed after ion implantation, i.e. in praxi the implanted matrix is exposed to a defined thermal budget at elevated temperature below the melting temperature of the matrix usually for durations from several seconds up to several minutes. During that thermal treatment the system not only undergoes phase separation but also anneals the accumulated radiation damage caused by energetic particle collisions during implantation. In some cases it is beneficial to perform the FIB implantation already at slightly elevated temperature in order to prevent amorphization of a single-crystalline target such as c-Si.

After phase separation the complex ensemble of precipitates undergoes processes of coarsening and interface smoothing which can finally result in the formation of elongated structures like rods or wires in the center of the implantation profile that are oriented parallel to the scanning direction of the FIB during implantation. However,

the state at which a NW structure has formed does not correspond to the system's equilibrium state. The fact that NWs are inherently unstable from the viewpoint of thermodynamics is thoroughly discussed in chapter 4. Consequently, it can be stated that the formation of NWs by FIB-based IBS is of transient nature, i.e. the state where a NW is formed is an intermediate state of the system on its pathway towards equilibrium. However, the NW structure can be "stabilized" for technological applications by cooling down the system so that its further evolution at much lower temperatures is hampered kinetically.

It should be noted that the fabrication of NW structures using FIBs suffers one decisive practical drawback, namely the serial operation mode of FIB units. Once FIB units operating with multiple beams in parallel will be available one can consider this FIB-based IBS of NW structures to become of technological and commercial importance for a controlled synthesis of NW structures that are laterally embedded in a substrate. Up to date, however, this FIB-based nanostructure synthesis remains a fascinating play ground for basic materials research where various aspects ranging from far-from-equilibrium processing to the relaxation dynamics of high-gradient heterogeneous systems can be encountered.

As outlined above, the NW synthesis using FIBs proceeds in two steps: the FIB implantation and a subsequent thermal treatment during which phase separation and NW formation take place. Likewise, this chapter is divided into two major sections: At first, a simulation method is presented to model realistic FIB line scan implantation profiles. This method is based on the well-known TRIM-code, however, it considers the realistic beam current density profile of a FIB of several tens of nanometers in width as well as the dynamic recession of the target surface due to local sputtering. The second section provides atomistic insight into the processes of phase separation and NW structure formation based on lattice KMC simulations. Finally, it is explained why NW structures are formed at all despite the Plateau-Rayleigh instability according to which bodies of cylindrical geometry are inherently unstable (cf. chapter 4).

3.1 FIB Line Scan Implantation Profiles

In most cases of ion-beam-based generation of supersaturated solid solutions, broad area ion implantations are performed where the width of the ion beam current density profile (10^{-3} to 10^{-2} m) is several orders of magnitude larger than the projected range of the implanted particles (10^{-9} to 10^{-6} m). Broad area ion implantations usually aim at a homogeneous ion distribution over the implanted area, i.e. the ion fluence Φ which is defined as the number of implanted ions per unit area ought to be constant over the whole target. Thus, the resulting ion depth profile is laterally homogeneous resembling in many cases a Gaussian distribution whose mean is defined as the projected range R_p and whose halfwidth ΔR_p is referred to as longitudinal straggling [191].

However, if the ion implantation is conducted with an ion beam that is focused in both lateral directions y and z, the beam current density profile $j(y,z)$ approximately reads (cf. section 3.1.1):

$$j(y,z) = j_0 \times \exp\left[-\frac{(y-y_0)^2}{2\sigma_{\text{FIB},y}^2}\right] \times \exp\left[-\frac{(z-z_0)^2}{2\sigma_{\text{FIB},z}^2}\right] \, , \tag{3.1}$$
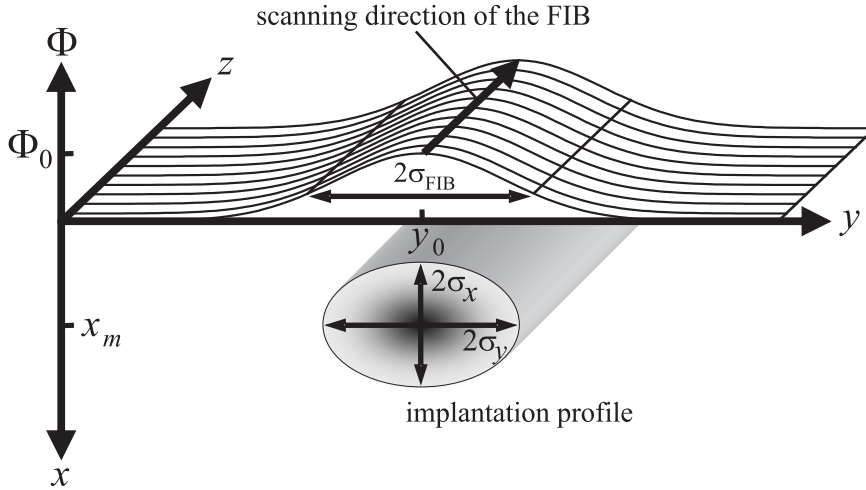
Figure (3.2): A schematic representation of a FIB line scan implantation along the z-direction with a Gaussian FIB current density profile centered at y_0. The resulting implantation profile has a cylindrical Gaussian shape with an elliptical cross-section.

where j_0 is the maximum current density at the center of the profile given by the coordinates (y_0, z_0) and $\sigma_{\mathrm{FIB},y/z}$ denote the widths of the FIB current density profile in both lateral directions. Consequently, if an ion beam, which is focused equally in both lateral directions, is linearly and homogeneously scanned over the target (say in z-direction) at normal incidence with respect to the initial target surface the total ion fluence becomes a y-dependent function given by:

$$\Phi = \Phi(y,z) = \Phi_0 \times \exp\left[-\frac{(y-y_0)^2}{2\sigma_{\mathrm{FIB}}^2}\right] \;, \tag{3.2}$$

where Φ_0 is the maximum fluence at the center of the FIB profile which scales linearly with j_0 at constant scanning speed (cf. Fig. 3.2). The integration of $\Phi(y,z)$ from $y = -\infty$ to $y = +\infty$ gives the line density of implanted ions along z if one neglects sputtering of implanted ions and ion scattering. If the ion beam is focused to such a degree that $2\sigma_{\mathrm{FIB}}$ is in the range of the projected range an implantation profile is obtained with a particular shape resembling a cylindrical Gaussian distribution whose longitudinal axis coincides with the scanning direction of the FIB (cf. Fig. 3.2). The location of highest concentration of implanted ions in the matrix coincides laterally with the maximum of the FIB current density profile. Vertically, this location (projected range) depends on further implantation parameters, e.g. ion energy, the mass ratio between the ions and the target atoms, and the sputtering coefficient. In a first approximation (neglecting sputtering) it can be stated that the corresponding 3D implantation profile can be perceived as a spatial convolution of the lateral FIB current density profile with the vertical depth profile of a broad area ion implantation, i.e. it resembles a cylindrical Gaussian distribution with an elliptical cross-section.

After these general aspects on the shape of FIB implantation profiles the atomistic modeling of realistic implantation profiles of FIB line scans based on the binary collision approximation code TRIM will be demonstrated in the following focusing on two examples which have become recently relevant in view of novel fabrication methods of plasmonic and electronic nanostructures (cf. chapter 1), namely the FIB implantation of:

- Co ions (60 keV) into c-Si to synthesize $CoSi_2$ NW structures from which chains of $CoSi_2$ NCs can further evolve which are suitable as plasmonic structures in the infrared [192] (cf. subsection 4.6.2) and

- Si ions (30 or 60 keV) into SiO_2 to synthesize Si NW structures embedded in the dielectric matrix applicable as single-electron devices or full-depletion transistors (cf. subsection 4.6.2).

Before that, a survey is given of fundamental ion-solid interactions that play a role in the implantation parameter range discussed in the frame of this work. For a profound insight into the field of ion-solid interactions, the interested reader is referred to the works by Rimini [193], Nastasi [191], Smith [194], and Sigmund [195].

3.1.1 Fundamental Ion-Solid Interactions

A solid undergoes structural modifications if it is exposed to a beam of energetic ions. On its trajectory through the solid target, an energetic ion persistently looses energy and momentum in interactions with the target atoms until it comes to rest at a certain distance beneath the sample surface. Two principal physical processes are involved in decelerating the projectile, namely elastic collisions with the target nuclei and inelastic interactions with the electron shells of the target atoms. The energy and momentum transfer to the target atoms initiates a collision cascade in the surface-near region of the target, the duration of which is in the order of 10^{-13} s. Taking ordinary ion fluxes during broad area implantations in the order of 10^{12} cm^{-2}s^{-1} into account, it is therefore justified to assume that collision cascades do not overlap with one another – neither spatially nor temporally. Commonly, a total stopping cross section S is defined which incorporates the energy losses per unit length due to nuclear and electronic effects as well as the atomic density n of the target (nS is denoted as "stopping power"):

$$S(E) = -\frac{1}{n}\left(\frac{\mathrm{d}E}{\mathrm{d}x}\right) = -\frac{1}{n}\left[\left(\frac{\mathrm{d}E}{\mathrm{d}x}\right)_{\mathrm{nu.}} + \left(\frac{\mathrm{d}E}{\mathrm{d}x}\right)_{\mathrm{el.}}\right] = S_n(E) + S_e(E) \;. \qquad (3.3)$$

Nuclear and Electronic Stopping. The sequence of nuclear collisions forms a collision cascade in the target. In a binary collision (BC) a defined amount of energy T is transferred from the incoming particle to the target atom which is assumed to be at rest. The BC are assumed to be elastic, i.e. energy and momentum are conserved. If the transferred energy exceeds a characteristic value, the displacement threshold energy E_d, the target atom is expelled from its initial site, which results in a local modification of the atomic configuration in the target. With regard to energy and momentum conservation, $S_n(E)$ is defined as

$$S_n(E) \equiv \int_0^{T_{\max}} T \mathrm{d}\sigma(T) \;, \qquad (3.4)$$

where

$$T = \frac{4m_1 m_2}{(m_1 + m_2)^2} E \sin^2\frac{\theta_c}{2} \quad \text{and} \quad T_{\max} = T(\theta_c = 180°) \;. \qquad (3.5)$$

Here, m_1, m_2, E, and θ_c denote the masses of the particles involved in the BC, the energy of the incident particle, and the scattering angle in the CM system, respectively [191]. The scattering cross section $d\sigma(T)$ additionally depends on the repulsive potential V by which the particle collision is characterized. Due to shielding effects of the innermost electron shells, one generally assumes a screened Coulomb potential with regard to the distance r of the interacting atoms with the atomic numbers Z_1 and Z_2:

$$V(r) = \frac{Z_1 Z_2 e^2}{4\pi\epsilon_0 r} \, \chi\left(\frac{r}{a}\right) \, , \tag{3.6}$$

where χ and a denote the screening function and the screening length, respectively. The other variables bear common meaning. Numerous variations of χ have been proposed in the past to describe the potentials of as many projectile-target combinations as possible. A universal screening function

$$\chi_{\text{uni}}(y) = 0.1818 \, e^{-3.2y} + 0.5099 \, e^{-0.9423y} + 0.2802 \, e^{-0.4028y} + 0.02817 \, e^{-0.2016y} \tag{3.7}$$

was established by Ziegler, Biersack, and Littmark including a universal screening length

$$a_{\text{uni}} = \frac{r}{y} = \frac{0.8845 \times a_0}{(Z_1^{0.23} + Z_2^{0.23})} \, , \tag{3.8}$$

where $a_0=0.053$ nm denotes the first Bohr radius of the hydrogen atom [196]. For mathematical convenience, reduced units for E and x were introduced:

$$\varepsilon = \frac{m_2}{m_1 + m_2} \times \frac{4\pi\epsilon_0 a_{\text{uni}}}{Z_1 Z_2 e^2} \times E \quad \text{and} \quad \xi = N\pi a_{\text{uni}}^2 \times \frac{4m_1 m_2}{(m_1 + m_2)^2} \times x \, . \tag{3.9}$$

In the present work, Co or Si ions with energies up to 60 keV are considered for implantation into Si or SiO$_2$ targets, respectively. For the two examples of 60 keV Co colliding with Si and 60 keV Si with Si the respective values for ε amount to 0.42 and 1.35, thus, the low energy regime (after Rimini [193] for all cases where $\varepsilon < 10$) can be assumed here for which an analytical fit function for $S_n(\varepsilon)$ is available [191]:

$$S_n(\varepsilon) = \left(\frac{d\varepsilon}{d\xi}\right)_n = \frac{0.5\ln(1 + 1.1383\varepsilon)}{\varepsilon + 0.01321\varepsilon^{0.21226} + 0.19593\sqrt{\varepsilon}} \, . \tag{3.10}$$

Besides nuclear collisions, the projectile looses energy in inelastic interactions with the electron shells of the target atoms, i.e. electronic excitations or ionizations occur which are often accompanied by the disintegration of chemical bonds. For low particle energies[1] a linear dependence between $S_e(\varepsilon)$ and the particle velocity (i.e. $\sqrt{\varepsilon}$) is assumed in accordance with Lindhard-Scharff:

$$S_e(\varepsilon) = \left(\frac{d\varepsilon}{d\xi}\right)_e = k\sqrt{\varepsilon} \, , \text{ where } \; k = \frac{Z_1^{2/3} Z_2^{1/2} \left(1 + \frac{m_2}{m_1}\right)^{3/2}}{12.6 \times \left(Z_1^{2/3} + Z_2^{2/3}\right)^{3/4} m_2^{1/2}} \, . \tag{3.11}$$

In the two cases discussed above the k-values amount to $k_{60\,\text{keV Co}\rightarrow\text{Si}}=0.120$ and $k_{60\,\text{keV Si}\rightarrow\text{Si}}=0.146$. Thus, comparing $S_n(\varepsilon)$ with $S_e(\varepsilon)$ one finds that nuclear collisions clearly dominate the stopping process for the present ion-target combinations for the given ion energy. This result is corroborated by TRIM simulations (cf. subsection 3.1.2).

---

[1]i.e. the projectile is significantly slower than the shell electrons: $v \ll v_0 Z_1^{2/3}$, where v_0 is the velocity in the first Bohr orbit: $v_0 = \frac{2\pi e^2}{h} = \alpha \times c = 2.1877 \times 10^6$ m·s^{-1}.

Surface Erosion. Sputtering plays a very important role during the FIB implantation. Due to the Gaussian-like FIB current density profile the sputtering rate varies locally to a high degree which results in the formation of a sputtering groove whose trough is located at y_0 (cf. Fig. 3.1 and Fig. 3.2). Due to the random nature of the collision cascade, a certain fraction of the energy transferred in nuclear collisions with the target atoms is stored close to the surface of the target. If the energy transfer is large enough to overcome the surface binding energy E_b an atom of the outermost atomic layers may leave the matrix if the momentum transfer points into the direction of the surface normal. The decisive quantity describing this phenomenon of surface erosion is the sputtering yield Y_s which is defined as ratio between the number of emitted atoms and the number of incident particles. Sigmund determined the dependence of Y_s on the physical parameters involved as follows [191, 197]:

$$Y_s(E_0) \propto \frac{1}{n E_b} \times \alpha \times S_n(E_0) \; . \tag{3.12}$$

Here, α denotes a function of the mass ratio (m_2/m_1) (cf. Fig. 9.3(a) in Ref. [191]). α increases with the angle of incidence β measured from the surface normal:

$$\alpha(\beta) = \frac{\alpha(0)}{\cos \beta} \; . \tag{3.13}$$

This scaling behavior is valid for most ion-target combinations for angles of incidence up to 60°. Between 60° and 80° $\alpha(\beta)$ passes through a maximum. At angles of ion incidence above 80°, Y_s decreases again drastically and can even become zero under grazing incidence (ion scattering). E_b is usually equated with the heat of sublimation $\Delta_s H°$(for Si: $\Delta_s H°$=450 kJ/mol; E_b=4.7 eV). However, the determination of Y_s for dielectric compounds like SiO_2 is rather complicated. In general, E_b, S_n, and α differ from element to element in a compound. Thus, preferential sputtering usually occurs which leads to a composition change of the surface region. Furthermore, chemical effects may influence the sputtering behavior of a surface which consists of miscellaneous atomic species. Obviously, the analytical calculation of the sputtering coefficients becomes a very difficult task. Therefore, computer simulations like TRIM or even better TRIDYN (cf. subsection 3.1.2) can be applied to determine the sputtering coefficient numerically including the full statistics of the ion implantation process. Those numerical results decisively depend on the predefined surface binding energies. In the case of SiO_2, the heat of formation $\Delta_f H$ as well as the enthalpy of the dissociation of molecular oxygen ΔH^{diss} have to be taken into account. It is not expected that oxygen is enriched at the surface because it is likely to form volatile oxygen molecules which are free to leave the target [198]. Using the following tabulated materials parameters: $\Delta_f H(SiO_2)$=9.44 eV and $\Delta H^{\mathrm{diss}}(O_2)$=5.17 eV [199] one gets in accordance with Eqn. 17 in Ref. [198]: E_b(Si-Si)=4.7 eV, E_b(O-O)=0 eV, and E_b(Si-O)= $\frac{1}{2}\Delta_s H$(Si) $+ \frac{3}{4}\Delta_f H(SiO_2) + \frac{3}{4}\Delta H^{\mathrm{diss}}(O_2)$=13.3 eV. Given the above values and ion-target combinations one finds under normal incidence for ion energies of 60 keV the following total sputtering coefficients: $Y_s(\mathrm{Co} \xrightarrow{60\,\mathrm{keV}} \mathrm{Si})$=2.3 and $Y_s(\mathrm{Si} \xrightarrow{60\,\mathrm{keV}} \mathrm{SiO_2})$=2.0. These are the low-fluence limits; in the high-fluence limit (stationary implantation profiles) the respective sputtering coefficients obtained by TRIM read $Y_s(\mathrm{Co} \xrightarrow{60\,\mathrm{keV}} \mathrm{CoSi_2})$=3.9 (assuming the surface-near formation of $CoSi_2$ in the stationary state) and $Y_s(\mathrm{Si} \xrightarrow{60\,\mathrm{keV}} \mathrm{Si})$=1.3 (assuming the surface-near formation of SiO_x with x$\ll$1).

Radiation Damage. In collision cascades the atomic configuration of the target material is vigorously modified. Nuclear damage arises from the recoil of matrix atoms from their original position in the lattice. In the case of broad area implantations, the maximum of the vertical damage profile is slightly closer to the surface than the projected range. If T exceeds E_d, a so-called "Frenkel pair" is produced, i.e. the recoil atom comes to rest as interstitial atom elsewhere in the matrix leaving behind a vacancy at its initial site. Due to the forward momentum of the projectile, the distributions of interstitial atoms and vacancies do not completely coincide. Accordingly, for a Si target there comes a vacancy-rich region into being extending from the surface down to approximately $0.8R_p$ with a maximum at $0.5R_p$ (so-called "$R_p/2$ effect"). In addition, a zone enriched with interstitial atoms between R_p and $2R_p$ is generated [200]. Besides displacement collisions, also replacement collisions occur where the projectile takes the place of the recoiled matrix atom. The number of dpa's serves as common measure of the nuclear damage. It is proportional to the ion fluence. For example, crystalline semiconductors are fully amorphized at RT and below if about each atom of the crystal is displaced at least once, i.e. at a nuclear damage around 1 dpa. Metals on the contrary have enough kinetics that they can hardly be amorphized at RT. Some materials are far more sensitive to nuclear damage than semiconductors and are already amorphized at lower damage, e.g. crystalline quartz turns into a-SiO$_2$ at 0.04 dpa [201]. In the present work, however, it is assumed that the Si ions are implanted into thermally grown SiO$_2$ which is an amorphous material from the beginning. In the case of Co implantation into c-Si, however, RT implantation would amorphize the implanted region. Here, amorphization can be suppressed by elevating the temperature of the target during implantation. Thus, the mobility of point defects increases significantly due to the temperature dependence of the point defect diffusivity $D \propto \exp\left(-E_a/k_B T\right)$, where E_a denotes the diffusion activation energy. Accordingly, Frenkel pairs become less stable resulting in interstitial-vacancy recombination, thus, the damage is partially annealed. Therefore, the crystallinity of the Si substrate can be preserved depending on the ratio between the rates of ballistic displacements and thermally activated recombination, i.e. depending on the balance between ion flux and implantation temperature. This indicates that the temperature regime during ion implantation may exert substantial influence on the dynamics of the compositional changes in the matrix – including phase separation.

Target Swelling. For the situations discussed in the frame of this work, high fluences (from several $10^{16}\,\mathrm{cm}^{-2}$ up to few $10^{17}\,\mathrm{cm}^{-2}$) are locally implanted into the target. Consequently, the surface-near stoichiometry may change up to 30 % in some cases. If the target volume was kept constant, the implantation would lead to a local increase of atomic density which gives rise to strain in the implanted region. The resulting stress causes an expansion of the target material which causes the target to swell. For broad area implantations of Si into SiO$_2$ this target swelling effect has been verified [120] and is therefore expected to play a role in the case of FIB line scan implantations, too. However, the case of Co implantation into c-Si the case is very much different. Provided that Co is implanted at slightly elevated temperature which prevents amorphization of the crystalline Si target (8 atoms per unit cell) the formation of the Si-rich cobalt silicide phase CoSi$_2$ (12 atoms per unit cell: 8 Si and 4 Co, cf. Fig. 3.6) can be expected to happen directly during implantation [168, 202]. Since CoSi$_2$ and c-Si have both a cubic

crystal structure (CaF_2 and diamond structure, respectively) and a lattice mismatch of only -1.2% (g_{CoSi_2}=0.5364 nm; g_{Si}=0.543 nm) it can be assumed that the implanted Co is fully incorporated into the matrix as $CoSi_2$ precipitates within c-Si without changing to the volume of the target significantly [168].

FIB Characteristics. FIB units are mostly deployed as micromechanical tools for milling, drilling, dimpling, grinding, polishing etc. of solid materials, e.g. for lithographic mask repair [203], for the preparation of TEM specimens [204, 205], or for sculpting crystalline and amorphous targets [206, 207]. Due to the characteristics of ion optical systems a point-like ion source is required for a high focusing of the ion beam. To fulfil this requirement, Gallium ions are most commonly used due to the fact that Ga is almost liquid at RT[2], i.e. a point-like liquid droplet of Ga serves as ion source [208]. In order to provide ion species other than Ga, liquid metal alloy ion sources were developed which are characterized by a eutectic melting temperature of a binary or even ternary alloy that is much lower than the melting temperatures of the individual constituents[3]. Thus, a rich series of elements is nowadays available for FIB implantation, e.g. Au, Bi, Be, Co, Cr, Er, Fe, Ge, In, Li, Nd, Ni, Pr, Pt, Si [208, 209, 210]. Consequently, these elements can be considered not only for micromechanical applications but also for a direct implantation aiming at the IBS of new phases embedded in the target material. If a liquid metal alloy ion sources is used, the FIB unit must contain a Wien filter in order to separate the individual constituents that are simultaneously extracted from the ion source by an electric field. In general, the mass resolution of such filters is sufficient to separate the naturally occurring isotopes of the respective elements. In this perspective, Co has the advantage to have just one naturally occurring isotope: ^{59}Co. Thus, the splitting of the FIB into multiple beams on the path through the mass sensitive ion optics does not occur. In the case of Si implantation one has to be aware of the fact that besides ^{28}Si (atomic percent abundance: 92.23%) a considerable amount of Si ions is implanted as individual ^{29}Si (4.67%) and ^{30}Si (3.10%) beams which impinge on the substrate in a distance some micrometers away from the region that is targeted with the ^{28}Si beam.

In view of the shape of the FIB profile, i.e. the lateral beam current density profile, it is usually assumed that FIB profiles obtained from common FIB columns resemble a Gaussian distribution [208]. However, evidence exists that there is an exponential halo in superposition to the main beam which can be seen in Fig. 3.3 for the FIB unit at FZD showing the measured beam current density profile of a focused 60 keV Co^{++} ion beam[4]. Doubly charged ions were chosen to increase the ion energy which has virtually no influence on the ion-solid interactions discussed above. Regarding the atomistic modeling of the ion implantation profile and the subsequent phase separation, this exponential halo is not expected to change the simulation results due to its large FWHM compared to the primary peak of the main beam. For the FIB profile a simple Gaussian shape of some tens of nanometers in width can therefore be assumed throughout this work. Since the investigation of this chapter were mainly motivated in view of experimental investigations on FIB-based NW synthesis, the characteristic

---

[2]For Ga: $T_{melting} = 29.8\,°C$

[3]For example, the binary alloy $Au_{82}Si_{18}$ has a eutectic melting temperature of $T_m = 364\,°C$ compared to $T_{m,Au} = 1064\,°C$ and $T_{m,Si} = 1410\,°C$.

[4]By courtesy of C. Akhmadaliev, L. Bischoff, and B. Schmidt.
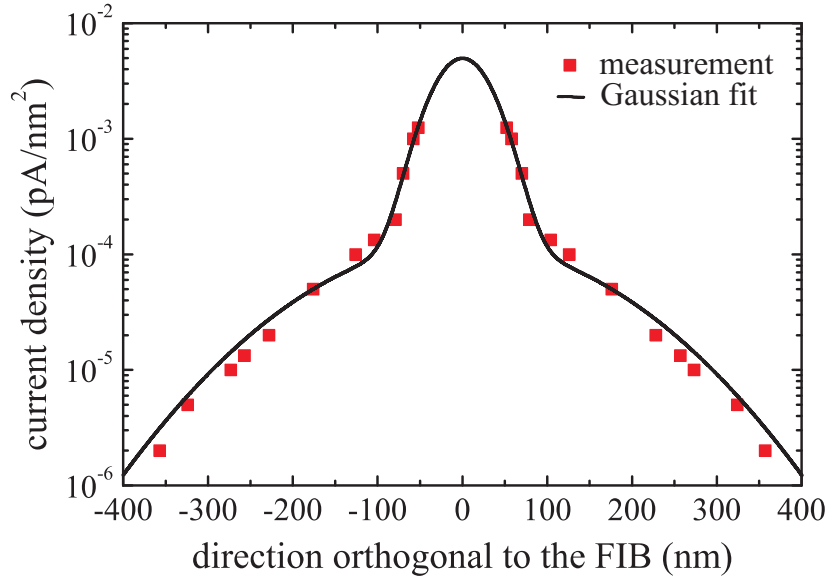
Figure (3.3): Profile of a $60\,\mathrm{keV}$ focused Co^{++} ion beam. Here, the total current was $42\,\mathrm{pA}$. According to Gaussian fittings, the FWHM of the peak and the halo are $61.8\,\mathrm{nm}$ and $264.2\,\mathrm{nm}$, respectively. The integrated peak current density is $76\,\%$ of the total one (cf. Fig. 1 of Ref. [211]).

parameters of the FIB system at FZD (which is also typical for other FIB units), a IMSA-Canion 31Mplus Orsay Physics FIB, is mentioned briefly for the sake of completeness: ion energy: 10 to $30\,\mathrm{keV}$ (I^+); current: 0.001 to $22\,\mathrm{nA}$; max. current density: $\sim 20\,\mathrm{Acm}^{-2}$; Wien filter: $m/\Delta m = 35$; target heating: up to $700\,^\circ\mathrm{C}$; min. spot size: $14\,\mathrm{nm}$ (for Ga) [212]. Apparently, the ion current density in the center of the profile can be orders of magnitude higher than in the case of common broad area implantations (even compared to high-current implanters). However, even in the extreme case of an ion flux in the center of the FIB profile in the order of $10^{20}\,\mathrm{cm}^{-2}\mathrm{s}^{-1}$ the approximation that collision cascades do not overlap still holds for the present parameter range which legitimates BC approximation calculations of the implantation profile which are portrayed in the following. For a discussion about analog and digital FIB-scanning modes see the following subsection.

3.1.2   Modeling of FIB Line Scan Implantation Profiles

The physical principles portrayed above are the basis to understand the various processes involved during ion implantation. However, for a quantitative description of an ion implantation experiment, in which arbitrary target compositions and implantation parameters are given, this analytical apparatus is inefficient. Therefore, quantitative examinations are usually performed by computer simulations in which arbitrary ion-target combinations can be considered. In this connection various simulation methods exist that are suitable to model ion implantation, such as MD simulations, Boltzmann transport equation methods, or MC simulations based on the BC approximation. In praxi, the TRIM (or SRIM[5]) code [196, 213] has become dominant in the ion beam community due to its rather simple operation mode and moderate computation speed. Thus, implantation profiles or radiation damage distributions can easily and rapidly be calculated on ordinary desktop computers nowadays. There are further developments

---

[5]The SRIM program can be downloaded at `www.srim.org`.

of TRIM such as TRIM-DYNAMIC [214], TRIDYN [198, 215], or Crystal-TRIM [216]. With these programs, surface erosion, dynamic changes in the atomic composition of the target, dynamic and preferential surface erosion, target swelling, channeling effects etc. can be studied additionally. For a comprehensive insight into the subject of computer modeling of ion-solid interactions, the reader is referred to Eckstein's monograph [217] and the numerous references given therein. The modeling of realistic FIB line scan implantation profiles has been based on TRIM, thus, a concise overview over the mechanisms of this code is required.

The TRIM Code. The TRIM code (**T**ransport and **R**ange of **I**ons in **M**atter) describes the trajectory of an incident ion (interpreted as pseudoparticle) through the target as a series of BCs with target atoms at rest. Thermal vibrations of matrix atoms around their positions are neglected (i.e. $T = 0\,K$) because the mean amplitude of the lattice vibration at RT and below is only few percent of the lattice parameter[6]. The momentum transfer during a single projectile-target collision is much shorter than the period of a lattice vibration at RT ($\approx 10^{-12}\,s$). Thus, the target atoms can legitimately be assumed to be motionless at RT and below. In the standard TRIM code, the target atoms are quasi-randomly distributed in space which applies nicely to amorphous materials, even though a short range order does always occur in reality. The spatial randomness is a rather good approximation for crystalline targets, too, since in praxi ion implantation is mostly performed under a 7° misalignment of the ion beam with respect to the normal of the target surface (low-index) in order to avoid channeling. The path of the ion is characterized by a constant free path length λ which the projectile travels between two successive BCs. Here, λ is given by the inverse cube root of the atomic density. From a numerical point of view, the stochastic nature of the ion trajectory is realized by a randomly generated impact parameter for each individual BC. From this, each nuclear collision is computed, i.e. the nuclear energy loss as well as the polar deflection angle are calculated using the universal screening potential (or ZBL potential) given by equations 3.6, 3.7, and 3.8. Thereafter, the azimuthal scattering angle is randomly determined. Besides that, the electronic energy loss of each particle in motion is recorded on the path between successive BCs. Consequently, positional, directional, and energetic changes of the projectile describe its trajectory through the target. All target atoms which are set into motion due to collisions and, thereby, participate in the collision cascade are traced likewise. Thus, the entire collision cascade is examined which comes to a general standstill within $10^{-13}\,s$ after the ion impinges on the target surface. The standard TRIM code, however, does not consider stoichiometric changes of the target which occur in the case of high fluence ion implantations. In other words, each new ion trajectory is calculated for a pristine target which clearly shows the approximative character of this simulation method.

   Prior to each TRIM simulation run, ion and target parameters have to be declared (ion energy, angle of incidence, number of implanted pseudoparticles, target composition, atomic densities etc.). Furthermore, certain element-specific energy parameters are predefined, namely E_d (the displacement energy), E_s (the surface binding energy), and E_b (the bulk binding energy which is subtracted from the nuclear energy transfer T).

---

[6]Assuming the Debye-Waller theory, the mean square amplitude is given by $\langle u_i^2 \rangle = \frac{3\hbar^2}{Mk\Theta} \times \left(\frac{T^2}{\Theta^2} \int_0^{\Theta/T} \frac{x\,dx}{e^x - 1} + \frac{1}{4} \right)$. For Si ($\Theta_{Si} = 640\,K$) at RT: $\sqrt{\langle u_i^2 \rangle} \cong 0.007\,nm$ ($= 0.015\,a_{Si}$).

The determination of E_b is not uniform throughout the literature. Some authors (e.g. [218]) set E_b equal to zero, although E_b is generally interpreted as vacancy formation energy, i.e. as the minimum energy of an atom to leave its site. In the present cases, where strong covalent bonds are considered (Si, SiO_2 targets), E_b was set to $2\,eV$. The choice of E_b is mainly a matter of convention. In TRIM, a few eV are employed as standard values; the TRIDYN convention is $E_b = 0$ yielding good results for the sputtering yields of most elements [198, 215]. A new choice of E_b requires and adjustment of E_s in order to obtain the same sputtering yield [217]. A further so-called "cutoff" energy E_c declares the termination of the particle motion through the solid. At the moment when the total particle energy becomes smaller than E_c it is assumed to have arrived at its final position. In any case, E_c needs to be smaller than E_b in order to treat sputtering properly. Besides implantation profiles, nuclear damage distributions are of interest in the present study. The measure of choice with regard to nuclear damage is the number of displacements per target atom (dpa). In TRIM, atomic displacements are defined as a sum of vacancy production and replacement collisions.

For further insight into the realm of TRIM, the interested reader is referred to Refs. [196, 213, 217] and the extensive information on the SRIM-website.

Adoption of TRIM to Gaussian FIB Current Density Profiles.   In the literature there exists one attempt to model FIB implantations with a TRIM-like code called FIBSIM which combines dynamic MC simulations of the collision cascades with a cell-based topography simulation to study sputtering of 2D targets [219, 220]. Thereby, the evolution of the target surface can be studied due to non-uniform sputtering. Focus of this investigation was the erosion of sample edges and the drilling of a hole into a target, e.g. applications for which very high ion fluences and high angles of incidence are characteristic. Although this code seems to produce reasonable results it is unfortunately not freely available, yet. Consequently, a separate and simple model had to be developed to tackle the present problems to simulate the 3D implantation profile and the nuclear damage distribution of homogeneous FIB line scan implantations which decisively determine the possibility for the post-implantation synthesis of NW structures. As discussed above, the FIB current density profile is of Gaussian shape from which a Gaussian fluence profile in one lateral direction follows if one considers a homogeneous FIB line scan over the target (so-called analog mode).

In the present attempt to model the homogeneous FIB line scan implantation the surface of the 3D simulation cell representing the target is discretized into a square mesh with a fine spacing of $0.5\,nm$. Then, a straight line along the surface is defined by which the z-axis of the Cartesian coordinate system is given. Thus, the direction parallel to the surface and orthogonal to that line is the y-axis which crosses the z-axis in y_0 (cf. Fig. 3.2). The x-axis points into the depth of the target where x_0 coincides with the initial target surface. After these definitions the ion fluence profile $\Phi = \Phi(y, z)$ is calculated after Eqn. 3.2, i.e. the number of ions I is determined which impinge on each node of the square mesh representing the surface[7]. For a homogeneous FIB line scan along z the ion fluence loses its z-dependence, thus, $\Phi = \Phi(y)$. Then, 3D ion range and collision data from standard TRIM calculations for several 10,000 pseudoparticles are calculated for the implantation and target parameters of interest.

---

[7]For example, the total number of implanted ions per node amounts to $I=125$ for a local ion fluence of $5 \times 10^{16}\,cm^{-2}$.
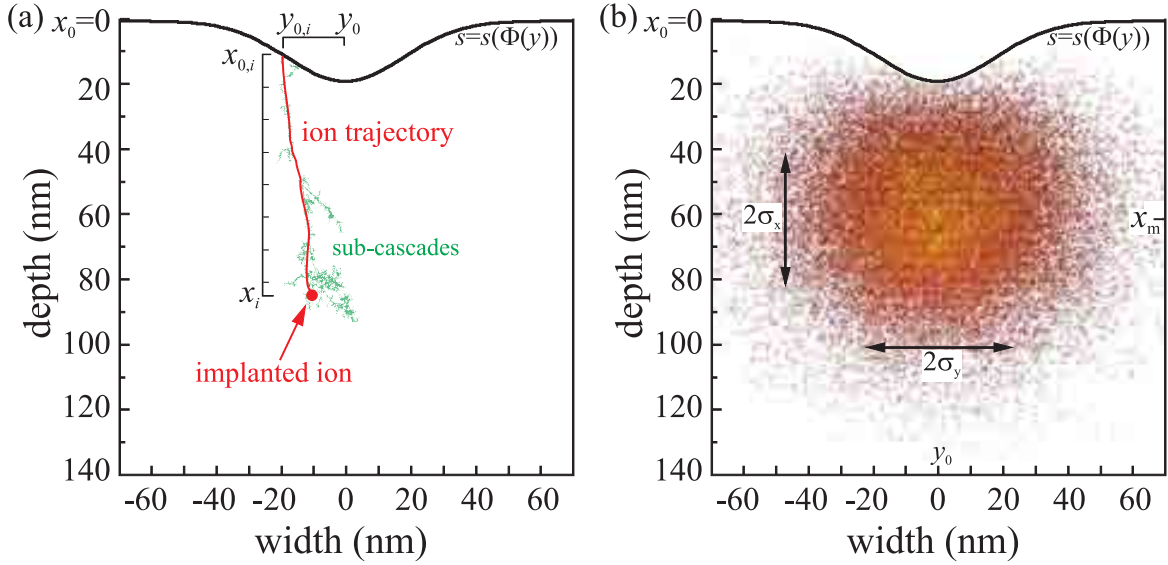
Figure (3.4): (a) A schematic representation of the TRIM-based modeling of a FIB line scan implantation profile considering a Gaussian FIB current density profile (cross-section). The surface s recesses locally as a function of the local ion fluence $\Phi(y)$. (b) Example of a FIB implantation profile (cross-section) for the implantation of Co (60 keV) into Si ($\Phi_0 = 4 \times 10^{16}$ cm^{-2}, $2\sigma_{FIB} = 50$ nm). The color code indicates the local Co concentration in the Si target (see text for details). The 1D cross-sections at x_m and y_0) are plotted in Fig. 3.5.

From this data set, pseudoparticle trajectories and corresponding collision details are chosen randomly and are assigned iteratively to the nodes of the surface mesh according to the computed number of ions I that are locally implanted into each node. After each pseudoparticle implantation the local x-coordinate of the target surface is changed because of local sputtering (cf. Fig. 3.4 (a)). In other words, it is assumed that each ion impact causes a local recession of the surface in the corresponding surface element. Thus, for each pseudoparticle i ($1 \leqslant i \leqslant I$) there is an individual location of impact given by the coordinate set ($x_{0,i}; y_{0,i}; z_{0,i}$) where $x_{0,i}$ is given by

$$x_{0,i} = x_0 + \frac{\Omega Y_s}{\nu}(i - 1) \ . \tag{3.14}$$

Here, $\nu = 0.25$ nm^2 is the area of a cell of the previously defined surface mesh, Ω is the volume of the target atoms and Y_s denotes the sputtering coefficient that is computed
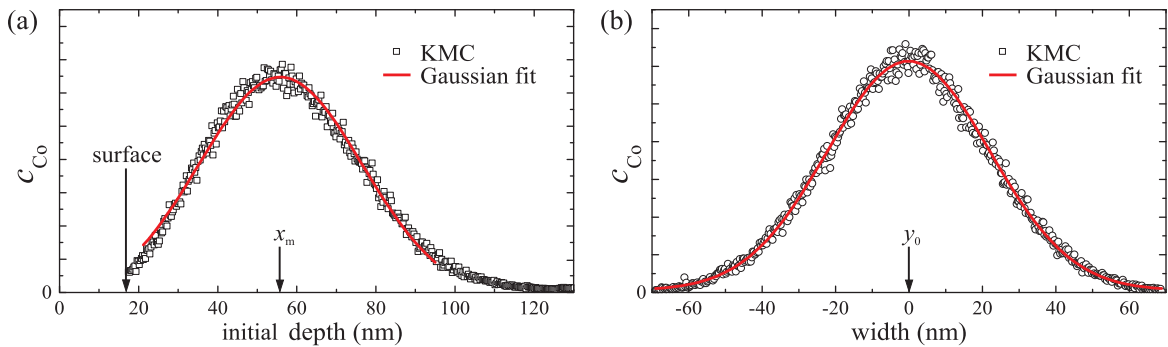
Figure (3.5): Cross-sections through the center ($x_m; y_0$) of the FIB implantation profile shown in Fig. 3.4 (b) in x-direction (a) and in y-direction (b). The Gaussian fits of the Co distribution correspond to $2\sigma_x = 41$ nm and $2\sigma_y = 45$ nm, respectively (cf. Fig. 3.2). Thus, the implantation profile is of cylindrical Gaussian shape with a nearly spherical ($\sigma_x = \sigma_y$) cross-section.

with TRIM for the respective implantation conditions under normal incidence. This is an approximation that is crucial for the whole procedure since the sputtering coefficient depends on the angle of ion incidence (cf. Eqn. 3.13) that changes locally when the sputtering groove develops.

Consequently, the degree of surface erosion is maximal where the fluence is maximal, i.e. at y_0, where the trough of the sputtering groove develops. This groove takes over the Gaussian shape of the ion fluence profile. The slope of the surface profile is maximal at the inflection points of the Gaussian where the above approximation of local sputtering using the sputtering coefficient under normal incidence produces the greatest error because Y_s scales approximately with $\cos^{-1}(\beta)$ (β is the local angle of incidence whose tangent equals the surface slope which increases dynamically with increasing fluence). From the author's viewpoint an error of $Y_s(\beta)$ up to a factor of two compared to $Y_s(0)$ under normal incidence would be tolerable at the inflection points and one would still get reasonable implantation and damage profiles since the lion share of ions is implanted at the center of the FIB profile where the surface slope remains close to zero. Consequently, surface slopes at the inflection points up to 60° are justifiable which corresponds to a critical peak fluence Φ_0 in the case of 60 keV Co implantation into Si of approximately $1 \times 10^{17}\,\mathrm{cm}^{-2}$ and in the case of 60 keV Si implantation into SiO$_2$ of about $3 \times 10^{17}\,\mathrm{cm}^{-2}$ for $2\sigma_{\mathrm{FIB}} = 50\,\mathrm{nm}$. Evidently, there is an individual critical peak fluence for each ion-target combination and FIB parameter set. Above these critical peak fluences this method to model FIB line scan implantation profiles becomes doubtful. Fortunately, for the ion-target combinations considered here, these critical peak fluences are well above the minimal Φ_0 values required to achieve a local degree of supersaturation in the target that is high enough for continuous NW structure formation during post-implantation phase separation. For peak fluences above the critical value it is expected that the developing surface profile of the sputtering groove transforms from a Gaussian shape to a U-like shape (cf. Fig. 3 in Ref. [220]).

A further critical issue is the local swelling of the target due to ion implantation which may have influence on implantation and damage profiles, too. Compared to broad area implantations where swelling occurs one-dimensionally, i.e. into direction of the target surface normal, the swelling is a 2D problem for cylindrical Gaussian implantation profiles obtained here (cf. Fig. 3.4 (b)). The extra volume in the center of the implanted region can expand into a certain radial angle symmetric around y_0, i.e. in normal but to a certain degree also in lateral direction. A quantitative analysis of this radial swelling effect would require in the spirit of a finite element calculation the splitting of the target cross-section into a 2D mesh of infinitesimal small elements like in the case of TRIDYN where for broad area implantation simulations the target is composed of 1D slices which are allowed to alter in width and number due to local changes of the atomic density with increasing ion fluence [198, 215]. This 2D meshing would be a tremendous complication of the present method and it would most probably result merely in second order corrections of the FIB line scan implantation profiles presented here. Therefore, no target swelling has been assumed for the determination of the FIB implantation profiles in the frame of this work. This assumption holds perfectly well in the case of Co implantation into Si if one assumes that already during implantation the Si-rich cobalt silicide CoSi$_2$ is formed. Then, no target swelling occurs because the partial atomic density of Si is nearly equal in CoSi$_2$ as well as Si (cf. Fig. 3.6). However, for the FIB line scan implantation of Si into SiO$_2$, the Si excess
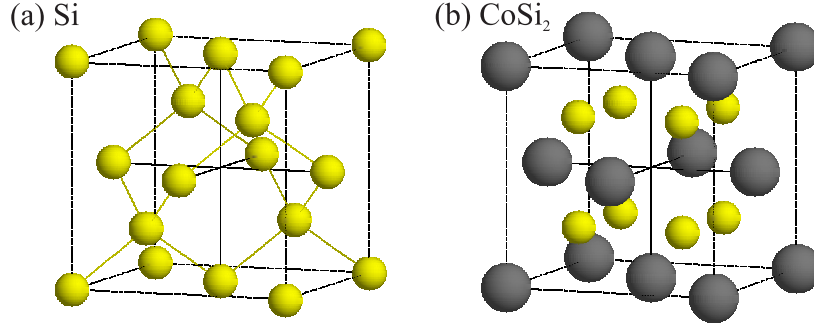
(a) Si   (b) CoSi$_2$

Figure (3.6): Cubic unit cells of (a) Si (diamond structure; Strukturbericht designation: A4) and (b) CoSi$_2$ (CaF$_2$ structure; Strukturbericht designation: C1). The lattice mismatch between these two structures is about 1.2% ($g_{Si} = 0.543$ nm; $g_{CoSi_2} = 0.5364$ nm). Thus, the partial atomic density of Si is nearly equal in both materials (≈ 50 Si/nm^3).

causes certainly swelling in the high-fluence regime where the standard TRIM code also shows less exact implantation profiles.

Simulation of Realistic FIB Line Scan Implantation Profiles.   As an example of FIB line scan implantation profiles, in Fig. 3.7 the cross sections of such profiles are plotted for four different peak fluences for the case of 60 keV Co implantation into Si with $2\sigma_{FIB} = 50$ nm in each case. Accordingly, the maximum concentration of Co in the Si target can reach up to the order of 20 at.% in the center of the implantation profile. In comparison, this value is about 5 at.% lower than the maximum
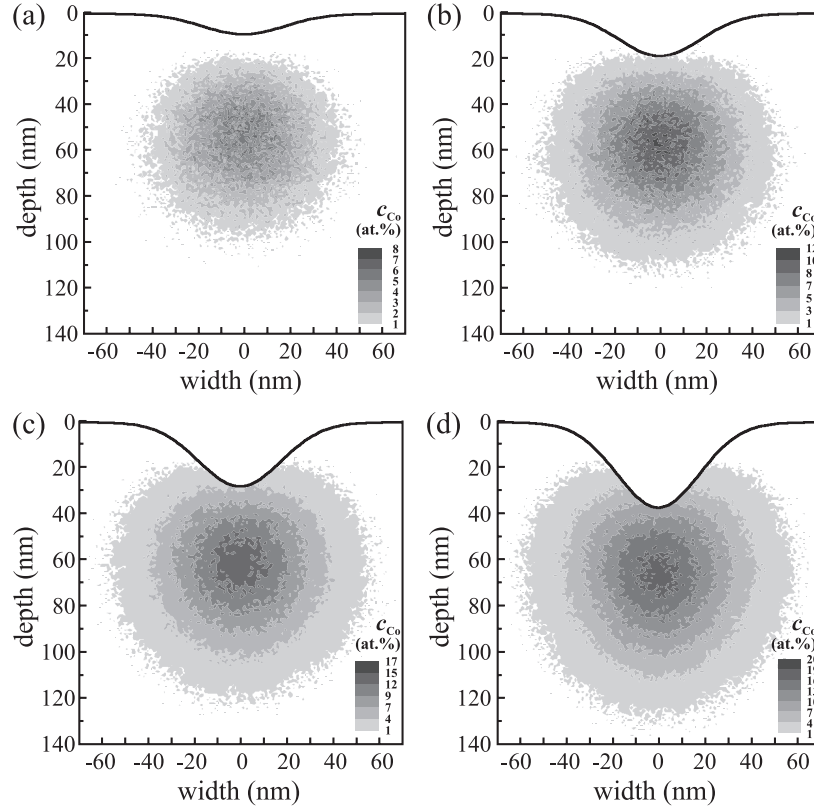
Figure (3.7): FIB implantation profiles (cross-sections) for the implantation of Co (60 keV) into Si ($2\sigma_{FIB} = 50$ nm) for (a) $\Phi_0 = 2 \times 10^{16}$ cm^{-2}, (b) $\Phi_0 = 4 \times 10^{16}$ cm^{-2}, (c) $\Phi_0 = 6 \times 10^{16}$ cm^{-2}, and (d) $\Phi_0 = 8 \times 10^{16}$ cm^{-2}. The gray scale indicates the local Co concentration.

Co concentration in corresponding broad area implantations which can be seen in Fig. 3.8 where broad area implantation profiles are depicted that were computed with TRIDYN [198, 215] for the same ion-target parameters like in the case of Fig. 3.7. In the TRIDYN simulations, the direct formation of $CoSi_2$ is assumed by setting the atomic volume of Co to an artificial negative value in order to avoid swelling of the target and to guarantee that the atomic density of the target can grow locally from $49.8\,at/nm^3$ for c-Si towards $77.2\,at/nm^3$ for c-$CoSi_2$. The formation enthalpy of $CoSi_2$ was taken into account for the calculation of the (2×2) surface binding energy matrix ($E_{Si\text{-}Si}{=}4.70\,eV$, $E_{Co\text{-}Co}{=}4.43\,eV$, $E_{Si\text{-}Co}{=}5.37\,eV$) according to Eqn. 7 in Ref. [198] in order to describe sputtering properly. For $\Phi_0 = 8 \times 10^{16}\,cm^{-2}$, the concentration of Co in the target c_{Co} reaches 24 at.% compared to nearly 19 at.% in the case of FIB line scan implantation. This lower value of maximum concentration is expected because of lateral straggling of ions implanted at y_0 where Φ is maximal. In return, less particles straggle laterally into the center of the profile as in the case of broad area implantations.

Concerning the surface erosion, the broad area implantation case (cf. Fig. 3.8, dark yellow curve) leads to a recession of the surface of about 35 nm, which is also reached at the trough of the sputtering groove in the FIB line scan implantation case (Fig. 3.7 (d)). Consequently, the above discussed procedure of dynamic surface recession delivers reasonable results at least for surface regions with small slopes.

For these specific implantation parameters the shape of the implantation profile resembles a cylindrical Gaussian with a nearly spherical cross-section whose symmetry is only disturbed by the sputtering groove. In Fig. 3.5, the 1D cross-sections through the center of the FIB implantation profile shown in Fig. 3.4 (b) along x and y are plotted. Accordingly, the vertical width $2\sigma_x$ ($=41$ nm) and the lateral width $2\sigma_y$ ($=45$ nm) of the implantation profile are nearly equal, thus, the 3D implantation profiles is of Gaussian shape with nearly spherical cross-section which makes it suitable for NW structure formation during post-implantation phase separation (cf. section 3.2). Moreover, the lateral width $2\sigma_y$ is nearly equal to the width of the FIB current density profile $2\sigma_{FIB}$ which is expected because of the fact that the 3D FIB line scan implantation profiles can conceptually be interpreted as a convolution of the Gaussian FIB current density profile and the quasi-Gaussian ion implantation profile of common broad area implantations.
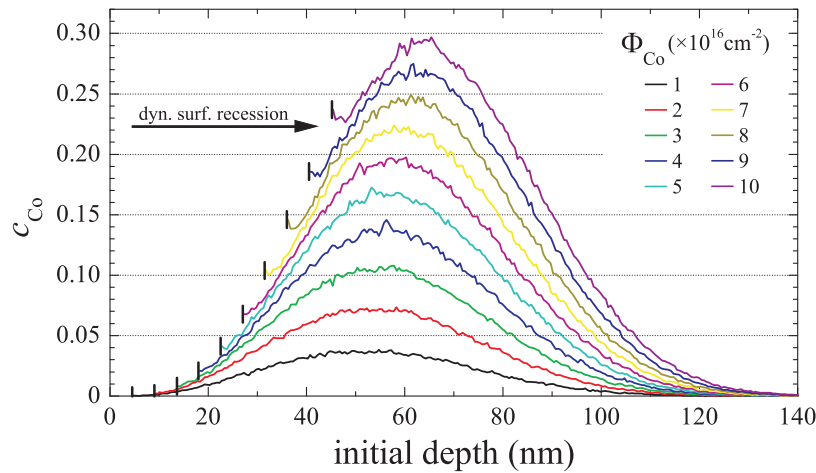

Figure (3.8): TRIDYN simulation results showing the implantation profiles of a broad area implantation of Co (60 keV) into Si under normal incidence for increasing Co fluence Φ_{Co}. The vertical black lines at the beginning of each profile indicate the respective sample surface positions.

For FIB line scan implantation into a crystalline target such as c-Si aiming at the formation of new phases, the accumulated radiation damage is an important parameter regarding ion-beam-induced amorphization of the crystal. It has been discussed earlier (cf. subsection 3.1.1) that above a critical threshold the Si target can be assumed to be fully amorphized, namely at 1 dpa. In order to understand the recrystallization of an amorphized region during post-implantation thermal treatments, it is necessary to know the shape of the boundary between the amorphous region and the region remaining crystalline. In Fig. 3.9, the nuclear damage has been plotted for the case of 60 keV Co implantation into Si ($\Phi_0 = 5 \times 10^{16} \, \mathrm{cm}^{-2}$, $2\sigma_{\mathrm{FIB}} = 50 \, \mathrm{nm}$). Accordingly, the boundary has an inverse-Ω shape for this ion-target parameter set. The 1 dpa damage line extends about 45 nm in width to each side from y_0 and about 100 nm into depth relative to the initial sample surface. During annealing the recrystallization fronts will move radially towards the center of the implantation profile. Thus, crystal defects such as dislocations will certainly accumulate where the countermoving frontiers finally meet, namely in the center of the implantation profile. These defects are expected to disturb the simultaneous phase separation process (heterogeneous nucleation, defect decoration etc.) because of their inherent randomness.

Therefore, in the case of Co implantation into Si it is beneficial to perform the FIB implantation at elevated temperature in order to prevent target amorphization. The nuclear damage that occurs during a single collision cascade will be produced likewise, however, this damage has the chance of being annealed already during implantation due to the thermally activated kinetics (e.g. diffusion) in the system. Thus, less damage would accumulate and the crystallinity of the target can be preserved. The great advantage is that the forming crystalline $CoSi_2$ phase is embedded coherently (A-type precipitation) or semi-coherently (B-type precipitation) in the single-crystalline Si matrix [168]. In other words, the growing $CoSi_2$ phase takes over the crystal orientation of the c-Si matrix. Thus, during NW structure formation single-crystalline $CoSi_2$ NWs can be formed. The effects of implantation temperature on $CoSi_2$ crystallinity and microstructure was thoroughly investigated for broad area implantations. Despite many other influential process parameters (ion energy, fluence, flux), an optimum temperature range to avoid amorphization and to synthesize $CoSi_2$ was found (350 °C to 400 °C) [168]. In homogeneous FIB line scan implantations the ion flux can be orders of magnitude higher causing an increase in the local production rate of defects. Moreover, in real FIB experiments two operation modi are possible which complicates the situation: At first, the *analog mode* where the FIB is linearly scanned over the target with constant velocity and constant current density profile. Secondly, the *digital mode* where the implanted target area is discretized into a pixel mesh and the beam is scanned with iterative steps from pixel to pixel with a defined time during which the FIB dwells on each pixel. Thus, dwell time, pixel size, pixel repetition frequency, and pixel distance become further process parameters. The dynamics of defect creation and relaxation is therefore highly complicated in reality. All these effects can not be simulated simultaneously for elevated temperature implantations since such a simulation would require not only the nuclear collision computation but also thermally activated atomistic processes in the target that require a profound knowledge on thermodynamical data under simultaneous ion irradiation which are unknown. There has been experimental attempts, however, to study defect creation and recombination for the FIB implantation of Co into Si to synthesize $CoSi_2$ for the latter FIB operation mode
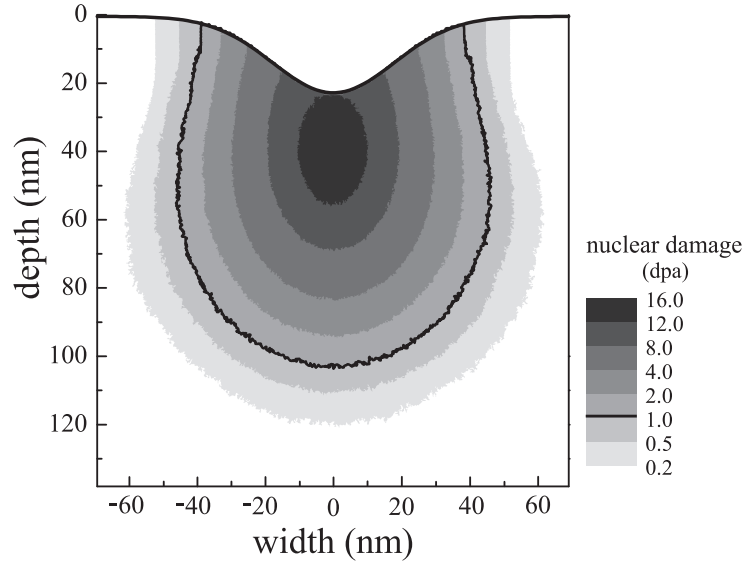
Figure (3.9): Nuclear damage profile (cross-section) for the FIB line scan implantation of Co (60 keV) into Si ($\Phi_0 = 5 \times 10^{16}\,\mathrm{cm}^{-2}$, $2\sigma_{\mathrm{FIB}} = 50\,\mathrm{nm}$) showing an inverse-$\Omega$ shape. The black line indicates the threshold of 1 dpa above which one can assume the Si target being amorphized at low implantation temperature (i.e. RT and below).

which show at least that amorphization is prevented during FIB implantation at elevated temperatures in the range of 400 °C for relatively short dwell times [221, 222, 223]. In the frame of this work, however, neither any time-dependence of the ion fluence nor any finite temperature during implantation is considered ($T=0\,\mathrm{K}$) for the modeling of implantation and damage profiles.

The second example of FIB line scan implantation of Si into SiO$_2$ is deployed to shed light on the dependence of the shape of the implantation profile on ion energy and the width of the FIB current density profile. In Fig. 3.10, for two typical ion energies of 30 keV and 60 keV and FIB current density profiles whose widths are in the sub-200 nm range are plotted for the same peak fluence of $\Phi_0 = 5 \times 10^{16}\,\mathrm{cm}^{-2}$ in each case. The shape of the cylindrical Gaussian implantation profiles is characterized best by the ratio of its lateral and vertical widths (cf. Fig. 3.2). The special case of a cylindrical Gaussian implantation profile with spherical cross-section is obtained for $\sigma_y = \sigma_x$. This condition is nearly given for Figs. 3.10 (b) and (f) where the ratio of σ_y and σ_{FIB} is close to unity. Consequently, for cases where the lateral straggling ΔR_p of the ions is close to σ_{FIB} one can expect a nearly spherical cross-section of the implantation profile which would meet best the requirements for a post-implantation formation of structures with spherical cross-sections (wires, rods). In those cases where σ_{FIB} is clearly smaller than ΔR_p (cf. Figs. 3.10 (a) and (e)) "plum-like" cross-sections of the implantation profiles are achieved where the main axis of the ellipsoid is vertical to the target surface. The extreme case of $2\sigma_{\mathrm{FIB}} = 0$ would correspond to implantation profiles directly computed with TRIM where all pseudoparticles impinge at the same position on the target surface, thus, the lateral width $2\sigma_y$ would correspond to twice the lateral straggling. On the contrary, if $2\sigma_{\mathrm{FIB}}$ is clearly larger than ΔR_p (cf. Figs. 3.10 (d) and (h)) a cross-section of the implantation profile is obtained where the main axis of the ellipsoid is horizontal to the target surface. The extreme case of $2\sigma_{\mathrm{FIB}} \gg \Delta R_p$ would correspond to a broad area implantation.

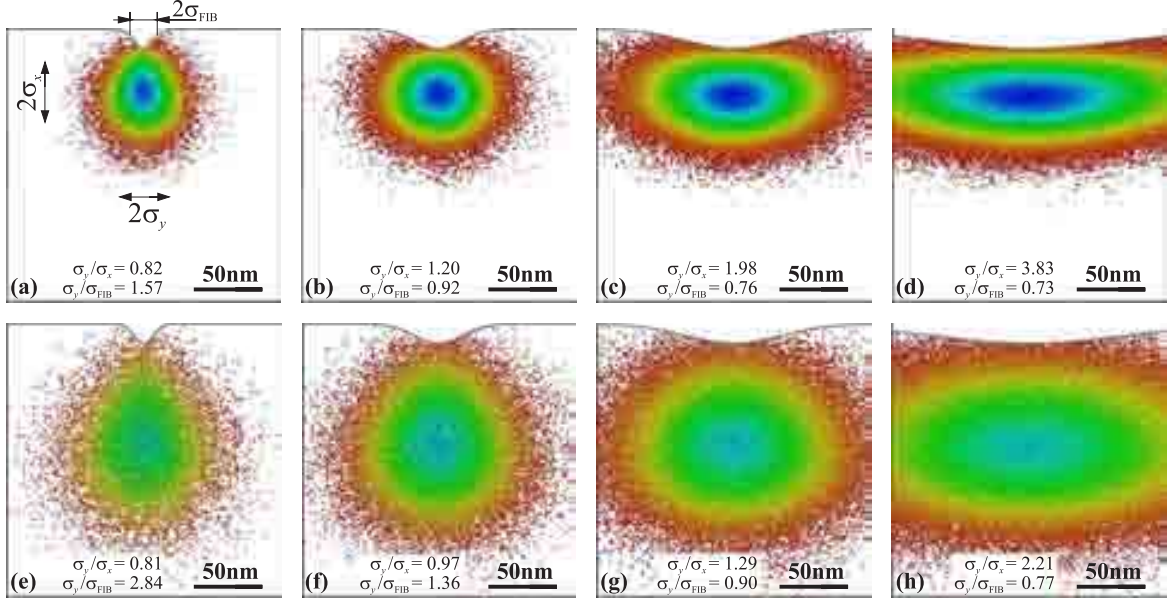In all these examples, the trough of the sputtering groove does only slightly disturb

Figure (3.10): FIB implantation profiles (cross-sections) for the implantation of Si into SiO$_2$ for ion energies of 30 keV (a-d) and 60 keV (e-h). The width of the FIB current density profile ranges from 20 nm (a,e); 50 nm (b,f); 100 nm (c,g) up to 200 nm (d,h). The peak fluence amounts to $\Phi_0 = 5 \times 10^{16}$ cm^{-2} in each case. In the figures, the ratio between lateral and vertical width of the implantation profile σ_y/σ_x and the ratio between lateral width of the implantation profile and the width of the FIB current density profile $\sigma_y/\sigma_{\mathrm{FIB}}$ are given. The color key indicates the relative local Si excess concentration in the target. The maximum Si excess concentration is achieved in (d) in the center of the implantation profile with 14.5 at% (the other cases: (a) 7.1 at%, (b) 11.9 at%, (c) 13.3 at%, (e) 2.5 at%, (f) 4.7 at%, (g) 7.0 at%, and (h) 8.5 at%).

the symmetry of the implantation profile. For higher peak fluences, however, the trough will come closer to the region of maximum concentration of the implanted species. Due to this dynamic development of the sputtering groove, the depth at which the ions come to rest with respect to the initial sample surface increases steadily until a stationary regime is reached where the trough of the sputtering groove "touches" the region of maximum concentration. This situation has to be avoided if one seeks the formation of buried NW structures during the subsequent annealing procedure. Further implantation would then not lead to higher ion concentrations in the target, i.e. the implantation profile would be shoved forward into the target while deepening the groove. Thus, the question arises whether the achieved maximum concentration of the implanted species is high enough to cause NW structure formation during post-implantation phase separation. In the following section it is demonstrated that a minimum volume concentration (about 30 vol.%) of the generated phase is required to obtain percolated, i.e. continuous NW structures in the center of the implantation profile. In the case of Co implantation into Si to form CoSi$_2$ this is achieved easily because one Co atom and two Si atoms form one formula unit CoSi$_2$. Thus, to obtain a high enough CoSi$_2$ volume concentration is possible with a minimum peak fluence of $\Phi_0 = 4 \times 10^{16}$ cm^{-2} for $2\sigma_{\mathrm{FIB}} = 50$ nm (cf. Fig. 3.4 (b)). In this case, the CoSi$_2$ volume fraction in the center of the implantation profile amounts to 35 vol.%. The trough of the sputtering groove is a few tens of nanometers away from the forming CoSi$_2$ NW structure which becomes, therefore, fully embedded into the Si target. However, for the synthesis of embedded Si NW structures in SiO$_2$ the situation turns out to be more difficult. Considering the practically available ion energies and FIB profiles width used in Fig. 3.10, a minimum

peak fluence of $\Phi_0 = 1.5 \times 10^{17}\,\mathrm{cm}^{-2}$ for $2\sigma_{\mathrm{FIB}} = 50\,\mathrm{nm}$ is required to achieve in the center of the implantation profile about 30 vol.% Si excess. For this case, the trough of the sputtering groove would nearly touch the region of highest Si excess concentration (separation of less than 5 nm). Thus, during post-implantation phase separation the Si phase forming within SiO_2 would also form directly at the target surface where unwanted effects are expected to disturb the structure formation process inside the matrix strongly (e.g. surface segregation or chemical impact of the ambient atmosphere [224]).

In conclusion, in this section it was demonstrated how the widely accepted TRIM code can be used to simulate 3D implantation and damage profiles of FIB line scan implantations where the width of the FIB current density profile is in the order of the projected range of the ions. In those cases, Gaussian fluence profiles give rise to cylindrical Gaussian implantation profiles whose cross-sections have nearly spherical symmetry. This symmetry is disturbed by grooves which develop towards the center of the implantation profile due to local surface erosion. The cross-section of nuclear damage profiles typically have an inverse-Ω shape. Moreover, it was clarified that a minimum peak concentration of implanted ions in the target may be reached by FIB line scan implantations in order to guarantee the post-implantation formation of continuous NW structures as discussed in the following.

3.2   FIB-based Ion Beam Synthesis

In the previous section the TRIM-based modeling of FIB line scan implantation profiles was discussed. In this section, the post-implantation processes of phase separation and NW structure formation are examined on the atomistic level by means of lattice KMC simulations (cf. chapter 2) which take 3D implantation profiles as initial atomic distributions. This procedure of treating energetic ion implantation and subsequent phase separation independently by different simulation methods was applied in a similar manner in various previous investigations [11, 17, 115, 120, 121]. As stated previously, phase separation can already proceed during implantation if the kinetics is fast enough which can be the case for ion implantations at elevated temperatures. However, the combination of ion implantation and phase formation in one computer model is a highly complex task due to the high dimensionality of the process parameter space and due to the uncertain basis of materials and thermodynamic data for ion-irradiated systems[8] Thus, the atomistic modeling of the exact evolution of real systems in which ion-implantation and phase separation proceed simultaneously is practically impossible up to date.

The present investigation does explicitly not focus on a particular real system in order to predict its exact spatio-temporal development during a subsequent thermal process under well-defined conditions. The aim is to give qualitative and semi-quantitative descriptions and predictions about reaction pathways on which supersaturated systems, in which the supersaturation varies locally to a high degree due to the shape of a FIB line scan implantation profile, can evolve considering the simple atomistic dynamics of the 3D Ising model. Thereby, the process parameter space can be kept relatively low-dimensional.

---

[8]In general, materials properties and thermodynamic data are available for equilibrium conditions only.

3.2.1 Phase Separation and Nanowire Structure Formation

A FIB line scan implanted matrix represents a system which is locally in a state far from thermodynamic equilibrium. Such a solid-state system is characterized by high supersaturation gradients where the highest degree of supersaturation is located in the center of the implantation profile (cf. Fig. 3.5). During the post-implantation thermal treatment phase separation into a heterogeneous mixture of phases takes place which goes along with material redistribution. However, the relaxation dynamics in such high-gradient material systems is strongly local (diffusion controlled regime).

The only possible method to describe this kind of relaxation processes on an atomistic level are 3D lattice KMC simulations (cf. section 1.4). In the following, KMC results are presented which rely on the dynamics of the Ising model considering a rigid f.c.c. lattice, thus, simplifications are made concerning atomic interactions, discreteness of diffusional jumps of atoms to free NN lattice sites only etc. (cf. chapter 2). The KMC simulations represent a binary phase-separating system consisting of one sort of particles embedded in an ideal, chemically inert matrix (in other words: the "vacuum" of the simulation). This is a further crucial simplification because matrix effects (e.g. stress, heterogeneous nucleation at defects etc.) are not taken into account.

Nonetheless, typical FIB line scan implantation profiles obtained by the method described previously are taken as initial atomic distributions for this KMC model. The 3D spatial coordinates of the implanted atoms are projected onto the nearby nodes of the KMC lattice, thus, preserving length scale and thereby concentration. For the time being, it is assumed that the system is closed after ion implantation, i.e. material exchange with the surroundings is not allowed. Thus, the system's relaxation is driven by the reduction of its free energy. This driving force is strongest in the center of the implantation profile where the degree of supersaturation is maximal.

In chapter 2, it was shown that the early stage of phase separation can be differentiated in nucleation or spinodal decomposition depending on the degree of supersaturation, i.e. depending on the lattice occupation or the particle concentration (cf. Fig. 2.5). There exists a temperature-dependent critical lattice occupation c_s which separates these two modi of phase separation (cf. spinodal curve in Fig. 2.4). Below c_s nucleation of precipitates governs the phase separation; whereas above c_s spinodal decomposition is dominant. For temperatures significantly lower than the critical temperature, c_s is in the range between 25% and 30% for the f.c.c. Ising model which has already been shown by previous investigations [116, 120]. The distinction between nucleation and spinodal decomposition is only meaningful in the early stages of phase separation. Nevertheless, the term "spinodal structure" referring to the continuous structure in the center of the implanted region is used throughout this chapter. For a thorough discussion on spinodal decomposition at later stages of phase separation the interested reader is referred to [144].

Considering a typical 3D FIB line scan implantation profile with cylindrical Gaussian shape and nearly spherical cross-section (cf. Fig. 3.7 (d)), Fig. 3.11 depicts the spatial distribution and separation of the two modi of phase separation shortly after quenching from the as-implanted state to the annealing temperature at which phase separation takes place. Here, periodic boundary conditions are applied in both lateral directions of the 3D simulation cell with a volume of $(512{\times}512{\times}512)\ a^3$. The lower cell boundary as well as the surface are passive, thus, the system is closed and the number
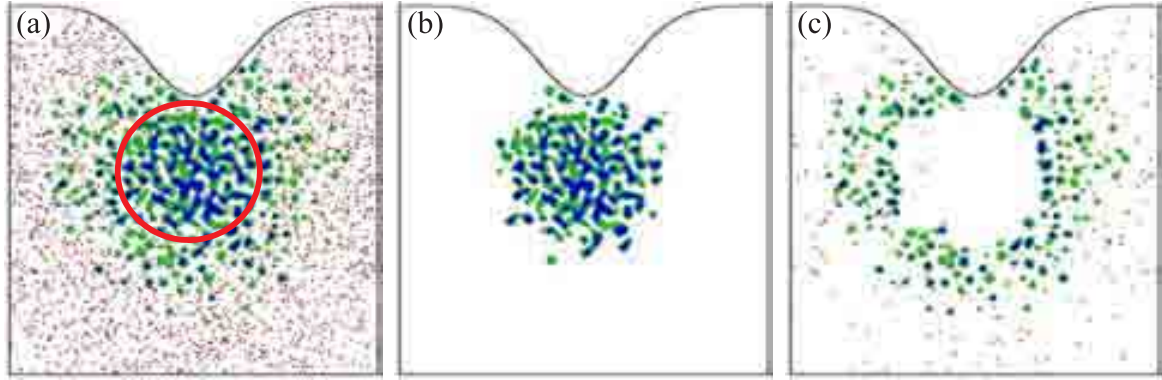
Figure (3.11): Cross section of (a) a 3D FIB line scan implanted impurity profile (cf. Fig. 3.7 (d)) that shorty after quenching (30×10^3 MCS, $\tilde{\varepsilon}_{NN,f.c.c.} = 1.1$) undergoes phase separation (b) via spinodal decomposition in the center and (c) via nucleation in the periphery of the profile. The boundary between these two modi is indicated by the red circle. Outside the region of phase separation the implanted particles are solved in the matrix mainly as monomers (red; not drawn in (c)) but also as temporary subcritical precipitates (dimers (orange), trimers (yellow)).

of particles is constant (canonical ensemble). For the sake of clearness, only a thin slab (cross-section) of the simulation cell is drawn. Apparently, in the center of the implanted region the degree of supersaturation is above c_s (in this case: $c_{max} = 46\%$), thus a spinodal structure appears (isolated in Fig. 3.11 (b)). As shown in Fig. 3.5 (b), the lateral distribution of implanted atoms decreases Gaussian-like, thus, at the location where $c = c_s$ (cf. red circle in Fig. 3.11 (a)) the modus of phase separation changes abruptly into the nucleation mode (cf. Fig. 3.11 (c)). Like the concentration of implanted ions, the density of the forming precipitates decreases radially from the spinodal-nucleation-boundary until a degree of local impurity concentration is reached that corresponds to the region in the binary phase diagram which lies outside the coexistence curve, i.e. where the local concentration is lower than the maximum solid solubility, thus, phase separation does not occur ($c < c_n$, cf. Fig. 2.4). Here, the particles are solved mainly as monomers in the implanted matrix which is locally in equilibrium, therefore.

For the same 3D FIB line scan implantation profile the influence of the annealing temperature is portrayed in Fig. 3.12, where in comparison with Fig. 3.11 the configuration of the phase-separated system is drawn for a lower (cf. Fig. 3.12 (b-)) and a higher (cf. Fig. 3.12 (b+)) annealing temperature shortly after quenching. In the low-temperature case, the dimension of the precipitate halo surrounding the spinodal structure extends further into the surrounding matrix in comparison with the intermediate temperature case. Since the maximum solid solubility of implanted impurity particles in the matrix is temperature-dependent ($c \propto \exp(-E_a/k_B T)$) the concentration of monomers (red dots) is lower there. On the other hand, the monomer concentration is much higher in the high-temperature case (cf. Fig. 3.12 (b+)). Thus, less material undergoes phase separation and structure formation in the center of the implanted region. The spatial extension of the precipitate halo is therefore smaller in the high-temperature case.

In Figs. 3.12 (a)-(d) and in Fig. 3.13, a picture series is shown which expresses the long-term evolution starting from the same 3D FIB line scan implantation profile until the state where a NW structure has formed in the center of the implanted region beneath the surface[9]. Apparently, the relaxation pathway of that system is very

---

[9]This large-scale simulation cell with 2^{26} lattice sites contains nearly 4.6×10^6 active particles.
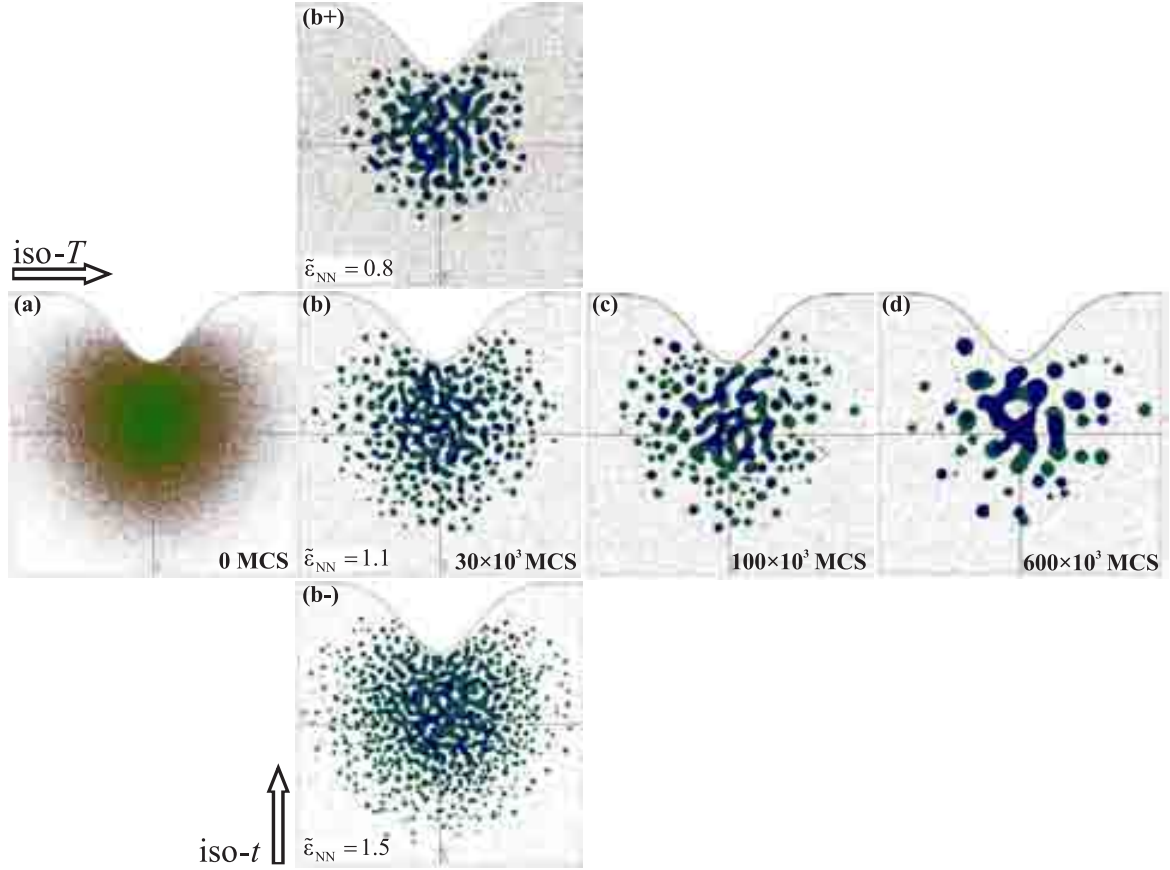
Figure (3.12): (a) Cross-section of a typical FIB line scan implantation profile (cf. Fig. 3.7 (d)) which shortly after quenching ($t = 30 \times 10^3$ MCS) undergoes phase separation (b) at an intermediate temperature (cf. Fig. 3.11; $\tilde{\varepsilon}_{NN,f.c.c.} = 1.1$), (b-) at a lower temperature ($\tilde{\varepsilon}_{NN,f.c.c.} = 1.5$), and (b+) at a higher temperature ($\tilde{\varepsilon}_{NN,f.c.c.} = 0.8$). In (c) and (d), the later stages of evolution (growth of the spinodal structure; coarsening of the precipitate halo) are depicted for the intermediate temperature case.

complex since very distinct processes occur in the course of evolution. All structures in the system (spinodal structure and precipitates) undergo after the first stage of phase separation a coarsening (or ageing) procedure at the end of which only the spinodal structure survives whereas all precipitates in its periphery have dissolved. In the spirit of Ostwald ripening (cf. chapter 2), the spinodal structure has despite its irregular interface on average a lower interface curvature κ (cylindrical shape: $\kappa \propto 1/r$) from the beginning of the evolution onwards. Thus, the precipitate ensemble (spherical shape: $\kappa \propto 2/R$) loses its material constantly via volume diffusion to the spinodal structure due to the curvature-dependent solubility (Gibbs-Thomson). However, the halo of precipitates itself undergoes an Ostwald-like ripening process. During this process it occurs that certain precipitates grow within a finite time window because clusters in their neighborhood become subcritical acting as material source. The growth of larger clusters, however, is only of short duration until those clusters become subcritical themselves and their material is dissolved, too. At the long perspective, however, every cluster becomes subcritical at its own time and dissolves finally. Thus, the spinodal structure accumulates all material that has been involved in the phase

---

It took nearly two years of computation on a single high-end processor to simulated the course of evolution which extends over seven orders of magnitude of simulation time.
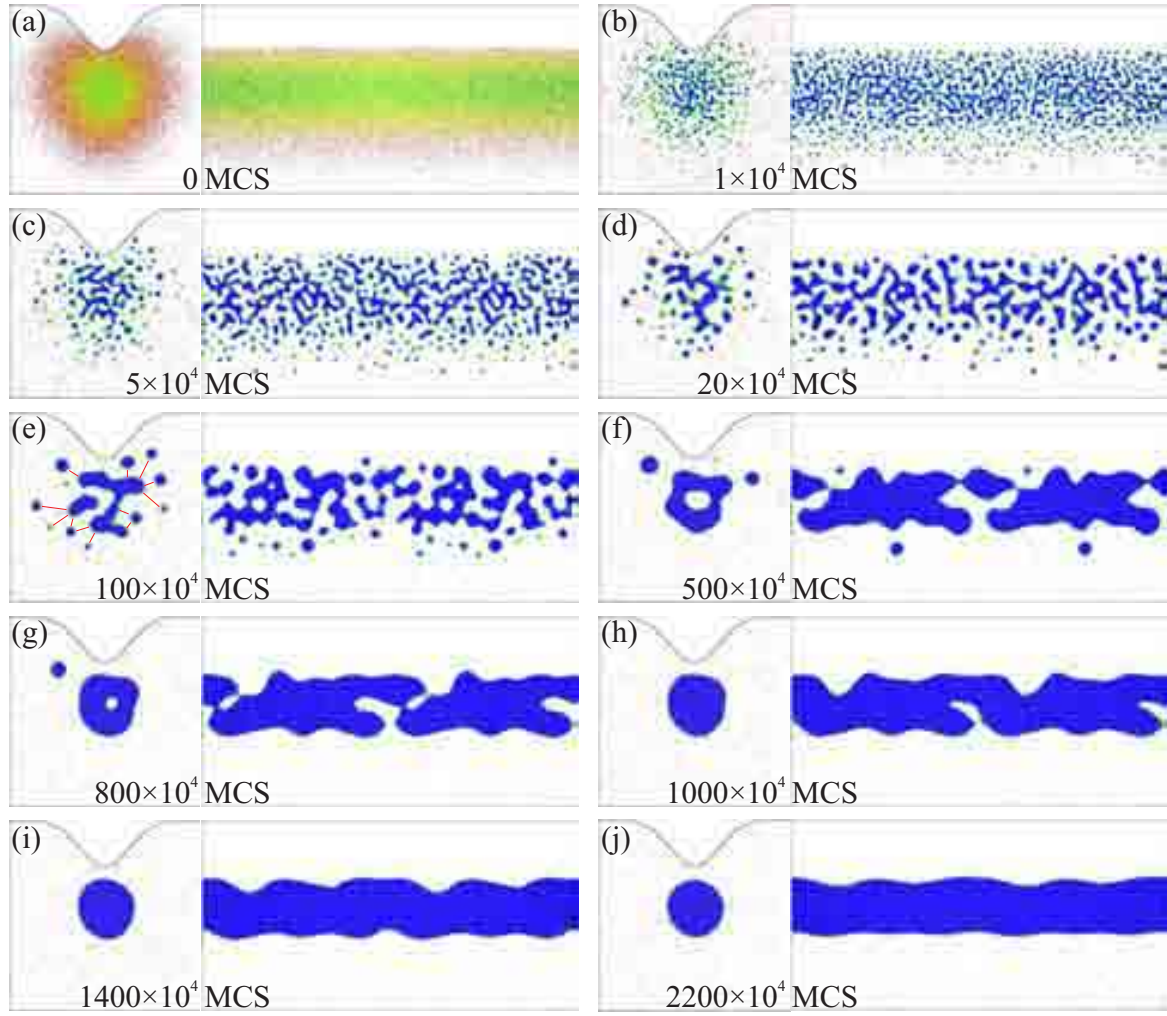
Figure (3.13): KMC image series depicting the evolution from (a) the as-implanted state (cf. Fig. 3.7 (d)) via (b) phase separation , (c-g) coarsening, (h, i) smoothing of highly curved interfaces to (j) the formation of a cylindrical NW structure beneath the surface (left: cross-section of a thin slab; right: vertical length-section of a thin slab through the center). The process temperature was kept constant throughout the simulation at $\tilde{\varepsilon}_{NN,f.c.c.} = 1.1$. The red lines in (e) indicate the denuded zone which appears in a self-organizing manner between in the cluster halo and the spinodal structure (see text for details).

separation from the beginning. This process causes material redistribution driven by the capillary force via volume diffusion that is directed radially towards the center of the implanted region. It can also be interpreted as Ostwald ripening in the neighborhood of a absorbing sink (= the spinodal structure). The existence of the precipitate ensemble is therefore of transient nature. Similar scenarios in view of the evolution of precipitate ensembles in the neighborhood of a flat interface were investigated previously [120, 121]. In these studies, a "denuded" zone appeared in a self-organizing manner between the strong absorbing sink and the NC ensemble due to the diffusional screening between the sink and the NC ensemble. This diffusional screening occurs likewise in classical Ostwald ripening situations between individual clusters. It is characterized by the screening length λ_B which is named after Brailsford and which denotes the length scale of interactions among precipitates, i.e. it expresses the distance beyond which the diffusional interaction is screened by the remaining cluster ensemble [225]:
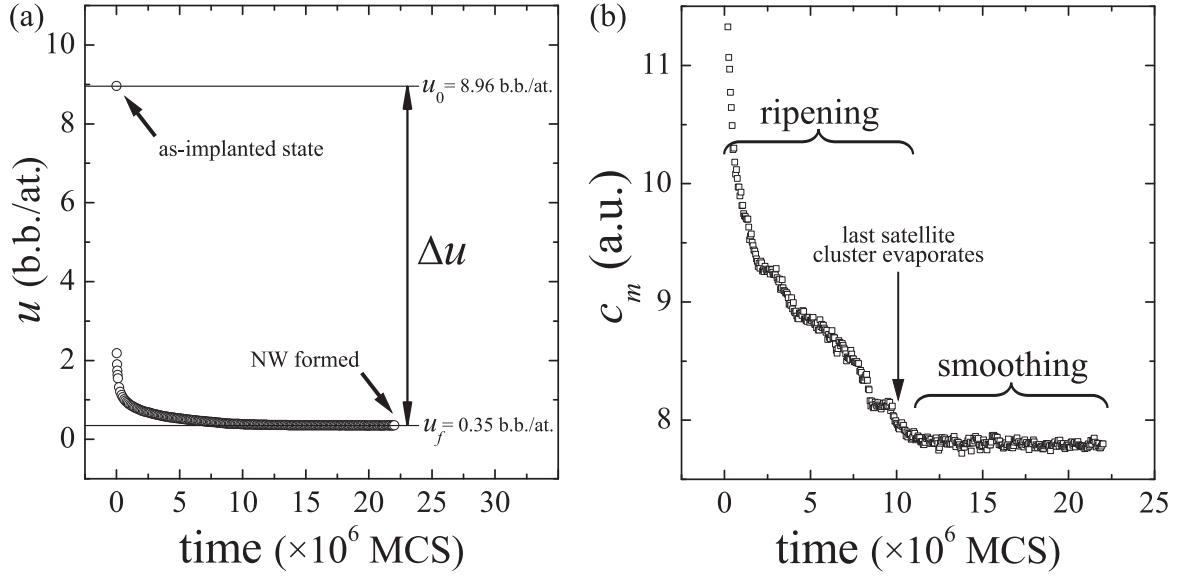
Figure (3.14): (a) Time-development of the average internal energy density u starting from the as-implanted state up to the final state of NW structure formation. (b) Corresponding time-development of the monomer concentration c_m in the system.

$$\lambda_B = \frac{1}{\sqrt{4\pi n(t)\bar{\bar{R}}(t)}} \; , \tag{3.15}$$

where $n(t)$ is the cluster density and $\bar{R}(t)$ denotes the mean cluster radius. It has been shown that this diffusional screening can cause self-organization processes during coarsening in spatially finite cluster ensembles usually starting from the ensemble boundaries [179, 226]. Thus, the appearance of a self-organizing denuded zone between the spinodal structure and the surrounding precipitates is expected to occur during coarsening in the present case, too. However, the depiction of that denuded zone is hardly possible due to the irregular shape of the spinodal structure which is characterized by an inhomogeneous and highly curved interface whose location does not clearly follow a spatial symmetry. Thus, a projection of the 3D structure onto a 2D subspace or the slicing through the structure do not give clear impressions of that denuded zone. In Fig. 3.13 (e), an expert's eye is able to detect a denuded area where in the cross-section representation about ten NCs appear which radially surround the highly-curved spinodal structure in nearly the same distance (red lines).

   The NW formation process is driven by the reduction of the system's free energy. Since the present simulations are carried out at temperatures well below the critical temperature, the free energy reduction can be approximated with the reduction of internal energy which can directly be measured during the KMC simulation (cf. section 2.2). The computation of entropy of a system in a non-equilibrium state, in which phase-separated structures with spatial inhomogeneity exist, is still subject to scientific debate although some approximations do exist in the literature [136]. In Fig. 3.14 (a), the average internal energy density $u = U/N$, where N is the total number of particles, is plotted vs. simulation time. In the as-implanted state the system is characterized by a very high internal energy $u_0 = 8.96$ b.b./at. In the final state of NW formation, the average internal energy density is more than one order of magnitude

smaller at $u_f = 0.35$ b.b./at. This development clearly shows the reduction of internal energy in the course of evolution. Moreover, the strength of the driving force of the processes can be measured by the rate with which the internal energy is reduced: $\mathrm{d}u/\mathrm{d}t = \dot{u}$. In Fig. 3.14 (a) it can be seen that the internal energy reduction from the as-implanted state and the first stages of phase separation proceeds with a very high rate of $\dot{u} = -3.5 \times 10^{-4}$ b.b./at·MCS. The internal energy reduction rate during coarsening is significantly lower at about $\dot{u} = -10^{-7}$ b.b./at·MCS. The subsequent interface smoothing procedure is even lower with $\dot{u} = -3 \times 10^{-9}$ b.b./at·MCS. Thus, the characteristic stages of structure coarsening and interface smoothing can be nicely discriminated.

In this connection, the time-dependent monomer concentration $c_m(t)$ is of interest, too, since conclusions can be drawn from it about the development of the critical cluster size. According to the Gibbs-Thomson equation, the monomer concentration in the matrix depends on the critical cluster radius R_c [180]:

$$c_m = c_{m,\infty} \left[\exp\left(\frac{2\gamma\Omega}{k_B T} \frac{1}{R_c} \right) \right] \ . \tag{3.16}$$

Consequently, c_m decreases with time during coarsening as shown in Fig. 3.14 (b). Again, coarsening and interface smoothing can be discriminated nicely by a cascade-like decrease (coarsening) and a plateau (interface smoothing). During coarsening, the average cluster size increases [180] which causes c_m to decrease permanently. In Fig. 3.14 (b), a cascade-like reduction of c_m can be observed which refers to the evaporation of individual clusters at their own time: the smaller ones in the early stage, the bigger ones in the later stage of coarsening. There are exceptional moments in the final stage of coarsening when only some clusters of nearly equal size remain. Then, $c_m(t)$ shows a plateau for a short while. In the moment when the last cluster in the periphery of the spinodal structure becomes subcritical and starts evaporating (cf. Fig. 3.13 (g)), c_m shows a discontinuity and decreases abruptly to the value that corresponds to the monomer concentration above the interface of the spinodal structure (cf. Fig. 3.14 (b)). During interface smoothing, c_m is practically constant which explains that the average curvature of the spinodal structure is already close to the curvature of the final state when the cylindrical NW structure has formed (also seen in $\dot{u}$).

Earlier in this section, the spatial average of the internal energy density, u, was discussed. However, u shows locally significant differences in the system throughout the NW structure formation procedure. In Fig. 3.15, the cross-section of the system is drawn where the local internal energy density is indicated for (a) the as-implanted state and (b) the final state where the NW structure has formed. In the as-implanted state, u is highest in the center of the implantation profile which stands to reason because of the maximal degree of supersaturation there. At the end of the evolution, u_{max} is about one order of magnitude lower, however, the maximum of u has shifted towards the interface of the cylindrical NW structure. In other words, the atoms at the interface of the NW structure store relatively more internal energy than those in the NW bulk.

A further crucial issue regarding the formation of NW structures based on FIB line scan implantation profiles is the effect of the peak concentration c_{max} on the phase separation modus in the center of the profile. It has been demonstrated that if spinodal decomposition occurs in the center of the implanted region the formation of continuous
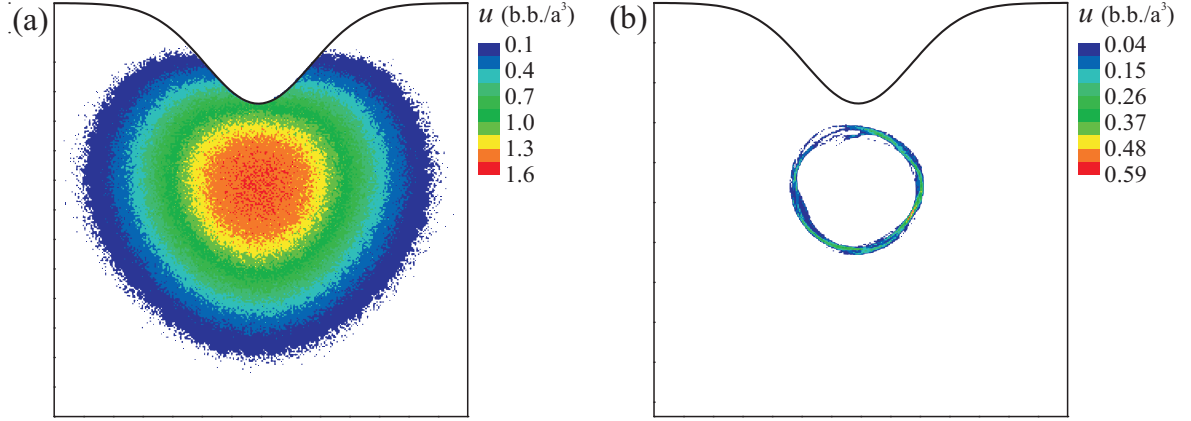
Figure (3.15): Internal energy density plot (cross-section): (a) in the as-implanted state of the FIB line scan implantation (cf. Fig. 3.7 (d)) and (b) in the the final state of NW formation ($\tilde{\varepsilon}_{NN,f.c.c.} = 1.1$, $t = 2200 \times 10^4$ MCS).

NW structures is given through coarsening and interface smoothing. However, for initial particle distributions where c_{max} is below c_s only nucleation takes place in the center of the profile. Regarding the diffusional screening in the cluster ensemble, neighboring clusters can only coalesce, percolate, and finally form a continuous NW structure if they get material supply from the surrounding concentration field. In general, coalescence of clusters in the center of the implanted region is more likely than in the periphery because of the higher cluster density which has been established there due to the higher degree of supersaturation. In the beginning it was assumed that after ion implantation the system is closed, i.e. material supply for the central clusters can only come from dissolving clusters in the periphery of the cluster ensemble. In the spirit of a self-organizing evolution of a cluster ensemble discussed above, the radially symmetric catchment area of monomers must be large enough for this purpose. Unfortunately, in all KMC simulation runs performed this particular situation has never been observed. In almost all cases large clusters formed due fluctuations away from the center of the implantation profile and disturbed thereby the material support of the central clusters so that interconnected chains of coalescing central clusters were not found.

On the contrary, for an open system further material supply could be achieved (e.g. by further ion implantation) during the growth stage of the central clusters. Then, a coalescence of central clusters forming a continuous NW structure seems possible. The fact that additional material supply by ion implantation leads to cluster coalescence and structure formation has been shown in experiment and simulation for the synthesis of buried layers. For example, in the SIMOX process buried SiO_2 layers are formed in c-Si by a high-temperature implantation of oxygen where the growing SiO_2 phase, which is fully embedded in the c-Si matrix, is continuously supplied with additional oxygen forming further SiO_2 [115, 227, 228]. This strategy is therefore promising also for the synthesis of continuous NW structures in such systems where the maximum concentration in the center of the implanted region does not exceed c_s.

In Fig. 3.16, a series of KMC runs is depicted where different c_{max} values were considered keeping all the other parameters constant. In all cases the system was closed, i.e. there is no additional material support available. Starting from cylindrical Gaussian particle profiles with spherical cross-section the role of the critical peak concentration becomes evident. In Fig. 3.16 (a) with $c_{max}=10\%$, phase separation leads only to
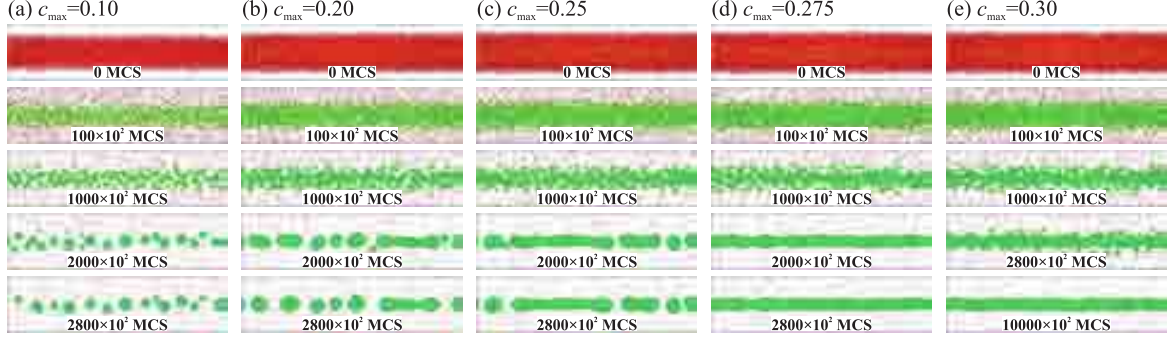
Figure (3.16): Longitudinal views on phase separation and structure formation procedure starting from cylindrical Gaussian impurity profiles for different peak concentrations c_{max} keeping all other process parameters constant ($2\sigma = 50\,\mathrm{a}$, $\tilde{\varepsilon}_{NN,f.c.c.} = 1.5$, cell size $(128 \times 128 \times 512)\,\mathrm{a}^3$).

nucleation of precipitates. During coarsening a chain of large NCs in the center develops. The clusters in the periphery dissolve. However, too little material is available for NC coalescence. In the second case depicted in Fig. 3.16 (b) with c_{max}=20%, the growth of central clusters leads partially to coalescence so that short rod-like structures are formed here and there. In the next situation (cf. Fig. 3.16 (c)), where c_{max} amounts to 25%, there is already spinodal decomposition in the center of the profile taking place. However, the spinodal structure does not remain continuous in the longitudinal direction due to fluctuations during phase separation and coarsening which results merely in the formation of relatively long rods. A continuous NW structure is first observed for c_{max}=27.5% (cf. Fig. 3.16 (d)). Naturally, for all c_{max} >27.5% a NW structure is always formed (cf. Fig. 3.16 (e)). Consequently, there exists a critical range of c_{max} (between 25% and 27.5% for the present simulation parameters) where fluctuations can disturb the formation of a continuous NW structure. Therefore, for practical situations c_{max} should be above that critical range if one seeks the guaranteed formation of continuous NW structures. The existence of such a critical range of c_{max} has been verified very recently in real experiments in view of the synthesis of CoSi$_2$ NW structures in c-Si (001) where – in qualitative agreement with the KMC results of Fig. 3.16 – a transition was observed from the synthesis of a CoSi$_2$ NC chain to the synthesis of a continuous CoSi$_2$ NW structure with increasing peak fluence of the Co-FIB [229].

The estimation of the diameter of a FIB-synthesized NW can be performed as follows if an ideal cylindrical Gaussian implantation profile with spherical cross-section is given. Neglecting those particles which are solved in the matrix, one has to consider material conservation during the NW formation process. Thus, the number of atoms in the implantation profile equals the number of atoms forming the NW:

$$N_{\mathrm{NW}} = N_{\mathrm{P}} \ . \tag{3.17}$$

Giving an atomic density in the wire of c_{NW} and the atomic density in the implantation profile $c_{\mathrm{P}} = c_{max} \times \exp\left(-\rho^2/2\sigma^2\right)$, where ρ is the radial distance from the center of the profile and 2σ is the width of the profile, Eqn. 3.17 can be rewritten and one gets

$$c_{\mathrm{NW}}\,\mathrm{d}V = c_{\mathrm{P}}\,\mathrm{d}V \tag{3.18a}$$

$$c_{\mathrm{NW}} \int\limits_0^{2\pi}\int\limits_0^{R}\int\limits_0^{L} \rho\,\mathrm{d}z\mathrm{d}\rho\mathrm{d}\varphi = \int\limits_0^{2\pi}\int\limits_0^{\infty}\int\limits_0^{L} \rho \times c_{max} \times \exp\left(-\frac{\rho^2}{2\sigma^2}\right)\mathrm{d}z\mathrm{d}\rho\mathrm{d}\varphi \tag{3.18b}$$

$$c_{\mathrm{NW}}R^2 = 2c_{\max}\sigma^2 \qquad\qquad (3.18c)$$

$$R = \sigma\sqrt{2\frac{c_{\max}}{c_{\mathrm{NW}}}}\ . \qquad\qquad (3.18d)$$

According to Eqn. 3.18d, NW diameter and implantation profile width scale linearly if the other values are constant and if $c_{\max}$ exceeds the critical peak concentration in the profiles above which NWs form. Moreover, the NW diameter scales with the square root of the peak concentration in the implantation profile.

3.2.2 Perturbing Effects

Due to the characteristics of the KMC model with f.c.c. Ising dynamics (cf. chapter 2), the above results on FIB-based NW structure formation contain various idealizations and simplifications compared to real systems. The experimental FIB-based synthesis of NW structures may therefore be confronted with effects which may perturb or even hamper the reaction pathways of NW structure formation illustrated by the above computer experiments (cf. [211, 230]).

Material Absorption by a Semi-Infinite Matrix. Prior to the presentation of the KMC results on NW structure formation starting from FIB line scan implantation profiles it was assumed that the KMC simulation cell boundaries prevent atoms from leaving the cell. This may indeed be the case for particular experimental situations like for laterally repeated FIB line scan implantations into a thin layer atop a substrate where the layer-substrate interface acts as diffusion barrier for the implanted ion species (cf. Fig. 3.17 (a)). For example, this would be the case for a focused Co implantation into a thin SOI layer where the top-Si/SiO$_2$ interface plays the role of a diffusion barrier for Co. Then, the finiteness of the KMC simulation cell would nicely be fulfilled and the above demonstrated principles would be applicable concerning the applied boundary conditions of the simulation cell. However, if a single FIB implantation is performed into the surface region of a semi-infinite matrix in which the concentration of the implanted species is well below its maximum solid solubility, then the matrix acts as a strong sink for the implanted particles, thus, the former precondition of material conservation would no longer hold (cf. Figs. 3.17 (b) and (c)).
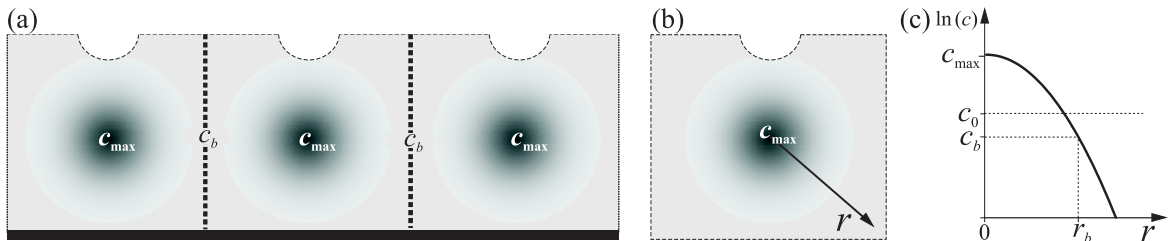
Figure (3.17): (a) Laterally repeated FIB line scan implantation into a thin layer atop a substrate that acts as diffusion barrier for the implanted particles, thus, reflecting a KMC simulation cell with lateral periodic boundaries and a passive bottom boundary. (b) Single FIB line scan implantation into a semi-infinite matrix. (c) Corresponding concentration profile of the implanted particles in the semi-infinite matrix which can act as strong sink for diffusing particles if the initial particle concentration in the matrix is below the solid solubility c_0.
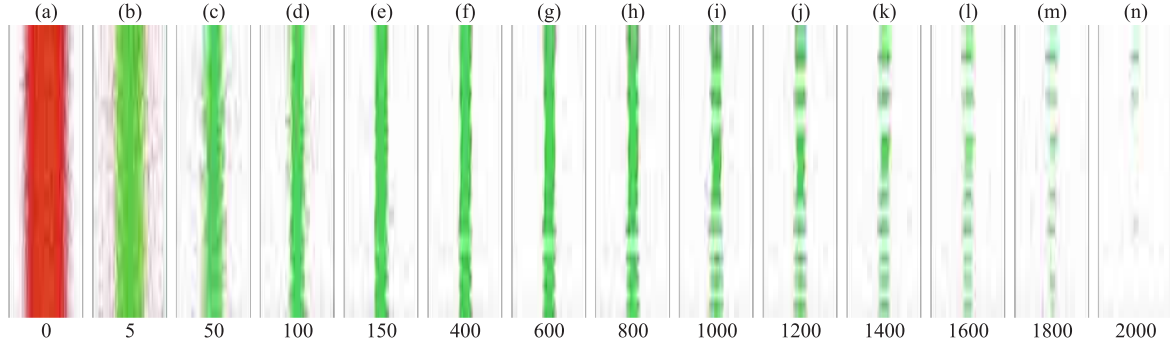
Figure (3.18): Action of absorbing interfaces in radial direction of the cylindrical Gaussian implantation profile (c_{max}=0.30; cf. Fig. 3.16 (e)). In this case the strength of absorption is given by a probability p_{abs}=0.05 which determines the annihilation of a particle if it crosses the simulation cell boundaries in radial direction.

To investigate the absorbing effects of a semi-infinite matrix, the hitherto periodic/passive boundaries of the KMC simulation cell were turned into absorbing ones (thus, keeping the cell size constant) which approximately reflects the situation of a single FIB implantation into a semi-infinite non-saturated matrix. In Fig. 3.18, the evolution of a FIB line scan implantation profile is depicted for slightly absorbing cell boundaries in all directions orthogonal to the longitudinal axis of the cylindrical Gaussian (p_{abs}=0.05). The implantation profile parameters and the process conditions are the same as those of Fig. 3.16 (e) where at $c_{max} = 30\%$ NW structure formation had been observed. Here, however, there is no continuous NW structure formed (cf. Fig. 3.18 (d-f)). Since particles are absorbed at the cell boundaries there is a diffusional flux of particles away from the center of the implantation profile, and less particles remain there for phase separation, coarsening and NW structure formation. Moreover, the structures which are formed are of highly transient nature, i.e. they literally evaporate and deliver monomers which diffuse into the semi-infinite matrix because no local equilibrium (i.e. local detailed balance of evaporating and condensing particles) between the structures and the vapor phase can be obtained. Consequently, in the presence of an absorbing matrix the peak concentration, above which the formation of continuous NW structures is expected, increases with the strength of absorption, i.e. with the net material flux directed away from the implanted region which is given by diffusivity and solubility of the migrating species.

It is noteworthy that the concentration field around the FIB line scan implantation profile is 2D with a radial symmetry, approximately. Due to the characteristics of the diffusion equation in cylindrical coordinates, the absorbing effects of the matrix are therefore much stronger than in the case of broad-area implantations aiming at the formation of buried layers. There, the concentration field on which particles diffuse out of the implanted region into the absorbing matrix is merely 1D. Moreover, the monomer concentration c above a flat layer is smaller than above a curved one in the case of NW structures (Gibbs-Thomson) which gives rise to an additional effect of higher material flux j away from the FIB line scan implantation profile at constant diffusivity D.

In the long run, the extreme case can occur where all locally implanted particles diffuse away from the implanted region during the post-implantation thermal treatment (cf. Fig. 3.18 (n)). Consequently, it would be beneficial for real experiments with voluminous target to saturate the target prior to the local FIB implantation in order to avoid material loss during annealing.

Heteronucleation at Defects. In subsection 3.1.1 it was pointed out that during ion implantation manifold defects are generated in the target even at elevated implantation temperatures. During the post-implantation thermal treatment the annealing of such defects and phase separation proceed simultaneously. However, the presence of defects in the target may seriously perturb the phase separation processes. Heterogeneous nucleation of precipitates may occur, i.e. the energetic barrier to be overcome during nucleation is usually reduced due to defects. Moreover, extended defects may have preferential directions (such as the {311}-defect in c-Si), thus, phase separation and NW structure formation can be directed away from the scanning direction of the FIB. Thus, structures can grow along unwanted directions which has been observed in the case of CoSi$_2$ NW structure formation in c-Si [230].

Stress Effects. Stresses may occur in ion-implanted systems due to swelling of the matrix (e.g. Si or Ge in SiO$_2$ [231]) and/or by a lattice mismatch between the nucleated phase and the host matrix (e.g. CoSi$_2$ in c-Si [232], cf. Fig. 3.6). In general, stress affects the mobility of atoms because additional work must be done against the stress field during diffusional jumps, i.e. the potential energy landscape through which migrating atoms move, is altered due to lattice distortions. Because of the anisotropy of stress fields, the rates of atomic jumps becomes direction-dependent [128]. The atomic jump rate in the absence of stress is proportional to $\exp(-H/(k_B T))$ (cf. Eqn. 2.10), where H is the energy barrier of the particular jumping process. In the presence of stress, however, an energy term must be added to this energy barrier which represents the work A that must be done during the jump against the stress field (= external force field), thus, the jump rate becomes proportional to $\exp(-(H + A)/(k_B T))$. Due to the anisotropy of stress fields which are described by stress tensors, A depends on the direction of the jump. Thus, atoms migrating in a stress field will move in such directions which minimize their interaction with the stress field. Although the ratio between A and H is in general considered to be smaller than unity, stress may have considerable impact on the FIB-based formation of NW structures – also because stress can influence nucleation and dissociation processes [128]. Earlier in the chapter it was demonstrated that the concentration profiles of implanted particles show high gradients. Therefore, the stress fields can be assumed to have high gradients, too, which complicates stress-related effects in the present context tremendously. Any analytical or numerical description of stress related effects during FIB-based IBS of NW structures (e.g. the implementation of KMC into a FEM model) is beyond the scope of this work.

Surface Effects. Earlier in this chapter (cf. subsection 3.1.2) is was shown that the peak concentration of typical FIB line scan implantation profiles is some tens of nanometers away from the sample surface. With increasing peak fluence, however, the sputtering groove comes closer to that region of highest concentration. Thus, the region where phase separation and NW structure formation take place may come close to the sample surface where disturbing events like preferential nucleation (surface segregation) [233] or chemical reactions with the ambient can occur [224]. These processes could overshadow or even prevent the formation of continuous NW structures.

3.2.3   Synthesis of Nanowire Junctions

The application of NWs as interconnects (e.g. for the transport of electrical current in integrated circuits) requires their linkage to other structures. In this perspective, it is briefly demonstrated that junctions of NWs can the fabricated by the method of FIB-based IBS, too.

The crossing of two (or more) FIB line scans causes the superposition of the individual implantation profiles in the target. The individual branches of the cross evolve independently from one another and will form NWs. However, there is an exceptional situation in the region where the profiles cross since more material is implanted there than in the individual branches. This causes locally a higher supersaturation, thus, locally different driving forces act during evolution which also plays a crucial role in the long-term evolution of a NW cross where the crossing point is a point of preferential instability (cf. subsection 4.6.2). Besides the implantation profiles the sputtering grooves overlap, too. Consequently, in the region of the crossing point surface erosion is more pronounced than in the branches. This may lead to alterations of the subsequent processes of phase separation, coarsening, and interface smoothing because the implantation profile is located closer to the surface at the crossing point (cf. subsection 3.2.2).

For illustration, Fig. 3.19 depicts the evolution of a system where in the beginning two cylindrical Gaussian impurity profiles with spherical cross-sections and with the same peak concentration (c_{max}=0.4) and profile width ($2\sigma = 50$ a) are crossed orthogonally. The resulting particle distribution profile is therefore an approximation of a realistic crossed FIB line scan implantation profile where enhanced sputtering at the crossing point would lead locally to a shift of the distribution of the implanted particles into the depth of the target. Despite this simplification, the formation of NWs in the branches of the crossed profiles is expected (c_{max}=0.4), thus, the region of the crossing point the peak concentration amounts to about $2c_{max}$. In Fig. 3.19, the upper
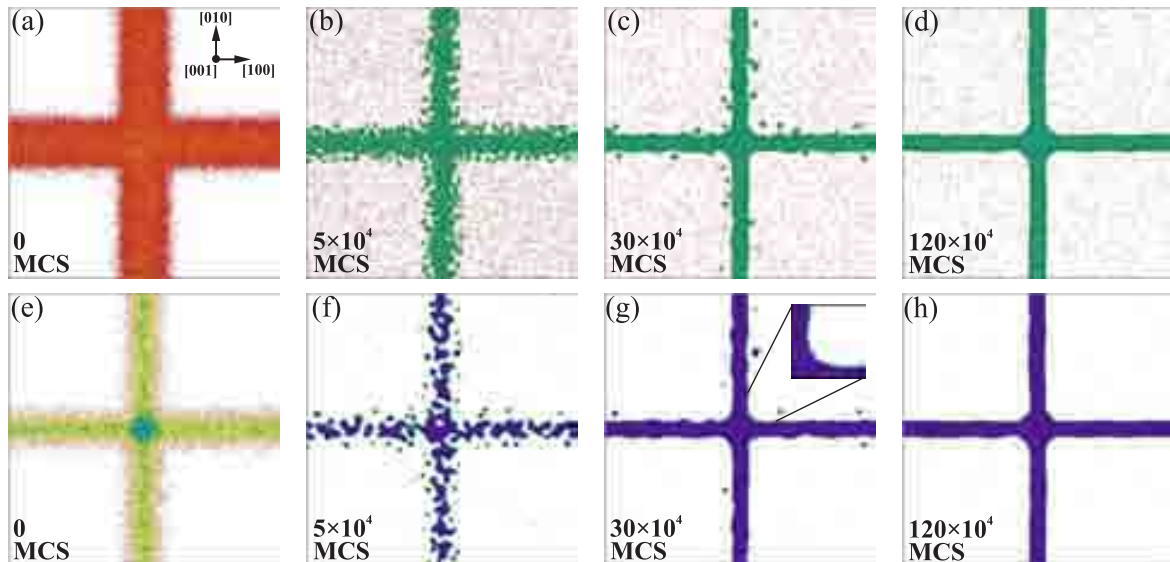
Figure (3.19): Evolution of two cylindrical Gaussian impurity distributions with spherical cross-section which are superimposed under a right angle ($\tilde{\varepsilon}_{NN,f.c.c.} = 1.5$; $2\sigma = 50$ a; $c_{max} = 0.4$; upper row: top-view; lower row: corresponding horizontal cross-sections). The system evolves from the as-implanted state (a, e) via phase separation (b, f) and coarsening (c, d) to the formation of a NW cross (d, h). The inclusion in (g) refers to a rounding effect at the crossing point.

row shows the evolution in top view whereas the lower row depicts corresponding cross-sections as very thin horizontal cuts through the center of the structures. Accordingly, the additional amount of implanted material in the center has beneficial effects on the formation of the cross. The spinodal structure in the center is much more pronounced than in the branches of the cross. This additional volume of the separated phase at the crossing point causes an additional rounding at the point where the two NWs cross under a right angle (cf. the inclusion in Fig. 3.19 (g)), thus, it helps reducing the local curvature at the crossing point which may have a stabilizing influence on the long-term evolution of the NW cross which is subject to capillarity-driven interfacial instabilities (cf. subsection 4.6.2). In Fig. 3.19, the FIB-based IBS of NW-crosses consisting of NWs with equal diameter was demonstrated. Likewise, NW-crosses consisting of NWs with different diameters can be fabricated by varying the peak fluence for the individual FIB line scan implantations keeping all other parameters constant. Thus, particular structures which are of interest in view of the self-organized fabrication of NW transistors can be obtained (cf. subsection 4.6.2).

3.3 Nanowire Formation despite the Plateau-Rayleigh Instability

Previously it was demonstrated how NW structures can form by phase separation from supersaturated solid solutions with cylindrical Gaussian concentration profiles. This process is driven by the reduction of free energy whose dominating part at temperatures much lower than the critical temperature is the internal energy (cf. Fig. 3.14). This finding may come as a surprise given the fact that NW structures are inherently unstable objects from the viewpoint of thermodynamics which has been demonstrated in chapter 1 already. During their free evolution they transform into chains of separated particles – a classical process known as Plateau-Rayleigh instability. The atomistic nature of this capillary instability in the solid state is thoroughly discussed in chapter 4. Here, however, an important question must be addressed: Why are NW structures formed at all during evolution and why does the system not directly evolve towards the state of a particle chain given the fact that the particle chain is an energetically more favorable configuration for the system than the NW structure?

Obviously, the answer to this question can not be given with energetic arguments. It must be tackled from a kinetic point of view. The microscopic dynamics of the system is characterized by diffusional jumps of atoms to free NN lattice sites in the 3D Ising model. The diffusion length λ is associated – in accordance with the Einstein relation – with the mean square displacement: $\lambda = \sqrt{x^2} \propto \sqrt{Dt}$, where D is the particle diffusivity and t is the simulation time [115]. Consequently, material redistribution processes which are characterized by different length scales will proceed on different time scales.

In the present case, the processes leading to NW structure formation (phase separation of supersaturated FIB line scan implantation profiles, coarsening, and interface smoothing) are processes with increasing characteristic length scales (cf. Fig. 3.13). Therefore, they proceed subsequently as demonstrated above (cf. Fig. 3.14). From Fig. 3.13 it can be concluded that the characteristic length scale in the final process of NW formation (i.e. interface smoothing) lies in the range of the NW radius.
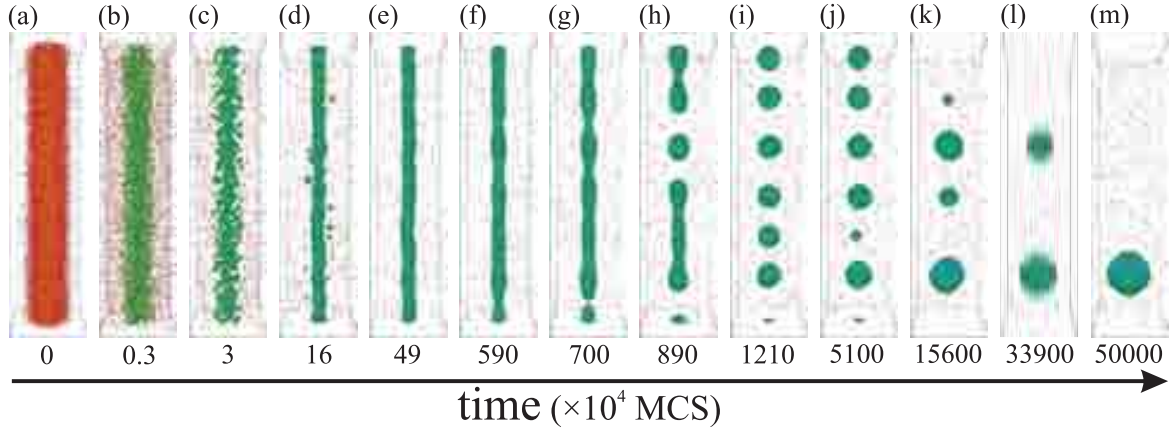
Figure (3.20): Evolution of a cylindrical Gaussian FIB implantation profile ($\tilde{\varepsilon}_{NN,f.c.c.} = 1.5$; $2\sigma = 40$ a; $c_{max} = 0.35$; cell: $(128 \times 128 \times 512)$ a^3) demonstrating how a highly supersaturated matrix (a) with high supersaturation gradients relaxes via phase separation (b), coarsening (c, d), interface smoothing (d), the intermediate formation of a NW (e), the Plateau-Rayleigh instability (f-j), NW fragmentation, and coarsening (j-l) towards the final state of thermodynamic equilibrium (m).

The Plateau-Rayleigh instability, however, has a characteristic length scale larger than the circumference of the NW. Considering solely surface diffusion, it was calculated that the typical length at which NWs disintegrate into NC chains is about the ninefold of the initial NW radius [234]. Here lies the answer to the above question. The time scale at which the Plateau-Rayleigh instability shows any effects on the system's configuration is therefore significantly larger than for all other previous processes before which lead to NW formation. Thus, there is a time window in the evolution of the system between NW formation and NW disintegration in which the NW structure can be preserved (regarding its technological application as NW) if the temperature at which the system evolves is reduced drastically ("frozen NWs").

Furthermore, the state at which the system has reached the NC chain configuration is not yet the ultimate state of thermodynamic equilibrium. After NC chain formation, a further coarsening process will lead to an additional free energy reduction at the end of which one single particle remains in the system which is in contact with its equilibrium vapor phase. This series of individual evolutionary stages is depicted in Fig. 3.20. Starting from a cylindrical Gaussian particle distribution the system evolves through a sequence of well-separated stages until it reaches thermodynamic equilibrium:

1. phase separation,

2. coarsening,

3. interface smoothing,

4. NW formation,

5. Plateau-Rayleigh instability,

6. fragmentation, and

7. coarsening.

In Fig. 3.21 (a), the time-development of the reduction of the internal energy density is plotted which expresses the chronological separation of the evolutionary stages very nicely (Please note the double-logarithmic scaling). The corresponding time-development of the monomer concentration in the finite (and closed) simulation cell
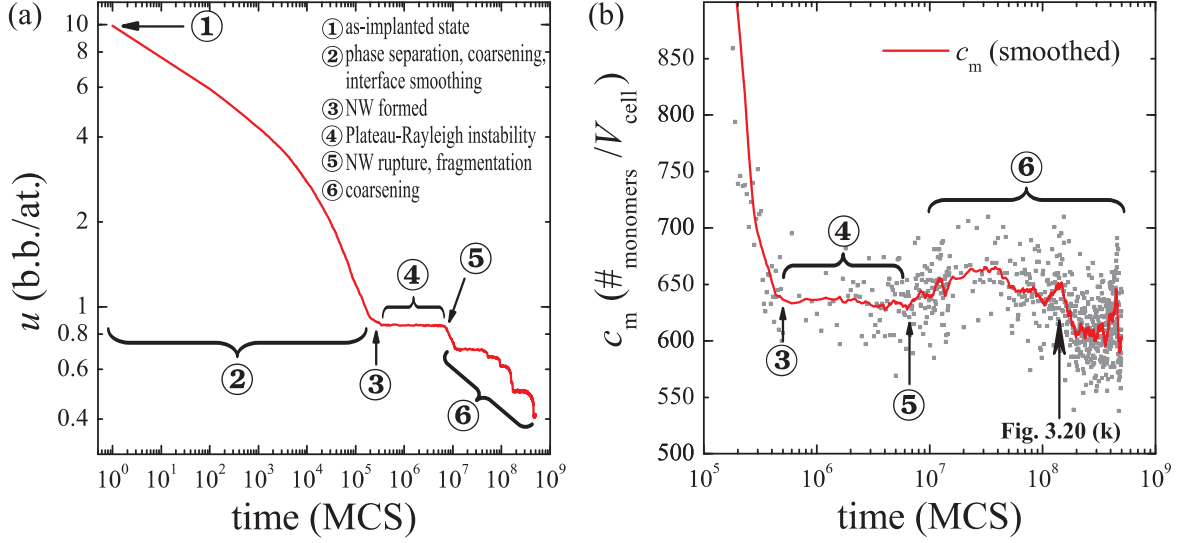
Figure (3.21): (a) Reduction of the average internal energy density u during the evolution of a cylindrical Gaussian FIB implantation profile depicted in Fig. 3.20. (b) Corresponding time-development of the monomer concentration c_m.

is shown in Fig. 3.21 (b). Temporary peaks appear in $c_m(t)$ (cf. also Fig. 3.20 (k)) which refer to the evaporation of subcritical NCs during coarsening which prove the characteristics of Eqn. 3.16.

In conclusion, it has been demonstrated by kinetic arguments and lattice KMC simulations that NWs are formed as transient structures on the system's relaxation pathway from FIB line scan implantation profiles towards thermodynamic equilibrium.

Chapter 4

Capillarity-driven Shape Evolution of Nanostructures

This chapter deals with the self-organized shape evolution of single-crystalline nanostructures with a strong emphasis on structures of cylindrical geometry like wires, rods, or cylindrical pores. Such structures spontaneously transform under the diffusion-mediated capillary force into chains of spherical particles or voids in a self-organizing manner (relaxation towards equilibrium). This classical capillary instability phenomenon, which is named after the Belgian physicist Joseph Antoine Ferdinand Plateau (1801-1883) and the English physicist Lord Rayleigh (*alias* John William Strutt; 1842-1919), is portrayed in the beginning of the first section. Thereafter, results of the atomistic modeling of the Plateau-Rayleigh instability using the lattice KMC method are presented and discussed. For this purpose, structures of different geometries (e.g. infinite NWs, finite NWs (nanorods), tubes, or toroidal structures) have been investigated under various parameters (e.g. size, temperature, crystallographic orientation). Moreover, predictions of reaction pathways are outlined by means of which functional nanostructures can be fabricated in a self-organizing manner making use of the Plateau-Rayleigh instability.

In cylindrical structures, the system-inherent capillary force triggers material transport aiming at the overall reduction of the surface free energy. In real systems this material redistribution process is generally subject to external fields and/or forces, e.g. stress fields, electric or magnetic fields, temperature gradients, chemical effects from the ambient etc. all of which can effect the system's relaxation pathway towards equilibrium. The lattice KMC method offers in this respect the unique possibility to study the free evolution (i.e. the evolution free from external impact) of nanoscale structures based on an idealized atomistic dynamics.

4.1 The Plateau-Rayleigh Instability

The Plateau-Rayleigh instability is considered a classical interfacial instability in the course of which the surface free energy of a freely evolving cylindrical body is reduced by its capillarity-driven transformation into a chain of spherical particles of certain minimal distance and size [21]. This instability is of great practical importance, e.g. in the process of ink-jet printing [235, 236]. The Plateau-Rayleigh instability takes place spontaneously, i.e. a cylindrical system is inherently unstable and does not need to overcome

any activation barrier, unlike the capillary instability of thin films which are metastable [21]. In other words, the surface of a cylinder is a reservoir of potential energy (cf. Fig. 3.15) that is spontaneously released during a relaxation process – in analogy to the relaxation of a compressed (or stretched) spring. Under the constraint of volume conservation, the system approaches thereby a state closer to thermodynamic equilibrium. Despite this energetic view, the microscopic kinetics of this relaxation process can be very different: liquids are redistributed by hydrodynamic flow along surface-undulation-induced pressure gradients [237], whereas in solid-state systems atomic diffusion along curvature-gradient-induced concentration gradients leads to material flux [234].

In the following, the Plateau-Rayleigh instability of 3D cylinders is discussed thoroughly. As a "by-product" an extended view (generalization) on the capillary instability of cylinders in n-dimensional space ($n > 2$) is given in appendix B. There, the willing reader is "abducted" from 3D- into hyper-space where capillary phenomena can be encountered (among of which the Plateau-Rayleigh instability) which are of fundamental physical importance, for instance, in cosmology.

Surface Free Energy Gain. Motivated by Savart's experimental observations of liquid jets coming out of a circular orifice [238], Plateau was the first to explain why a cylindrical body undergoes a shape transformation by developing axisymmetric surface undulations along its longitudinal axis, that these undulations grow in time, and that the structure finally disintegrates at the undulation necks leaving a chain of separated droplets behind [22]. Plateau stated correctly that a minimum undulation wavelength, which equals the circumference of the cylinder, is required in order to gain surface free energy during this process.

By considering a harmonic perturbation on the cylinder surface it can be seen that the development of axisymmetric surface undulations of a minimum wavelength λ_c leads to the reduction of surface free energy (cf. Fig. 4.1):

$$R(z) = R^* + \epsilon \cos(qz) \;, \tag{4.1}$$

where R^* equals in a first approximation the radius of the unperturbed cylinder R_0, ϵ has a very small positive value ($\epsilon \ll R_0$), z is the coordinate along the cylinder's longitudinal axis, and q denotes the undulation wave vector, i.e. $q = 2\pi/\lambda$, λ being the wavelength of the perturbation [23, 237].

The change in surface free energy ΔF_s between the undulated and the smooth cylinder can be calculated by evaluating the integral

$$\Delta F_s = \tilde{F}_s - \bar{F}_s = 2\pi\gamma \left(\int_0^\lambda R(z)\sqrt{1 + \left(\frac{\mathrm{d}R(z)}{\mathrm{d}z}\right)^2}\,\mathrm{d}z - R_0\lambda \right) \;, \tag{4.2}$$
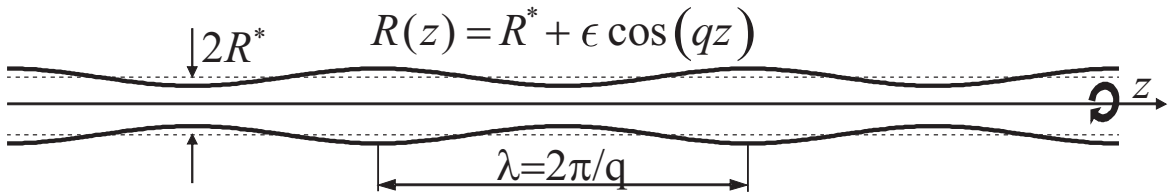
Figure (4.1): A schematic representation of a cylindrical body with an axisymmetric harmonic surface undulation, the so-called "unduloid".

where γ is the surface tension that is assumed to be isotropic in this case. Since the perturbation ought to be small, the square root term can be approximated with a Taylor series, thus,

$$\Delta F_s \approx 2\pi\gamma \left(\int_0^\lambda R(z) \left[1 + \frac{1}{2} \left(\frac{\mathrm{d}R(z)}{\mathrm{d}z} \right)^2 \right] \mathrm{d}z - R_0 \lambda \right) . \tag{4.3}$$

Evaluating the integral and keeping only terms up to the second order of epsilon one finds

$$\Delta F_s = \frac{\pi\gamma\epsilon^2\lambda R_0}{4} \left[\left(\frac{2\pi R_0}{\lambda} \right)^2 - 1 \right] . \tag{4.4}$$

This result clearly shows that the surface free energy is lowered ($\Delta F_s \leq 0$) if the wavelength of the perturbation verifies the inequality

$$\lambda \geq 2\pi R_0 . \tag{4.5}$$

Consequently, perturbations with $\lambda \geq 2\pi R_0$ are favorable for the system; they are therefore stable and ought to grow in time. On the contrary, those perturbations with $\lambda < 2\pi R_0$ cause the surface free energy to rise, thus, they are energetically unfavorable and ought to decay in time.

Analogously, non-axisymmetric perturbations can be considered, i.e.

$$R(z, \phi) = R^* + \epsilon \cos(qz) \cos(n\phi) , \tag{4.6}$$

where ϕ is the azimuthal angle of the cylindrical coordinate system. It was found that such perturbations are always unstable, i.e. for all $n \geq 1$ they cause an increase in surface free energy, thus, non-axisymmetric perturbations ought to decay in time [23, 237].

The constraint of the above ansatz is the conservation of volume of the unperturbed cylinder with length λ: $\bar{V}_{\mathrm{cyl}} = \pi R_0^2 \lambda$. Various authors set R^* equal to R_0 [23, 234, 237]. This gives a volume conservation up to the second order of ϵ as the calculation of the volume of the perturbed cylinder $\tilde{V}_{\mathrm{cyl}}$ reveals:

$$\tilde{V}_{\mathrm{cyl}} = \pi \int_0^\lambda R(z)^2 \mathrm{d}z = \pi \int_0^\lambda \left(R_0 + \epsilon \cos \left(\frac{2\pi z}{\lambda} \right) \right)^2 \mathrm{d}z = \pi R_0^2 \lambda + \frac{\pi\lambda\epsilon^2}{2} . \tag{4.7}$$

Motivated by experimental observations on the evolution of liquid cylinders where the mean radius around which the harmonic undulation develops was found to be slightly smaller than the initial radius, Yuen was the first to calculate the surface undulation using a non-harmonic ansatz [21, 239]:

$$R^* = R_0 - \frac{\epsilon^2}{4R_0} , \tag{4.8}$$

which results in a much better agreement of the volume conservation condition up to the forth order of ϵ:

$$V = \pi R_0^2 \lambda + \frac{\pi\lambda\epsilon^4}{16R_0^2} . \tag{4.9}$$

Perturbation Dynamics. Plateau incorrectly concluded that the capillarity-induced disintegration of a cylinder proceeds always with the minimum wavelength which equals the circumference of the cylinder $\lambda_c = 2\pi R_0$ [22].

In 1879, Rayleigh showed analytically in his renown paper *"On the instability of jets"* [23] in the spirit of a harmonic perturbation analysis combined with a Langrange method that the wavelength found by Plateau is only the smallest wavelength among an infinite number of perturbation wavelengths $\{\lambda_1; \lambda_2; ...\}$ which render a cylindrical body unstable, i.e. which fulfill Eqn. 4.5. These perturbations are initially represented by their amplitudes $\{\epsilon_{1,0}; \epsilon_{2,0}; ...\}$ which have developed after a time t by $\{\epsilon_{1,0} \exp(k_1 t); \epsilon_{2,0} \exp(k_2 t); ...\}$. During the early stage of evolution, a selective competition of these exponential growth rates $\{\exp(k_1 t); \exp(k_2 t); ...\}$ takes place as a result of which a harmonic perturbation with maximal growth rate and with corresponding wavelength λ_m emerges. The time dependence of the perturbation amplitudes is given by

$$\frac{\mathrm{d}\epsilon_i}{\mathrm{d}t} = \dot{\epsilon_i} = k_i \epsilon_i. \tag{4.10}$$

The amplification factors k_i are given by [23, 240]:

$$\frac{\dot{\epsilon_i}}{\epsilon_i} = k_i = \left[\frac{C}{R_0^3} \times \frac{I_1(qR_0)}{I_0(qR_0)} \times (qR_0 - q^3 R_0^3) \right]^{1/2} , \tag{4.11}$$

where C summarizes material parameters of the liquid. Rayleigh found that the wavelength with maximum growth rate amounts to:

$$\lambda_m = 9.016 R_0 . \tag{4.12}$$

Given this result, it could be concluded that λ_m is constant throughout the entire transformation of a cylinder into a particle chain. However, the above derivation relies on the fact that the surface perturbations are small and harmonic. With growing amplitude of the undulation these assumptions no longer hold which can give rise to changes in λ_m and k_i.

The later stages of the Plateau-Rayleigh instability have been discussed controversially in the literature. Experimental observations on the evolution of liquid jets indicate that deviations from the above harmonic treatment can occur, e.g. experiments on the Plateau-Rayleigh instability of liquid jets by imposing audio-frequency disturbances show that non-linear effects may dominate the growth processes of the perturbation which can explain why liquid jets often disintegrate into droplets with smaller ligaments (also called satellite droplets) in between [236, 241].

Moreover, computer simulation on nanoscale liquid jets show large local differences from the classical theory, mainly due to thermal fluctuations [8, 9].

Almost a century after Rayleigh's seminal work, Nichols and Mullins were the first to treat the capillary instability of *solid* cylinders analytically [234]. From a LSA they deduced very similar results for the wavelength with maximum growth rate for the early stage of the capillary-driven transformation of cylinders by atomic diffusion. They discriminated various diffusion channels: surface diffusion, volume diffusion inside the cylinder, and volume diffusion outside the cylinder (cf. Fig. 4.2). In all cases they started with a linear harmonic surface undulation given by Eqn. 4.1 using $R^* = R_0$.
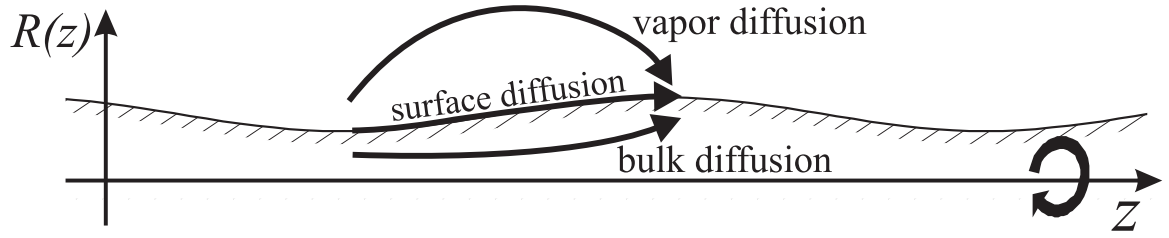
Figure (4.2): The possible diffusion pathways during the development of axisymmetric thickness undulations of a crystalline cylinder in contact with its vapor phase.
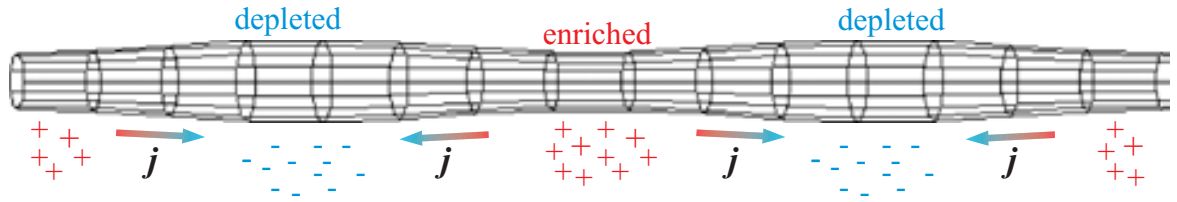
Figure (4.3): A schematic representation of a cylinder with growing axisymmetric undulation ($\lambda > 2\pi R_0$): the material flux j is directed towards regions of lower chemical potential (depleted).
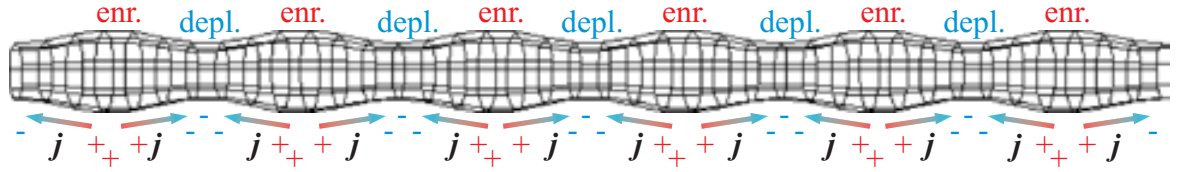
Figure (4.4): A schematic representation of a cylinder with decaying axisymmetric undulation ($\lambda < 2\pi R_0$): the material flux j is directed towards regions of lower chemical potential (depleted).
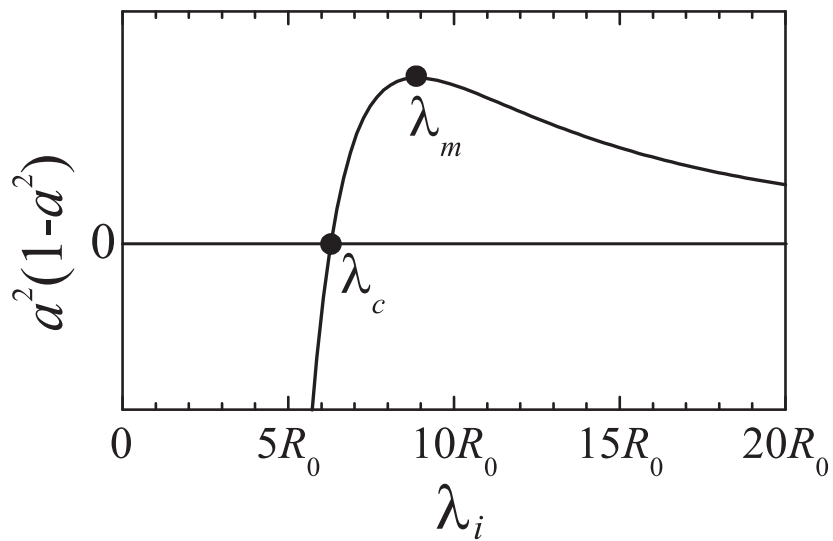
Figure (4.5): Plot of the perturbation growth rate vs. perturbation wavelength (cf. Eqn. 4.17). Perturbations with $\lambda < \lambda_c$ decay, whereas perturbations with $\lambda > \lambda_c$ grow. The perturbation mode with λ_m grows fastest.

For surface diffusion they consider an approximate expression for the mean curvature K at any point of the undulated cylinder surface,

$$K = \frac{1}{R(z)} + \frac{\mathrm{d}^2 R(z)}{\mathrm{d}z^2} \; , \tag{4.13}$$

where the first term denotes the azimuthal curvature (always convex) and the second term represents the longitudinal curvature (convex at shoulders; concave at necks) of the undulated cylindrical structure (cf. Fig. 4.3 and Fig. 4.4). The perturbation dynamics is tackled by considering the outward normal velocity at any point of an arbitrary surface which is undergoing capillary-driven shape changes given by [32]

$$\frac{\partial \mathbf{n}}{\partial t} = B \nabla_s^2 K \; , \tag{4.14}$$

where ∇_s^2 denotes the surface Laplacian and B is a constant summarizing materials parameters:

$$B = \frac{\gamma c_s D_s \Omega^2}{k_B T} \; , \tag{4.15}$$

where γ is the surface tension assumed to be isotropic in this case, c_s is the surface areal density of the mobile species, D_s is the surface diffusivity, Ω is the atomic volume, and $k_B T$ have their usual meaning. For the perturbation growth rates k_i, Nichols and Mullins obtained

$$\frac{\dot{\epsilon}_i}{\epsilon_i} = k_i = B q^2 \left(\frac{1}{R_0^2} - q^2 \right) = \frac{B}{R_0^4} \left[\left(\frac{2\pi R_0}{\lambda} \right)^2 \left(1 - \left(\frac{2\pi R_0}{\lambda} \right)^2 \right) \right] \; . \tag{4.16}$$

Thus, zero growth rate is again fulfilled for the critical wavelength $\lambda_c = 2\pi R_0$. Defining $a = (2\pi R_0)/\lambda$ one gets

$$k_i = \frac{B}{R_0^4} \left[a^2 \left(1 - a^2 \right) \right] \; . \tag{4.17}$$

The relevant term regarding the time dependence of the ϵ's is $[a^2 (1 - a^2)]$ (cf. Fig. 4.5). Accordingly, the growth rates of the perturbation modes are positive for $\lambda \geq 2\pi R_0$ (cf. Eqn. 4.5 and Fig. 4.3). The maximum growth rate is given for

$$\lambda_{m,\,\mathrm{surface}} = \lambda_c \sqrt{2} = 2\pi R_0 \sqrt{2} \cong 8.886 R_0 \; , \tag{4.18}$$

which is very close to Rayleigh's outcome (cf. Eqn. 4.12). For all perturbations with $\lambda < 2\pi R_0$ the growth rates are negative, i.e. the perturbations decay in time (cf. Fig. 4.4). A further important consequence of Eqn. 4.16 is the fact that for surface diffusion the characteristic time of perturbation growth k_i^{-1} scales with R_0^4 for constant ratio R_0/λ. Under the assumption that the rupture time[1] of a cylindrical structure is linearly correlated with k_i^{-1} it is anticipated that the rupture time of a cylindrical structure scales with R_0^4 for surface diffusion-dominated systems (cf. Fig. 4.18).

---

[1]The rupture time is defined as the time span which elapses between the unperturbed state of the cylinder until the moment when the cylindrical structure disintegrates at the undulation necks (pinch-off).

Assuming that a cylinder evolves with a constant $\lambda_m = 2\pi R_0 \sqrt{2}$ the emerging spherical particles ought to be isochore with a radius

$$R_{NC} = R_0 \sqrt[3]{\frac{3\pi}{\sqrt{2}}} \approx 1.88\, R_0 \ . \tag{4.19}$$

For the two other cases of volume diffusion inside the cylinder and volume diffusion outside the cylinder Nichols and Mullins applied the linearized Gibbs-Thomson equation (cf. section 2.6) expressing the difference in concentration Δc of the diffusing species above and below a curved surface with respect to the concentration c_0 above or beneath a planar one [234]:

$$\Delta c = \frac{\gamma \Omega K}{k_B T} c_0 \ . \tag{4.20}$$

They obtained the following results for the respective maximum growth rates:

$$\lambda_{m,\,\text{int. vol.}} = 9.02 R_0 \quad \text{and} \tag{4.21a}$$
$$\lambda_{m,\,\text{ext. vol.}} = 12.96 R_0 \ . \tag{4.21b}$$

Nichols and Mullins emphasized that these results merely hold for small amplitudes and that the actual undulation wavelength until the final rupture of the cylinder may deviate but should lie close to λ_m [234].

The differences in λ_m between the three diffusion channels indicate that in real systems, where usually all three diffusion channels are simultaneously open, the disintegration of a cylindrical structure via the Plateau-Rayleigh instability into a particle chain is subject to irregularities due to the superposition of perturbation modes of different diffusion channels.

Surface Tension Anisotropy. So far, the Plateau-Rayleigh instability of cylindrical structures with isotropic surface tension has been discussed. However, in crystalline materials the surface tension is anisotropic (cf. section 2.5) which gives rise to modifications of the capillary instability of crystalline NWs. It has to be noted that only single-crystalline cylindrical structures are discussed here since the instability of polycrystalline cylinders is additionally influenced by grain boundary energies.

The first analytical approach in this regard was carried out by Cahn under the simplifying assumption that all confining surfaces (facets) parallel to the longitudinal axis of a crystalline cylinder have the same surface tension, yet, that the surface tension varies as the orientation relative to that axis changes [242], i.e.

$$\gamma = \gamma(\psi) \quad \text{where} \quad \psi \equiv \frac{\partial R}{\partial z} \ . \tag{4.22}$$

Thus, γ can be expanded about the orientations $\psi = 0$:

$$\gamma = \gamma_0 + \psi \frac{\partial \gamma}{\partial \psi} + \frac{\psi^2}{2} \frac{\partial^2 \gamma}{\partial \psi^2} + ... \tag{4.23}$$

Cahn comes to the conclusion that axisymmetric perturbations grow if their wavelength exceeds

$$\lambda_c = 2\pi R_0 \sqrt{1 + \frac{1}{\gamma} \frac{\partial^2 \gamma}{\partial \psi^2}} \ , \tag{4.24}$$

which gives for isotropic γ the former result: $\lambda_c = 2\pi R_0$.

Apparently, the critical wavelength λ_c is decreased if $(\partial^2\gamma)/(\partial\psi^2)$ is slightly negative. In the extreme (but unrealistic) case of $(\partial^2\gamma)/(\partial\psi^2) < -\gamma$ the critical wavelength is zero, i.e. all axisymmetric perturbations grow. On the contrary, λ_c is increased for positive values of $(\partial^2\gamma)/(\partial\psi^2)$ which is the case if $\gamma(\psi)$ has a minimum at $\psi = 0$. Nevertheless, since the increase of λ_c must be finite it can be concluded that any single-crystalline cylinder is unstable regardless of its crystal orientation and the orientation of its confining facets.

Glaeser revealed that the wavelength with maximum growth rate fulfills the same requirement as in the case of isotropic γ [243, 244]:

$$\lambda_m = \lambda_c\sqrt{2} = 2\pi R_0\sqrt{2}\sqrt{1 + \frac{1}{\gamma}\frac{\partial^2\gamma}{\partial\psi^2}} \; . \tag{4.25}$$

Regarding the growth kinetics of the perturbations, Glaeser found

$$k_i = \frac{B}{R_0^4}\left[a^2\left(1 - \left(1 + \frac{1}{\gamma}\frac{\partial^2\gamma}{\partial\psi^2}\right)a^2\right)\right] \; , \tag{4.26}$$

which reduces to Eqn. 4.17 for isotropic γ. Consequently, also for single-crystalline cylinders the rupture time is expected to scale with R_0^4 in the case of surface diffusion.

Cahn pointed out that the theory of the capillary instability of crystalline cylinders with arbitrary orientation of the longitudinal axis is highly complicated [242], particularly if the cylinder exhibits surfaces (facets) with different surface tension so that $\gamma = \gamma(\phi, \psi)$ where ϕ is the azimuthal angle of the cylindrical coordinate system, e.g. a [110]-oriented NW with f.c.c. lattice exhibits pronounced {111}- and {100}-facets parallel to the longitudinal axis (discontinuity in $\gamma(\phi, \psi)$; cf. section 4.2). For NWs with confining facets of different crystallographic orientation a further complication of the perturbation dynamics arises from the fact the solubility and diffusivity of ad-atoms on these facets depend on their orientation. Moreover, the idealized mathematical treatment considers only flat facets, i.e. cusps at the facet edges are not tractable with this method. For nanoscale systems, however, cusped regions can contribute considerably to the system's free energy [160]. Thus, it can be expected that the capillary instability of crystalline NW structures can deviate from the ideal results outlined above.

Control of the Capillary Instability.   There are various physical effects which cause the dynamics of the Plateau-Rayleigh instability of real crystalline cylindrical structures to differ from the above theoretical considerations. The following list gives a concise overview over important effects regarding changes in the perturbation growth (suppression or promotion). Some of them are discussed more closely later in this chapter.

- suppression:

    - surface energy anisotropy (if $\partial^2\gamma/\partial\psi^2$ is positive; e.g. Refs. [242, 243, 245, 246] and this work (cf. subsection 4.2.6))
    - quantum effects (e.g. Refs. [247, 248])
    - effects due to the substrate (e.g. Refs. [249, 250] and this work; cf. subsection 4.2.8)

> – radial thermal gradients (e.g. Ref. [251])
> – collisional mixing (this work; cf. section 5.2)

- promotion:

  > – surface energy anisotropy (if $\partial^2\gamma/\partial\psi^2$ is slightly negative; e.g. Refs. [242, 243, 245, 246] and this work; cf. subsection 4.2.6)
  > – periodic longitudinal thermal gradients (this work; cf. subsection 5.1.1)
  > – collisional mixing (this work; cf. section 5.2)

4.2 Shape Evolution of Infinite Nanowires

In the following, results of lattice KMC simulations on the Plateau-Rayleigh instability of single-crystalline NWs are presented. These simulations are based on the atomistic dynamics of the 3D NN-Ising model (cf. chapter 2). If not stated otherwise, the initial atomic configuration is that of a cylinder with radius R_0. Furthermore, the temperature is kept constant throughout each simulation, i.e. under the assumption of equal bond strength $\tilde{\varepsilon}_{NN}$ is time-independent.

4.2.1 Plateau-Rayleigh Instability Exemplar

A typical reaction pathway of the Plateau-Rayleigh instability of a single-crystalline cylindrical NW structure is depicted as image series in Fig. 4.6 (cf. a similar GIF animation[2]). Here, a NW with f.c.c. lattice structure whose longitudinal axis is [001]-oriented (R_0=12 a; N=225 792 atoms) evolves at $\tilde{\varepsilon}_{NN,f.c.c.}$=2.0, i.e. far below the critical temperature. Periodic boundary conditions are applied in all three spatial directions, i.e. the NW structure is connected with itself along the longitudinal axis whose length equals the length of the simulation cell (L=1024 a, thus, $R_0 \ll L$). According to the dynamics of the conserved-order-parameter NN-Ising model all diffusion channels are open in this case (cf. section 2.4).

Starting from a smooth surface, small axisymmetric perturbations develop locally in the first stage of evolution (cf. Fig. 4.6 (b-f)). These undulations grow and after a certain time (rupture time) the first pinch-off occurs (cf. Fig. 4.6 (k)). Later, the remaining NW fragments further disintegrate at the undulation necks until a state is reached where a chain of isolated spherical NCs remains (cf. Fig. 4.6 (v)).

In section 3.3 it is demonstrated that this state is not yet the equilibrium state of the system. The NC ensemble constituting the chain undergoes in a further stage of evolution an Ostwald ripening process (cf. subsection 2.6.1) at the end of which a single NC remains that corresponds to the ultimate equilibrium state (cf. Fig. 3.20).

4.2.2 Thermal Fluctuations

According to the analytical theory described above the Plateau-Rayleigh instability ought to cause a homogeneous and regular disintegration of the NW structure, i.e. one would expect that the pinch-offs at the undulation necks are synchronous and that the

---

[2]The GIF animation is located at: `http://www.roentzsch.org/Rayleigh/index.html`
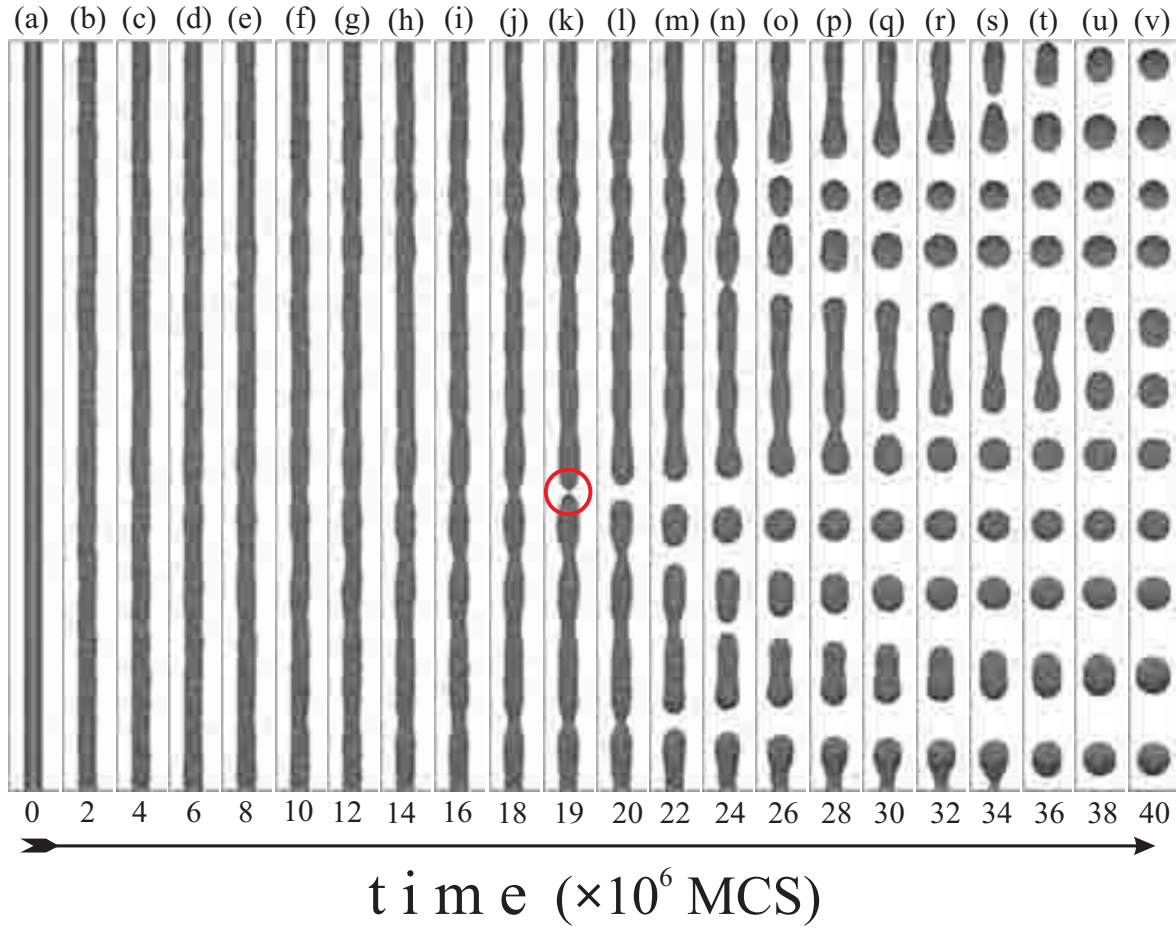
Figure (4.6): Lattice KMC simulation of the evolution of a [001]-oriented single-crystalline f.c.c. NW which transforms under the action of the diffusion-mediated capillary force into a chain of NCs ($R_0 = 10\,\mathrm{a}; L = 1024\,\mathrm{a}; \tilde{\varepsilon}_{NN,f.c.c.} = 2.0$).
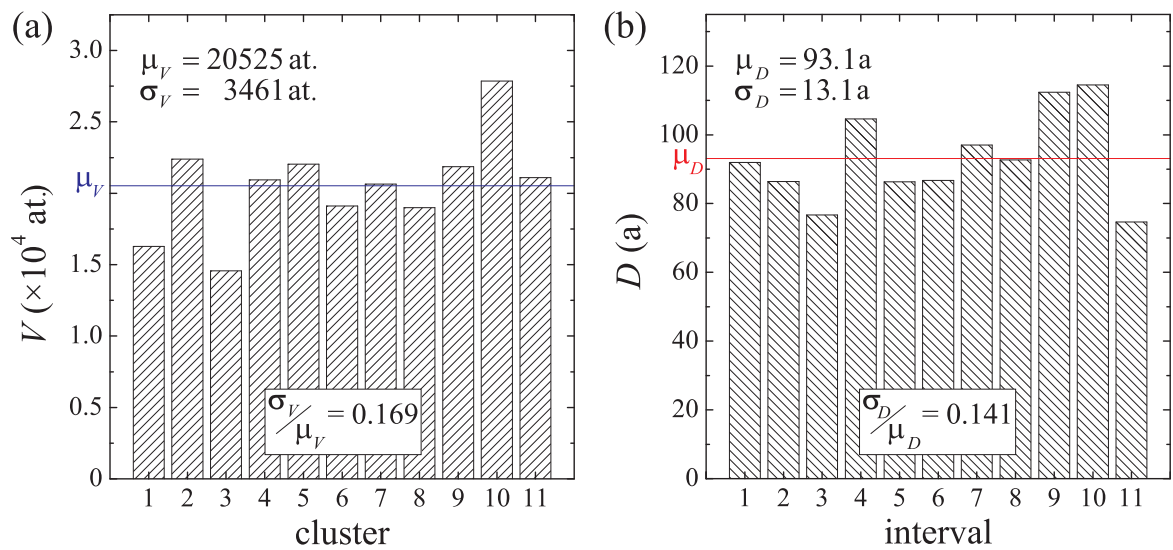
Figure (4.7): Statistics of the lattice KMC simulation on the Plateau-Rayleigh instability shown above in view of (a) volume V and (b) distance D of the NC chain in the final state (cf. Fig. 4.6 (v)).

distance and therefore the volume of the resulting NCs are equal. However, the above lattice KMC simulation delivers a different picture of the Plateau-Rayleigh instability, namely, that all these features are subject to thermal fluctuations. It is commonly accepted, that fluctuations are novel aspects of nanoscale science, i.e. they can have a significant contribution to the overall properties of the structure [252].

From Fig. 4.6 it can be concluded that the perturbation amplitude does not grow homogeneously in a realistic system. The reason for these irregularities is due to the inherent kinetics of the perturbation build-up process. Different from the LSA which preassumes a single harmonic surface perturbation (axisymmetric along the z-axis) which either grows or decays, in the present case the evolution starts from a smooth surface where the perturbation build-up process can only be initiated by local thermal fluctuations of the atomic configuration. Thus, small perturbations appear locally in the first stage of evolution along the z-axis. Since these individual perturbations are not necessarily spatially coherent (phase-shifts), their spatial superposition results in deviations from the harmonic ansatz of the LSA.

Information along the longitudinal axis is propagated by atomic diffusion whose characteristic length scales with the square root of time (Einstein relation). Thus, surface perturbations (capillary waves) which develop locally do not interact instantaneously with perturbations developing at distant surface positions. Consequently, phase shifts between distant perturbations occur which in the case of destructive superposition can retard the perturbation amplitude growth locally resulting in an inhomogeneous evolution of the NW along the z-axis. Moreover, it can not be expected that only perturbations with the mathematically exact maximum growth rate develop (cf. Fig. 4.5). Thus, perturbations with wavelengths close to the wavelength which corresponds to the maximum growth rate are likely to occur which further complicates the dynamics of the Plateau-Rayleigh instability in real systems. Those regions where the perturbation amplitude growth is not disturbed are advanced in time, i.e. they are the locations where the NW disintegrates first. This can nicely be seen by looking at the image series of Fig. 4.6 under grazing incidence in the direction orthogonal to the NW axis. For example, the neighborhood of the region where the first pinch-off occurs (cf. Fig. 4.6 (k)) exhibits already in the stage of perturbation build-up regular surface undulation which
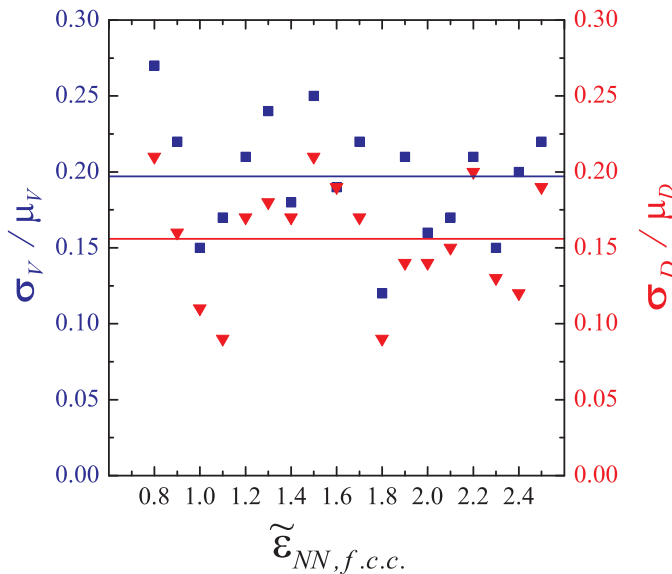
Figure (4.8): Statistics of the Plateau-Rayleigh instability in view of the relative standard deviations of NC volume, V, and NC distance, D, indicating that the disintegration of a NW is subject to system-inherent fluctuations over a broad temperature range ($\tilde{\varepsilon}_{NN}$) in the range between 10% and 25%.

cause advanced evolution locally.

The statistics of the above presented exemplar of the Plateau-Rayleigh instability in view of NC volume V and distance D of the final state (cf. Fig. 4.6 (v)) is seen in Fig. 4.7. The relative standard deviation of V and D which is defined as the ratio of the standard deviation σ to the mean μ is in the 15% range for both values. These fluctuations are system-inherent. They occur over a large parameter range in view of temperature, size (length, radius), crystallographic orientation etc.

In Fig. 4.8, for example, the statistics regarding NC volume and distance is plotted over a wide temperature range keeping all other parameters constant. Accordingly, relative standard deviation of V and D scatter homogeneously between 10% and 25%, thus, the temperature has apparently no systematic influence on the structural (ir-)regularity of the resulting NC chain (at least not in the examined temperature range).

A further lattice KMC simulation series focused on the influence which the initial simulation cell length has on the fluctuations during the Plateau-Rayleigh instability. For reasons of efficient lattice KMC encoding only simulation cell lengths of the power of two (in units of s.c. lattice constants; cf. Fig. A.3) were considered[3]. In this regard, in Fig. 4.9 (a-g), the isochronal states of disintegrated NWs are drawn with cell lengths ranging from $L = 2^5$ a to 2^{11} a ($R_0 = 10$ a; $\tilde{\varepsilon}_{NN,f.c.c.} = 1.3$). Merely for $L = 2^5$ a, the NW does not disintegrate which stands to reason since L is about only half of the critical wavelength $\lambda_c = 2\pi R_0$. The case $L = 2^6$ a reflects the critical one since here $L \simeq \lambda_c$: only one perturbation wavelength with $\lambda \simeq \lambda_c$ fits into the simulation cell, thus, the NW disintegrates into one particle only. For all $L > \lambda_c$ the NW evolves into a chain of NCs. In Fig. 4.9 (h) and Tab. 4.1, the respective statistics of NC volume and distance are presented up to $L = 2^{14}$ a. These values indicate that the relative standard deviations of these quantities are nearly equal for $R_0/L < 0.02$ (cf. Fig. 4.9 (e)).

In lattice KMC simulations only finite cell lengths can be considered, thus, the question of surface perturbation self-interference arises because of the commonly applied periodic cell boundary condition. If the wavelength with maximum growth rate is commensurable with the cell length, i.e. if the cell length equals an integer multiple of the wavelength with maximum growth rate (possible magic numbers in the R_0/L ratio), one might expect the fastest disintegration with the highest regularity in NC volume and distance because of standing capillary waves. However, simulations with different R_0 (using discrete, monoatomic surface layer intervals) at constant cell length did not reveal such behavior. The lattice KMC simulation with the largest cell length ($L = 2^{14}$ a; $R_0/L = 0.00061$) revealed fluctuations regarding NC volume and distance that are not different from the cases with higher R_0/L ratio up to $R_0/L = 0.02$. Consequently, the occurring fluctuations appear to be system-inherent and are definitely not due to commensurability/incommensurability issues between simulation cell length and developing perturbation wavelength.

To conclude, the above presented statistics reveal that the Plateau-Rayleigh instability of single-crystalline NWs is subject to system-inherent fluctuations regarding volume and distance of the resulting NCs. The respective relative standard deviations are found to be in the range between 10% and 20%. These fluctuations may pose diffi-

---

[3]Modular arithmetic is an essential part for the lattice KMC encoding on the bit-level (cf. appendix A); the rings of the congruence classes $\mathbb{Z}/L\mathbb{Z}$, where $L=2^n$ ($n \in \mathbb{N}$) denotes the simulation cell length, are applied. For example, the addition $L+1$ results in 1 which is implemented using the bitwise operation AND: $((L+1)\&L)=1$ (cf. Tab. A.1).
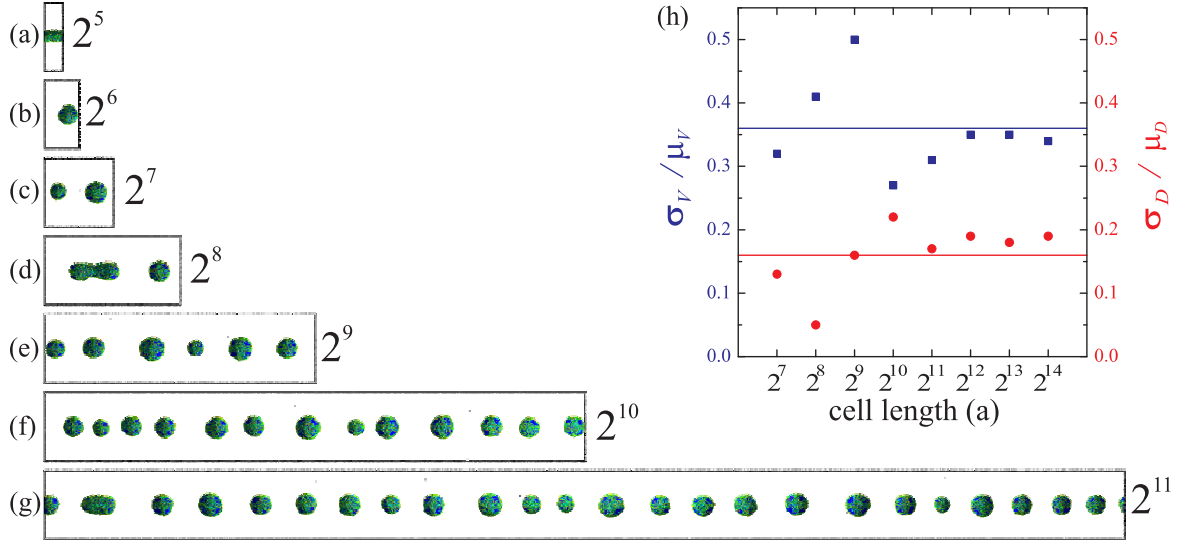
Figure (4.9): (a)-(g) Isochronal states of the Plateau-Rayleigh instability of [001]-oriented f.c.c. NWs ($t = 5.5 \times 10^6$ MCS; $R_0 = 10a$; $\tilde{\varepsilon}_{NN,f.c.c.} = 1.3$) with varying simulation cell length L. (h) The corresponding statistics regarding NC volume V and distance D. The cases with $L = 2^{12...14}$ a are not drawn.

cell length L (a)	NCs	μ_V (at.)	σ_V (at.)	σ_V/μ_V	μ_D (a)	σ_D (a)	σ_D/μ_D
$2^5 = 32$	-	-	-	-	-	-	-
$2^6 = 64$	1	9856.0	-	-	64.0	-	-
$2^7 = 128$	2	9874.5	3134.5	0.317	64.0	8.4	0.132
$2^8 = 256$	2	19759.0	8007.0	0.405	128.0	5.8	0.045
$2^9 = 512$	6	13153.3	6627.6	0.504	85.3	13.3	0.156
$2^{10} = 1024$	13	12148.5	3318.6	0.273	78.8	17.2	0.219
$2^{11} = 2048$	24	13158.2	4138.9	0.315	85.3	14.7	0.172
$2^{12} = 4096$	49	12891.2	4562.2	0.354	83.6	15.8	0.189
$2^{13} = 8192$	93	13581.2	4686.5	0.345	88.1	15.6	0.177
$2^{14} = 16384$	191	13228.2	4488.8	0.339	85.8	16.3	0.190

Table (4.1): Statistics of the Plateau-Rayleigh instability regarding the number of resulting NCs, their volume V and distance D for varying simulation cell lengths L (cf. Fig. 4.9).

culties regarding the employment of this self-organized NC chain formation process in view of functional NC chain structures where isochore and isodistant NCs are required (e.g. for the formation of metal particle chains applicable as SPP waveguides; cf. section 4.6). Later it is shown that these system-inherent fluctuations can be suppressed by periodic temperature gradients along the NW axis (cf. subsection 5.1.1).

4.2.3 Internal Energy Reduction

Due to the inhomogeneous evolution the course of the Plateau-Rayleigh instability of a solid cylinder can be separated into two stages: Firstly, the build-up of axisymmetric undulations along the NW until the first pinch-off occurs and, secondly, the NW fragmentation (i.e. cascade-like series of later pinch-offs) during which the NW decomposes

(a)

(b)
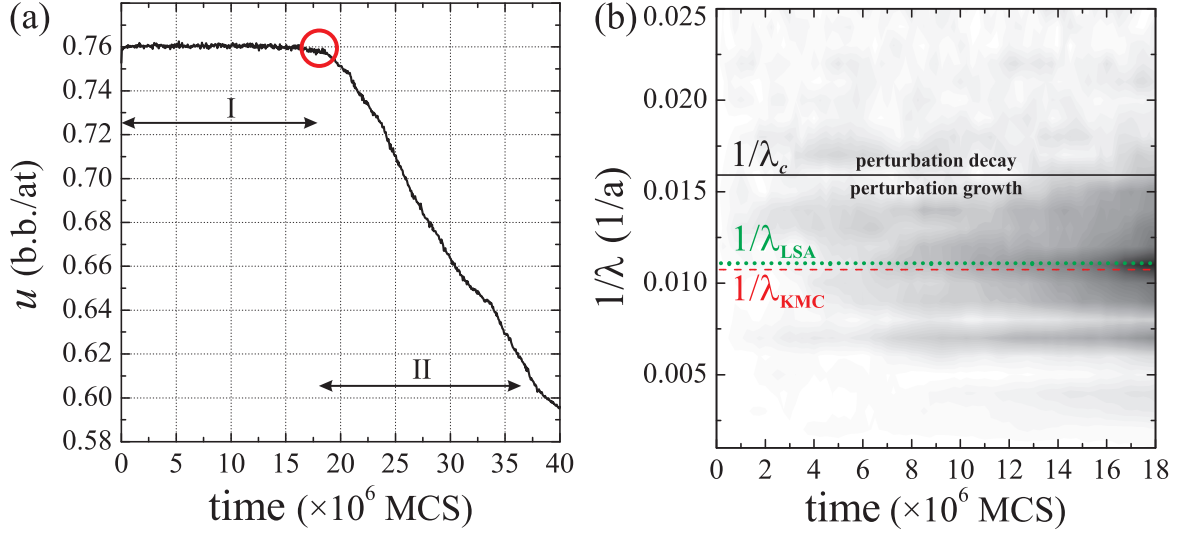
Figure (4.10): (a) Specific internal energy vs. simulation time demonstrating that the Plateau-Rayleigh instability proceeds in two stages (cf. Fig. 4.6): I. Development of axisymmetric undulations along the NW; II. NW fragmentation (starting at a $u(t)$-discontinuity, cf. circle). (b) Fourier spectrum of the line density of the corresponding NW expressing the perturbation mode selection.

completely into a chain of isolated NCs. These two stages can be discriminated by the time-development of the specific internal energy. For the Plateau-Rayleigh instability exemplar of Fig. 4.6, in Fig. 4.10 (a), the time-development of the specific internal energy $u(t) = U(t)/N$ (N: total number of particles) is plotted which is a good approximation for the development of the specific free energy since the simulation is carried out at low temperature ($\tilde{\varepsilon}_{NN,f.c.c.}$=2.0; cf. Fig. 2.6 (b)) so that the contribution of entropy to the free energy can be neglected (cf. section 2.2). The two characteristic stages are clearly reflected in $u(t)$ in terms of slope, i.e. in terms of the specific energy reduction rates: $(-\mathrm{d}u/\mathrm{d}t)_I = 8.5 \times 10^{-11}$ bb/at·MCS and $(-\mathrm{d}u/\mathrm{d}t)_{II} = 8.2 \times 10^{-9}$ bb/at·MCS, thus, the two stages differ significantly by two orders of magnitude.

The rupture time t_r is also subject to fluctuations as Fig. 4.11 reveals where $u(t)$ of five lattice KMC runs with fully identical initial parameters but different random number seeds are plotted, thus, resulting in statistically similar but microscopically dissimilar simulation pathways (here: R_0=10 a; L=1024 a; $\tilde{\varepsilon}_{NN,f.c.c.}$=1.3). The relative standard deviation of t_r is in the 5% range, it amounts to $\sigma_{t_r}/\bar{t}_r = 0.047$.

4.2.4   Perturbation Fourier Spectrum

For the Plateau-Rayleigh instability exemplar of Fig. 4.6, in Fig. 4.10 (b) the Fourier spectrum of the atomic line density along the main axis of the NW is plotted as a function of time. Thus, the perturbation growth can directly be observed. The gray scale intensity is plotted linearly in a.u. Accordingly, a wavelength with maximum growth rate emerges: $\lambda_{KMC} = 93.1$ a $= 1.48 \times 2\pi R_0$ which is slightly larger than the value obtained from the LSA where $\lambda_{LSA} = \sqrt{2} \times 2\pi R_0 \approx 1.41 \times 2\pi R_0$. The Fourier spectrum indicates that perturbations develop with wavelengths close to the wavelength with maximum growth rate. Particularly in the very first stage of undulation build-up ($t < 5 \times 10^6$ MCS) some short-wavelength perturbations develop with $\lambda_c < \lambda < \lambda_{KMC}$. However, after this initial stage of evolution the perturbation with λ_{KMC} catches up with those short-wavelength perturbations and finally wins this perturbation wave-
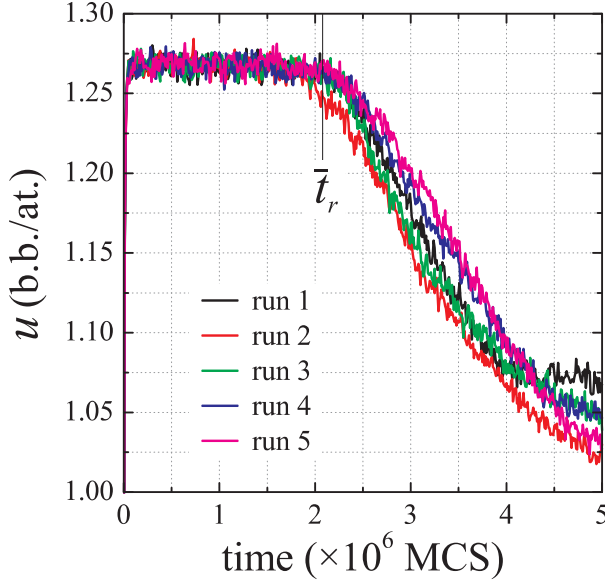
Figure (4.11): Specific internal energy u plotted versus time of five runs with fully identical initial parameters except the random number seed. The relative standard deviation of the rupture time amounts to $\sigma_{t_r}/\bar{t}_r = 0.047$.

length selection. These results further point out that for a [001]-oriented f.c.c. NW considered here the crystallographic anisotropy does not severely influence the perturbation wavelength at $\tilde{\varepsilon}_{NN,f.c.c.} = 2.0$, i.e. $\frac{\partial^2 \gamma}{\partial \psi^2} \ll 1$ (cf. Eqn. 4.25). Moreover, since the obtained mean NC distance lies close to the wavelength with maximum growth rate, which the LSA predicts for the dominance of surface diffusion, it becomes obvious that volume diffusion through the surrounding medium and through the bulk of the NW does not significantly contribute to material redistribution, i.e. the Plateau-Rayleigh instability of single-crystalline NWs is obviously governed by surface diffusion.

4.2.5 Effect of Initial Undulations

It has been shown that the diffusion-mediated capillary instability of a smooth single-crystalline NW is subject to thermal fluctuations regarding volume and distance of the resulting NCs due to the perturbation build-up process. On the contrary, if the initial NW surface is already regularly undulated with a constant wavelength $\tilde{\lambda}$ the capillary instability can lead to quite different results[4]. In Fig. 4.12, these two scenarios are compared: On the one hand a smooth cylindrical structure ($R(t_0)=R_0=14$ a) referring to the above discussion evolving into an irregular NC chain, on the other hand an axisymmetrically pre-undulated cylindrical structure with small undulation amplitude $\epsilon=0.14R_0$ ($R(t_0)=R_0-\epsilon\cos(2\pi z/\lambda_{\mathrm{LSA}})$) evolving into a regular and long-range-ordered chain of isodistant and isochore NCs, i.e. $\sigma_V/\mu_V \approx 0$ and $\sigma_D/\mu_D \approx 0$ (for all cases: NWs with [001]-orientation; $\tilde{\varepsilon}_{NN,f.c.c.}=1.3$; $L=2^9$ a). Their distance coincides with the periodicity of the initial undulation. Here, $\tilde{\lambda}$ is chosen to coincided with the perturbation wavelength with maximum growth rate from the LSA by Nichols and Mullins (cf. section 4.1). Apparently, the $\tilde{\lambda}$ is directly adopted by the system as the wavelength of disintegration. The growth of perturbations with other wavelengths is suppressed, thus, they do not have any influence on the reaction pathway.

Several cases of the capillarity-driven evolution of pre-undulated cylindrical structures where $\tilde{\lambda}$ does not equal λ_{LSA} are depicted in Fig. 4.13 ($\epsilon=0.28R_0$ in each ca-

---

[4]For example, regular surface undulations can be obtained during the synthesis of NWs (growth-induced effects) [253].
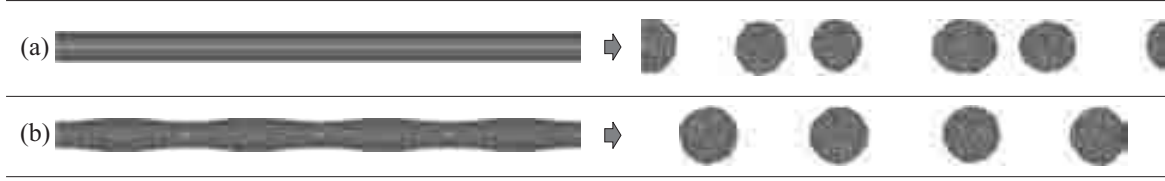
Figure (4.12): Initial (l.h.s.) and final (r.h.s) states of the Plateau-Rayleigh instability (a) of a smooth cylinder and (b) of a cylindrical structure with an initial harmonic undulation (cf. text for details).

se). Accordingly, regularity of the NC chain is obtained for a wide range of $\tilde{\lambda}$ (cf. Figs. 4.13 (a)-(f)) where $\tilde{\lambda}$ scales from $(4...0.69)\lambda_{\mathrm{LSA}}$. In all these cases of appearing regularity, the structure directly disintegrates with the given wavelength of the initial undulation. Fig. 4.13 (f) corresponds to the critical case where $\tilde{\lambda}=\lambda_c$: the structure disintegrates although the growth rate is theoretically zero. The reason for this is most likely due to non-linear or kinetic effects not considered by the LSA theory.

For all cases with $\tilde{\lambda}<\lambda_c$ (cf. Fig. 4.13 (g, h)) the reaction pathway is totally different from the above ones. The initial perturbations have wavelengths which correspond according to the LSA to negative growth rates (cf. Fig. 4.5). This is indeed the case here where the initial undulations smooth out in the first stage of the KMC run (not shown; cf. Fig. 4.4). After surface smoothing the cylindrical structure searches at a later stage its own wavelength of disintegration. This process is naturally subject to fluctuations leading to irregularities as seen in Fig. 4.13 (g, h). A similar behavior is expected for $\tilde{\lambda}\gg\lambda_{\mathrm{LSA}}$.

The domain in which $\tilde{\lambda}$ leads to the direct and regular disintegration of the pre-undulated structure depends on the initial undulation amplitude ϵ. It has been observed that for very small ϵ (undulation amplitudes in the range of a single atomic layer; results not shown) that the initial undulations are destroyed by thermal fluctuations and that the system then evolves as if the initial surface had been perfectly smooth.
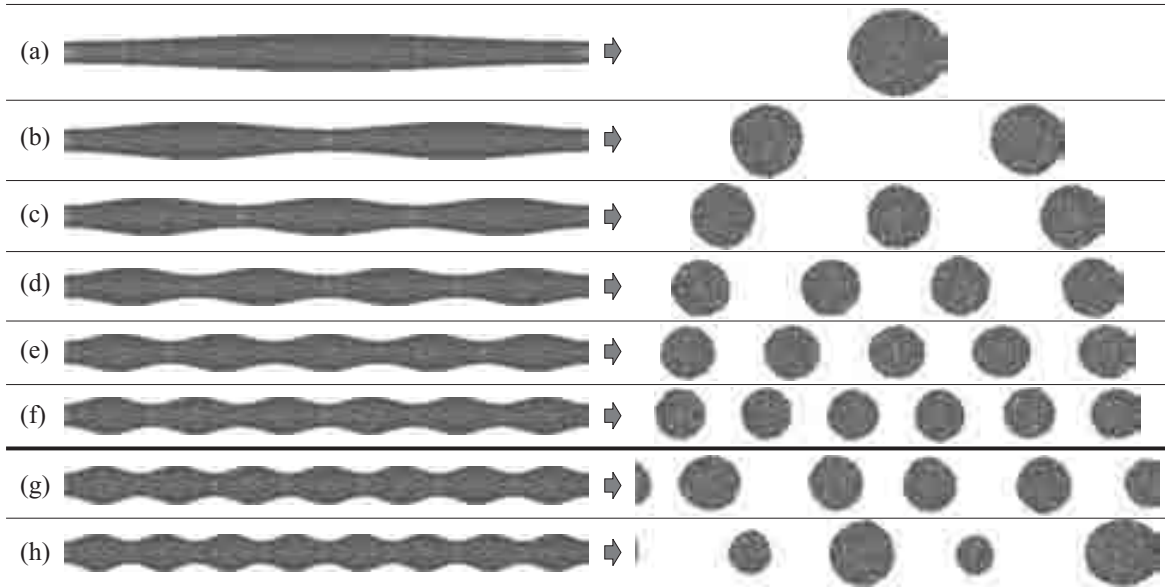
Figure (4.13): Initial (l.h.s.) and final (r.h.s) states of the Plateau-Rayleigh instability of cylindrical structures that have initial harmonic undulations with varying undulation wavelengths (cf. text for details).

Consequently, there is a minimum $\epsilon_{\min}=\epsilon_{\min}(\tilde{\lambda})$ required in order to reach direct and regular disintegration of the structure with $\mu_D = \tilde{\lambda}$.

4.2.6 Surface Tension Anisotropy

The surface tension is an expression of the specific surface free energy, i.e. it contains a strong temperature dependence (entropy contribution). Therefore, surface tension anisotropy effects are expected to be pronounced at temperatures much lower than the critical one[5] which has been demonstrated for example for cylindrical pores in sapphire [243, 246] or for CoSi$_2$ NWs coherently embedded in c-Si [230]. As the system approaches T_c, the anisotropy effects are practically lost and the Plateau-Rayleigh instability of single-crystalline cylindrical structures ought to be independent of the crystallographic orientation of the cylinder.

In section 4.1 it has been outlined that the confining surfaces (=facets) of a single-crystalline cylindrical structure change the characteristics of the surface perturbation growth and, therefore, may influence the characteristic measures like rupture time and distance as well as volume of the resulting NCs. From the analytical treatment it can be expected that NWs with facets, that are parallel to the longitudinal axis and that have a minimal surface tension, sustain the action of the capillary force longer compared to those NWs which are confined by facets with higher surface tension (weaker driving forces). In other words, confining surfaces with low surface tension can stabilize a NW structure. For the following KMC simulations on surface tension anisotropy phenomena during the Plateau-Rayleigh instability only structures with f.c.c. lattice have been considered for which the most stable ones are {111}-facets (cf. Tab. 2.2).

Surface tension anisotropy is particularly pronounced at low temperatures which can be seen in analogy to Fig. 2.11 in Fig. 4.14 (a-e) and Fig. 4.15 (a-e) where cross sections are shown of [001]- and [110]-oriented NWs, respectively, in a quasi-equilibrium state in dependence of temperature (i.e. for varying $\tilde{\varepsilon}_{NN.f.c.c.}$).

Again, the lattice KMC method reproduces fine agreement with the Wulff-theorem if one compares the low-temperature cross sections with the ideal Wulff-construction in Fig. 4.14 (f) and Fig. 4.15 (f), respectively. For the f.c.c. lattice, [110]-oriented NWs which are confined by four {111}-facets and two {100}-facets are expected to be the most stable ones under the capillary force.

This expectation is met considering Fig. 4.16 where isochronal states ($t = 2.5 \times 10^7$ MCS) of four single-crystalline NWs are drawn which differ in crystallographic orientation. All these NW main axis orientations lie in the (100)-plane. In these simulations the temperature is very low compared to the critical one, thus, surface tension anisotropy effects are very pronounced. The [011]- and the [001]-oriented NW have sustained the Plateau-Rayleigh instability thus far, whereas the other two NWs already show pronounced axisymmetric surface undulations. The [014]-oriented NW structure even exhibits its first pinch-off. If one looks close to the inclusion in Fig. 4.16 (b) the NW surface structure is seen in atomistic resolution. It can be observed that the undulated surface of this [012]-oriented NW actually exhibits low-index facets, dominantly {111}-ones which appear to "cut" the NW structure. This can be explained by the fact that the [012]-direction of the NW axis does not lie in a {111}-plane, i.e. at T=0 the Wulff-plot of the [012]-oriented NW cross section does not

---

[5]In other words, facets are indicators of order.
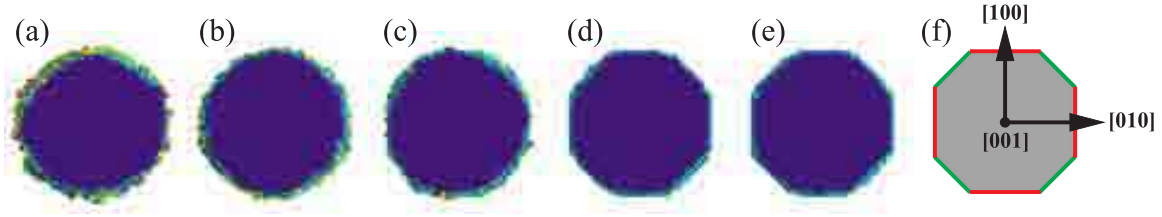
Figure (4.14): Series of cross section of a [001]-oriented NW with f.c.c. crystal structure for different temperatures: (a) $\tilde{\varepsilon}_{NN}=1.0$, (b) $\tilde{\varepsilon}_{NN}=1.5$, (c) $\tilde{\varepsilon}_{NN}=2.0$, (d) $\tilde{\varepsilon}_{NN}=5.0$, (e) $\tilde{\varepsilon}_{NN}=10.0$, and (f) according to a Wulff construction where the red and green lines indicate {100}- and {110}-facets, respectively.
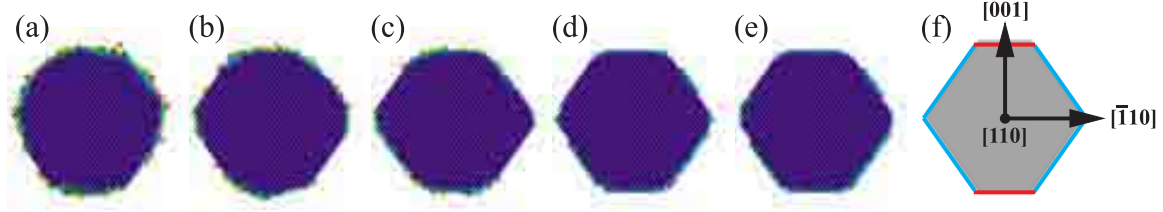
Figure (4.15): Series of cross sections of a [110]-oriented NW with f.c.c. crystal structure for different temperatures: (a) $\tilde{\varepsilon}_{NN}=1.0$, (b) $\tilde{\varepsilon}_{NN}=1.5$, (c) $\tilde{\varepsilon}_{NN}=2.0$, (d) $\tilde{\varepsilon}_{NN}=5.0$, (e) $\tilde{\varepsilon}_{NN}=10.0$, and (f) according to a 3D Wulff construction where the red and blue lines indicate {100}- and {111}-facets, respectively.

exhibit {111}-facets. However, at non-zero temperature these {111}-facets with the lowest overall surface tension start developing (by surface diffusion). This process of the growth of facets with discretely different orientation from the original surface is called "thermal grooving" [25, 32]. It further leads also to sharp cusp lines (edges) in-between the facets which can also be observed in the inclusion of Fig. 4.16 (b) (sawtooth-like surface topology). Consequently, those NWs which do not have confining {111}-facets at $T=0$ are destabilized by them at non-zero temperature, i.e. they literally carve the NW structure into individual NCs under the same discrete angle under which the NW main axis orientation cuts the {111}-plane (for example, this angle is 39.2° for the [012]-oriented NW shown in the inclusion of Fig. 4.16 (b)). For the f.c.c. lattice this is true for all low-index NW orientations except the [011]- and the [112]-oriented ones which have four and two confining {111}-facets at $T=0$, respectively. Even the [001]-oriented NW shown in Fig. 4.16 (d) is later cut by {111}-facets (not shown). This process, however, takes much longer since from the kinetic point of view its confining {100}- and {110}-facets (cf. Fig. 4.14 (f)) slow down the growth of {111}-facets.

In Fig. 4.17 the stability of f.c.c. NWs ($R_0=8\,a$) with different orientations is plotted for three different temperatures (assuming equal bond strength; low-T: $\tilde{\varepsilon}_{NN,f.c.c.}=2.5$; intermediate-$T$: $\tilde{\varepsilon}_{NN,f.c.c.}=1.9$; high-$T$: $\tilde{\varepsilon}_{NN,f.c.c.}=1.3$) expressed by the respective rupture time t_r (statistical error of about 5%) which is directly related to the surface perturbation growth rate. Accordingly, for the high-T case (low surface tension anisotropy) there is not any significant influence of the NW orientation on the NW stability; all NWs disintegrate nearly at the same time. For the intermediate-T case, however, the [011]-oriented NW (four confining {111}-facets) is by far the most stable one whose t_r is two orders of magnitude larger compared to the other orientations. In the case of low temperature, this tendency has even increased as one would expect: the rupture time of the [011]-oriented NW is more than four orders of magnitude larger than for the other orientations. As mentioned above, the [112]-oriented NW ought to be also rather
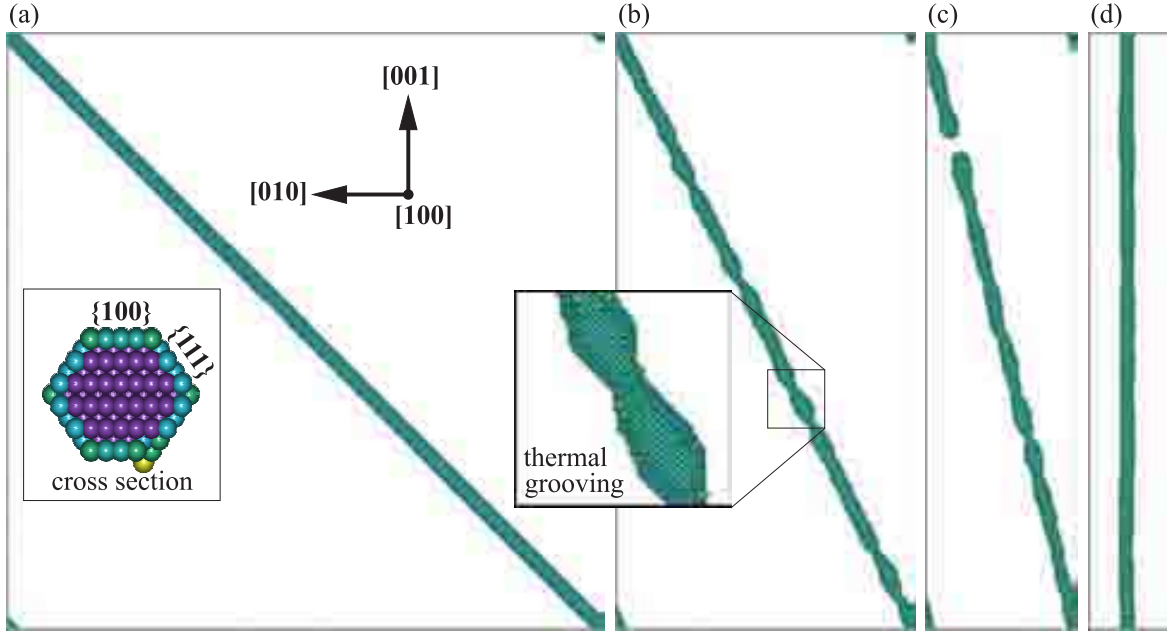
Figure (4.16): Lattice KMC micrographs of isochronal states of the Plateau-Rayleigh instability of four f.c.c. NWs with different crystallographic orientations: (a) [011]-, (b) [012]-, (c) [014]-, and (d) [001]-oriented (in each case: $\tilde{\varepsilon}_{NN,f.c.c.}$=3.5; R_0=6 a; t=2.5 × 10^7 MCS).
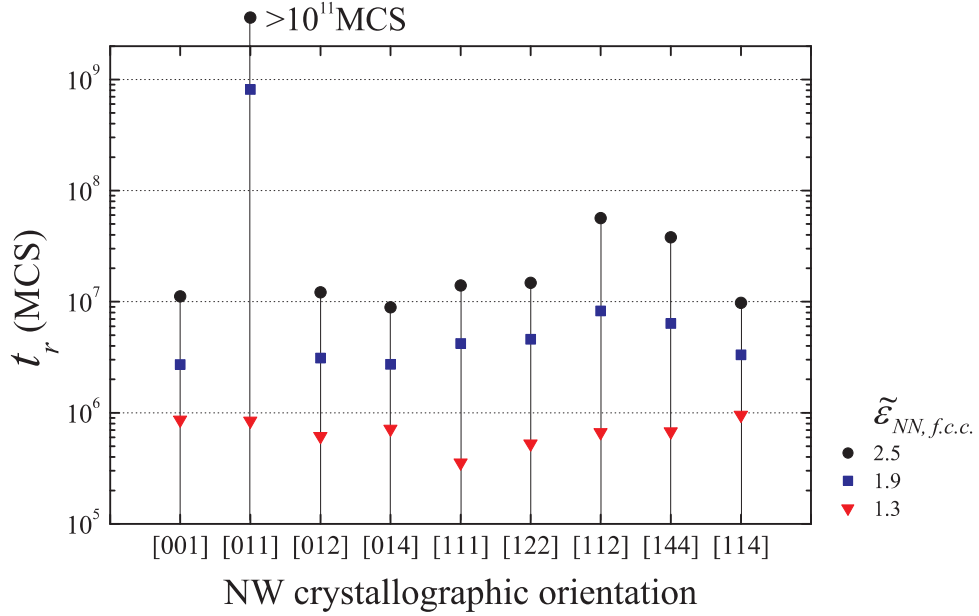
Figure (4.17): NW rupture time t_r for different low-index crystallographic orientations of f.c.c. NWs (R_0=8 a) at three characteristic temperatures assuming equal bond strength.

stable in the case of noticeable surface tension anisotropy (two confining {111}-facets); this is indeed the case in the low-T simulation.

According to the analytical treatment by Glaeser, not only the perturbation growth rate (expressed by t_r) but also the wavelength with maximum growth rate λ_m is influenced by surface tension anisotropy (cf. section 4.1): for confining facets with lowest surface tension λ_m ought to be considerable larger than for the isotropic case where $\lambda_{m,\mathrm{iso}} = \sqrt{2} \times 2\pi R_0$ (in the present cases: R_0=8 a, thus, $\lambda_{m,\mathrm{iso}}$=71 a). In the present context, the mean distance between the emerging NCs, μ_D, is a direct measure for

orientation	[001]	**[011]**	[012]	[014]	[111]	[122]	**[112]**	[144]	[114]
high-T	73 a	**90 a**	71 a	58 a	73 a	69 a	**89 a**	58 a	67 a
intermediate-T	64 a	**362 a**	63 a	65 a	55 a	76 a	**125 a**	83 a	67 a
low-T	64 a	**724 a**	63 a	58 a	73 a	76 a	**156 a**	97 a	60 a

Table (4.2): Mean NC distance μ_D of the forming NC chain during the Plateau-Rayleigh instability for different NW orientations and three characteristic temperatures (cf. Fig. 4.17).

λ_m; the corresponding values of μ_D are listed in Tab. 4.2. Accordingly, the two cases with confining {111}-facets (NWs with [011]- and [112]-orientation; bold typed) show a significant increase in μ_D with decreasing temperature, i.e. with increasing surface tension anisotropy, up to a factor of ten in the case of [011]-orientation. In the other cases the values of μ_D scatter homogeneously around $\lambda_{m,\text{iso}}$=71 a.

Most single-crystalline NW structures found in reality have main orientations with facets of lowest surface tension which is mostly due to the NW growth process [1, 230, 254]. In these cases, the temperature during the Plateau-Rayleigh instability acts as control parameter in view of the mean distance and consequently the mean size of the emerging NCs (volume conservation). This feature is particulary interesting in view of Plateau-Rayleigh instability based formation processes of functional NW chains (cf. section 4.6). In real experiments, however, the temperature-time-transition relation has strong impact on the practicality of a process [128], thus, the surface-tension-anisotropy-induced increase in μ_D and μ_V has upper limits since the process duration strongly increases as the temperature decreases (reduced kinetics).

Regarding fluctuations, the conducted lattice KMC simulations did not reveal any noticeable influence of the surface tension anisotropy on the regularity of the resulting NC chain, i.e. the relative standard deviation of NC volume and distance are in the same 10% to 20% range found earlier.

To summarize, the presented results demonstrate strong influence of surface tension anisotropy effects on the dynamics of the Plateau-Rayleigh instability of single-crystalline NWs. At low simulation temperature, facets with lowest surface tension exhibit stabilizing effects if they confine the NWs, i.e. if the NW main axis lies in the corresponding facet plane (negative $(\partial^2\gamma)/(\partial\psi^2)$; cf. section 4.1). In this connection it was found, that the wavelength with maximum growth rate can rise significantly (up to ten times) compared to the isotropic surface tension case which can be used as control parameter to adjust mean distance and mean volume of the resulting NCs. On the other hand, facets with lowest surface tension can lead to effects of "thermal grooving" if the NW main axis does not lie in the corresponding facet planes. Surface tension anisotropy effects do obviously not influence the regularity of the NC chain.

4.2.7   Perturbation Growth Rates

The dynamics of the Plateau-Rayleigh instability is determined by the surface perturbation growth rates. The LSA (cf. section 4.1) predicts that these rates scale inversely with the fourth power of the initial NW radius ($k_i \propto R_0^{-4}$; cf. Eqn. 4.17) under the assumption of a constant ratio between R_0 and the perturbation wavelength. In this connection, lattice KMC simulations have been conducted during which the rupture time t_r was measured as a function of R_0. t_r can be perceived as a reciprocal measure
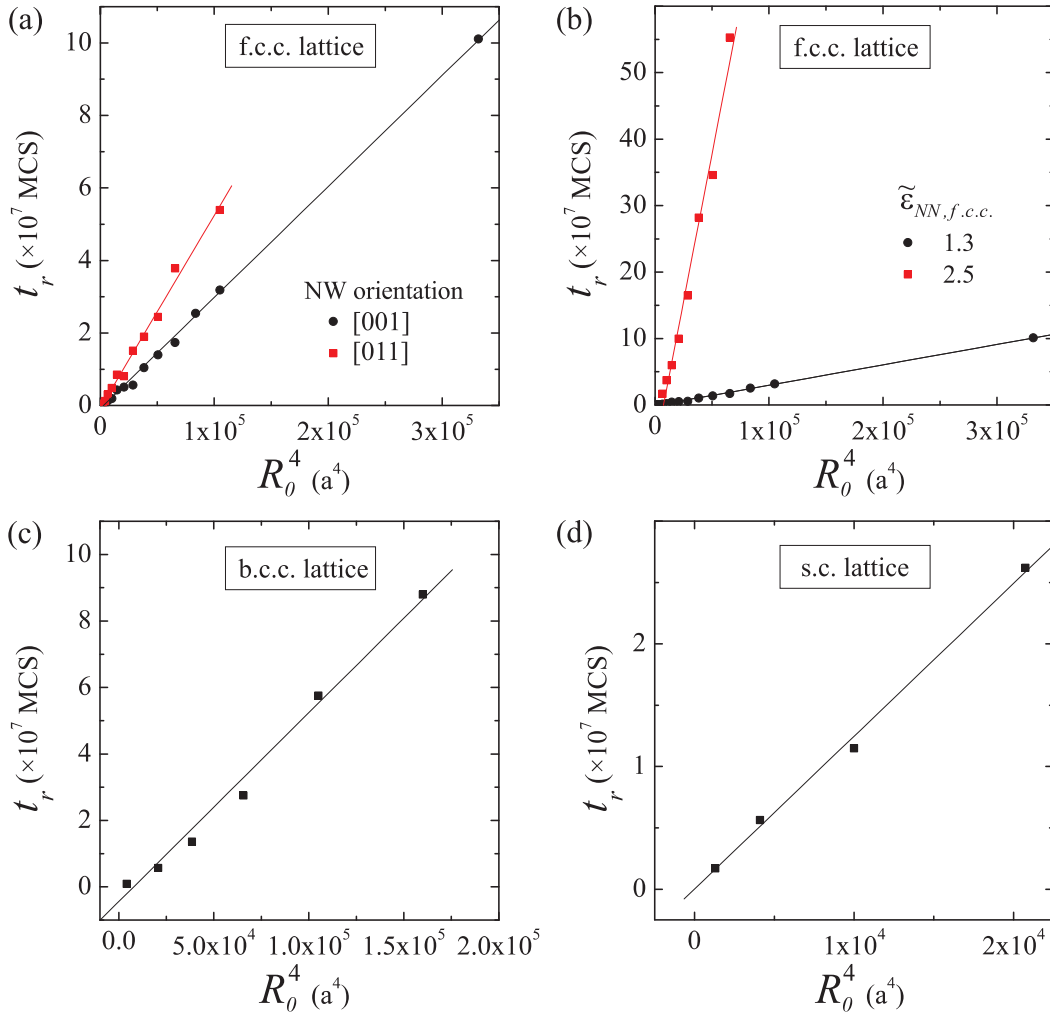
Figure (4.18): $t_r(R_0^4)$-plots which express that the perturbation growth speed scales linearly with the fourth power of the initial NW radius during the Plateau-Rayleigh instability: (a) f.c.c. NWs with different orientation ($\tilde{\varepsilon}_{NN,f.c.c.}$=1.3), (b) f.c.c. NWs at different temperature but equal orientation ([001]-oriented NWs), (c) b.c.c. NWs with [001]-orientation at $\tilde{\varepsilon}_{NN,b.c.c.}$=2.0, and (d) s.c. NWs with [001]-orientation at $\tilde{\varepsilon}_{NN,s.c.}$=2.0.

of the maximum growth rate in the system which corresponds to λ_m.

The prediction of the LSA on the scaling of t_r is nicely confirmed by lattice KMC simulations which can be seen in the $t_r(R_0^4)$-plots in Fig. 4.18 as the data points arrange along regression lines. The plots in Fig. 4.18 (a) show the results for [001]- and [110]-oriented f.c.c. NWs at equal temperature ($\tilde{\varepsilon}_{NN,f.c.c.}$=1.3). Apparently, the slope of the regression line in the case of [110]-orientation is 1.8-times larger than in the case of [001]-orientation ($R_0^4 k_{[110]}$=1.85 × 10^{-3} a^4/MCS; $R_0^4 k_{[001]}$=3.3 × 10^{-3} a^4/MCS), i.e. the perturbation with maximum growth rate grows faster for a [001]-oriented NWs than for a [110]-oriented one. This effect can be explained by the fact that the average ad-atom concentration on {111}-facets[6] is smaller compared to {100}-facets[7] ($B \propto c_s$; cf. Eqn. 4.15 and Fig. 2.19 for ρ=0).

Likewise, the growth of the perturbation with maximum growth rate scales with the temperature which can be seen in Fig. 4.18 (b) where the rupture times are plotted

---

[6]Dominant confining facets of [110]-oriented NWs (cf. Fig. 4.15).
[7]Dominant confining facets of [001]-oriented NWs (cf. Fig. 4.14).

for a high and a low temperature ($\tilde{\varepsilon}_{\text{high-}T}$=1.3 and $\tilde{\varepsilon}_{\text{low-}T}$=2.5) for a [001]-oriented NWs in each case. It stands to reason that the perturbation growth rate is lower for lower temperature because of the lower atomistic kinetics ($B \propto (c_s D_s)$, where c_s and D_s scale exponentially with T; cf. Eqn. 4.15).

Thus far, the perturbation growth of the Plateau-Rayleigh instability has been examined only for f.c.c. NWs. The plots in Figs. 4.18 (c) and (d) show the results of respective b.c.c. and s.c. lattice KMC simulations at constant temperature for [001]-oriented NWs in each case ($\tilde{\varepsilon}_{NN,b.c.c.}$=2.0; $\tilde{\varepsilon}_{NN,s.c.}$=2.0). Accordingly, both lattice types give the NW stability scaling behavior, i.e. $k_i \propto R_0^{-4}$.

In summary, lattice KMC simulations focusing on the rupture time of Plateau-Rayleigh instability for different lattice types, crystal orientations, and temperatures meet one of the important predictions of the LSA (cf. section 4.1), namely, that the growth rate of the perturbation with maximum growth rate scales reciprocally with the fourth power of the initial NW radius.

4.2.8   Role of a Supporting Substrate

In order to study the free capillarity-driven evolution of a NW structure all external forces and fields have to be eliminated which is practically impossible in real experiments. Particularly, if the NW structure comes close to the stage of fragmentation a supporting matrix is required in order to keep the position of the forming NCs. Of course, one exception would be to carry out the experiments under microgravity where weightlessness is provided which has been done for the examination of capillary phenomena in liquid systems [181].

In this regard, the role of the interaction between a single-crystalline NW structure and the supporting matrix comes into focus as it may influence the dynamics of the Plateau-Rayleigh instability (breaking of the axisymmetry of the surface perturbations). In section 2.7 it has been shown that the interaction energy ε_{AB} between the NW and the substrate determines the wetting characteristics. In Fig. 4.19 (a), two relevant cases are compared: $\tilde{\varepsilon}_{\text{AB}}$=0 and $\tilde{\varepsilon}_{\text{AA}} \gg \tilde{\varepsilon}_{\text{AB}}$>0 with $\tilde{\varepsilon}_{\text{AB}}$:$\tilde{\varepsilon}_{\text{AA}}$=0.13. Starting from a smooth cylinder (R_0=12 a; L=2^{10} a; $\tilde{\varepsilon}_{\text{AA}}$=1.5; [001]-oriented; f.c.c. lattice) both scenarios lead to the disintegration of the structure and to the formation of a NC chain with the usual irregularity caused by thermal fluctuations. The corresponding specific internal energy development is plotted in Fig. 4.19 (b) which shows that in the case of wetting the Plateau-Rayleigh instability is retarded by a factor of 1.5 (rupture time) compared to the non-wetting case. This is due to the fact that the driving force (surface free energy gain) is smaller in the case of wetting which can be nicely seen comparing the $u(t)$'s in terms of their respective slopes.

For attractive NW-substrate interactions with $\tilde{\varepsilon}_{\text{AA}} \approx \tilde{\varepsilon}_{\text{AB}}$ total wetting can be anticipated. This scenario does not correspond to the concept of the Plateau-Rayleigh instability since the resulting structure would strongly deviate from a cylindrical one. Therefore, the above discussion for $\tilde{\varepsilon}_{\text{AA}} \gg \tilde{\varepsilon}_{\text{AB}}$ is fully sufficient for most of the practical scenarios.

In comparison to real systems, the above lattice KMC simulation of a supported NW structure includes an idealization, namely a homogeneous contact area between the substrate and the NW. The contact area in real systems, on the contrary, is usually inhomogeneous (roughness, chemical contamination etc.) so that the interaction between
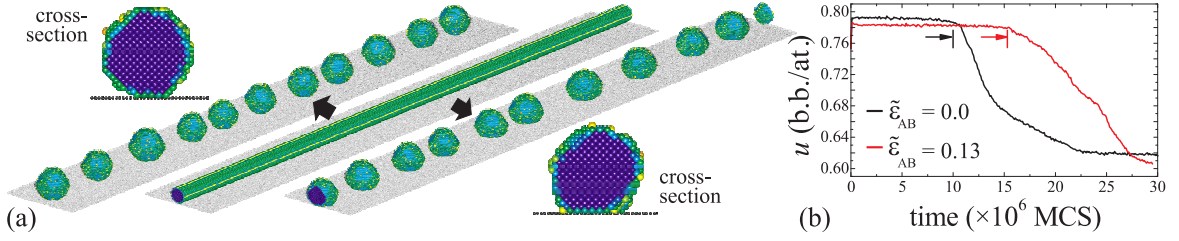
Figure (4.19): (a) Final states of the Plateau-Rayleigh instability of cylindrical structures supported by a substrate for a non-wetting case ($\tilde{\varepsilon}_{AB}=0$; l.h.s.) and a small attractive interaction ($\tilde{\varepsilon}_{AB}=0.2$; $\tilde{\varepsilon}_{AA}=1.5$; r.h.s.). (b) Corresponding development of the specific internal energy $u=u(t)$ indicating that an attractive NW-substrate interaction causes a retardation of the Plateau-Rayleigh instability.

NW and substrate is expected to fluctuate spatially. These fluctuations directly lead to a spatially inhomogeneous shape evolution which can be an explanation for observed irregularities in real systems (cf. Fig. 1.1 (a) where the Plateau-Rayleigh instability is depicted for a Cu NW supported by SiO_2).

4.3 Shape Evolution of Finite Nanowires (Nanorods)

The Plateau-Rayleigh instability of cylindrical structures with finite length (=rods) differs from that of infinite cylinders to a considerable degree. Finite cylinders deserve, therefore, closer consideration since in realistic experiments one often deals with finite rather than infinite structures (cf. the discussion on nanofluidic channel fabrication using finite cylindrical pores in section 4.6).

Unlike infinite cylinders, rods have ends which are surface regions of higher chemical potential than the surface of the cylinder wall in-between[8]. Consequently, ad-atoms migrate along a chemical potential gradient from the ends towards the center of the rod. Naturally, the cylindrical regions of the rod, which are far away from the ends, evolve according to the original Plateau-Rayleigh instability, i.e. axisymmetric surface undulations can develop there by thermal fluctuations which finally cause the rupture of the structure at the undulation necks. These two processes: ad-atom diffusion from the ends in inward direction and the undulation build-up on the cylindric surface superimpose.

The diffusion of ad-atoms away from the ends leads to a swelling of the ends ("bulging effect"; cf. also the rims of the dewetting stripe in Fig. 4.37) which goes along with their recession; in other words, the rod shortens. These swollen ends are sources of capillary surface waves which travel in inward direction along the surface of the rod exciting perturbations on the cylinder surface. The range of these capillary waves scales with the surface diffusion length $x_s \propto \sqrt{D_s t}$ (Einstein relation). The perturbation mode selection is advanced in the regions close to the ends of the rod. Consequently, the evolution of a rod is locally different. The ends of the rod evolve faster than the center where the usual perturbation mode selection according to the Plateau-Rayleigh instability takes place with the perturbation growth rates discussed above (cf. section 4.1 and subsection 4.2.7).

---

[8]For ends with hemispherical shape the surface curvature is that of a sphere with $K = 2/R_0$, thus, double the curvature of the cylinder wall (cf. Eqn. 1.3).
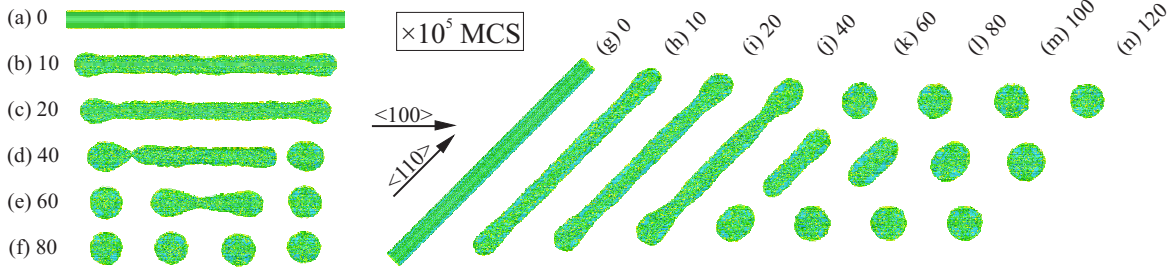
Figure (4.20): Series of lattice KMC micrographs (longitudinal view) showing the reaction pathways on the capillary instability of finite cylinders with (a-f) [001-] and (g-n) [011]-orientation (f.c.c. lattice; L_0=400 a; R_0=12 a; $\tilde{\varepsilon}_{NN,f.c.c.}$=1.3).

In Figs. 4.20 (a-f), an example of the capillarity-driven evolution of a [001]-oriented rod is given (f.c.c. lattice; L_0=400 a; R_0=12 a; $\tilde{\varepsilon}_{NN,f.c.c.}$=1.3). Accordingly, the ends of the rod swell and cause the advanced rupture of the structure behind the swelling. Thus, two new ends are formed in the remaining part of the rod and the process is repeated. Apparently, the disintegration of the rod structure takes place in a cascade-like manner starting from the periphery towards the center. Just in the case of $L_0 \gg R_0$ (results not shown) the central region of the rod can independently develop local axisymmetric surface perturbations that cause the rupture of the rod before the inward-moving ends arrive there.

Like for infinite NW structures surface tension anisotropy effects play a role in the capillary instability of rods. Compared to the former case, Figs. 4.20 (g-n) show the evolution of a [011]-oriented f.c.c. rod. The other geometrical and physical parameters are exactly the same as in the case of [001]-orientation. Obviously, the swelling of the ends and their pinch-off from the structure proceed qualitatively in the same manner. However, the [011]-oriented rod shrinks stronger so that the peripheric NCs become larger. Earlier it has been demonstrated that the perturbation wavelength with maximum growth rate λ_m depends on the surface free energy. It was found that for the f.c.c. lattice {111}-facets exhibit the largest λ_m. Since [011]-oriented rods are predominantly confined by {111}-facets (cf. Fig. 4.15) it stands to reason that swelling of the end is more elongated than in the case of [001]-orientation. The remaining central part of the rod structure is consequently shorter; it does not disintegrate further but spheroidizes into a single NCs.

To illustrate the reduction of the specific internal energy u and thereby the relaxation towards equilibrium during the capillary instability of a rod, in Fig. 4.21 $u(t)$ is plotted for the two examples shown in Fig. 4.20 (red and blue graph, respectively). These $u(t)$-plots can be compared with the equivalent cases of the capillary instability of infinite cylindrical structures under the same process conditions (f.c.c. lattice; R_0=12 a; $\tilde{\varepsilon}_{NN,f.c.c.}$=1.3). The comparison reveals that the first stage of evolution of rods does not show any plateau in $u(t)$ which appears, however, in the cases of infinite NWs indicating the perturbation build-up process (cf. Fig. 4.10 (a)), i.e. the swelling of the ends of the rod goes along directly with a substantial reduction of internal energy. The moment when the first pinch-off occurs (=rupture time) is in all cases indicated by a discontinuity in $u(t)$. For both orientations, the rod disintegrates earlier than the infinite counterpart which reflects the advanced evolution in the peripheric regions of the rod. The second stage of further fragmentation of the rods is expressed by a cascade-like decrease of u. The simple reason why the system of the [011]-oriented rod
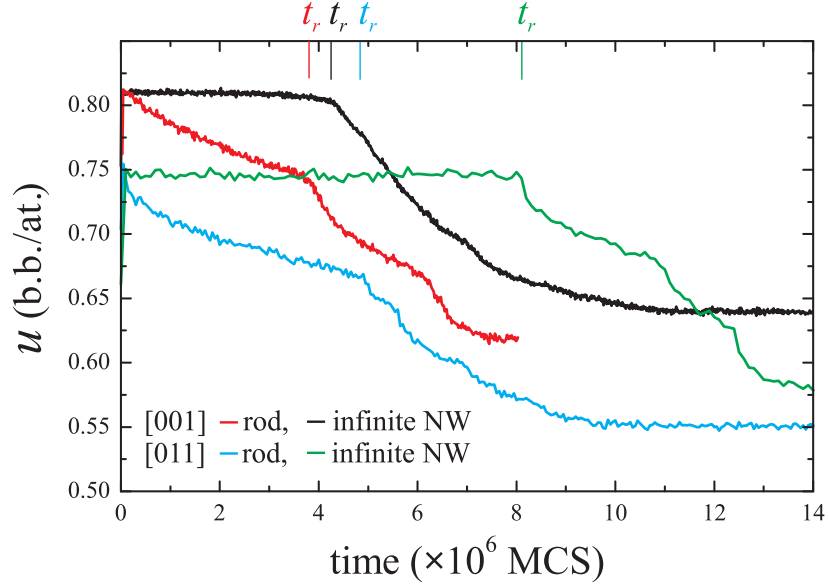
Figure (4.21): Development of the specific internal energy u during the capillarity-driven instability of finite and infinite cylindrical structures and for different crystallographic orientations (f.c.c. lattice). The corresponding lattice KMC micrographs are shown in Fig. 4.20).
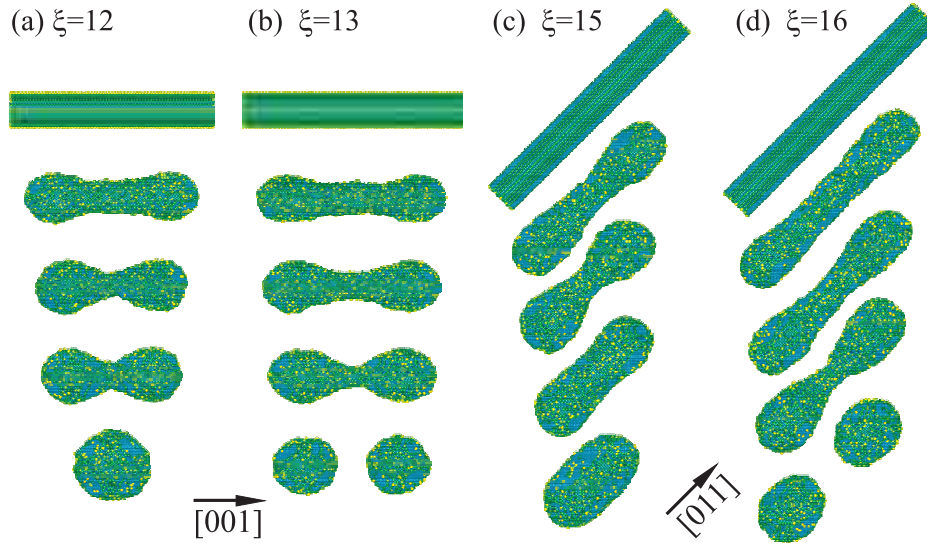
Figure (4.22): Series of lattice KMC micrographs (longitudinal view) demonstrating the existence of a critical length-to-radius ratio ξ_c which determines whether a finite cylinder spheroidizes or disintegrates under the capillary force (in all cases: f.c.c. lattice; $R_0 = 12$ a; $\tilde{\varepsilon}_{NN,f.c.c.} = 1.3$).

reaches a significantly lower energetic state than the [001]-counterpart lies in the fact that the former transforms into three NCs, the latter into four.

A further issue regarding the capillary instability of finite cylinders is the ratio between initial length and radius,

$$\xi = L/R \ , \tag{4.27}$$

by which two distinct reaction pathways are anticipated:

1. spheroidization into a single NCs if $\xi < \xi_c$ or

2. disintegration (via Plateau-Rayleigh instability) into multiple NCs if $\xi > \xi_c$,

where ξ_c denotes a critical value. In a first consideration one expects that ξ_c is in the range of $\lambda_m = 2\pi R_0\sqrt{2}$ resulting from the LSA of the Plateau-Rayleigh instability (for isotropic surface tension), i.e. $\xi_c = \lambda_m/R_0 = 2\pi\sqrt{2} \approx 8.88$. However, the lattice KMC simulations shown in Fig. 4.22 reveal that ξ_c is considerably larger. In Figs. 4.22 (a) and (b), the capillarity-induced transformation of [001]-oriented rods (f.c.c. lattice; R_0=12 a; $\tilde{\varepsilon}_{NN,f.c.c.}$=1.3) is shown where surface tension anisotropy effects ought to be insignificant (cf. subsection 4.2.6). Here, ξ_c lies in-between 12 and 13, i.e. $\xi_c \approx \frac{3}{2}\lambda_m/R_0$ for isotropic surface tension. As λ_m increases if the confining facets are those of lowest surface tension (cf. Eqn. 4.25) a larger value for ξ_c is anticipated for [011]-oriented rods which is confirmed by Figs. 4.22 (c) and (d). For lower temperature (higher surface tension anisotropy) this effect becomes stronger, i.e. [011]-oriented rods with very high aspect ratio can shrink and spheroidize into a single NCs (results not shown).

In the case of pairs of noble metal NCs (cf. Figs. 4.22 (b) and (d)) their inter-particle distance can be measured via the distance dependence of their plasmon coupling [255, 256] which in return opens ways and means to control in-situ the progress of the capillarity-driven instability of nanorods.

4.4 Shape Evolution of Tubular Structures

4.4.1 Surface vs. Volume Diffusion Regime

In subsection 2.6.2 it has been demonstrated that hollow spherical particles shrink due to outward vacancy diffusion (Gibbs-Thomson effect). A similar scenario is given in the case of tubes which can be perceived as hollow cylindrical pores which can be fabricated for instance using the Kirkendall effect [257]. Again, due to the curvature difference between inner surface (concave) and the outer surface (convex) vacancies diffuse outwards in radial direction, thus, causing the tube to shrink and leaving a solid cylinder behind. However, there is a second reaction pathway possible, namely the disintegration of the hollow core into a chain of voids according to the Plateau-Rayleigh instability (pea-pod-like structure). The weighting factor between these two reaction pathways is the dominance of the respective diffusion channels, i.e. the dominance of either volume diffusion or surface diffusion.

In Fig. 4.23, KMC simulation results are shown for the two respective scenarios ($R_{0,\text{out}} = 20$ a; $R_{0,\text{in}} = 7a$; $\tilde{\varepsilon}_{NN,f.c.c.} = 1.2$). Only for better visualization the tube is cut longitudinally into two halves which are opened up in order to reveal the interior. On the left hand side (cf. Figs. 4.23 (a-d)) the tube evolution is governed by volume diffusion (suppression of surface diffusion). The hollow fiber core shrinks until it breaks into tiny spherical residues which instantaneously evaporate (cf. Fig. 4.23 (c)); this breakage is due to the inhomogeneities in the outward diffusion of vacancies and has nothing to do with a Plateau-Rayleigh instability effect. On the right hand side (cf. Figs. 4.23 (e-h)) surface diffusion is promoted. Obviously, the Plateau-Rayleigh instability of the hollow core leads to the formation of a chain of voids. Experimentally the dominance of one diffusion channel over the other could be adjusted for example by the processing atmosphere which can accelerate (reducing ambient) or retard (oxidizing ambient) surface diffusion. Not shown in Fig. 4.23 is the later stage of evolution where the Plateau-Rayleigh instability will cause the undulation of the outer surface as well. For Figs. 4.23 (a-d)), a common Plateau-Rayleigh instability is anticipated. However, for
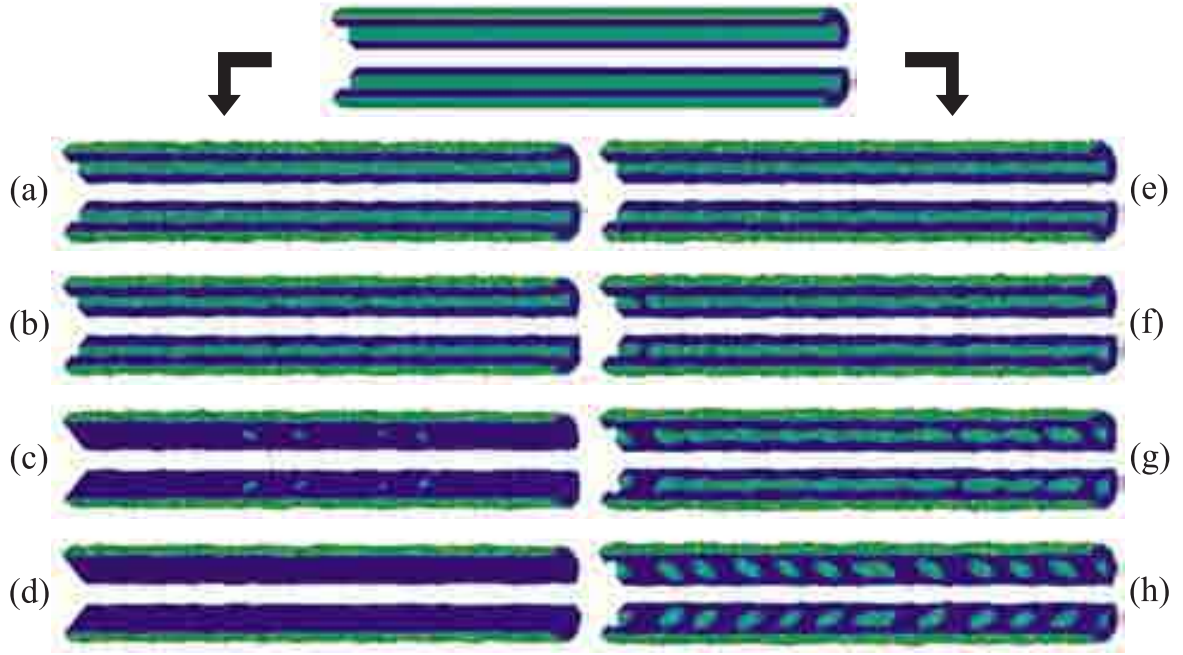
Figure (4.23): Two possible pathways of the evolution of a hollow [001]-oriented cylinder (tube; $R_{0,\text{out}} = 20\,a$; $R_{0,\text{in}} = 7a$; $\tilde{\varepsilon}_{NN,f.c.c.} = 1.2$): (a-d) volume diffusion dominated evolution; (e-h) surface diffusion dominated evolution ((a, e) 10×10^4 MCS; (b, f) 20×10^4 MCS; (c, g) 35×10^4 MCS; (d, h) 60×10^4 MCS).

Figs. 4.23 (e-h) disturbances are expected, particularly when undulation necks appear at positions where a void exists directly beneath the neck. Then, an accelerated rupture occurs. On the other hand, if a void is positioned directly in-between two undulation necks a spherical particle can form during the fragmentation stage with a hollow core inside.

4.4.2 Draining of Metal-Filled Tubes

The draining of carbon tubes (several micrometers long and some tens of nanometers in diameter) which have a cylindrical single-crystalline Cu filling (core) has been observed very recently during in-situ TEM investigations at elevated temperatures (600 °C) [258]. The physical mechanism of this puzzling phenomenon is not yet understood. The capillary force is suggested here as driving principle of this solid-state process.

CNT-like tubes have been produced at the GSI in Darmstadt by etching the tracks of the swift-heavy-ion-irradiated polymer film that has a content of carbon, thus, leaving isolated cylindrical pores with carbonized walls (several nanometers thick) behind in the polymer film. After etching these pores have been filled electrochemically with Cu forming single-crystalline cores [259]. Thereafter, the remaining polymer is etched away and Cu-filled CNT-like tubes are left behind. During in-situ TEM investigations at elevated temperatures (600 °C) it was found that the Cu pours out at the open end of the tube forming Cu droplets there. Throughout this process the Cu remained crystalline [258].

Lattice KMC simulations demonstrate qualitatively the same behavior indicating that a diffusion process is responsible for the draining of the tube. In this respect, in Fig. 4.24 a series of configurations is presented where a cylindrical structure is geometri-
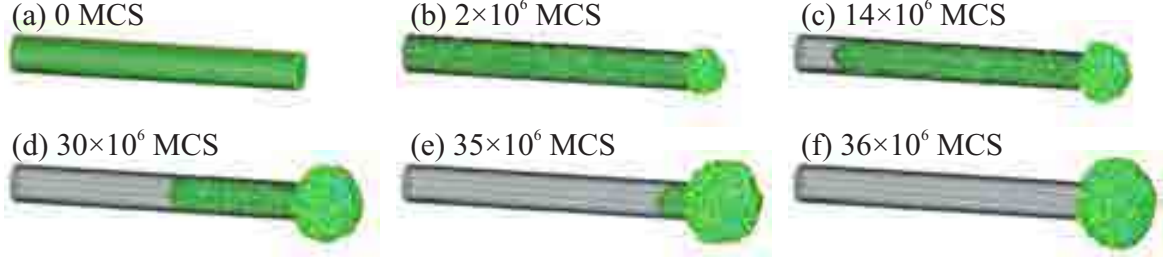
Figure (4.24): Capillarity-induced draining of a filled tube which is open at one end (R_t=10 a; l_0=180 a; $\tilde{\varepsilon}_{NN,f.c.c.}$=1.0).
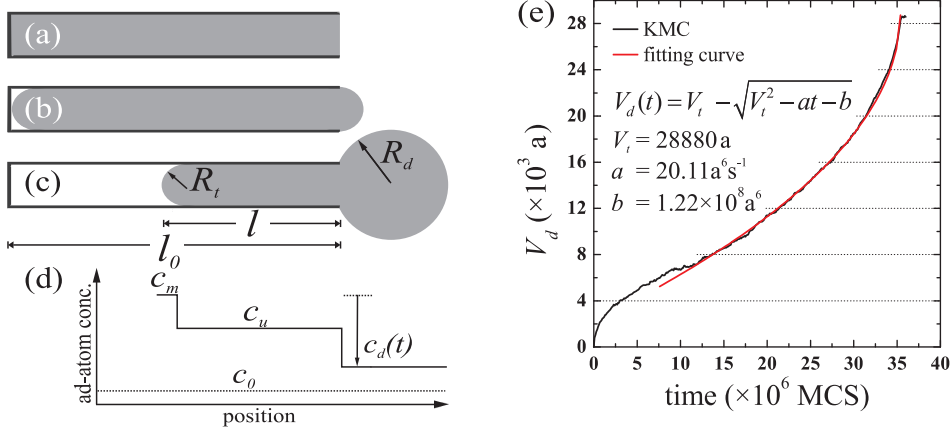
Figure (4.25): (a-d) A schematic representation of the capillarity-induced draining of a filled tube and definition of the geometrical parameters. (e) Measured and fitted droplet volume $V_d(t)$ of the KMC simulation shown in Fig. 4.24.

cally confined in a tube that is open at one end ($R_t = 10$ a; $l_0 = 180$ a; $\tilde{\varepsilon}_{NN,f.c.c.} = 1.0$). It is assumed that there is no attractive interaction between the filling and the tube which would approximately refer to the Cu-C interaction in the present context. During the first stage of evolution the filling swells out at the open end forming a meniscus there which grows forming a droplet. As evolution proceeds the entire material diffuses out of the tube and a single droplet, in which all material cumulates, is left behind at the open end of the tube. If both ends of the tube were open (symmetric system) the material would still pour out on one side due to a fluctuation-induced symmetry breaking in the first stage of evolution.

In view of solid-state capillarity, this draining process can be analytically described as follows (cf. Fig. 4.25 (a-d); [113]): After a starting stage, the curvature of the inner meniscus is higher than that of the droplet causing a gradient of chemical potential (ad-atom concentration) from the inside of the tube to the outside initiating a diffusive flux j of ad-atoms towards the open end (cf. Eqn. 1.6). The diffusive flux shortens the length of the remaining filling inside the tube; because of volume conservation the droplet volume grows (cf. Fig. 4.25 (c)):

$$j \, dt = -\pi \rho R_t^2 \, dl = \rho \, dV_d = 4\pi \rho R_d^2 \, dR_d \ . \tag{4.28}$$

According to Fick's law the diffusion flux reads

$$j = 2\pi R_t D \frac{(c_m - c_d)}{l} = 2\pi R_t D \times \frac{c_0(1 + R_c/R_t) - c_0(1 + R_c/R_d)}{l} \ . \tag{4.29}$$

where the linearized Gibbs-Thomson equation was implemented (c_0 is the ad-atom

concentration on a planar surface; R_c is the capillary length). The length of the filling is correlated with the volume of the droplet:

$$\frac{4\pi}{3}R_d^3 = V_d = \pi R_t^2(l_o - l) \ . \tag{4.30}$$

From Eqn. 4.28, Eqn. 4.29, and Eqn. 4.30 follows

$$\frac{\mathrm{d}V_d}{\mathrm{d}t} = j/\rho \tag{4.31a}$$

$$= 2\pi R_t R_c Dc_0 \left(1 - R_t/R_D\right) / \left(\rho l R_t\right) \tag{4.31b}$$

$$= \frac{2\pi R_c Dc_0}{\rho} \left(1 - R_t/R_D\right) / \left(l_0 - V_d/\left(\pi R_t^2\right)\right) \tag{4.31c}$$

$$= \frac{2\pi^2 R_t^2 R_c Dc_0}{\rho} \left(1 - R_t/R_D\right) / \left(\pi R_t^2 l_0 - V_d\right) \tag{4.31d}$$

$$= \frac{2\pi V_t R_c Dc_0}{l_0 \rho} \left(1 - R_t/\sqrt[3]{3V_d/(4\pi)}\right) / \left(V_t - V_d\right) \tag{4.31e}$$

$$= \frac{2\pi V_t R_c DC_0}{l_0 \rho} \left(1 - \sqrt[3]{4\pi R_t^3/3}/\sqrt[3]{V_d}\right) / \left(V_t - V_d\right) \tag{4.31f}$$

$$= \frac{2\pi V_t R_c Dc_0}{l_0 \rho} \left(1 - \sqrt[3]{V_m/V_d}\right) / \left(V_t - V_d\right) \tag{4.31g}$$

After a starting stage: $V_d \gg V_m$; $\left(V_m = \frac{4\pi R_t^3}{3}\right)$, thus, the cube root can be neglected. Summarizing material constants $F = R_c Dc_0/\rho$ and geometrical parameters $G = 4\pi V_t/l_0$ one obtains with $a = FG$:

$$\frac{\mathrm{d}V_d}{\mathrm{d}t} = \frac{a}{2\sqrt{V_t - V_d}} \ , \tag{4.32}$$

which has the solution

$$V_d(t) = V_t - \sqrt{V_t^2 - at - b} \ , \tag{4.33}$$

where b is the integration constant. In Fig. 4.25 (e), $V_d(t)$ of the KMC simulation depicted in Fig. 4.24 is plotted. Eqn. 4.33 is fitted to the measured curve of $V_d(t)$ which results in a very good agreement.

In order to prove or disprove the mechanism suggested here, thorough in-situ TEM investigations on the draining of metal filled tubes are required monitoring the droplet volume growth meticulously.

4.5 Shape Evolution of a Torus: Reaction Pathway Rivalry

The capillarity-driven evolution of a torus is exciting because two processes of surface free energy minimization compete with each other, thus, distinct reaction pathways can be anticipated. A torus can transform on the one hand into a ring of several particles via a Plateau-Rayleigh-like disintegration process [260] and on the other hand into a

single central particle by an inward shrinking process. The control parameter of this process rivalry is the ratio between the two characteristic radii $\rho = R/r$ (cf. Fig. 4.26).

A torus can be perceived as a finite cylinder whose ends are connected with each other. Its spatial parameterization is given by

$$x = (R + r\cos\phi)\cos\psi \tag{4.34a}$$
$$y = (R + r\cos\phi)\sin\psi \tag{4.34b}$$
$$z = r\sin\phi \,, \tag{4.34c}$$

where R and r are the major and the minor radius ($R > r$); ϕ and ψ are the polar and the azimuthal angle, respectively (cf. Fig. 4.26). Its overall surface area reads $S_t = 4\pi^2 Rr$ and its volume is given by $V_t = 2\pi^2 Rr^2$ [261].

From the viewpoint of surface curvature, toroidal structures are very complex. The principal curvatures in an arbitrary point N on the torus surface are given by [262]

$$k_1 = \frac{1}{r} \quad \text{and} \quad k_2 = \frac{\cos\phi}{R + r\cos\phi} \,. \tag{4.35}$$

Thus, the mean curvature $K = (k_1 + k_2)/2$ reads

$$K = \frac{R + 2r\cos\phi}{2r\left(R + r\cos\phi\right)} \,, \tag{4.36}$$

whereas the Gaussian curvature $G = k_1 k_2$ is given by

$$G = \frac{\cos\phi}{r\left(R + r\cos\phi\right)} \,. \tag{4.37}$$

Consequently, there exists a gradient of curvature from the outer equator ($\phi = 0$; $G > 0$) to the inner equator ($\phi = \pi$; $G < 0$) of the torus which gives rise to a gradient of chemical potential, e.g. a gradient of ad-atom concentration from the outside to the inside of the torus. This concentration gradient initiates a material flux $j_\phi \propto \nabla_s K$
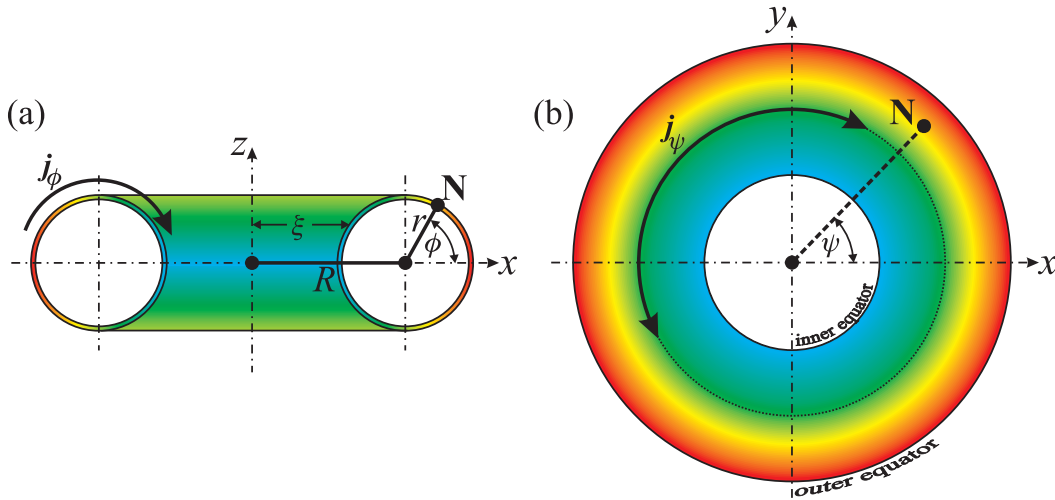
Figure (4.26):   A schematic representation of a torus: (a) cross-section view and (b) top view. The color scale from red to blue indicates the Gaussian curvature of the torus from positive (red) to negative (blue) values.
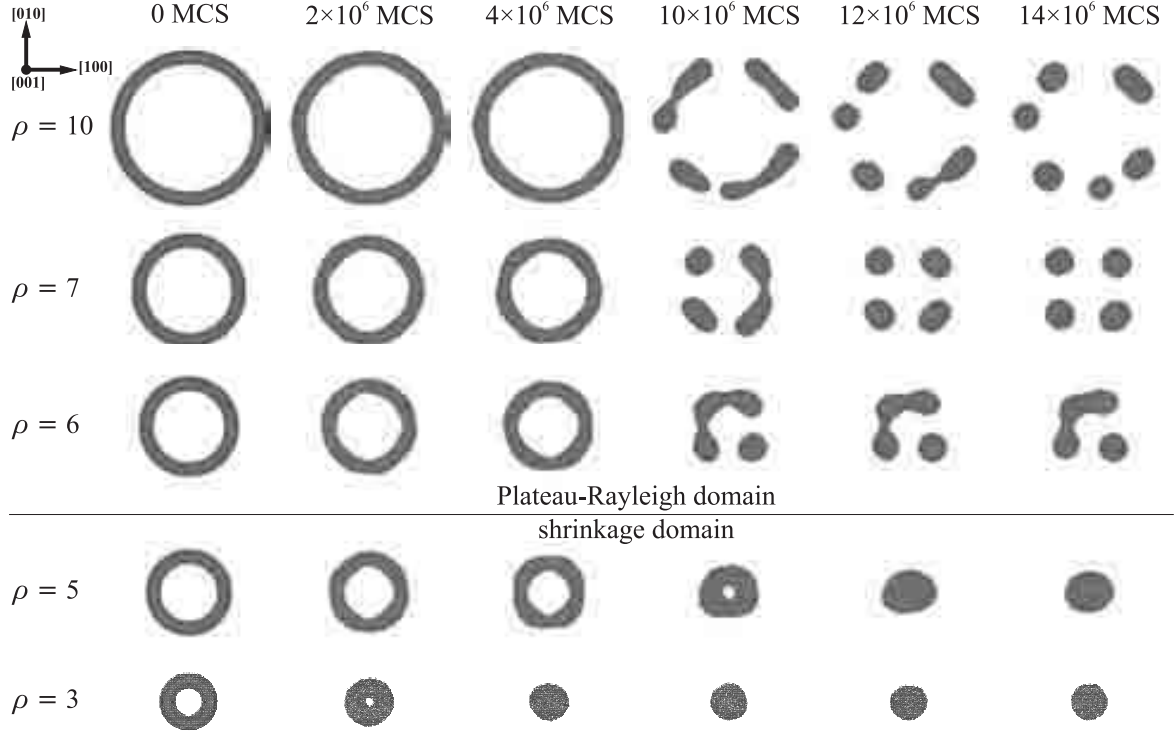
Figure (4.27): Reaction pathway matrix of the evolution of single-crystalline tori with different ratios $\rho = R/r$ ($\tilde{\varepsilon}_{NN,f.c.c.}$=1.3; r=12 a).

which causes the torus to shrink (cf. Fig. 4.26 (a)). For small ρ this radial shrinkage is the dominating process of the free evolution of a toroidal structure. There is a second process, however, which leads to the build-up of thickness undulations along the longitudinal direction of the torus. Thus, in the spirit of the Plateau-Rayleigh instability, a material flux j_ψ (cf. Fig. 4.26 (b)) will lead to the formation of an annular chain of particles. For large ρ, this process dominates the evolution of the torus. The limit $\rho = \infty$ would result in the classical Plateau-Rayleigh instability.

Apparently, the capillarity-induced evolution of a torus is complex which makes an analytical description of the evolution dynamics in the spirit of a LSA very difficult, particulary for the cases where both processes participate noticeably in the evolution. Again, the lattice KMC method provides rather simple ways and means to tackle this issue. In Fig. 4.27, the evolution of tori of different ρ-values is presented (reaction pathway phase diagram). Accordingly, for $\rho \leq 5$ the radial shrinkage process dominates, whereas for $\rho \geq 6$ the Plateau-Rayleigh instability governs the evolution. The "phase boundary" of these two domains is therefore in the interval $5 < \rho < 6$.

Due to the underlying lattice (single-crystalline torus) faceting effects ("thermal grooving") occur which can lead to regular particle positions in the Plateau-Rayleigh domain. Here, a f.c.c. lattice was considered where {111}-facets "cut" the ring regularly (cf. subsection 4.2.6). The case $\rho = 7$ shows in this regard a very regular arrangement where the resulting NCs form the corners of a square. For larger ρ this regularity is lost. This particular feature of the torus instability could be of importance for the self-organized formation of regular particle arrays, e.g. for the fabrication of meta-materials, particularly of 4-cut split-ring resonators [263, 264].

Toroidal structures can be achieved in a capillarity-driven dewetting process of pre-structured ultra-thin films (combined "top-down" and "bottom-up" approach). In
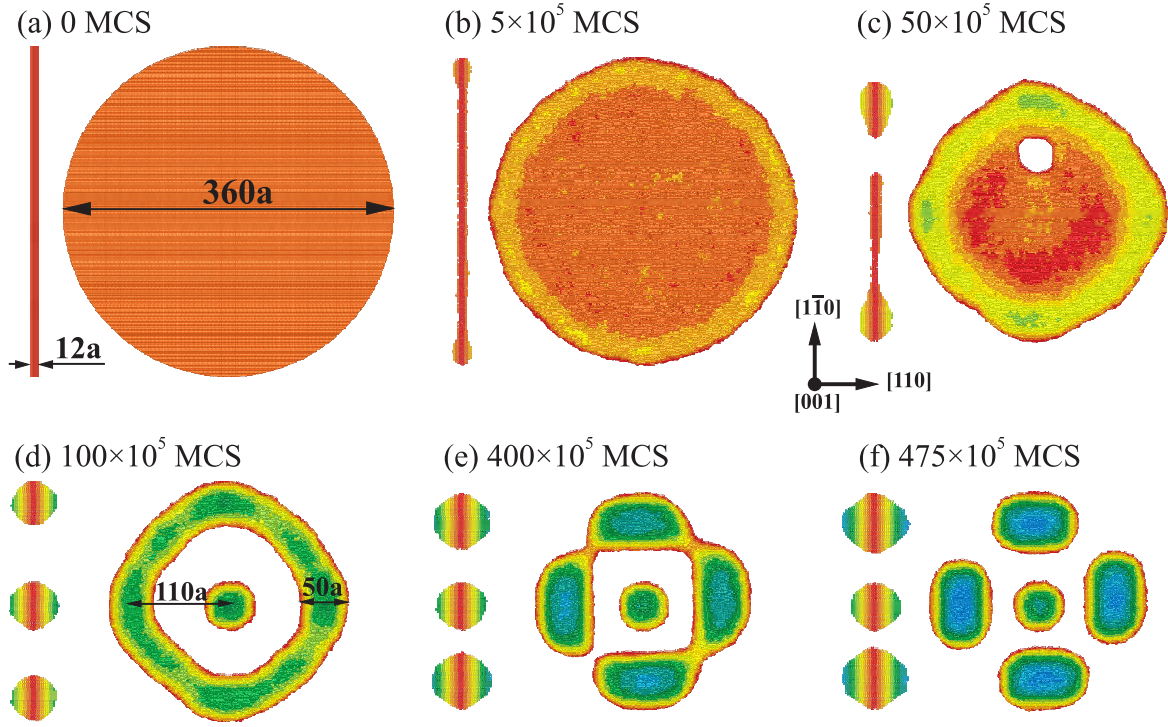
Figure (4.28): (a-d) Capillary-driven transformation of an ultra-thin single-crystalline circular disc (f.c.c. lattice) into a toroidal structure with a spherical particle in the center (l.h.s thin vertical cross section; r.h.s. top view; $\tilde{\varepsilon}_{NN,f.c.c.}=1.3$). (e, f) The system further evolves into a regular pattern of clusters. The colors indicate the surface height profile (red = center of the disc; blue = topmost atoms of the finial state).

this regard, Fig. 4.28 shows a picture series of the reaction pathway of a circular disc which transforms under the surface-diffusion-mediated capillary force into a torus with a single NC at its center (cf. Fig. 4.28 (d)). There is no substrate considered here which is a rough simplification of the dewetting of supported films. Nonetheless, in the first stage of evolution the edges of the disc swell (= rim formation; cf. Fig. 4.28 (b)), i.e. material diffuses in the inward-direction. The surface region where the swollen rim goes over to the flat surface in the center of the disc becomes concave, consequently, the ad-atom concentration becomes minimal there. The resulting ad-atom current is directed toward this concave region, thus, ad-atoms from the planar surface of the disc migrate in outward radial direction so that the thickness of the disc, particularly close to the rim, decreases. Consequently, the disc breaks up closely behind the rim (cf. Fig. 4.28 (c)), and the remaining material in the central region of the former disc forms a spherical agglomerate (cf. Fig. 4.28 (d)). At this stage, the swollen rim has transferred into a toroidal structure which evolves further according to the scenarios outlined above. In the present case the ratio between the main and the minor radius of the torus is large enough to allow the further disintegration of the torus according to the Plateau-Rayleigh instability, i.e. a ring of NCs finally appears with a single NC at the ring's center (cf. Fig. 4.28 (f)). Obviously, the emerging ring of NCs appears to be regular which is due to surface tension anisotropy effects discussed above ({111}-facets cut the f.c.c. torus regularly along the [011]-directions; cf. Fig. 4.28 (e)).

4.6 Self-Organized Formation of Functional Nanostructures

Thus far, the capillary instability of nanostructures has been discussed from a fundamental point of view. Now, this basic considerations are going to be extended into the technological "environment". For various cases it will be discussed how the capillary instability of nanostructures can be employed for the self-organized formation and modification of functional structures.

4.6.1 Fabrication of Nanofluidic Channel Networks

In recent years, "lab-on-a-chip" systems have attracted great attention in materials science. Basic building blocks of such high-throughput systems are miniaturized fluidic channels and channel networks for the fabrication of which complex processing steps are required [265, 266]. In this regard a rather simple fabrication method is being portrayed to generate channels and channel networks embedded in the single-crystalline matrix using capillarity-based self-organization.

Lattice KMC simulations on the self-organized fabrication of nanofluidic channel networks which are fully embedded in a single-crystalline matrix have been motivated by the ESS technique that has been recently developed by Japanese scientists aiming at SON structures which are an alternative for SOI in view of advanced CMOS technology [2, 55, 267]. Fabricating nanofluidic channels embedded in c-Si is the key to implement flow control, manipulation and/or analysis of fluids into electronic circuitry with a large-scale integration density (integrated nanofluidic solutions) [268, 269, 270].

The SON technique can be briefly summarized [55]: At first, regular arrays of cylindrical trenches are etched into (001)-Si. The trenches are up to several micrometer in depth and some hundred nanometers in diameter; they represent inverse cylinders of finite length (semi-infinite cylindrical pore), thus, they are subject to the Plateau-Rayleigh instability. During a thermal process at elevated temperature (900-1100 °C) for several minutes in a hydrogen atmosphere (i.e. reducing ambient which promotes surface diffusion) these trenches disintegrate into chains of spherical voids (ESS). For a defined ratio between trench length and diameter only one spherical void is obtained. If neighboring trenches are in close proximity, the resulting voids can come in contact and thereby merge forming a connected buried ESS layer (cf. Fig. 7 in Ref. [2]). However, if only a single row of trenches is considered buried ESS channels can be obtained. In the following this SON technique is reproduced by means of the lattice KMC method[9]. Further simulations are presented which predict reaction pathways describing the connection of single channels to form networks and the formation of in- and outlets to the wafer surface.

At first, the instability of a single trench is considered which is a basic building block in the nanofluidic channel fabrication process (cf. Fig. 1 (a) in Ref. [55]). In Fig. 4.29, the evolution of a cylindrical trench is depicted as a series of successive states ($L = 120$ a; $D = 30$ a; $L' = 0.6L$; $D' = 1.6D$; $\tilde{\epsilon}_{NN,f.c.c.} = 1.5$). In the first stage of

---

[9]For all KMC simulations on nanofluidic channel formation the f.c.c. lattice is used, i.e. the results are not directly transferable to the formation of channels in c-Si which has diamond structure. Moreover, the dimension of the channels considered here is at least one order of magnitude smaller than in the real experiments performed on ESS formation. Nevertheless, the principal features are the same.
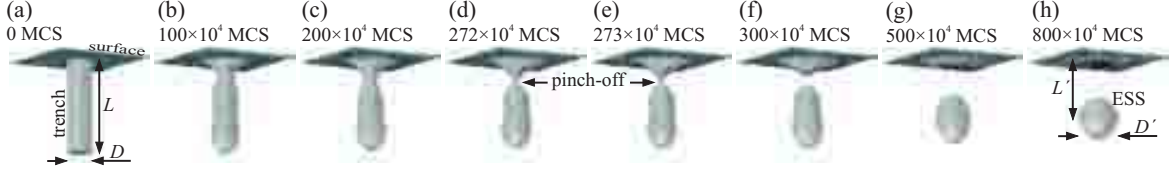
Figure (4.29): Capillarity-driven evolution of a cylindrical trench transforming into a spherical void (ESS) buried beneath the surface ($L = 120\,\text{a}; D = 30\,\text{a}; L' = 0.6L; D' = 1.6D; \tilde{\epsilon}_{NN,f.c.c.} = 1.5$).

evolution, the end of the trench swells causing its shrinkage in depth (cf. section 4.3). Simultaneously, the opening to the wafer surface decreases in width until the pinch-off. Subsequently, the remaining ESS spheroidizes and the surface bump flattens out.

Position and the volume of the remaining spherical void depends on the initial trench geometry. The formation of a single spherical void is given only for a defined range of the ratio ζ between initial trench depth L and its initial diameter D. In Fig. 4.30, a KMC image series is shown which describes the trench instability for increasing $= L/D$ with equal iterations ($L = 10\text{-}200\,\text{a}; \Delta L = 10\,\text{a}; D = 30\,\text{a}; \tilde{\epsilon}_{NN,f.c.c.} = 1.5$). Accordingly, for $\zeta < 2$ the entire trench flattens out and no ESS is formed. Above this critical value a single void is obtained whose volume increases with L (cf. Fig. 4.31 (a)). The voids are located at a depth of about $0.6L$ in each case (cf. Fig. 4.31 (b)). A second critical value of $\tilde{\zeta} \approx 5.3$ indicates the formation of two voids due to the disintegration of the cylindrical trench according to Plateau-Rayleigh (cf. critical length for fragmentation of a finite NW in section 4.3). However, for the formation of nanofluidic channels only one void is required, thus, $L < \tilde{\zeta}D$ has to be fulfilled.

In the literature on the SON technique it is demonstrated that trenches with $D \ll L$ disintegrate into a chain of voids in a cascade-like process starting at the end in the bulk (cf. Fig. 8 in Ref. [267]). On the first view this behavior surprises – one would expect the opening to the wafer to pinch off before the remaining cylindrical rod disintegrates (cf. Fig. 4.30 for the cases $\zeta \geq 5.6$). The experimental observation is explained by the contamination of the surface at the trench opening with silicon nitride which strongly suppresses surface diffusion and thereby retards the capillarity-driven shape evolution locally [271].

In order to achieve an interconnected channel by the merging of neighboring voids the lateral pitch P of the trenches needs to be smaller than the void diameter D' (cf. Fig. 1 (b) in Ref. [55]). This situation is shown in Fig. 4.32 where trenches are aligned in a straight row; the trenches decouple in the first stage of evolution independently from the surface and merge later during spheroidization of the ESS forming a buried channel at a depth of about $0.6L$ with diameter $D_{\text{channel}} \approx 1.4D_{\text{trench}}$.

Not only straight channels can be obtained: By arranging trenches in a ring-like manner (cf. Fig. 4.33), a toroidal channel can be formed which might be applicable as resonator-like roundabouts in channel networks (cf. section 4.5).

A key requirement for nanofluidic devices is the fabrication of channel networks, i.e. channel junctions of various geometries (Y-, X-, or H-shaped) are needed. In this perspective, Fig. 4.34 depicts two reaction pathways to form X- and Y-junctions. The trenches forming the branches of these junctions must fulfill the same geometrical requirements like for basic channels. However, the crossing points deserve more careful consideration. Compared to a basic channel where a void has to merge with two neighboring voids left and right from it, the case of a channel junction is more complex because the merging of the central void with three or four neighboring voids is requi-
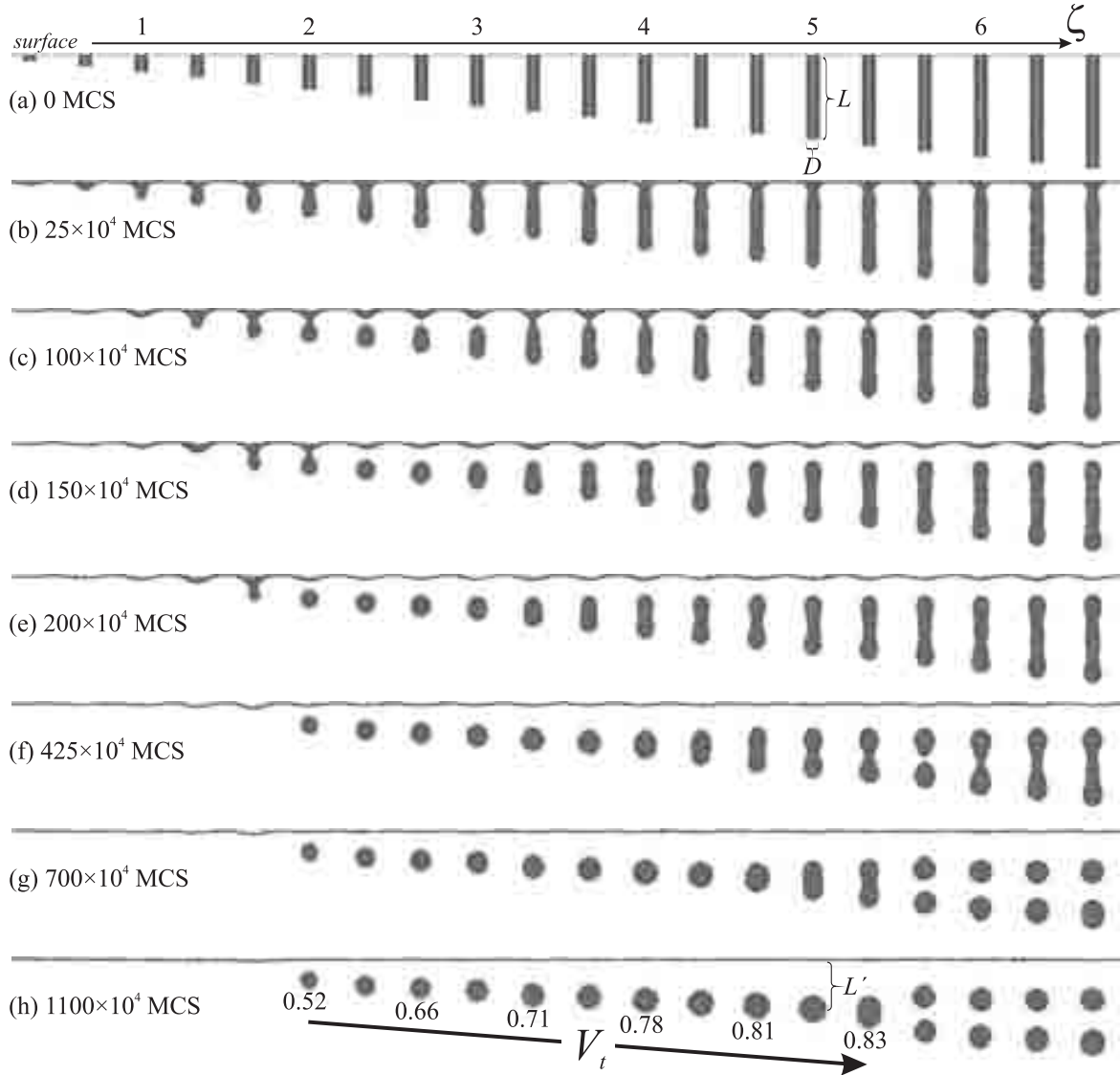
Figure (4.30): Capillarity-driven evolution of cylindrical trenches with increasing depth (from left to right) which transform into a spherical voids (ESS) if a critical ratio $\zeta = L/D \approx 2$ is exceeded ($L = 10\text{-}200\,\text{a}; \Delta L = 10\,\text{a}; D = 30\,\text{a}; \tilde{\epsilon}_{NN,f.c.c.} = 1.5$).
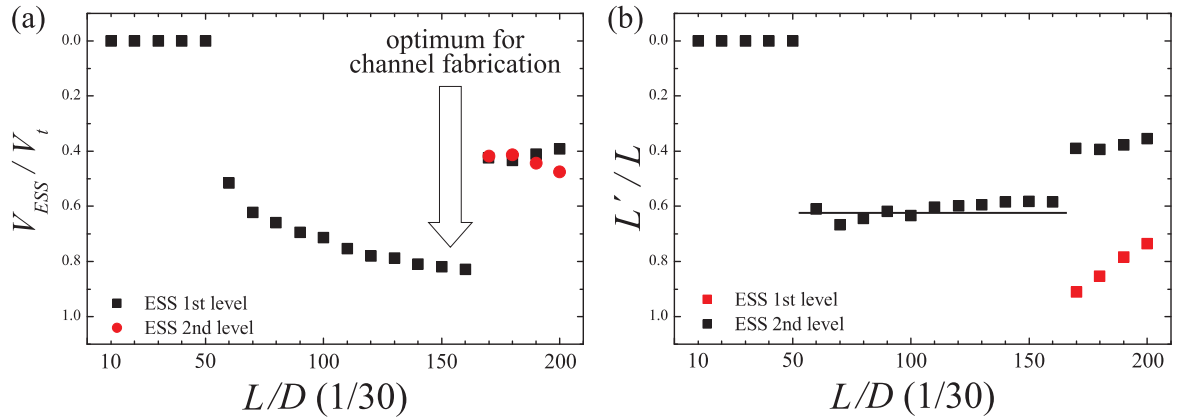
Figure (4.31): Statistics of the above trench series regarding (a) the volume of the forming ESS and (b) its position beneath the sample surface.
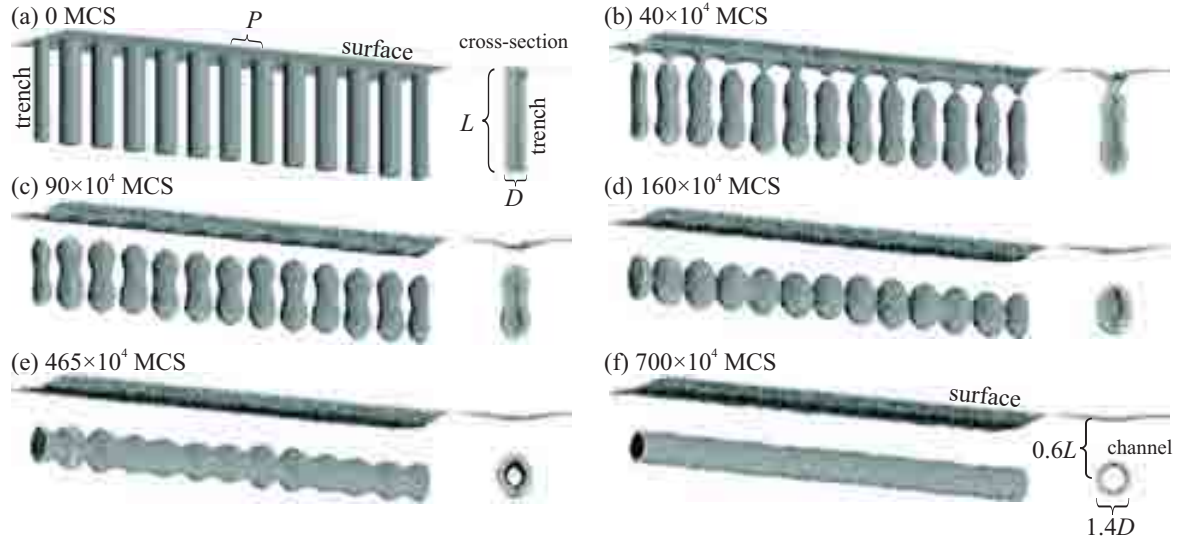
Figure (4.32): Reaction pathway of the formation of a straight channel (L=120 a; D=24 a; P=1.5D; $\tilde{\epsilon}_{NN,f.c.c.}$=1.5).
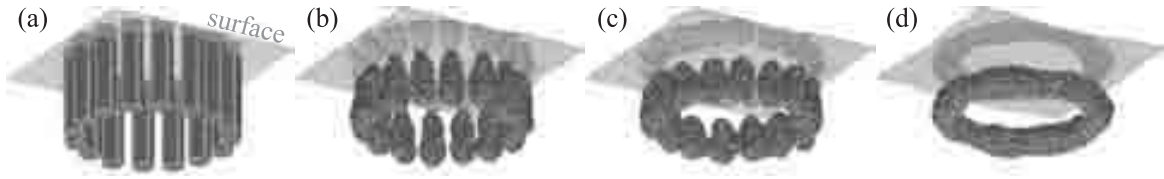
Figure (4.33): Reaction pathway of the formation of a toroidal channel (L=100 a; D=16 a; $\tilde{\epsilon}_{NN,f.c.c.}$=1.5).
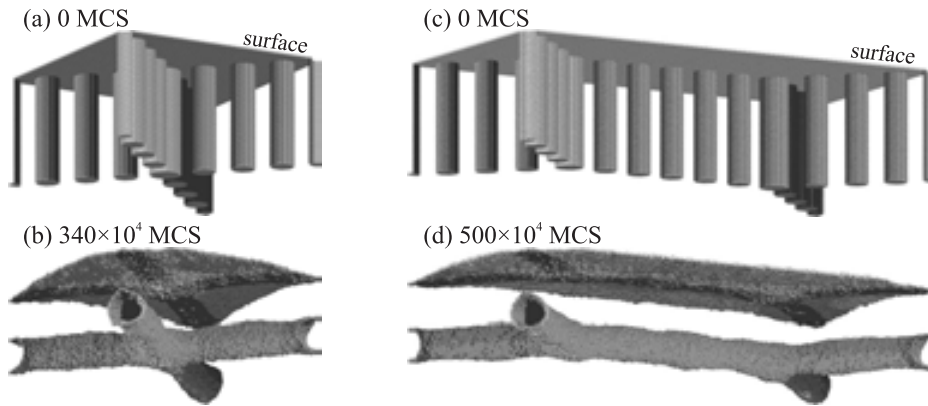
Figure (4.34): Reaction pathways of the formation of nanofluidic channel junctions: (a,b) X-junction; (c,d) Y-junction ($L = 120$ a; $D_{\mathrm{branch}} = 26$ a; $D_{\mathrm{central}} = 34$ a; $\tilde{\epsilon}_{NN,f.c.c.} = 1.5$).

(a) 0 MCS

surface   cross-
                                           section

(b) 60×10^4 MCS

(c) 250×10^4 MCS
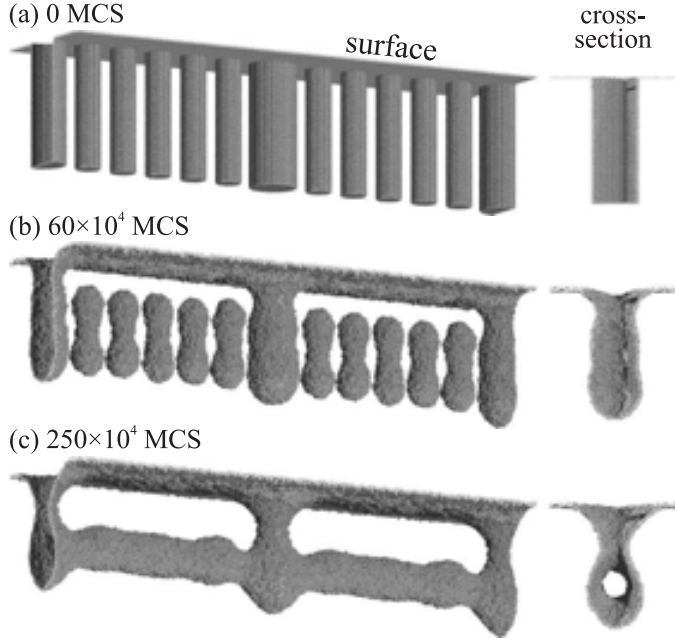
Figure (4.35): Reaction pathway of nanofluidic channel formation with in- and outlets (L=120 a; D_t=22 a; $D_{\text{in/out}}$=44 a; $\tilde{\epsilon}_{NN,f.c.c.}$=1.5).

red in this case. From a geometrical point of view there should not be any obstacle, however, there is one from a dynamic perspective because the decoupling of trenches and the merging of neighboring trenches is subject to fluctuations in time. Thus, particularly at channel junctions it can occur that the central void does not merge with all required branches if the volume of the central trench and its distance to the neighboring trenches are the same like in the case of the straight channel. Therefore, it is beneficial to increase its volume by choosing a larger initial trench diameter at the center which has been done in the case of X- and Y-junction formation in Fig. 4.34 (here: $D_{\text{central}} = 1.3 D_{\text{branch}}$). Likewise, H-junctions were obtained (not shown here).

Furthermore, the question of fluid supply for the buried channel networks has to be addressed. In order to provide or to withdraw fluids to the network in- and outlets are required, i.e. openings to the surface are needed. These openings could be achieved by a second etching step. However, there is simpler alternative, namely, the use of trenches of considerably larger diameter at positions where in- and outlets are wanted. Due to the smaller surface-to-volume ratio thicker trenches are longer stable against the action of the capillary force than thin trenches; the capillarity-induced material flux scales with the mean curvature which in turn scales inversely with the trench diameter. Thus, there is a time window in the channel fabrication process where thick trenches are still in contact with the surface, whereas thin trenches have already decoupled and merged into buried channels. In this regard, Fig. 4.35 exhibits an example for channel fabrication with simultaneous formation of in- and outlets (here, $D_{\text{in/out}} = 2D_t$). Naturally, if the evolution proceeds further, the thick trenches will also decouple from the surface and the in- and outlets would be sealed. Thus, a minute time control is required for the fabrication process, i.e. right after the channel formation the process temperature has to be decreased drastically in order to freeze the obtained structure, thereby, preventing further morphological transformations at finite time scales. Another reason for reducing the process temperature after channel formation lies in the fact that all types of channels are themselves subject to the Plateau-Rayleigh instability. Because of their larger diameter compared to the initial trench diameter the capillary force is

weaker, nevertheless, in the long-term perspective it will cause their disintegration into chains of voids, too.

4.6.2   How Nanowire Junctions Transform into Tunneling Devices, NW Transistors, or SPP Interferometers

Under the action of the capillary force NW junctions, NW ends, or connections of NWs to bulk pads are subject of advanced disintegration because the perturbations during the first stage of the Plateau-Rayleigh instability grow faster there (swelling). Consequently, NW junctions will disintegrate first at the crossing points before the branches fragmentize. This fact opens ways towards the self-organized fabrication of functional structures which are, however, only stable in a finite time window of evolution. Like in the case of nanofluidic channel fabrication evolution can be stopped and the wanted structure can be preserved by cooling down the system or by other means which reduce solubility and/or diffusivity of the migrating species, e.g. by the chemical composition of the process ambient.

There are numerous methods by which NW junctions can be produced both by top-down and by bottom-up fabrication processes [272, 273, 274]. In subsection 3.2.3, it has been demonstrated how NW junctions can be produced directly in an embedding medium by FIB-based ion beam synthesis. This methods is non-conventional since it represents a combined approach of top-down and bottom-up structuring. Conceptually similar, NW junctions can be produced by the dewetting of laterally pre-structured ultra-thin films. The pre-structuring can be performed by common lithographic means, whereas the capillary force transforms the pre-structured thin film into the wanted NW junction structure in a self-organizing manner [40, 41]. Fig. 4.36 refers to the scenario where a cross of stripes is shown which transforms under the action of the capillary force into a NW cross that later due to the Plateau-Rayleigh instability evolves into a structure suitable as SET device (see below). According to Fig. 4.36 the branches of the cross shrink laterally, i.e. they transform by surface diffusion into cylindrical structures. The corresponding shrinkage factor depends on the aspect ratio α between width W and height H of the stripe. Because of volume conservation, the radius of the resulting cylinder scales with $\sqrt{WH}$. However, only stripes with a maximal aspect ratio $\alpha_{\max}$ transform into a single cylindrical structure. Above this maximal aspect ratio the stripes internally disintegrates and a more complex structure pattern can emerge. The lattice KMC simulations conducted in this respect revealed that $\alpha_{\max} \simeq 15$
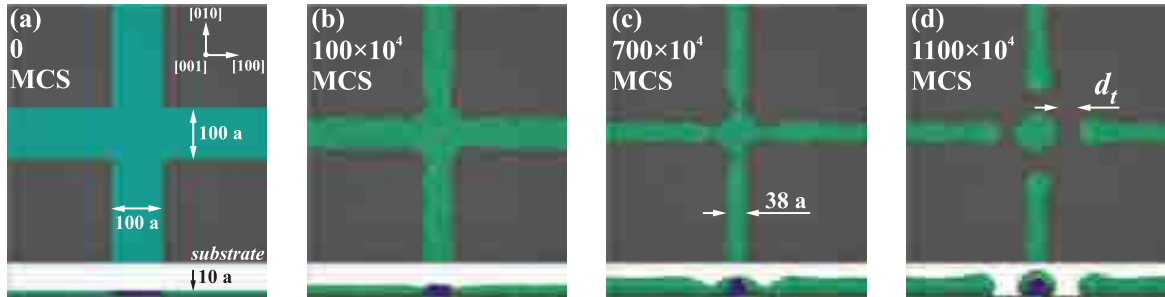
Figure (4.36): Capillarity-driven transformation of a cross of thin stripes (pre-structured e.g. by lithographic means) into a NW junction which further evolves into a structure suitable as SET device ($\tilde{\varepsilon}_{NN,f.c.c} = \tilde{\varepsilon}_{AA} = 1.1$; $\tilde{\varepsilon}_{AB} = 0.1$).
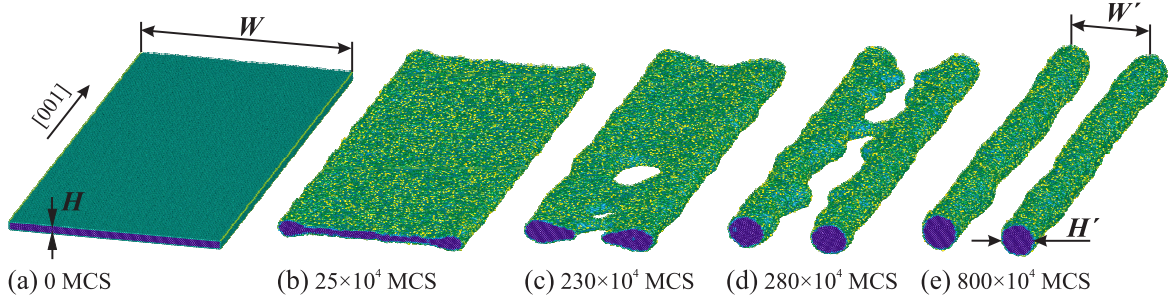
Figure (4.37): Capillary instability of a thin stripe whose width-to-height ratio is 20 (W=200 a; H=10 a; $\tilde{\varepsilon}_{NN,f.c.c.}$=1.1) which transforms into two parallel NWs (W=63 a; H'=35 a). Naturally, these NWs transform further via the Plateau-Rayleigh instability into chains of NCs (not shown; cf. Fig. 1.3).

for the specific simulation parameters (f.c.c. lattice, [001]-orientation of the stripe, $\tilde{\varepsilon}_{NN,f.c.c.}$=1.1). In Fig. 4.37, for example, the interesting case of a stripe decomposing into two isochor and parallel NWs with [001]-orientation is shown where $\alpha = W/H$=20.

Fig. 4.36 and Fig. 4.37 are presented here in order to show a few conceptual features how pre-structured thin films can disintegrate under the capillary force into NWs and NW junctions. In the future, far more thorough investigations are needed which are, however, beyond the scope of this work (particularly on dewetting of pre-structured ultra-thin SOI layers which has attracted attention recently [3, 37, 275]).

Multi-Terminal Single-Electron-Devices. The crossing point of a junction of NWs is a region of concave curvature (angles smaller than 180°), thus, material flux towards the crossing point is set into motion from the convex NWs which leads to the thinning of the NWs close to the crossing point that culminates in the rupture of the NWs from the central NC. This principle applies to any n-fold NW crosses ($n > 2$). In Fig. 4.38, the free evolution of a 6-fold NW cross is shown in a series of configurational states. The aim is to achieve in a self-organizing manner a structure applicable as multi-terminal single electron devices [38, 276]. Here, the NWs are directed into the [110]-directions that lie in a (111)-plane of the underlying f.c.c. lattice. The rupture time is subject to thermal fluctuation which is demonstrated in Fig. 4.39 (a). After the pinch-off the distance between the NWs and the central NC, which refers to the tunnel distance in view of SET applications, grows in the first stage with the cube root of time (cf. Fig. 4.39 (b)) which makes a control of the d_t possible.

There is a time window in the process which refers to a state where all NWs have separated from the central NC (cf. Fig. 4.38 (d)) before the NWs disintegrate later
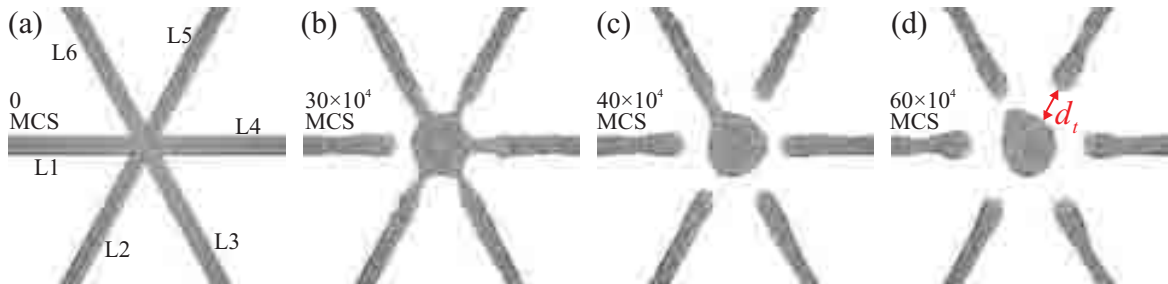
Figure (4.38): Free evolution of a 6-fold cross of [011-oriented] NWs in the f.c.c. (111)-plane transforming into a 6-terminal SET-like structure ($R_0 = 8$ a; $\tilde{\epsilon}_{NN,f.c.c.} = 1.3$).
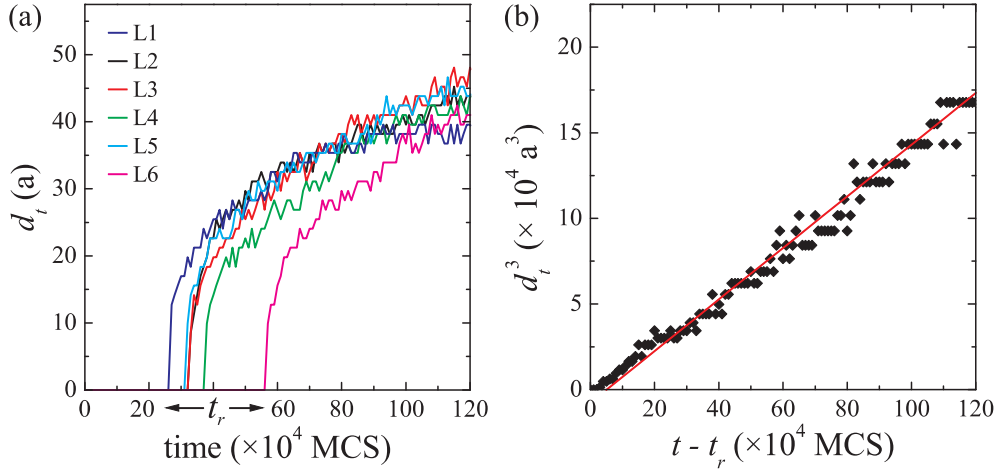
Figure (4.39): (a) The growth of the tunnel distances d_t after their appearance at the respective rupture times t_r for the six NWs of Fig. 4.38. (b) Growth-law of the tunnel distance d_t in the first stage after pinch-off at rupture time t_r.

according to the Plateau-Rayleigh instability. For SET applications different tunnel distances are needed [38]. This can be achieved by crossing NWs of different radii. Since large NWs have a smaller surface-to-volume ratio they withstand the action of the capillary force longer than thinner NWs. Consequently, the rupture of thin NWs from the central NC occurs earlier than that of thick ones. Thus, configurations can be achieved where the tunnel distance between the thin NWs and the central NC is larger than that of the thicker NWs which is adjustable based on the characteristic growth of the tunnel distance (cf. Fig. 4.39).

Nanowire Transistors.   The capillarity-induced formation of NW transistor structures is very similar to the previous concept. Here, junctions of semiconducting NWs with different diameter have to be conceived conceptually. Again, the crossing point is a region of advanced instability from which thin NWs separate earlier than thick ones because of the larger surface-to-volume ratio. An example is given in Fig. 4.40, where the ratio between thin and thick NW is 2:3. In Fig. 4.40 (c) a configuration is obtained where the thin NWs are separated from the junctions at equal distance from the former crossing point. These thin NWs can play the role of gate electrodes controlling the current flux through the thick NW whose structural integrity is still intact. Naturally, at later stages of evolution the thick NW will also disintegrate according to Plateau-Rayleigh. Again, one can preserve this structure by cooling down the system or reducing solubility and/or diffusivity of the migrating species.

Figure (4.40): Free evolution of two NW junctions consisting of NWs of different diameter transforming into a structure suitable as NW full-depletion transistor ($d_1 = 30\,\text{a}; d_2 = 20\,\text{a}; \tilde{\epsilon}_{NN,f.c.c.} = 1.5$).

Surface-Plasmon-Polariton Interferometers. A further example of the self-organized formation of functional structures which is based on the capillary instability of NW junctions is shown in Fig. 4.41 where a rectangular loop of NWs, which is connected at two opposite sides of the loop to further NW contacts, transforms into a structure suitable as SPP interferometer. Here, the two T-junctions as well as the corners of the L-turns are subject to advanced instability; in both cases there are angles smaller than 180°. During long-term evolution, all branches of the structure disintegrate into chains of NCs which can act as SPP waveguides [12, 13]. If at one contact a SPP signal is coming in (cf. Fig. 4.41 (d)), the T-junction acts as SPP-splitter with a power transmission of 100% (50% for each branch). Also L-turns exhibit nearly 100% power transmission (cf. Fig. 3-8 in Ref. [277]). If one side of the interferometer is placed in a SPP phase shift medium (gray area in Fig. 4.41 (d)) this SPP signal is modulated and SPP wave interference can be anticipated if the two branches of the SPP interferometer are reunited at the opposite T-junction (cf. conceptually Mach-Zehnder interferometer [278]).
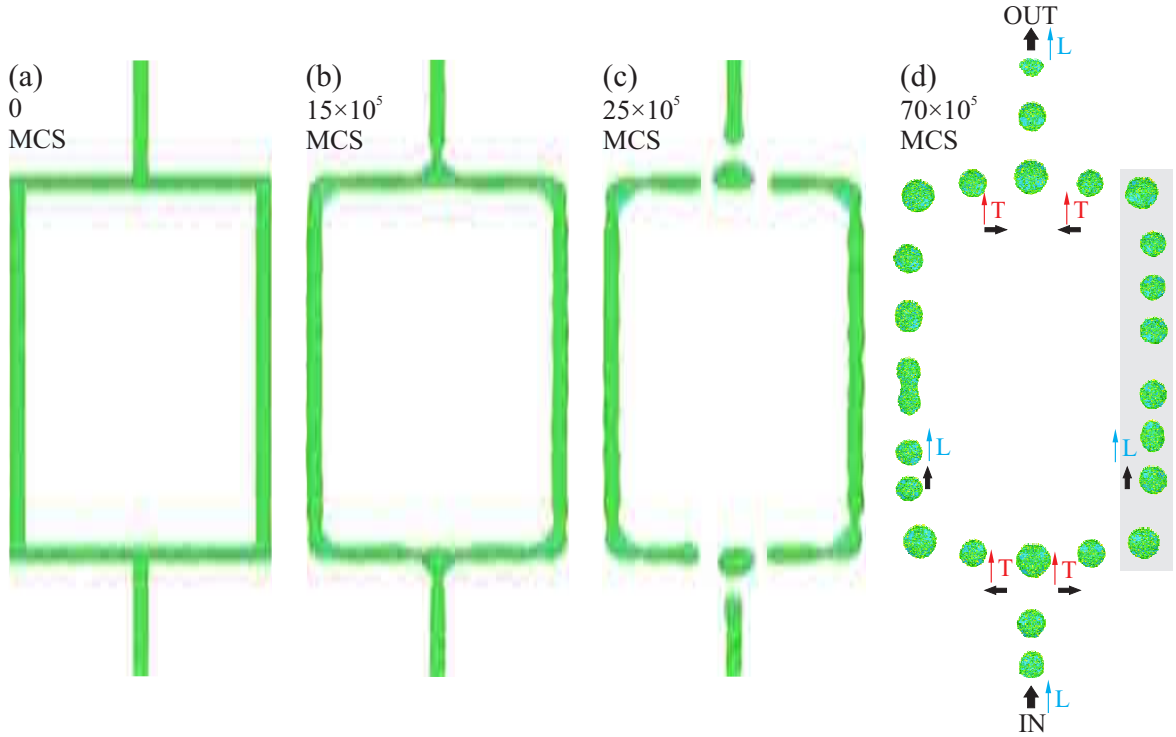
Figure (4.41): Free evolution of a rectangular loop of NWs ($410\,a \times 620\,a$), which is connected at two opposite sides of the loop to further NW contacts; this complex NW structure transforms into a NC structure suitable as SPP interferometer ($D = 24\,a; \tilde{\epsilon}_{NN,f.c.c.} = 1.3$). In SPP waveguides, routing (L-turn) and splitting (T-junction) proceed at transmission coefficients of nearly 100% [277]. The black arrows in (d) indicate the electromagnetic energy flow, whereas red and blue arrows represent longitudinal and transverse SPP modes, respectively (after Fig. 3-8 in Ref. [277]).

Chapter 5

Nanostructure Shape Evolution by Non-Equilibrium Processing

Contrary to the previous chapter where the free evolution of nanostructure shapes was examined, in this chapter it will be demonstrated how the capillarity-driven shape evolution of nanostructures can be influenced and thereby controlled by non-equilibrium processing based on:

1. applied periodic temperature fields and

2. collisional mixing.

In short, the nanostructure shape evolution discussed here is due to the simultaneous action of the system-inherent capillary force and externally applied force fields (superposition of driving forces). These cases have in common that the detailed balance (atomic attachment/detachment) is inherently violated (cf. Eqn. 2.8):

$$P\left(\varphi|\psi\right)W\left(\psi,t\right) \neq P\left(\psi|\varphi\right)W\left(\varphi,t\right) \ . \tag{5.1}$$

In view of the Plateau-Rayleigh instability of cylindrical nanostructures where thermal fluctuations cause the shape evolution to become inhomogeneous (cf. subsection 4.2.2), it will be shown here that applied periodic temperature fields along the longitudinal axis can be employed to suppress these fluctuations. T-gradients lead to uncompensated forces which trigger a biased material transport from hot to cold regions which intrudes into the perturbation mode selection in the initial stage of the Plateau-Rayleigh instability. A particular perturbation mode is preferentially excited whose periodicity coincides with that of the periodic T-field. In other words, the self-organizing system is "guided" along a specific reaction pathway resulting in regular and long-range-ordered NC chain structures. In a similar manner, it is demonstrated by computer simulations and real experiments that in-plane periodic temperature fields can be used to generate periodic surface structures in thin films such as ripples or hillock arrays [14].

In the second section, the effects of collisional mixing on the shape evolution of cylindrical nanostructures are investigated. In addition to thermally activated atomic jumps ballistic displacements of surface atoms are taken into account which occur for example during low-energy ion irradiation (sputtering is neglected here). These ballistic displacements excite the system, in other words, atomic configurations are

produced which are very unlikely obtained under equilibrium conditions (cf. Fig. 2.22). In extension to section 2.8, where it has been shown that the morphology of NCs can change in puzzling ways, it will be demonstrated here that the Plateau-Rayleigh instability of single-crystalline NWs can be either accelerated or retarded depending of the crystallographic orientation of the NW. Moreover, periodicity and shape of the emerging NC chain can be adjusted by the balance between collisional mixing and the capillary force ("driven" evolution).

5.1   Guided Evolution by Temperature Gradients

Structure evolution and pattern formation under external field gradients has a long history. In hydrodynamics, for example, flows driven by surface tension gradients, which can be achieved for example by temperature fields (thermocapillarity), electrical fields (electrocapillarity), or changes of the chemical composition of the ambient (solutocapillarity), are known since Carlo Marangoni's seminal works and are therefore named after him ("Marangoni convection" etc.) [24, 279, 280, 281, 282]. At micro- and nano-scale dimensions, already small temperature variations cause large thermal gradients which give rise to strong uncompensated forces along the phase boundary [282, 283]. The triggered material flow along the gradient from regions with high to low temperature can change the morphology of structures tremendously even on femtosecond time scales (high-gradient processing) [283, 284, 285, 286]. In particular, if these external fields are periodic in space, long-range-ordered periodic structures can be obtained which has been shown recently on a micrometer scale in the case of patterning of thin polymer films by in-plane periodic temperature fields [14, 287]. Like hydrodynamic flow, atomic diffusion in solid-state systems can be biased along the gradients of external fields as pointed out in section 2.4, e.g. by temperature fields ("thermo-migration") or by electric fields ("electro-migration") [156, 288, 289, 290, 291, 292, 293, 294]. Depending on the dominating diffusing species (atoms or vacancies) the material migrates along the T-gradient either in the cold or the hot regions, i.e. from regions with high to low concentration of the dominating diffusing species.

5.1.1   Suppressing Thermal Fluctuations during the Plateau-Rayleigh Instability of Nanowires

In the context of the present subsection, static periodic temperature fields are considered (hot and cold regions in alternating order) along the longitudinal axis of single-crystalline NW structures. The periodic temperature gradients intrude into the perturbation mode selection during the initial stage of the system-inherent Plateau-Rayleigh instability (cf. section 4.1) which has been formerly identified to be subject to considerable thermal fluctuations in the case of a freely evolving system (cf. subsection 4.2.2). Here lies the motivation for this non-equilibrium processing, namely, to provide ways and means to excite defined perturbation modes by the applied field and to suppress thereby these disturbing fluctuations in order to obtain regular and long-range-ordered NC chain structures.

Since surface diffusion is the dominant diffusion channel during the capillary instability of cylindrical structures, material diffuses along the T-gradient from hot to cold
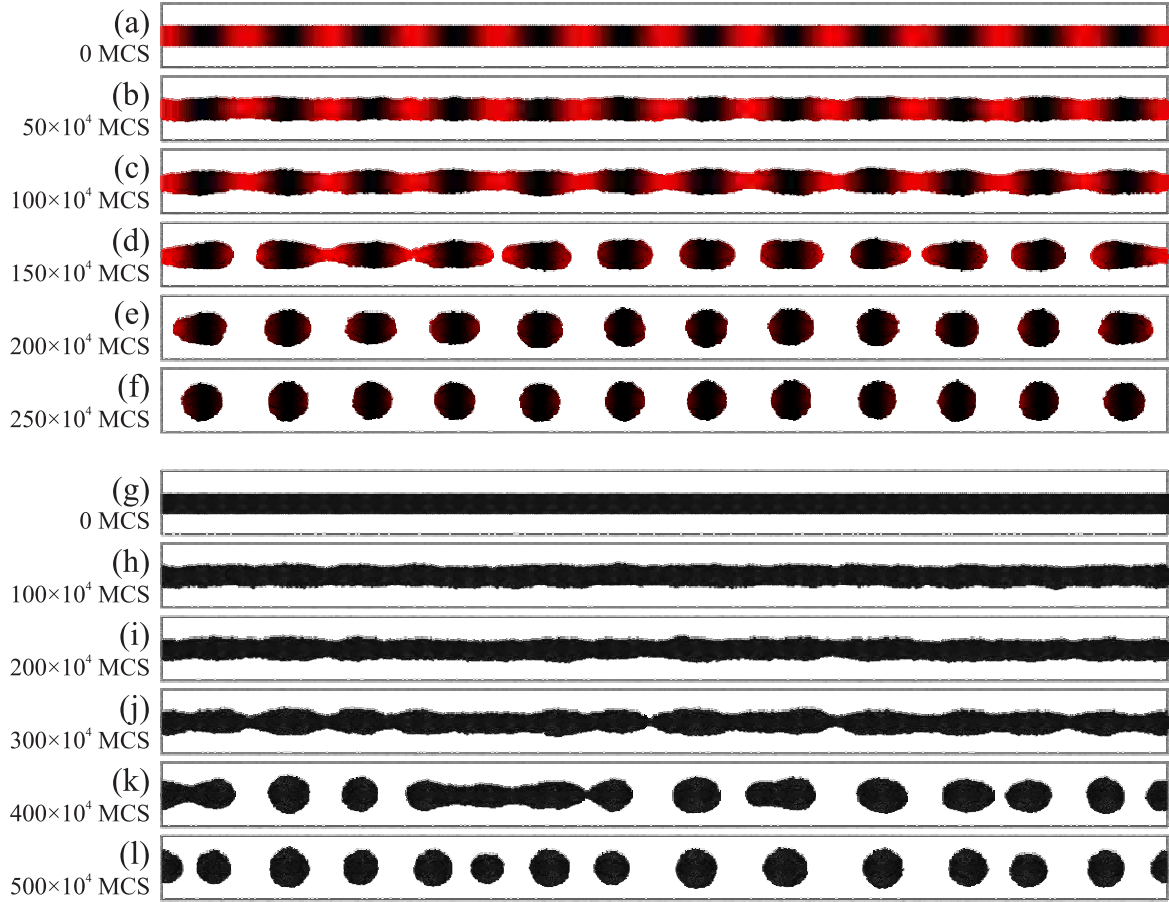
Figure (5.1): "Taming" fluctuations during the Plateau-Rayleigh instability by longitudinal periodic temperature fields: (a-f) the "guided evolution" with $\Delta T{=}20$ K and $\alpha{=}12$ ($\lambda{=}0.96\lambda_m$; color key from red ($T{=}T_0{+}\Delta T$) to black ($T{=}T_0$)) compared to (g-l) the "free evolution" with $\Delta T{=}0$ K. In both cases a f.c.c. lattice with NN-Ising dynamics is considered with $T_0{=}1800$ K and with the following initial cylinder parameters: [001]-orientation, $R_0{=}10$ a, $L{=}2^{10}$ a.

regions. This biased migration becomes plausible by considering the chemical potential μ along the surface of a undulated NW structure (oriented along z-axis) in the stationary state: μ (i.e. ad-atom concentration c_s) is constant along the entire surface (cf. Eqn. 1.7):

$$d\mu = 0 = \kappa \frac{d\gamma}{dz} + \gamma \frac{d\kappa}{dz} \ . \tag{5.2}$$

Consequently, the curvature effects are compensated by the temperature effects ($c_s \propto \exp[-E_a/(k_B T(z))]$): in other words, hot regions are concave (neck) and cold regions are convex (shoulder).

   In Fig. 5.1, the two scenarios of a guided and a freely evolving NW structure are compared. In Figs. 5.1 (a-f), a cylindrical structure is exposed to a static and harmonic temperature profile along the z-axis ($R_0{=}10$ a; $L{=}2^{10}$ a):

$$T(z) = T_0 + \Delta T \cos^2(\alpha \pi z) \ , \tag{5.3}$$

where α denotes the number of periods per simulation cell length which is adjusted in such a way that the one T-field period corresponds approximately to $\lambda_m = 2\pi R_0 \sqrt{2}$ of the freely evolving cylinder shown in Figs. 5.1 (g-l). In both cases, the base line
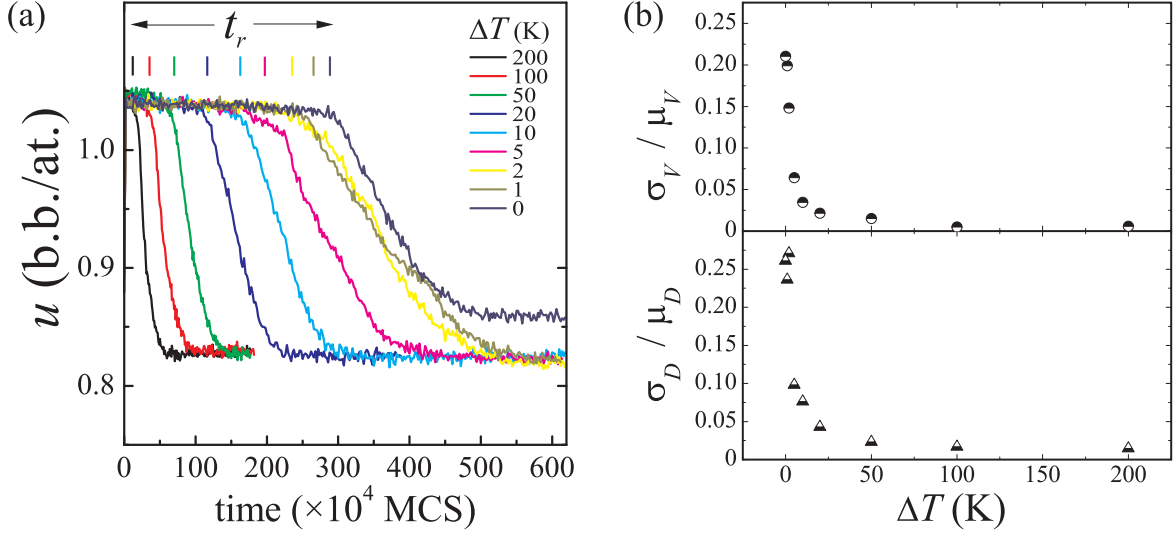
Figure (5.2): (a) Specific internal energy development $u(t)$ during the guided evolution of cylindrical structures ([001]-orientation, R_0=10 a, L=2^{10} a) for different values of ΔT where in all cases T_0=1800 K and α=12 (cf. Fig. 5.1 for ΔT=20 K). (b) Corresponding statistics showing the relative standard derivation of volume V and distance D of the emerging NCs.

temperature T_0 amounts to 1800 K which corresponds to $\tilde{\varepsilon}_{NN,f.c.c.}$=1.3 taking a diatomic bond strength of $\varepsilon_{NN,f.c.c.}$=0.2 eV into account (cf. section 2.4). In the simulation shown in Figs. 5.1 (a-f) ΔT amounts to 20 K, thus, $\Delta T/T_0 \approx 0.01$. This relatively small temperature variation is sufficient to excite a perturbation mode on the cylinder surface which corresponds to the periodicity of the T-field with $\lambda \approx \lambda_m$. This perturbation grows homogeneously in the system which leads to synchronic pinch-offs at isodistant undulation necks (cf. Fig. 5.1 (d)) compared to the scenario of the freely evolving cylinder where the perturbation grows inhomogeneously (cf. Figs. 5.1 (j) and (k)). Due to the excitation of a single perturbation mode perturbations with other wavelengths do not develop. This process does not depend on the crystal orientation of the NW, i.e. the outcomes for NW structures with other crystal orientations are equal (results not shown).

In Fig. 5.2 (a), the specific internal energy development $u(t)$ is plotted for different values of ΔT keeping the other values constant. It can be deduced that the stronger the T-gradient is the faster the NW structure disintegrates (rupture time t_r); in other words, the perturbation growth rate scales with the temperature gradient. Moreover, the duration of NW fragmentation scales inversely with the temperature gradient (cf. the slopes of $u(t)$ in Fig. 5.2 (a)). The fact that the reaction pathways in the case of ΔT=0 reaches a higher level of u is explained by the number of NCs which amounts to 14 in the case ΔT=0 and twelve in the cases ΔT>0. Apparently, for every case ΔT>0 the system takes over the periodicity of the T-field ("guiding"), whereas the freely evolving cylinder ends up at a larger NC number due to thermal fluctuations; if for ΔT=0 identical simulations with different random number seeds are repeatedly performed the final NC number scatters in the interval from 12 to 14 (results not shown).

The statistics reflecting the regularity of the resulting NC chain structure with varying strength of the temperature gradient is presented in Fig. 5.2 (b). Here, the relative standard deviations of NC volume and distance are plotted vs. ΔT for the same simulation parameters as stated above. Accordingly, the regularity improves steadily
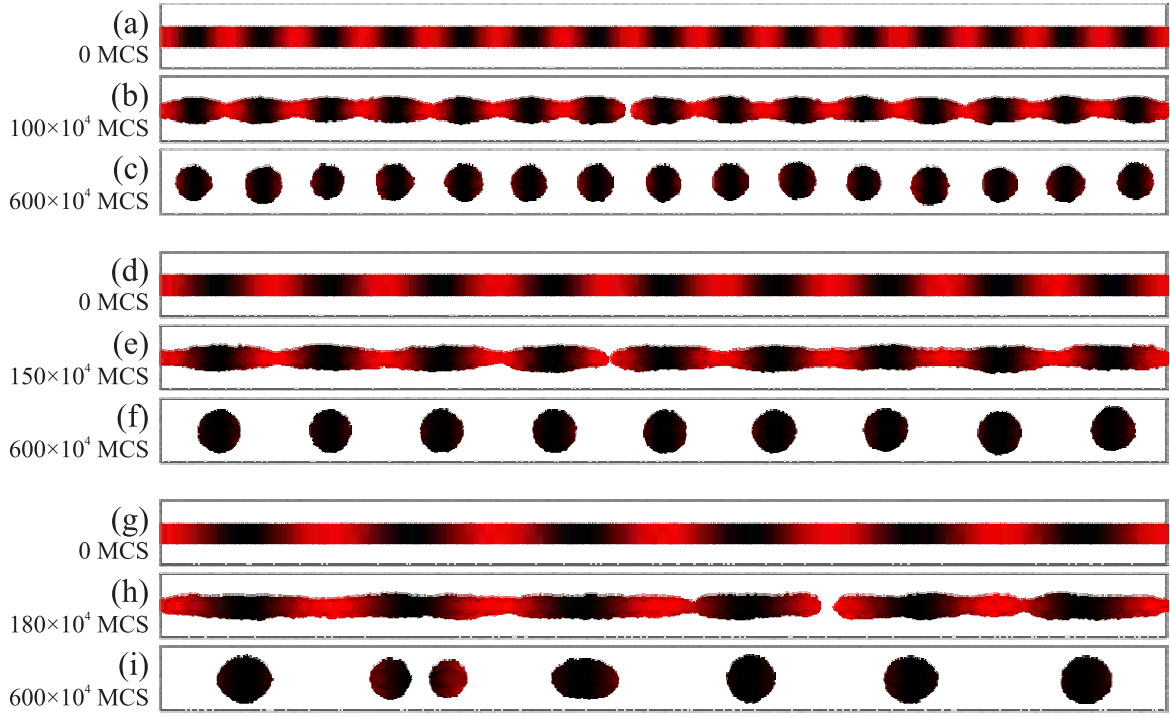
Figure (5.3): Stimulation of Plateau-Rayleigh instability perturbation wavelengths different from λ_m: (a-c) α=15 (λ=0.77λ_m), (d-f) α=9 (λ=1.27λ_m), (g-i) α=6 (λ=1.92λ_m). In all cases ΔT=20 K, T_0=1800 K (color key from red (T=T_0+ΔT) to black (T=T_0)), f.c.c. lattice with NN dynamics, [001]-orientation, R_0=10 a, L=2^{10} a.

with increasing ΔT. For the maximum ΔT=200 K the relative standard deviations reach about 1%, whereas for ΔT=0 the corresponding values lie in the usual range between 15% and 25% (cf. subsection 4.2.2). It is remarkable that already for ΔT=20 K ($\Delta T/T_0$≈0.01) both values are within the targeted range of below 5%.

So far, perturbation modes with a wavelength close to the wavelength which corresponds to the perturbation of maximum growth rate were excited by the periodic temperature field. In view of a control of the regularity of the emerging NC chain, a further and from a technological viewpoint perhaps more interesting question arises: To what extent is it possible to excite other stable perturbations with wavelengths different from λ_m? Thereby, not only regularity but also periodicity of the NC chain could be adjusted. In this regard, Fig. 5.3 depicts three scenarios where α is set to 15 (a-c), 9 (d-f), and 6 (g-i), respectively (again, ΔT=20 K, T_0=1800 K, [001]-orientation, R_0=10 a, L=2^{10} a). The first case with α=15 reflects the situation where a perturbation with a wavelength slightly above the critical wavelength $\lambda_c = 2\pi R_0$ is excited. From the analytical theory it is expected that the growth rate of this perturbation is positive but nearly zero (cf. section 4.1). Due to the temperature field the growth of this particular wavelength is stimulated over all others and the NW structure disintegrates with this short wavelength. The question whether wavelengths smaller than λ_c can be excited remains open[1]. It is expected that the cylinder transforms into a stationary unduloid, i.e. a cylindrical body with axisymmetric, harmonic undulations whose periodicity is taken over from the periodicity of the temperature field. On the contrary, wavelengths

---

[1]From the analytical theory for a freely evolving cylindrical system it can be anticipated that perturbation modes with a wavelength smaller than λ_c have negative growth rates.

clearly larger than λ_m can also be excited which is seen for $\lambda{=}1.27\lambda_m$ and $\lambda{=}1.92\lambda_m$ in Figs. 5.3 (d-f) and Figs. 5.3 (g-i), respectively. According to Fig. 5.3 (i) it becomes evident that there is a critical wavelength ratio λ/λ_m above which the fragments themselves disintegrate further. In the present case this critical ratio is at about two, i.e. for all λ with $\lambda_c{<}\lambda{<}2\lambda_m$ the periodicity of the temperature field controls the periodicity of the resulting NC chain. These boundaries are naturally dependent on the process parameters ΔT and α which determine the T-gradient and on T_0 which determines the baseline kinetics in the system. In general, it can be anticipated that the boundary of that interval towards larger λ's scales with the strength of the T-gradient.

If the wavelength of the periodic temperature profiles exceeds the critical value so that the forming fragments themselves disintegrate subsequently, a combined top-down / bottom-up process is possible: At first, the guidance of the applied temperature field (top-down step) leading to a streptococci-reminiscent rod chain and, secondly, the self-organized further disintegration of the emerging rods into clusters in the spirit of Figs. 4.22 (b) and (d) (bottom-up step).

Regarding combined processes, a further scenario is thinkable in real processes, if there are difficulties to generate for a sufficiently long time a steady temperature field: It could be possible that the periodic temperature field is only used for a short while to generate slight harmonic surface undulations, thus, giving the corresponding perturbation wavelength just a slight lead in the perturbation mode selection process during the later stages of the Plateau-Rayleigh instability which can then be executed at spatially homogeneous temperature in the spirit of subsection 4.2.5.

A general remark has to be given on the generation of periodic temperature fields of the kind anticipated in the present cases. In general, it is challenging to provide in the sub-micrometer range static temperature fields with considerable T-gradients because of the heat conduction properties of most crystalline materials. Thus, for real processes a pulsed operation of the heat source can be considered instead so that the T-gradient is established only for a short duration before the systems thermally equilibrates and cools down before the new pulse can be applied. In this regard, potential periodic heat sources are: laser interference patterns [295] or standing SPP patterns that dissipate heat due to non-radiative damping [14, 296, 297]. In any case, the system must be coupled to a heat sink in order to keep T_0 constant (e.g. a substrate).

In conclusion, it has been demonstrated that periodic temperature fields along the longitudinal axis of a cylindrical structure intrudes into the perturbation mode selection during the initial stage of the Plateau-Rayleigh instability. Thus, a perturbation mode with the same periodicity like the temperature field is excited, i.e. its growth is stimulated over the perturbations with different wavelength. Thus, thermal fluctuations which occur usually in freely evolving systems can be suppressed and long-range-ordered and regular NC chain structures are obtained which are needed for instance for SPP waveguiding applications to minimize SPP damping [12, 13].

5.1.2 Thin Film Patterning by Thermocapillarity

In this subsection, a method is presented to fabricate long-range-ordered thickness undulations in thin films (ripples, hillock arrays) by means of in-plane periodic temperature gradients which give rise to thermocapillary effects. In collaboration with Jon A. Schuller and Mark L. Brongersma (Stanford University) experiments and numerical
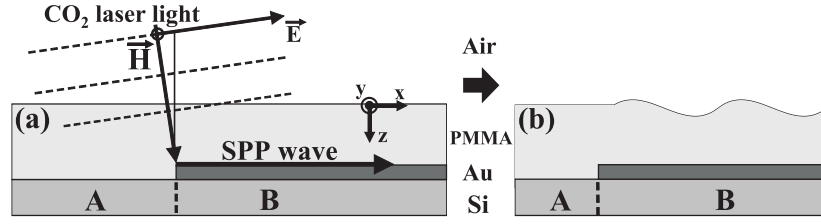
Figure (5.4): A schematic representation of (a) sample setup, experimental procedure, and (b) the periodic surface pattern obtained. The aspect ratio between amplitude and wavelength of the surface undulation obtained is overaccentuated for reasons of illustration.
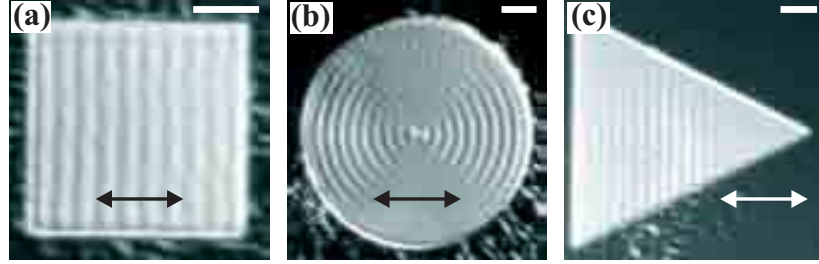
Figure (5.5): DIC micrographs showing periodic PMMA surface patterns: (a) ripples, (b) rings, and (c) hillocks. The arrows are parallel to $\vec{e_x}$. The white scale bars denote 30 μm.

calculations were performed on the regular patterning of thin PMMA films on a metal substrate [14]. These investigations aimed at a deeper understanding of the underlying mechanisms for creating the experimentally observed thickness undulations. The method, which uses periodic in-plane temperature fields induced by the damping of SPPs, was previously used to characterize SPP propagation and scattering [298]. Reflection pole method calculations [299] were used to determine the spatially dependent power losses generated by SPPs excited at a PMMA/metal interface. These power losses give rise to local heating in the film. Taking these losses as a spatially varying heat source, heat conduction calculations show that periodic in-plane temperature fields are produced which result in thermocapillary effects in the PMMA. Lattice KMC simulations reveal that such in-plane thermal gradients trigger a biased material transport. Although the microscopic kinetics of the lattice KMC method differs from that in a PMMA film (atomic diffusion along a T-gradient-induced concentration gradient vs. hydrodynamic flow along a T-gradient-induced pressure gradient) the macroscopic characteristics are equal (cf. section 1.2). It is expected that this non-equilibrium fabrication method of SPP lithography can be applied to other thin film systems (particularly thin polymer films) in order to achieve regular thickness undulations with long-range order.

In Fig. 5.4, sample structure and experimental procedure are drawn schematically. A 50 nm thick patterned metal film (45 nm Au, 5 nm Ti sticking layer) was deposited on a Si(001) wafer (500 μm thick). Afterwards, a 1 μm thick 495 k molecular weight PMMA film was spincoated over the whole wafer. The samples were then exposed for 1 s to CO_2 laser light (λ=10.64 μm) at RT. The 5 W quasi continuous-wave[2] linearly polarized laser beam ($\vec{E}=E\vec{e_x}$) was focused to a spot of approximately 200 μm diameter, illuminating the patterned Au structures at normal incidence. After laser irradiation, surface profiles were imaged with DIC and atomic force microscopy.

---

[2]The laser is excited with a 5 kHz, 5% duty cycle square waveform. Due to the slow response of the laser plasma ($\sim$100 μs rise and fall time) the resulting output is mostly constant with a small 5 kHz amplitude variation.

In Fig. 5.5 (a), a DIC micrograph is shown that clearly indicates a ripple structure on the PMMA. The periodic ripples only occur above the rectangular Au pads (region 'B' in Fig. 5.4). In those areas with no Au beneath the PMMA (region 'A' in Fig. 5.4), no periodic PMMA surface roughening is observed after laser irradiation. The ripple pattern is only periodic along the direction of laser polarization $\vec{e_x}$ as expected for a standing wave arising from a TM guided mode. The location (above Au) and observed polarization dependence (TM) strongly suggest that the ripple patterns are caused by SPPs. Furthermore, our electromagnetic simulations based on reflection pole method calculations [299] show that the structure supports a SPP mode with a wavelength of $10.2\,\mu$ m but no other waveguide modes. That SPPs induce the ripple structure becomes even more evident in the case of more exotic SPP interference patterns which are observed when Au pads of different geometries are illuminated (Figs. 5.5(b),(c)). The excitation of SPPs at curved or angled interfaces results in circular and triangular interference patterns that induce annular and hillock patterns on the PMMA surface, respectively.

Since the SPPs are excited from the edges of the Au pad, the optical field is given by (ignoring SPP reflections)

$$\vec{E}_{\text{tot}} = \left[\vec{E}_i(z) + \vec{E}_l(z)\mathrm{e}^{-ikx} + \vec{E}_r(z)\mathrm{e}^{+i(kx+\delta)} \right] \mathrm{e}^{-i\omega t} \ , \tag{5.4}$$

where $\vec{E}_i(z)$ corresponds to the standing wave produced by the incident laser reflected off the Au surface, $\vec{E}_{l,r}(z)$ are the SPPs excited at the left and the right edge of the structure, k is the SPP wavevector, and δ is the phase shift between the incident and SPP field. The damping of the optical field is given by

$$\frac{\partial u}{\partial t} = \omega \times \Im(\varepsilon) \times \frac{1}{2}\Re(\vec{E}_{\text{tot}} \bullet \vec{E}_{\text{tot}}^*) \ , \tag{5.5}$$

where u is the electromagnetic energy density [300]. With the above equation for $\vec{E}_{\text{tot}}$ the loss contains terms, that are only z-dependent, and interference terms, that have a periodicity along $\vec{e_x}$. Interference of the two counter-propagating SPPs with each other and with the incident laser result in periodicities with a wavelength of $\frac{1}{2}\lambda_{\text{SPP}}$ and λ_{SPP}, respectively. The measured ripple patterns on rectangular Au pads have a peak-to-trough distance of approximately 40 nm and a periodicity of 10.7±0.4 μm. The measured periodicity is attributed to interference of the incident laser with SPPs. The deviation of the measured periodicity from the calculated SPP wavelength (λ_{SPP}=10.2 μm) may be caused by off normal rays in the focused laser spot. The lack of a ripple pattern with a periodicity of $\frac{1}{2}\lambda_{\text{SPP}}$ is consistent with weak coupling to the SPPs ($E_i \gg E_{l,r}$). In Fig. 5.6, the losses in the PMMA and the Au layer are plotted assuming that 1% of the incident laser power is coupled to SPPs. Although the actual coupling is unknown, later it is shown that this estimation recaptures the qualitative features of the experiment. The optical absorption coefficient of PMMA at a wavelength of 10.6 μm, $\alpha_{\text{PMMA}} = 0.04\ \mu\text{m}^{-1}$, was used [301].

The calculated non-radiative damping of the optical fields was taken as the heat source $S(x,z)$ in a steady-state heat conduction calculation to determine the spatially dependent temperature profile in the PMMA. The resultant heat conduction equation, $\nabla\left(\lambda_i \nabla T\right) = S(x,z)$, has been solved numerically by a finite element method. Here, λ_i
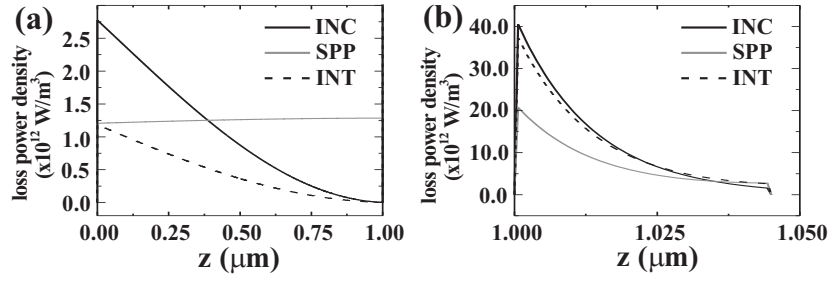
Figure (5.6): Power loss densities of the optical field (a) in the PMMA and (b) in the Au according to RPM calculations. The PMMA surface and the PMMA-Au interface are located at $z = 0.0$ μm and $z = 1.0$ μm, respectively. The losses (INC), (SPP), and (INT) are due to the incident field, the SPP, and the interference between the incident wave and the SPP.
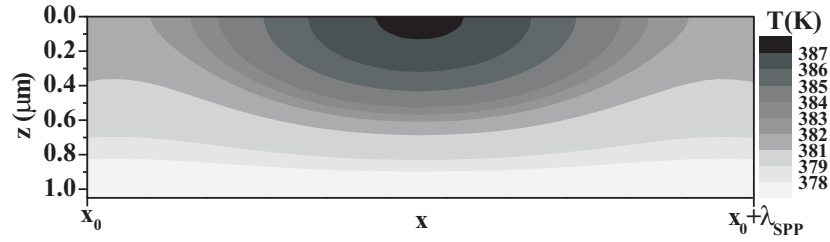
Figure (5.7): Stationary temperature field in the PMMA resulting from a heat conduction calculation assuming 1% coupling to the SPP and T=RT at the upper and lower boundary of the layer stack 1 mm air/1 μm PMMA/50 nm Au/500 μm Si/0.5 μm air. The temperature profile depends on the thermal contact to the sample holder. The assumed 0.5 μm air slit has the thermal resistivity of a carbon tape, approximately. The air-PMMA interface is located at $z = 0$. The T profile in air and in the substrate is not plotted.

denotes the heat conductivity of the ith material[3]. The heat source term is given by

$$S(x, z) = S_{\text{inc}}(z) + S_{\text{SPP}}(z) + S_{\text{int}}(x, z) \; , \tag{5.6}$$

where S_{inc} and S_{SPP} are the losses due to the incident field and the SPP, respectively. S_{int} denotes the loss that is periodic along $\vec{e_x}$ with a wavelength of λ_{SPP} due to damping of the SPP/incident laser interference pattern. In Fig. 5.7, the stationary temperature field for one period of λ_{SPP} is shown for the case of a 1% coupling to the SPP. Here, a mean temperature in the PMMA of 382 K is achieved which is slightly above the PMMA glass transition temperature at 378 K [302]. The lateral temperature gradient at the PMMA surface is about 1 K/μm. Taking the PMMA surface tension, $\gamma_{\text{PMMA}} = 4.11 \times 10^{-2}$ Nm^{-1} (at 20°C) [303], and its temperature coefficient, $\frac{\mathrm{d}\gamma}{\mathrm{d}T} = -\alpha = -7.6 \times 10^{-5}$ Nm^{-1}K^{-1} [303], into account it can be estimated that $\frac{\mathrm{d}\gamma}{\mathrm{d}x} = \frac{\mathrm{d}\gamma}{\mathrm{d}T}\frac{\mathrm{d}T}{\mathrm{d}x} = 76$ $\frac{\text{N}}{\text{m}^2}$. This surface tension gradient causes the PMMA to flow from hot to cold regions resulting in thickness undulations.

In the undulated PMMA layer, the Laplace pressure, $p = \kappa\gamma$, where κ is the local curvature and γ is the local surface tension, has to be position-independent in the stationary regime (cf. Eqn. 1.2 and Eqn. 5.2):

$$\mathrm{d}p = 0 = \kappa\frac{\mathrm{d}\gamma}{\mathrm{d}x} + \gamma\frac{\mathrm{d}\kappa}{\mathrm{d}x} \; . \tag{5.7}$$

---

[3]The following materials parameters were used: $\lambda_{\text{Air}} = 0.0245$ Wm^{-1}K^{-1}, $\lambda_{\text{PMMA}} = 0.16$ Wm^{-1}K^{-1}, $\lambda_{\text{Au}} = 317$ Wm^{-1}K^{-1} and $\lambda_{\text{Si}} = 148$ Wm^{-1}K^{-1}.

With the approximation $\kappa \approx \frac{\mathrm{d}^2 h}{\mathrm{d}x^2}$, where $h(x)$ describes the surface profile, one gets (cf. appendix C):

$$\frac{\mathrm{d}^3 h}{\mathrm{d}x^3} = \frac{\mathrm{d}^2 h}{\mathrm{d}x^2} \frac{\pi \alpha \Delta T}{\lambda \gamma} \sin \frac{2\pi x}{\lambda} \ . \tag{5.8}$$

Solving this equation numerically, one finds that the experimentally observed thickness undulation amplitude of Δh=40 nm requires a surface temperature variation of ΔT=5 K which is in agreement with the calculated temperature profile. Apparently, the system is stationary after 1 s of laser illumination. A larger amplitude of the thickness undulation would be obtained with a larger in-plane temperature gradient. This might be achieved by a higher laser power and/or with a pulsed laser. Yet, a mean temperature above the glass transition temperature of PMMA is required to ensure sufficient kinetics in the system.

Atomistic computer simulations were performed to describe the reaction pathway of the formation of thin film thickness undulations by periodic in-plane temperature gradients. In the KMC model portrayed in chapter 2 and appendix A (Ising-type potential with a NN interaction based on a f.c.c. lattice), a system with a $(256 \times 256 \times 64)$ simulation cell with periodic boundary conditions in the x-y-plane is considered. Referring to the scenario of Fig. 5.5 (a), the image series in Figs. 5.8 (a-d) depicts the reaction pathway of the thermocapillarity-induced ripple formation on a thin film. For the sake of simplicity, a stationary sinusoidal temperature profile, $T(x) = T_0 + \Delta T \sin(kx)$, is considered resembling the periodic temperature profile in Fig. 5.7 generated by the optical field. The mean temperature T_0=1800 K is high enough to supply sufficient thermal activation for a fast material transport. Due to the small size of the simulation cell a rather high temperature gradient ($\Delta T/T_0 = 0.2$) was used to achieve well-pronounced ripples with a short wavelength. According to Figs. 5.8 (a-d), a biased material transport from hot to cold regions in the film is observed, thus, surface ripples are formed with the periodicity of the temperature profile. This periodic material redistribution is in phenomenological agreement with the experiment. In Figs. 5.8 (e)
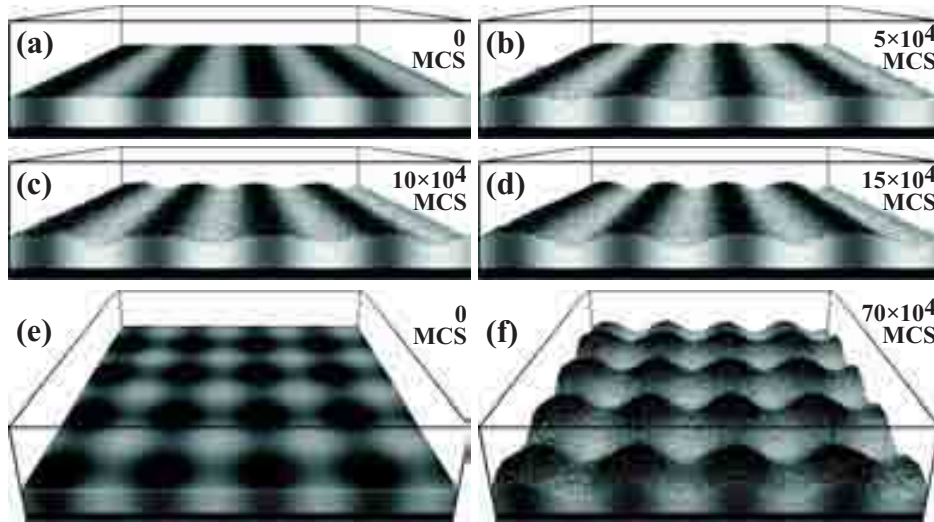
Figure (5.8): (a)-(d) Series of lattice KMC micrographs (perspective view) describing the thermocapillarity-induced ripple formation in a thin film. The color scale indicates the temperature in the film (dark gray = cold; light gray = hot). The black area illustrates the substrate. (e), (f) KMC snapshots on the formation of hillock arrays.

and (f), two sinusoidal in-plane temperature profiles are superimposed orthogonally, i.e. $T(x, y) = T_0 - \Delta T \sin(kx) \sin(ky)$. Resembling the experimental situation of Figs. 5.5 (b) and (c), this situation results in the formation of a hillock array on the surface. Patterns with equal spatial frequencies but smaller (larger) amplitudes were obtained assuming lower (higher) temperature gradients. To a certain extent, a controlled material redistribution seems to be possible by adjusting the steady-state temperature profile. Due to the general aspect of KMC simulations it is expected that this non-equilibrium fabrication process of regular thickness undulations may be applicable to other thin film systems, even in the sub-micrometer range.

In view of SPP-induced thermocapillarity, thin film structurization in the sub-micrometer range can indeed be anticipated. The wavelengths of SPP waves at metal/dielectric interfaces can reach the nanometer scale, whereas the frequencies remain in the optical range. The spatial resolution of this "SPP interference lithography" can be beyond the free-space diffraction limit of light which has been demonstrated recently for 1D and 2D periodical structures of 40 to 100 nm features that were patterned using interfering SPPs launched at 1D gratings [304, 305].

Nevertheless, it is challenging to provide static temperature fields in the sub-micrometer range with considerable T-gradients because of the heat conduction properties of most materials. Thus, for real processes a pulsed operation of the heat source ought to be considered instead so that the T-gradient is established only for a short duration before the systems thermally equilibrates and cools down before the new pulse can be applied. Therefore, the system must be coupled to a heat sink in order to keep the baseline temperature constant, i.e. a system is needed which is coupled to a thermal bath of lower temperature so that heat can dissipate from the system.

In conclusion, it has been demonstrated that long-range-ordered regular surface patterns on thin PMMA films can be obtained by SPP-induced thermocapillarity. Periodic in-plane temperature fields were achieved by the non-radiative damping of standing SPP waves at a PMMA/Au interface. Numerical calculations on optical power loss and heat conduction as well as kinetic Monte Carlo simulations provide strong evidence that thermal gradients are the driving force of the in-plane material transport.

5.2 Driven Evolution of Single-Crystalline Nanowires by Collisional Mixing

Fascinating and unexpected effects are observed if nanoscale solid-state systems are subject to collisional mixing (e.g. by ion irradiation) during their evolution at elevated temperature, as for instance, inverse Ostwald ripening, the shrinkage of nanocavities, or surface ripple formation by ion erosion some of which are outlined in section 2.8 where the implementation of a ballistic displacement algorithm for surface atoms into the lattice KMC method is described. It has been found that the stationary shape of NCs changes drastically if surface-near atoms are displaced at a rate ρ which defines the ratio between ballistic and thermally activated jump attempts (in ion irradiation scenarios ρ is a measure for the ion flux at constant temperature). In all simulations presented here, sputtering is *expressis verbis* not taken into account which refers for instance to a low-energy ion irradiation where merely ad-atoms are ballistically and isotropically generated but the sputtering yield is nearly zero (e.g. 150 eV Xe^+ onto Si
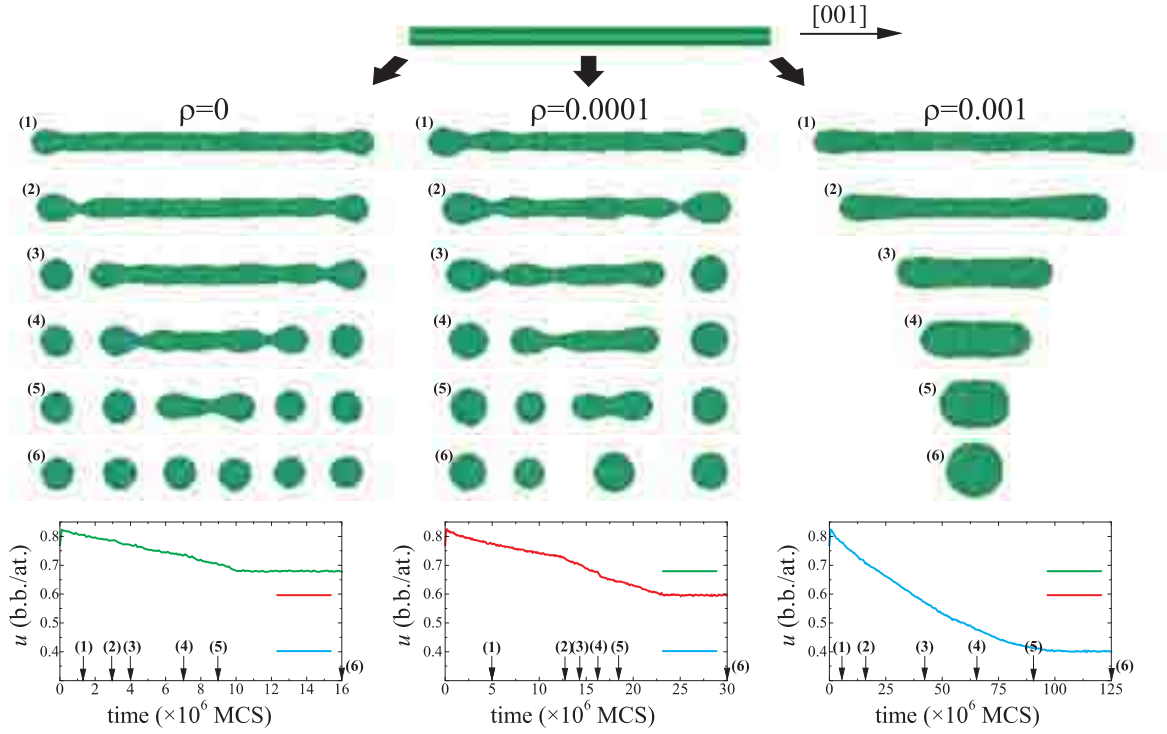
Figure (5.9): Lattice KMC micrographs and corresponding specific internal energy development $u(t)$ for the evolution of cylindrical structures of finite length (f.c.c. lattice, [001]-orientation, $\tilde{\varepsilon}_{NN,f.c.c.}=1.3$, $L=480$ a, $R_0=12$ a) at three values of $\rho=\{0; 0.0001; 0.001\}$.

with $Y\approx0.04$ according to TRIM simulations). In section 2.8, it has been concluded that in the stationary state the weighting of specific surface free energies is altered for $\rho>0$ compared to the pure thermal case $\rho=0$, i.e. in the frame of the present computer model facets emerge as confining surfaces under collisional mixing which are not present under quasi-equilibrium conditions ("ballistic crystal shapes"; cf. Figs. 2.20 and 2.21). Moreover, it was found that the ad-atom concentration c_s increases with increasing $\rho>0$ (cf. Fig. 2.19) which directly influences the material flux j_s causing material redistribution (cf. Eqn. 1.5). In short, collisional mixing of surface atoms drives the system by non-thermal excitation to energetically higher states (cf. Fig. 2.22), thereby, violating the detailed balance between ad-atom generation and annihilation.

Given the above remarks, it can be anticipated that the characteristics of the capillary instability of single-crystalline cylindrical structures are changed, particularly in view of the crystal orientation of these structures, if collisional mixing and thermally activated mass transport take place simultaneously.

As a first example, consider Fig. 5.9 where the shape evolution of a finite cylinder (f.c.c. lattice, [001]-orientation, $\tilde{\varepsilon}_{NN,f.c.c.}=1.3$, $L=480$ a, $R_0=12$ a) and the respective specific internal energy development $u(t)$ are drawn for three different values of $\rho=\{0; 0.0001; 0.001\}$. The case $\rho=0$ shows equal characteristics as discussed for cylinders of finite length in section 4.3, i.e. starting from the ends the rod disintegrates into a chain of NCs. For the two cases with $\rho>0$, however, the wavelength λ of the developing axisymmetric perturbations apparently increases with ρ, thus, the emerging NCs become larger and further separated. In the case $\rho=0.001$, the entire rod shrinks into a single NCs. This behavior suggests that the critical ratio ξ_c increases with ρ (cf. section 4.3).
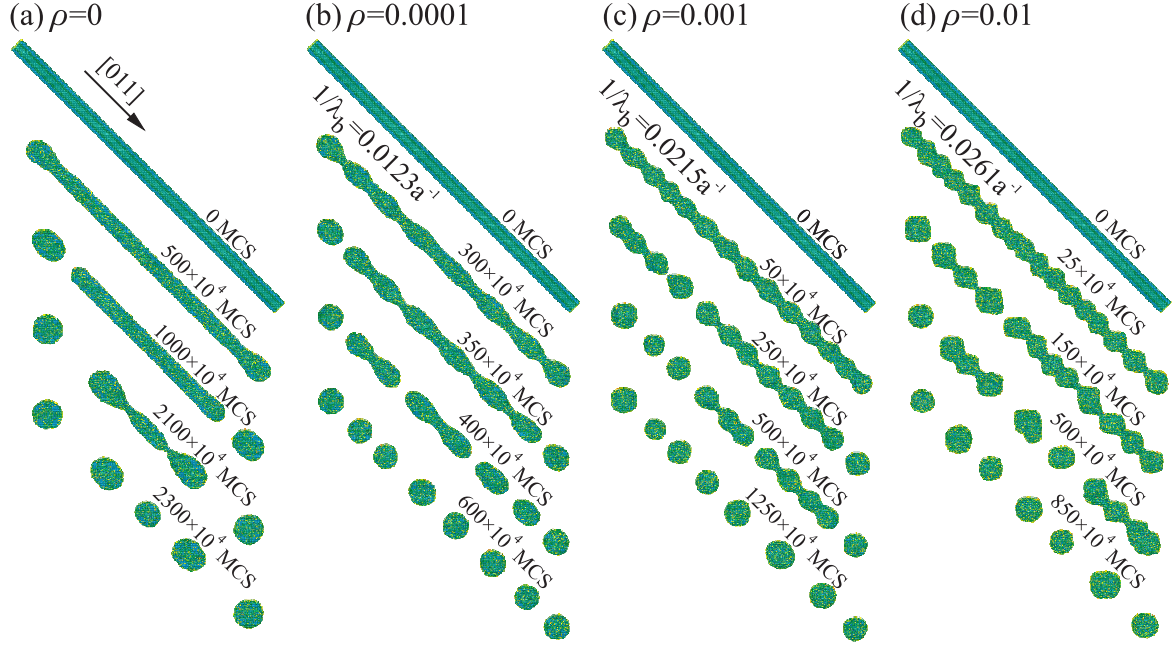
Figure (5.10): Lattice KMC micrographs depicting the evolution of cylindrical structures of finite length (f.c.c. lattice, [011]-orientation, $\tilde{\varepsilon}_{NN,f.c.c.}=1.3$, $L=650\,a$, $R_0=12\,a$) at four values of $\rho=\{0;0.0001;0.001;0.01\}$.
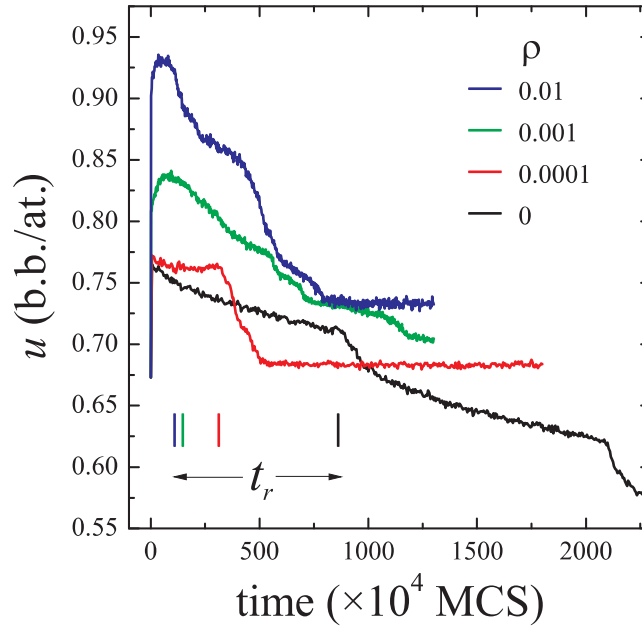
Figure (5.11): Specific internal energy development $u(t)$ for the respective series of lattice KMC micrographs depicted in Fig. 5.10.

Further it can be stated that parallel to the increase of the perturbation wavelength with maximum growth rate the rupture time t_r increases with ρ. These results can be interpreted in accordance with Fig. 2.22 where it was shown that collisional mixing excites the system energetically, i.e. in the present case the action of the capillary force which tends to relax the cylindrical structure during the Plateau-Rayleigh instability is counteracted and thereby retarded by collisional mixing (superposition of driving forces).
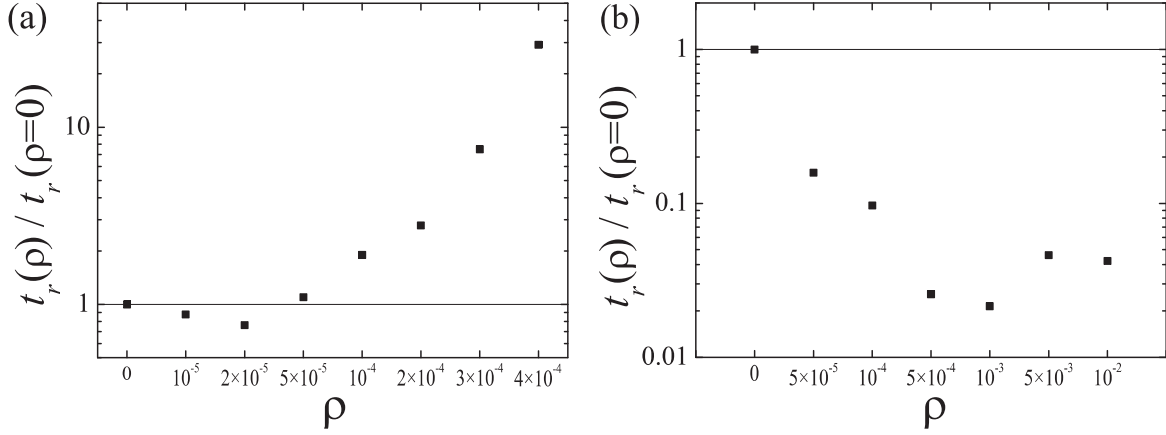
Figure (5.12):   Normalized rupture time $t_r(\rho)/t_r(\rho=0)$ for cylindrical structures (f.c.c. lattice; $\tilde{\varepsilon}_{NN,f.c.c.}$=1.3; R_0=12 a) with (a) [001]-orientation and (b) [011]-orientation.

The situation is different if finite cylinders of [011]-orientation are considered (cf. Fig. 5.10; f.c.c. lattice, $\tilde{\varepsilon}_{NN,f.c.c.}$=1.3, L=650 a, R_0=12 a). Here, it becomes obvious that collisional mixing can accelerate the dynamics of the Plateau-Rayleigh instability. In the initial stage of evolution, there appears a surface grooving effect caused by "ballistic facets" with (210)-orientation if one compares Fig. 5.10 (b-d) with (a) which reflects the quasi-equilibrium case where the capillary force acts solely. These {210}-facets which emerge under collisional mixing destabilize literally the {111}-facets which are the most stable ones under equilibrium conditions (cf. Fig. 2.20), thus, the stability of [011]-oriented NWs is overturned under collisional mixing. In view of the Plateau-Rayleigh instability, these quasi-axisymmetric and isodistant grooves act like surface perturbations with a wavelength λ_b. According to Figs. 5.10 (b-d), λ_b scales inversely with ρ. If $\lambda_b>\lambda_c$ (cf. Fig. 5.10 (b)) the Plateau-Rayleigh instability takes over λ_b as the perturbation wavelength with maximum growth rate and the cylinder disintegrates with the respective periodicity (like in the former case of a periodic temperature profile which stimulates the growth of a perturbation with a particular wavelength). However, if $\lambda_b<\lambda_c$ which is the case in Figs. 5.10 (c) and (d) λ_b first grows and soon after $\lambda_b\approx\lambda_c$ is reached the structures disintegrate into NC chains with nearly equal periodicity. Since the cylindrical nanostructure does not disintegrate for $\lambda_b(t=0) < \lambda_c$ (cf. section 4.1) there is a ripening process taking place ("groove coarsening") until $\lambda_b \approx \lambda_c$ is reached.

The development of the specific internal energy $u(t)$ for the KMC series shown in Fig. 5.10 is plotted in Fig. 5.11. Here, the interplay between capillary force, which tends to relax the structure, and the action of collisional mixing, which enables excitations of energetically unfavorable configurations, can be observed. Apparently, in the initial stage of evolution the specific internal energy increases drastically (excitation) the larger ρ becomes; i.e. the short-wavelength grooves cause an increase in the number of surface atoms on the [011]-oriented rod. The grooving effect of the ballistic facets causes a decrease in rupture time with growing ρ which can be explained by faster kinetics in the system due to enlarged ad-atom concentration and diffusivity contributing to higher material flux, therefore. Moreover, the wavelength of disintegration is near the critical one, i.e. the material has to be transported over shorter lengths than under comparable quasi-equilibrium conditions (ρ=0).

For infinite cylindrical structures a similar behavior is observed which is demonstrated in Fig. 5.12 and Fig. 5.13. In Fig. 5.12, the rupture time t_r is plotted as a
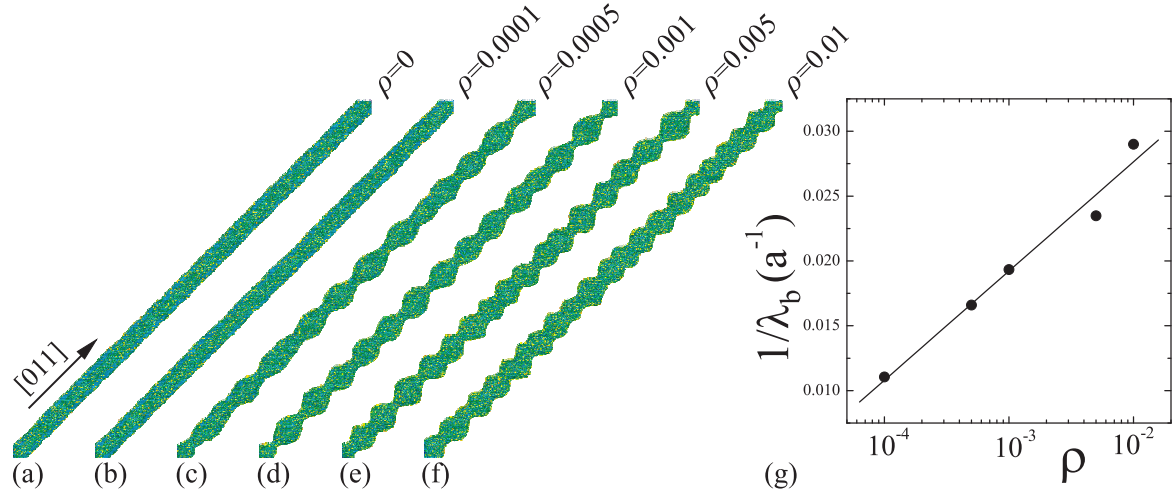
Figure (5.13): (a)-(f) Lattice KMC micrographs of the initial stage of the evolution of cylindrical structures (f.c.c. lattice, [110]-orientation, $\tilde{\varepsilon}_{NN,f.c.c.}$=1.3, L=650 a, R_0=12 a, t=1 × 10^5 MCS) which are subject to the system-inherent capillary force in superposition with collisional mixing for various values of ρ. The cylindrical structures appear sharpened at the ends; this phenomenon is due to the periodic boundary conditions applied to the simulation cell and is meaningless from a physical point of view. (g) The respective perturbation wavelength as a function of ρ.

function of ρ normalized to the case of quasi-equilibrium evolution (ρ=0) for [001]- and [011]-oriented cylindrical structures. In the case of [001]-orientation, it has to be stressed that there is a minimum for t_r in the interval $0 < \rho < 5 \times 10^{-4}$. At that low ρ-values the collisional mixing does not yet produce ballistic facets which are seen in Fig. 2.20 but merely isolated ad-atoms so that c_s is slightly enlarged which results in a moderately faster kinetics. For $\rho > 5 \times 10^{-4}$, however, the capillary instability of the [001]-oriented cylinder is retarded, whereas for the [011]-oriented one it is accelerated. In other words, these retardation and acceleration effects go along with lower/higher perturbation growth rates and longer/shorter wavelengths of the perturbations with maximum growth rates.

It has been seen in Figs. 5.10 (b-d) that the wavelength λ_b with which the ballistic {210}-facets cause grooving of the surface of [011]-oriented cylinders during the initial stage of evolution scales inversely with ρ. In Fig. 5.13, this tendency is more clearly seen for infinite [011]-oriented cylinders (f.c.c. lattice, $\tilde{\varepsilon}_{NN,f.c.c.}$=1.3, L=650 a, R_0=12 a) with various values of ρ after equal time (t=1 × 10^5 MCS). Obviously,

$$1/\lambda_b \propto \exp(\rho) \ , \tag{5.9}$$

which holds true over a large range of ρ (cf. Fig. 5.13 (g)).

On the first sight, the presented phenomena regarding collisional mixing effects on the capillary instability of cylindrical structures are not without contradiction: on the one hand ballistic {210}-facets destabilize [011]-oriented NW structures, on the other hand [001]-oriented ones are stabilized although {210}-facets ought to act in a similar manner there, too. This problem can be solved by the fact that the {111}-facets become much less stable than {001}- or {011}-ones under collisional mixing so that the tendency for {210}-facet-grooving is much lower for [001]-oriented cylindrical structures. Apparently, the action, the appearance, and the hierarchy of ballistic facets deserves examination in much more detail from the viewpoint of the lattice model

applied here. The discreteness of the KMC lattice limits the transferability of the results to real materials which preserve their crystallinity during collisional mixing, e.g. metals (but not semiconductors). However, it can be stated that structures which are relatively stable under quasi-equilibrium conditions because of confining facets with low surface tension can lose this stability under collisional mixing and vice versa. To prove this concept is a rather arduous task from an experimental perspective (ion irradiation experiments with quasi-zero sputtering yield) but also fundamental point of view (in reality, the ballistic generation of ad-atoms involves much more complex processes than just discrete displacements of atoms to empty NN lattice sites on the surface, e.g. the generation of multiple ad-atoms resulting from a single energetic collision or concerted effects). In this regard MD simulations, for example, can be of great help since they can provide more realistic results about the distribution of generated ad-atoms by single collision events. In the spirit of a multi-scale modeling ansatz (cf. section 1.4), the MD-ad-atom distributions could serve as an input for lattice KMC to study the long-term reaction path. Thereby, a more realistic behavior than presented here can be anticipated.

From the above results it can be concluded that collisional mixing as a type of non-equilibrium processing can change the morphology and the reaction pathways of nanoscale cylindrical systems tremendously. Although only structures with f.c.c. lattice were considered here, similar effects are anticipated for structures with other lattice types (cf. Fig. 2.21). A control of the morphological changes lies in the ratio ρ between ballistic and thermally activated jump rates (ion flux). By adjusting ρ one can drive the system along a path which corresponds to a macroscopic structure which would not emerge under quasi-equilibrium conditions. Here, cylindrical structures have mainly been discussed. However, this principle applies equally to structures of other geometries like thin films (ion-induced ripple formation [94, 188, 189, 190]) or perforated membranes (ion-beam sculpting [15, 306]).

Chapter 6

Summary and Major Statements

Formation and shape transformation of single-crystalline nanostructures due to the system-inherent capillary force in combination with external fields or forces have been investigated in the frame of this dissertation by means of atomistic computer simulations. The main emphasis has been put on nanostructures which have a cylindrical geometry such as nanowires (NWs), nanorods, or nanotubes. This work has been motivated by the ongoing trend to miniaturize functional structures which will cause a general rise in surface-to-volume ratios, thus, rendering solid-state capillary phenomena increasingly important in the future. It has been demonstrated that on the one hand diffusion-mediated capillary processes can be of practical use in view of non-conventional nanostructure fabrication methods based on self-organization mechanisms, on the other hand they can destroy the integrity of nanostructures which can go along with the failure of functionality. Additionally, it has been illustrated that capillarity-induced shape transformations are effected and can thereby be controlled by applied fields and forces (guided or driven evolution).

For the exploration (search, description, and prediction) of reaction pathways of nanostructure shape transformations, kinetic Monte Carlo (KMC) simulations have been the method of choice. Since the employed KMC code is founded on a cellular automaton principle, the spatio-temporal development of lattice-based N-particle systems (N up to several million) could be followed for time spans of several orders of magnitude, while considering local phenomena due to atomic-scale effects like diffusion, nucleation, dissociation, or ballistic displacements.

The major statements (*Thesen*) of this dissertation can be summarized as follows:

1.) The lattice KMC method is suitable to describe realistic reaction pathways regarding the shape evolution of single-crystalline nanostructures. In particular, this atomistic simulation method accounts for:

- diffusion-mediated material transport,
- phase separation of supersaturated solid-solutions,
- effects related to the Gibbs-Thomson equation like coarsening of particle ensembles or the shrinkage of hollow-core particles,
- substrate wetting/dewetting,
- surface tension anisotropy in accordance with the underlying lattice,

- thermocapillary phenomena, and
- ballistic displacements of atoms due to collisional mixing.

2.) In a combined top-down/bottom-up approach, embedded NW structures can be fabricated in a controlled manner by ion beam synthesis (IBS): Starting from a particular 3D implantation profile, which is generated by a focused ion beam (FIB) line scan implantation, the supersaturated system undergoes a complex series of capillarity-driven relaxation processes the time and length scales of which extend over several orders of magnitude:

   (a) phase separation via nucleation or spinodal decomposition,
   (b) coarsening (Ostwald ripening-like), and
   (c) interface smoothing.

   In order to form a NW structure, the FIB line scan implantation profile ought to have a cylindrical shape. Moreover, the degree of supersaturation in the center of the implantation profile has to exceed a critical value. The NW formation can be perturbed by various effects, e.g. the loss of implanted material by target absorption. The formation of a NW structure by FIB-based IBS corresponds to a transient state of the system on its relaxation pathway towards equilibrium (cf. statement 4).

3.) Realistic 3D FIB line scan implantation profiles can be simulated by adopting the well-known TRIM code, which is based on the binary collision approximation, to the peculiarities of a Gaussian ion current density profile of a FIB (beam width in the sub-100 nm range) taking dynamical changes of the target into account, for example, local surface erosion. For the studied ion-target combinations, $Co(60\,keV) \rightarrow Si$ and $Si(60\,keV) \rightarrow SiO_2$, the 2D nuclear damage profiles have an inverse-Ω shape.

4.) A single-crystalline NW structure is subject to the Plateau-Rayleigh instability. In order to reduce surface free energy, the system develops symmetric thickness undulations along the longitudinal axis. The undulated NW structure disintegrates (NW rupture) at the undulation necks leaving a chain of isolated nanoclusters (NCs) behind. In accordance with former analytical studies by Nichols and Mullins the rupture time is found to scale with the forth power of the initial NW radius. However, the capillary instability of NWs is found to be subject to thermal fluctuations leading to a spatially inhomogeneous undulation amplitude growth which results in irregular NC chains. The relative standard deviations of NC distance and NC volume are found in the 10% to 25% range.

5.) Two characteristic stages of the capillary instability of a single-crystalline NW can be deduced from the atomistic computer experiments performed:

   (a) development of thickness undulations and
   (b) fragmentation into a NC chain.

6.) The capillary instability of single-crystalline NW structures can be effected by initial thickness undulations which may impose their undulation wavelength on the system as the wavelength of NW disintegration. Thereby, the geometry of the resulting NC chain can be predetermined.

7.) The capillary instability of single-crystalline NW structures is subject to surface tension anisotropy effects at low temperatures. Hence, NW structures with similar macroscopic shape but with different crystallographic orientation may show diverse behavior regarding rupture time and undulation wavelength.

8.) The capillary instability of supported single-crystalline NWs is retarded in the case of an attractive interaction to the substrate.

9.) The capillary instability of a finite single-crystalline NW (rod) is a superposition of a swelling process at the ends of the rod with a Plateau-Rayleigh-like process in between. Two distinct reaction pathways are found which are determined by the initial length-to-radius ratio ξ:

   (a) the spheroidization into a single NC ($\xi < \xi_{crit}$) or
   (b) the fragmentation into two or more NCs ($\xi > \xi_{crit}$).

10.) The characteristics of the capillary instability of a hollow-core NW (tube) are determined by the weighting between volume and surface diffusion. In the volume diffusion dominated case the hollow core shrinks by a net outward diffusion of vacancies forming a solid NW. In the surface diffusion dominated case the hollow cylindrical core (inverse NW) evolves according to Plateau-Rayleigh into a chain of voids (pea-pod-like structure).

11.) The diffusion-mediated capillary force is suggested as dominant mechanism for the phenomenon of the draining of Cu-filled nanotubes which has been observed recently by Toimil-Molares and coworkers.

12.) The capillary instability of a torus is a superposition of a shrinkage process in radial direction and a Plateau-Rayleigh-like process in azimuthal direction. Two distinct reaction pathways can be anticipated which are determined by the initial ratio of the principal radii $\rho = R/r$.

13.) Toroidal structures can be achieved in a self-organizing manner by the capillarity-induced dewetting of circular discs.

14.) Crossing points of NW junctions are sites of advanced capillary instability.

15.) The capillary instability of cylindrical nanostructures can be employed to fabricate various functional structures, e.g.

   • nanofluidic channels and channel networks in single-crystalline matrices or
   • structures suitable as multi-terminal single-electron-transistor devices, NW transistors, or surface-plasmon-polariton (SPP) interferometers.

16.) Periodic temperature profiles along the longitudinal axis of a NW give rise to thermocapillary effects (biased material redistribution from hot to cold regions) which can guide the evolving NW structure along a specific reaction pathway. The evolving NW structure takes over the periodicity of the applied temperature profile if it is close to the periodicity of the structure-inherent capillary instability. Thereby, thermal fluctuations can be suppressed. The regularity of the obtained NC chain scales with the applied temperature gradient.

17.) Likewise, the thermocapillary force can be employed to achieve regular patterns on thin films. In-plane temperature gradients in initially flat films trigger a biased material redistribution from hot to cold regions resulting in the formation of surface ripples or hillock arrays (hot areas become concave; cold ones become convex).

18.) Periodic in-plane temperature fields can be achieved by the non-radiative damping of standing SPP waves at a PMMA/metal interface. Numerical calculations on optical power loss and heat conduction as well as KMC simulations provide strong evidence that thermal gradients are the driving force of the in-plane material transport resulting in long-range-ordered regular surface patterns on thin PMMA films. This suggests a novel method of SPP-lithography.

19.) Collisional mixing of surface atoms leads to alterations in the surface tension hierarchy of crystal facets, thus, the shapes of single-crystalline NCs can strongly deviate from the equilibrium crystal shape (Wulff construction); the term "ballistic crystal shape" is suggested.

20.) The superposition of ballistic and thermal driving forces (collisional mixing combined with the system-inherent capillary force) can change the morphology and the reaction pathways of nanoscale cylindrical systems tremendously: Single-crystalline NW structures which are relatively stable due to confining facets with low surface tension under the sole action of the capillary force can lose their stability under collisional mixing ("ballistic faceting") and vice versa. A control of the morphological changes lies in the ratio ρ between ballistically and thermally activated jump rates (weighting of driving forces). By adjusting $\rho > 0$ one can drive the system along a specific reaction pathway (non-equilibrium processing), which corresponds to a macroscopic structure that would not emerge under quasi-equilibrium conditions.

Appendix A

Lattice Kinetic Monte Carlo Encoding on the Bit Level

The lattice KMC method considers an artificial and spatially discretized microworld (cf. chapter 2) that consists of a rigid n-dimensional lattice ($n \in \mathbb{N}, n \geq 1$) which can be populated by atomic beings of different species. The atoms are allowed to migrate on the vertices of that rigid lattice with a defined probability according to their energetic state which is determined by the occupation of the lattice sites in their neighborhood.

In the 1970's, very efficient computer codes based on very fast bitwise instructions emerged in order to study lattice gas cellular automata and other spatially discrete systems [307, 308, 309]. Thus, reasonably large systems could be considered using the rather modest computational facilities at that time. With the advent of processors with clock frequencies in the GHz range and gigabytes of main memory the bit encoding can be used to simulate very large systems even on desktop computers. In the framework of this dissertation, KMC simulations of systems with up to several million active atoms on lattices consisting of a few hundred million lattice sites were carried out on single microprocessor units. For such a vast number of active particles, a very compact, fast, and efficient algorithm is needed

1. to store the spatial coordinates of the particles,

2. to determine the occupation of their neighboring lattice sites, and

3. to mimic particle migration on the lattice.

In order to take advantage of the development of modern compilers for the 64-bit processor architecture, the fundamental KMC routines that were originally written by Karl-Heinz Heinig in PASCAL in the 1990's, their specifications according to the physical scenarios and questions at hand, and all data evaluation tools were (re-)written in C/C++. The compilation was carried out with the Intel C/C++ compiler (versions 8.1 and 9.0) which turned out to produce the fastest executables on both Intel as well as AMD processors[1]. In the following, the bit encoding of the lattice KMC method is briefly illustrated.

---

[1]Either Intel Pentium IV, Intel Xeon, AMD Athlon64 FX55, or AMD Opteron processors were used with clock frequencies up to 3.4 GHz. Each processor was equipped with at least 1 GByte main memory.
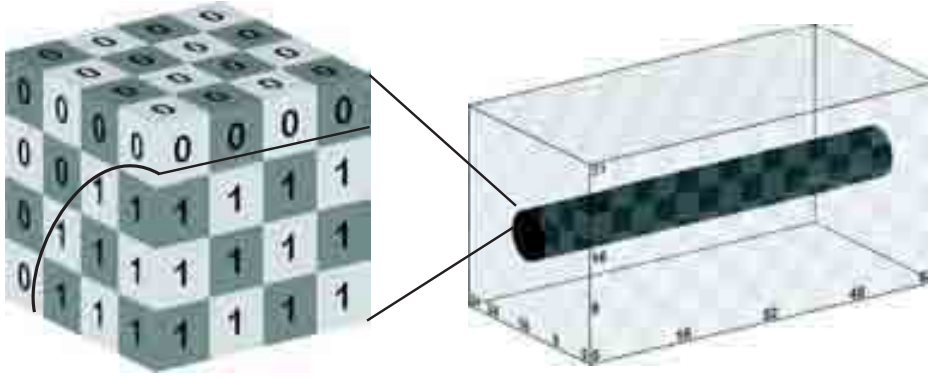
Figure (A.1): Cylindrical body with x_1-orientation embedded in the center of the simulation cell. The atoms forming the cylinder are represented in the bit-space by ones, whereas the surrounding matrix is represented by zeros.

The most compact way to represent atoms on a rigid lattice is the encoding on the bit level, i.e. occupied or empty lattice sites are expressed by ones or zeros, respectively [115, 308, 310]. The simplest case is a unary system, i.e. a system which contains particles of one sort only. Then, the rigid lattice consisting of α lattice sites which are populated by β particles ($\beta \leq \alpha$) can be interpreted as a single binary number with α digits that contains β ones and ($\alpha - \beta$) zeros. The zeros can be considered to be the system's "vacuum" or an inert matrix in which the active particles are embedded (cf. a GIF animation[2]). In Fig. A.1, a frequent example is depicted where an object of cylindrical geometry, whose main axis is x_1-oriented, is located in the center of a simulation cell with ($64{\times}32{\times}32$) sites.

For illustration, a 3D simple cubic lattice with ($512{\times}512{\times}512$) lattice sites in "real-space" is represented by a binary number of $2^{27}{=}134'217'728$ digits in "bit-space" for which a memory of only $2^{24}{=}16'777'216$ bytes is needed. Processors with 32- or 64-bit architectures are available at present, thus, the binary number representing the system can be constructed from 4- or 8-byte unsigned integers (cf. Fig. A.2). These basic bit-space building blocks have been constructed in such a way that they correspond to a ($4{\times}4{\times}2$) or a ($4{\times}4{\times}4$) subset of the 3D real-space.

Hence, one bit-space building block contains not only information about a specific particle of interest but also partially about its close neighborhood which may speed

---

[2]The GIF animation is located at: `http://www.roentzsch.org/RealBit/index.html`

<div style="text-align:center">system with
($64{\times}32{\times}32$) sites   ($4{\times}4{\times}4$) cube   rigid cubic lattice</div>
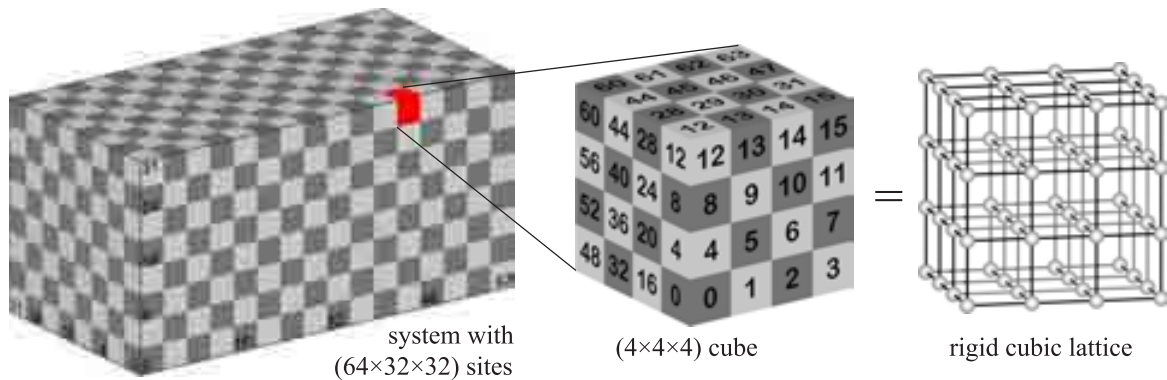
Figure (A.2): A schematic representation of a system with ($64{\times}32{\times}32$) sites of a rigid lattice. Consequently, the simulation cell is subdivided into ($16{\times}8{\times}8$) 64-bit-cubes.

bit-wise operation	instruction in C/C++
conjunction (AND)	&
disjunction (OR)	|
negation (NOT)	~
disambiguation (XOR)	^
shift left	<<
shift right	>>

Table (A.1): Overview of bitwise operations and their corresponding instructions in C/C++.

up the KMC code during the determination of atomic configurations in the jump routine [115]. Consequently, a single array of unsigned integers can represent the whole system.

Due to the sort of physical scenarios investigated, almost all KMC simulations were conducted at temperatures far below the transition temperature, i.e. the systems mostly displayed coexistence of phases (cf. Fig. 2.4). Thus, it was possible to compress the system-representing binary number very efficiently so that in many cases a memory of only some kilobytes is sufficient for the long-term storage of a single state of the whole system.

The bit encoding has even a greater advantage than merely storing data of atomic positions very compactly. Much more important is the fact that bitwise operations are used to mimic atomic migration to NN lattice sites, i.e. to execute the jumps of 1's in the bit-space (cf. Tab. A.1). These instructions are executed with the clock frequency of the processor, i.e. some 10^9 times per second, thus, atomic migration can be modeled very efficiently.

In the present work, only cubic lattice types where used which are illustrated in Fig. A.3. Accordingly, all cubic Bravais lattices as well as the diamond structure can be constructed from the simple cubic virtual lattice with the lattice spacing a. Hence, the NN distances for all the lattices can easily be written: $d_{s.c.} = a$; $d_{b.c.c.} = a\sqrt{3}$; $d_{f.c.c.} = a\sqrt{2}$; $d_{diam.} = a\sqrt{3}$.

At the beginning of a simulation, the bit space has to be filled with 1's according to the initial distribution of atoms in real space. In order to set an atom onto the ith digit (i.e. lattice site) of the binary number BN, only two bitwise logical operations have to be performed (cf. Tab. A.2).

If less than 50 % of the lattice sites are occupied during a simulation, the selection
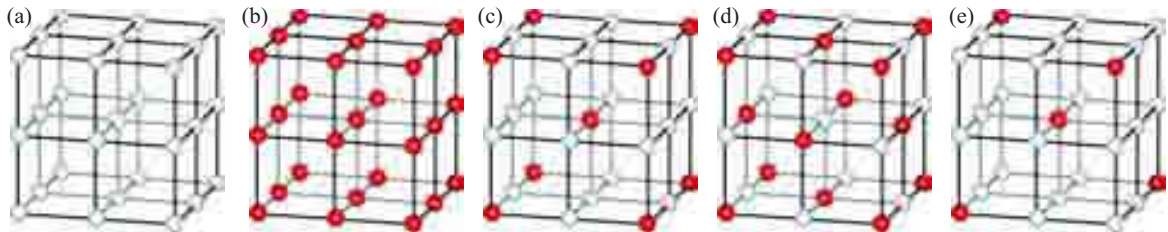
Figure (A.3): The rigid cubic lattices deployed in the KMC simulations: (a) The sites of the virtual lattice represented by the unsigned integer array from which the allowed sites (in red) of (b) the s.c. lattice, (c) the b.c.c. lattice, (d) the f.c.c. lattice, and (e) the diamond structure can be abstracted. For example, the instruction (x1^x2^x3)=0 "cuts" the f.c.c. lattice out of the virtual lattice where x1, x2, and x3 represent the spatial coordinates of the lattice sites.

	digit	α-1	...	i+4	i+3	i+2	i+1	i	i-1	i-2	i-3	i-4	...	0
A:	BN	0	...	0	0	0	0	0	0	0	0	0	...	0
B:	1<<i	0	...	0	0	0	0	1	0	0	0	0	...	0
	A | B	0	...	0	0	0	0	1	0	0	0	0	...	0

Table (A.2): Setting a single atom onto the ith site of the empty bit-space without affecting the other sites: `BN|(1<<i)`.

of the jumping atoms becomes very inefficient if the lattice sites are selected randomly in the bit-space without knowing in advance if they are empty or occupied. Thus, a double-book-keeping system is beneficial [113], i.e. in addition to the system-representing integer array also a list of the real-space coordinates of all atoms is stored (cf. Fig. A.4). The random selection of the atom which carries out a jump attempt can therefore be done within this list.

If an atom is randomly selected from the list it has to be found in the bit-space. Thus, transformations are needed to convert real-space into bit-space coordinates. For the transformation of the real-space coordinates of the ith atom $(x_{i1}; x_{i2}; x_{i3})$ into the digit of the i-containing ($4 \times 4 \times 4$) cube the following operation is required:

```
(xi1&3) | ((xi2&3)<<2) | ((xi3&3)<<4) .
```

Throughout a KMC simulation the atoms attempt to jump to neighboring lattice sites. In some simulations, up to 10^{14} jump attempts were carried out. The realization of a jump, i.e. the atom's migration in the bit space is a two-step procedure. At first the jumping atom has to be erased from its initial lattice site i and then it has to be written to the final empty lattice site $(i+1)$. Translated in the language of binary numbers these two procedures can easily be expressed by bitwise logical instructions (cf. Tab. A.3 and Tab. A.4).

Naturally, only finite systems can be considered in KMC simulations. Therefore, the simulation cell boundaries deserve closer consideration. System boundaries can be impermeable (passive or reflective), partially absorbing, or periodic depending on the physical scenario. In the present work, mostly periodic boundary conditions were applied, i.e. the simulation cell is periodically repeated in all spatial directions. For instance, atoms that jump over the right simulation cell boundary automatically jump again into the simulation cell at the left boundary. Thus, the number of atoms is conserved. Fig. A.5 depicts an example of a simulation cell that is periodically repeated
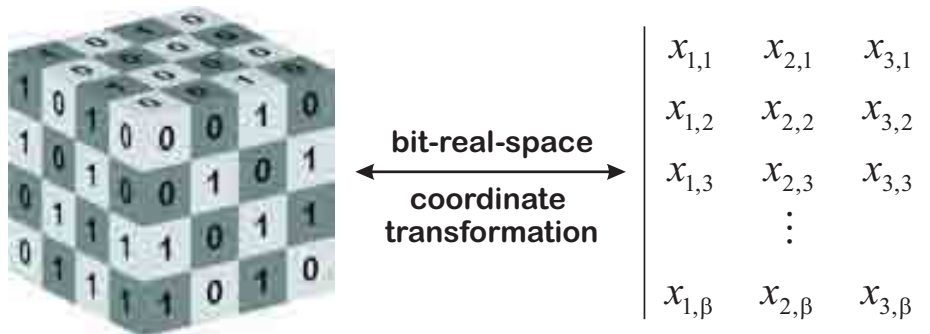
Figure (A.4): A schematic representation of the strategy of "double-book-keeping", i.e. keeping track of all active atoms in bit-space and in real-space coordinates.

	digit	α-1	...	i+4	i+3	i+2	i+1	i	i-1	i-2	i-3	i-4	...	0
A:	BN	1	...	1	1	0	0	1	1	1	0	0	...	1
B:	~(1<<i)	1	...	1	1	1	1	0	1	1	1	1	...	1
	A & B	1	...	1	1	0	0	0	1	1	0	0	...	1

Table (A.3): Erasing a single atom from the initial site i of the bit space without affecting the other sites: `BN & (~(1<<i))`.

	digit	α-1	...	i+4	i+3	i+2	i+1	i	i-1	i-2	i-3	i-4	...	0
A:	BN	1	...	1	1	0	0	0	1	1	0	0	...	1
B:	1<<(i+1)	0	...	0	0	0	1	0	0	0	0	0	...	0
	A | B	1	...	1	1	0	1	0	1	1	0	0	...	1

Table (A.4): Putting a single atom on the final site $(i+1)$ of the bit space without affecting the other sites: `BN | (1<<(i+1))`.

in two dimensions. However, there are other scenarios which are of interest, particularly in simulations of the FIB-based IBS of NW structures which are described in chapter 3. Supposing that ions of one sort are implanted into a voluminous target that contains virtually no impurities of that sort. During the phase separation the lion share of the implanted ion diffuses into the bulk of the target which acts as strong sink until the solid solubility for the implanted element has been reached. This case refers to strongly absorbing simulation cell boundaries. On the other hand, if the ions are implanted into a thin film atop a substrate, which acts as diffusion barrier, the out-diffusion into the small volume of that film would practically not influence the phase separation in the implanted region because the equilibrium concentration in the film is easily reached so that enough material remains for phase separation and NW structure formation. This example would refer to a reflective cell boundary towards the bottom of the simulation cell.
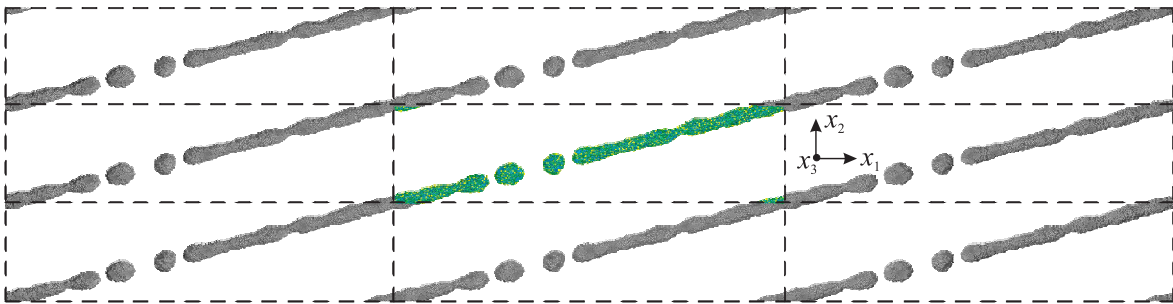
Figure (A.5): Example for periodic boundary conditions of a 3D lattice KMC simulation cell. For the sake of clarity, the periodicity of the cell is illustrated for the two directions x_1 and x_2 only.

Appendix B

Extended View:
The Plateau-Rayleigh Instability in
n-dimensional Space

The dimensionality of the space in which we live is related to the most fundamental questions of human existence, thus, it has been subject to philosophical, theological, and last but not least scientific debate for many centuries. To the knowledge of the author, the founding stone of human reflection on higher-dimensional spaces and in particular their projection onto subspaces was laid by Plato in the renown myth of the cave in the seventh book of his *Politeia* [311].

During the present studies concerning capillary-driven morphological transformations of cylindrical nanostructures the question arose whether hypercylinders are also subject to a Plateau-Rayleigh-like instability [312]. The evolution of hypercylindrical objects is particularly interesting in cosmology in view of black strings. Recently, it has been shown analytically by Cardoso and Dias that the key features of the instability of black strings can be reproduced using a thermodynamic analogy – namely the classical view of Plateau and Rayleigh – where the surface area is interpreted as the area of the event horizon [313]. However, real experiments on the evolution of higher-dimensional Euclidean systems is indeed challenging if not impossible. In contrast, the lattice KMC method provides simple means to execute computer experiments in systems with a spatial dimensionality larger than three.

The general description of the topology of a n-dimensional hypercylinder with $(n-1)$ spatial directions with radius R_0 and a longitudinal axis along x_n reads

$$\left[\sum_1^{n-1} (x_i - x_{i,0})^2 \right]^{1/2} \leq R_0 \ . \tag{B.1}$$

Cardoso and Dias found that the critical wavelength λ_c above which a n-dimensional hypercylinder becomes unstable against harmonic $(n-1)$-dimensional hypersurface perturbations reads [313]:

$$\frac{2\pi R_0}{\lambda_c} = \sqrt{n - 2} \ . \tag{B.2}$$

For $n=2$, the result is a stripe which – in analogy to a thin film (cf. Fig. B.1) – is not subject to capillarity-driven disintegration: $\lambda_c = \infty$. The stripe only disintegrates if

145
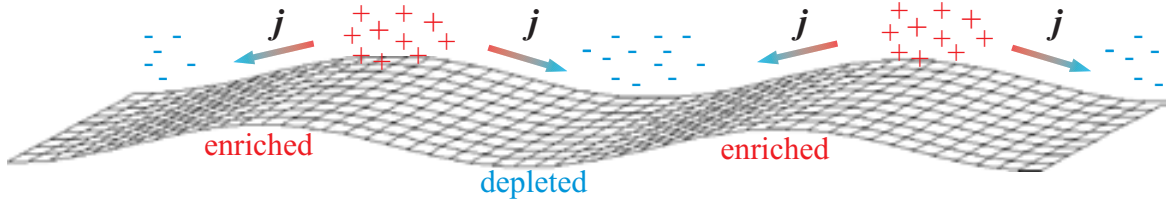
Figure (B.1): A schematic representation of a wavy surface layer whose undulations always decay irrespective of their wavelength or amplitude under the action of the capillary force: the material flux j is directed towards regions of lower chemical potential (i.e. from convex to concave areas).

the system overcomes an energetic barrier (nucleation of stable holes). For the case of $n=3$, a cylinder is given whose classical Plateau-Rayleigh instability has been discussed above. By means of lattice KMC simulations using a s.hc. lattice, the case $n=4$ is examined in the following; the aim is to show that hypercylinders are in principle subject to capillary instabilities based on the characteristics of the NN-Ising model.

Before the actual results on 4D hypercylinders are presented the reader is prepared regarding the perception of cylinders in the 4D Euclidean space. In the literature, there are various surveys on higher dimensional objects and how they can be visualized [314, 315]. Very often a dimensional analogy is used, i.e. one has to imagine how artificial beings that "live" in a 2D world would perceive 3D objects – in this connection the two key words are "projection" and "slicing". 3D objects can be projected onto a 2D subsystem, e.g. a finite cylindrical rod (R_0, L) projected on a 2D plane would lead to the impression of a circle of radius R_0 (if projected along the longitudinal axis) or of a $(2R_0 \times L)$-rectangle (if projected in a direction orthogonal to the longitudinal axis). Moreover, if the finite 3D cylinder is sliced through a 2D space (a plane) it is perceived again as circle that appears and disappears (if sliced along the longitudinal axis) or as a rectangle of length L and a width that grows from zero (=line) to the maximum value $2R_0$, shrinks again to zero (=line) and then disappears (if sliced in a direction orthogonal to the longitudinal axis). In Fig. B.2, the 3D-through-2D slicing is visualized for a cylinder which is periodically undulated along its longitudinal axis $(R_{\min}, R_{\max})$. Slicing (cf. red contours in Figs. B.2 (b) and (c)) results in a "pulsating" circle whose radius varies between $R_{\min}$ and $R_{\max}$ (if sliced along the longitudinal axis) or in a complex contour of growing and merging islands that swells towards an undulated stripe of maximum width, that shrinks again and separates into islands which disappear finally (if sliced radially). In analogy, if a 4D hypercylinder (with a 3D hypersurface) which is undulated periodically along the longitudinal axis is sliced through a 3D subspace it is perceived as a pulsating sphere whose radius varies between $R_{\min}$ and $R_{\max}$ or as a complex 3D contour depicted in Fig. B.3.
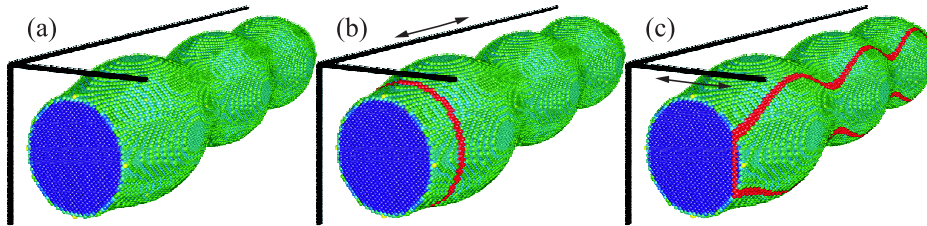
Figure (B.2): (a) Cylindrical body with harmonic undulations along its longitudinal axis (perspective view) which can be also perceived by 2D slicing (b) along the longitudinal axis as pulsating circle and (c) in the orthogonal direction as an undulated 2D contour (cf. text for details).
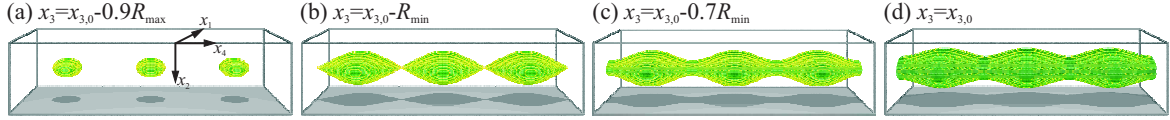
Figure (B.3): Schematic drawings of a 4D hypercylindrical body with harmonic undulations along its longitudinal axis x_4 which can be perceived by slicing through the 3D subspace along the radial direction as a series of 3D hypersurface contours (cf. text for details).

For the lattice KMC simulation of the capillary instability of a 4D hypercylinder a simple hypercubic Euclidean lattice is assumed, i.e. a lattice site has 8 NN sites. From the view point of the KMC algorithm, the 4D simulations rely on the same principles as their 3D counterparts (NN-Ising dynamics based on the conserved-order-parameter model with Metropolis transition probability, cf. chapter 2). Like 3D NWs, 4D hypercylinders are faceted due to the underlying lattice. The facets, however, are much more pronounced than in 3D systems since the number of NNs of surface atoms is relatively larger which also explains the higher critical temperature of the 4D and 5D NN-Ising models compared to the 3D version (cf. Tab. 2.1). For example, atoms of the (0001)-oriented 3D hypersurface have seven NNs (compared to eight NNs of 4D bulk atoms), whereas atoms of the (001)-oriented 2D surface have five NNs (compared to six NNs of 3D bulk atoms). Consequently, the surface energy of (0001)-facets in 4D hyperspace is larger than of (001)-facets in 3D space.

From a thermodynamical perspective, the free evolution leads to the minimization of the system's free energy regardless of the dimensionality of the system. In other words, the principles of capillarity aiming at the minimization of the free hypersurface energy ought to hold true in the present context. A typical simulation of the capillary instability of a [0001]-oriented 4D hypercylinder with initial radius R_0=4 a is shown in the image series of Fig. B.4 ($\tilde{\varepsilon}_{NN,s.hc.}$=1.9). Here, 3D countours of the three spatial coordinates (x_1, x_2, x_4) are plotted (cf. Eqn. B.1). The visualization along x_3 is realized by plotting the 3D contours for discrete x_3-values in descending order (numbers on the left hand side ranging from 4 to -4). Due to the faceting of the hypersurface the undulation build-up does not appear as roundly as schematically depicted in Fig. B.3. The first rupture of the 4D hypercylinder is seen in the right half of Fig. B.4 (c). Again, the reduction of the system's free energy is approximately represented by the reduction of internal energy since the simulation is carried out at a temperature low compared to the critical one, i.e. $F(t) = U(t) - TS(t) \approx U(t)$ (cf. section 2.2 and Tab. 2.1). The time development of $u(t) = U(t)/N$ is plotted in Fig. B.5. It shows the same characteristics like in 3D systems (cf. Fig. 4.10 (a)), namely two stages of evolution: undulation build-up (nearly a plateau in $u(t)$) and subsequent fragmentation into 4D hyperparticles. The first rupture is indicated again by a discontinuity in $u(t)$. Due to the very limited number of simulation runs reliable data on distance and size of the resulting 4D hyperparticles can not be given here. For this purpose, intensive simulations are required which were beyond the present scope.

For future investigations on hyperspace capillarity, lattice KMC simulations in even higher-dimensional systems are suggested. Moreover, KMC simulations based on lattices other than the s.hc. lattice could be implemented, e.g. the face-centered hypercubic lattice [60], in order to study crystal anisotropy effects. Although this subject is of very academic character on the first sight, experimental insight into hyperspace thermodynamics and kinetics might be very useful, particularly in view of cosmology [313, 316].
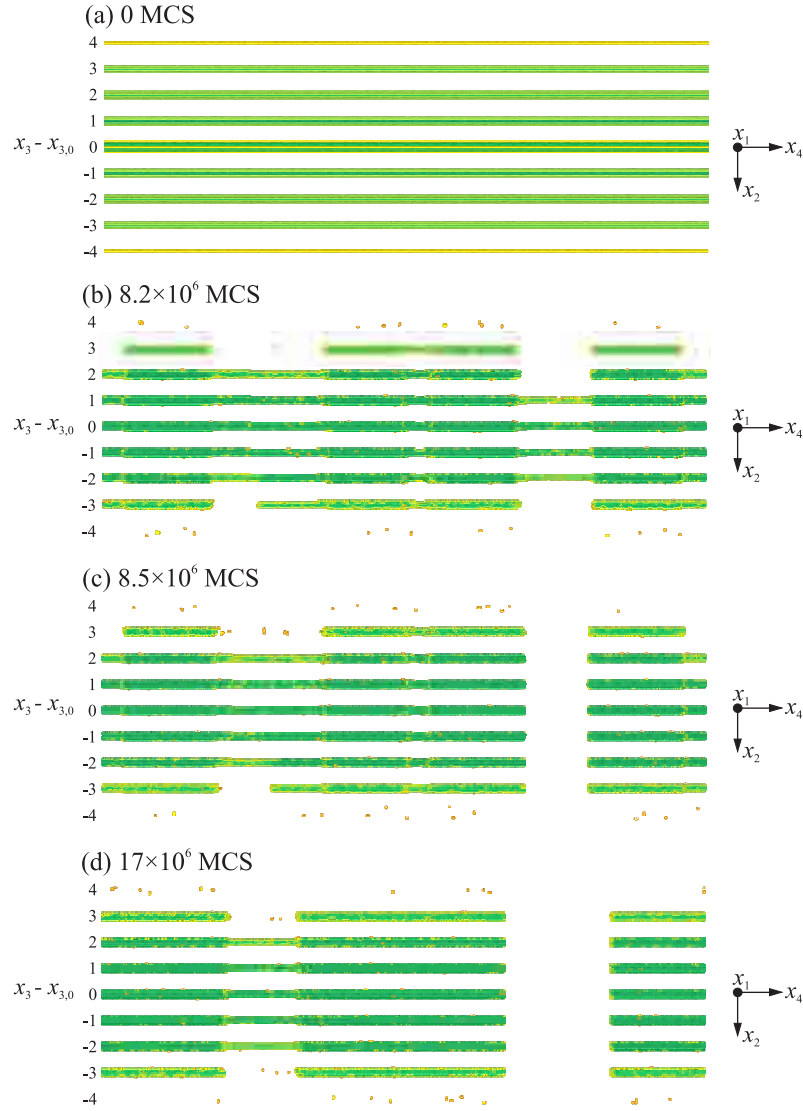
Figure (B.4): Lattice KMC micrographs on the capillary instability of a 4D hypercylinder ($\tilde{\varepsilon}_{NN,s.hc.}$=1.9; R_0=4 a; [0001]-orientation). 3D plots of the coordinates (x_1, x_2, x_4) are presented for each stage of evolution (longitudinal view); each 3D plot is individually depicted for discrete values of x_3 in descending order (numbers on the left hand side ranging from $(x_3 - x_{3,0})$ = 4 a to −4 a).
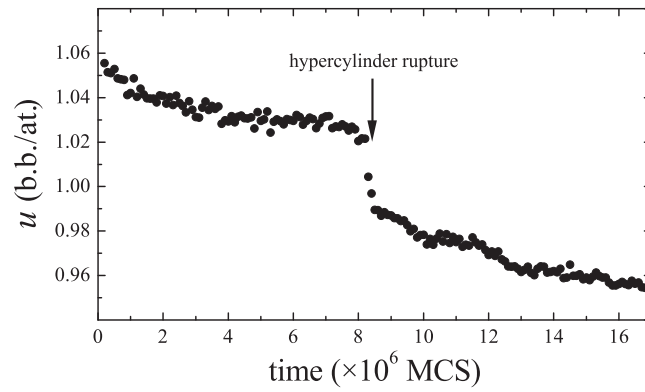
Figure (B.5): Specific internal energy plotted vs. simulation time of the capillarity-driven instability of the 4D hypercylinder depicted in Fig. B.4.

Appendix C

Surface Profile Calculation

For the calculation of the stationary undulation amplitude on the PMMA surface (cf. subsection 5.1.2) the following PMMA materials parameters are taken into account:

- PMMA surface tension: $\gamma = 4.11 \times 10^{-2}\,\text{N/m}$ (at 20°C)

- PMMA surface tension temperature coefficient: $\alpha = 7.6 \times 10^{-5}\,\text{N/m·K}$

- SPP wavelength: $\lambda = 10 \times 10^{-6}\,\text{m}$

- temperature difference in the PMMA film: $\Delta T = 0.5\,\text{K}$

It is assumed that the SPP wave, that is supported by the PMMA/Au interface, is damped non-radiatively in the PMMA and in the Au beneath. This damping causes a periodic in-plane temperature gradient in the PMMA. Thus, we can write in a harmonic approximation

$$T(x) = T_0 + \Delta T \cos\left(qx\right) \quad \text{where} \quad q = \frac{2\pi}{\lambda}\ . \tag{C.1}$$

In the experiment, undulations of the PMMA film thickness h are found which are periodic in x-direction with the periodicity of the temperature profile, thus,

$$h(x) = h(x + \lambda)\ . \tag{C.2}$$

It is proposed that the temperature gradient causes a material flux along the thermal gradient. Here, the stationary case is considered, i.e. it will be examined in the following what maximal thickness undulation can be expected for a given a stationary in-plane temperature gradient in the PMMA film. In the stationary case, the Laplace pressure p_L which is the product of curvature κ and surface tension γ has to be the same everywhere in the layer, thus,

$$\frac{\mathrm{d}p_L(x)}{\mathrm{d}x} = \frac{\mathrm{d}\kappa(x)}{\mathrm{d}x}\gamma(x) + \kappa(x)\frac{\mathrm{d}\gamma(x)}{\mathrm{d}x} = 0\ . \tag{C.3}$$

In most polymers, the temperature dependence of the surface tension reads:

$$\gamma(T) = \gamma_0 + \alpha\left(T_0 - T\right)\ . \tag{C.4}$$

Apparently, α represents the entropy contribution to the surface free energy (cf. Eqn. 2.14). Likewise, it is found for other types of material that the surface tension

decreases with increasing temperature, e.g. for copper $\gamma_{Cu} = (1.304 - 0.289 \times 10^{-3}[(T - 1356)/\text{K}]) \, \text{Nm}^{-1}$ [317].

Eqn. C.3 can be rewritten

$$\frac{\mathrm{d}\kappa(x)}{\mathrm{d}x}\gamma(x) = \kappa(x) \underbrace{\frac{\mathrm{d}\gamma(T)}{\mathrm{d}T(x)}}_{-\alpha} \frac{\mathrm{d}T(x)}{\mathrm{d}x} \quad . \tag{C.5}$$

The curvature $\kappa(x)$ of an arbitrary function $f(x)$ is given by

$$\kappa(x) = \frac{\frac{\mathrm{d}}{\mathrm{d}x}\left(\frac{\mathrm{d}f(x)}{\mathrm{d}x}\right)}{\sqrt{\left(1 + \left(\frac{\mathrm{d}f(x)}{\mathrm{d}x}\right)^2\right)^3}} \quad . \tag{C.6}$$

In the case of small amplitudes of the thickness undulations compared to the lateral wavelength of the SPP wave, i.e. for small surface curvatures, Eqn. C.6 can be approximated for $h(x)$ simply by

$$\kappa(x) \approx \frac{\mathrm{d}^2 h(x)}{\mathrm{d}x^2} = h''(x) \quad . \tag{C.7}$$

Thus, a differential equation of third order for $h(x)$ using Eqn. C.5 is obtained:

$$h'''(x) = h''(x) \times \frac{\alpha \Delta T q}{\gamma} \sin(qx) \quad . \tag{C.8}$$

It is evident that Eqn. C.8 is fulfilled by

$$h''(x) = \exp\left(\frac{-\alpha \Delta T}{\gamma}\cos(qx)\right) + C_1 \quad , \tag{C.9}$$

where C_1 is a constant which can be determined numerically using

$$C_1 = -\frac{1}{2\pi}\int_0^\lambda \exp\left(\frac{-\alpha \Delta T}{\gamma}\cos(qx)\right)\mathrm{d}x \quad . \tag{C.10}$$

With this equation for C_1 it can be assured that the average curvature of $h(x)$ is zero. The integration of Eqn. C.9 can not be done analytically, thus, it has to be solved numerically. To find a direct numerical solution for $h(x)$ with Eqn. C.9, $h''(x)$ is approximated. Since $h''(x)$ is a symmetric[1] and periodic function it can be developed in a Fourier series only with cosine elements. Thus,

$$h''(x) = \frac{a_0}{2} + \sum_1^\infty a_n \cos(nqx) \quad , \tag{C.11}$$

where the a_n's denote the Fourier coefficients

$$a_n = \frac{4}{\lambda}\int_0^{\lambda/2} h''(x)\cos(nqx)\mathrm{d}x \quad . \tag{C.12}$$

---

[1] i.e. $h''(x) = h''(-x)$

The integration of the Fourier series expression for $h''(x)$ was performed numerically using Maple 9. Taking the parameters given above into account one obtains in the stationary regime an approximate crest-to-though distance of 6 nm. The amplitude of the PMMA thickness undulation scales linearly with ΔT, thus, for the experimentally measured crest-to-though distance of approximately 40 nm a ΔT of approximately 5 K is needed in the stationary regime.

Bibliography

[1] M. E. Toimil-Molares, A. G. Balogh, T. W. Cornelius, R. Neumann & C. Trautmann. *Fragmentation of nanowires driven by Rayleigh instability*. Appl. Phys. Lett. **85** (2004) 5337.

[2] T. Sato, I. Mizushima, S. Taniguchi, K. Takenaka, S. Shimonishi, H. Hayashi, M. Hatano, K. Sugihara & Y. Tsunashima. *Fabrication of Silicon-on-Nothing Structure by Substrate Engineering Using the Empty-Space-in-Silicon Formation Technique*. Jpn. J. Appl. Phys. **43** (2004) 12.

[3] P. Sutter, W. Ernst, Y. S. Choi & E. Sutter. *Mechanisms of thermally induced dewetting of ultrathin silicon-on-insulator*. Appl. Phys. Lett. **88** (2006) 141924.

[4] E. Dornel, J.-C. Barbe, F. de Crecy, G. Lacolle & J. Eymery. *Surface diffusion dewetting of thin solid films: Numerical method and application to Si/SiO₂*. Phys. Rev. B **73** (2006) 115427.

[5] M. Strobel, K.-H. Heinig, W. Möller, A. Meldrum, D. S. Zhou, C. W. White & R. A. Zuhr. *Ion beam synthesis of gold nanoclusters in SiO₂: Computer simulations versus experiments*. Nucl. Instrum. Methods B **147** (1999) 343.

[6] M.-O. Ruault, F. Fortuna, H. Bernas & O. Kaitasov. *In situ study of in-beam cobalt silicide growth in silicon*. Nucl. Instrum. Methods B **84** (1994) 135.

[7] M. Moseler & U. Landman. *Formation, Stability, and Breakup of Nanojets*. Science **289** (2000) 1165.

[8] J. Eggers. *Dynamics of Liquid Nanojets*. Phys. Rev. Lett. **89** (2002) 084502.

[9] Y. S. Choi, S. J. Kim & M.-U. Kim. *Molecular dynamics of unstable motions and capillary instability in liquid nanojets*. Phys. Rev. E **73** (2006) 016309.

[10] P. W. Voorhees. *The Theory of Ostwald Ripening*. J. Stat. Phys. **38** (1985) 231.

[11] M. Strobel, K.-H. Heinig & W. Möller. *Three-dimensional domain growth on the size scale of the capillary length: Effective growth exponent and comparative atomistic and mean-field simulations*. Phys. Rev. B **64** (2001) 245422.

[12] J. R. Krenn. *Nanoparticle waveguides: Watching energy transfer*. Nature Mater. **2** (2003) 210.

[13] A. Polman & H. A. Atwater. *Plasmonics: optics at the nanoscale*. Mater. Today **8** (2005) 56.

[14] L. Röntzsch, K.-H. Heinig, J. A. Schuller & M. L. Brongersma. *Thin film patterning by surface-plasmon-induced thermocapillarity*. Appl. Phys. Lett. **90** (2007) 097703.

[15] J. Li, D. Stein, C. McMullan, D. Branton, M. J. Aziz & J. Golovchenko. *Nanoscale Ion Beam Sculpting*. Nature **412** (2001) 166.

[16] K.-H. Heinig, B. Schmidt, M. Strobel & H. Bernas. *Inverse Ostwald Ripening and Self-Organization of Nanoclusters due to Ion Irradiation*. Mater. Res. Soc. Symp. Proc. **647** (2001) O14.6.

[17] K.-H. Heinig, T. Müller, B. Schmidt, M. Strobel & W. Möller. *Interfaces under ion irradiation: growth and taming of nanostructures*. Appl. Phys. A **77** (2003) 17.

[18] M.-O. Ruault, F. Fortuna, H. Bernas, M. C. Ridgway & J. S. Williams. *How nanocavities in amorphous Si shrink under ion beam irradiation: An in situ study*. Appl. Phys. Lett. **81** (2002) 2617.

[19] H. J. Frost & K. C. Russell. *Recoil resolution and particle stability under irradiation*. J. Nucl. Mater. **103-104** (1981) 1427.

[20] B. Schmittmann & R. K. P. Zia. *Driven diffusive systems: An introduction and recent developments*. Phys. Rep. **301** (1998) 45.

[21] P.-G. de Gennes, F. Brochard-Wyart & D. Quere. *Capillarity and Wetting Phenomena: Drops, Bubbles, Pearls, Waves* (Springer, New York, 2004).

[22] J. A. F. Plateau. *Statique expérimentale et théorique des liquides soumis aux seules forces*

moléculaires (Gauthiers-Villars, Paris, 1873).

[23] J. W. S. Rayleigh. *On the Instability of Jets.* Proc. London Math. Soc. **10** (1879) 4.

[24] C. Marangoni. *Ueber die Ausbreitung der Tropfen einer Flüssigkeit auf der Oberfläche einer anderen.* Ann. Phys. Chem. **143** (1871) 337.

[25] W. W. Mullins. *Solid Surface Morphologies Governed by Capillarity.* In W. D. Robertson & N. A. Gjostein (eds.) *Metal Surfaces: Structure, Energetics and Kinetics*, chap. 2, p. 17 (American Society for Metals, Metal Parks, 1963).

[26] C. Herring. *Surface Tension as a Motivation for Sintering.* In W. E. Kingston (ed.) *The Physics of Powder Metallurgy*, chap. 8, p. 143 (McGraw-Hill, New York, 1951).

[27] W. Leszynski (ed.) *Powder Metallurgy* (Interscience Publishers, New York, 1961).

[28] G. C. Kuczynski. *Theory of Solid State Sintering.* In W. Leszynski (ed.) *Powder Metallurgy*, p. 11 (Interscience Publishers, New York, 1961).

[29] A. J. W. Moore. *Thermal Faceting.* In W. D. Robertson & N. A. Gjostein (eds.) *Metal Surfaces: Structure, Energetics and Kinetics*, chap. 5, p. 155 (American Society for Metals, Metal Parks, 1963).

[30] A. L. Pranatis & L. Seigle. *Sintering of Wire Compacts.* In W. Leszynski (ed.) *Powder Metallurgy*, p. 53 (Interscience Publishers, New York, 1961).

[31] C. Herring. *Some Theorems on the Free Energies of Crystal Surfaces.* Phys. Rev. **82** (1951) 87.

[32] W. W. Mullins. *Theory of thermal grooving.* J. Appl. Phys. **28** (1957) 333.

[33] W. W. Mullins. *Flattening of a Nearly Plane Solid Surface due to Capillarity.* J. Appl. Phys. **30** (1959) 77.

[34] W. W. Mullins & R. F. Sekerka. *On the thermodynamics of crystalline solids.* J. Chem. Phys. **82** (1985) 5192.

[35] The International Technology Roadmap for Semiconductors (ITRS), `http://www.itrs.net/Links/2005ITRS/Home2005.htm`.

[36] G. E. Moore. *Cramming more components onto integrated circuits.* Electronics **38** (1965) 114.

[37] R. Nuryadi, Y. Ishikawa & M. Tabe. *Formation and ordering of self-assembled Si islands by ultrahigh vacuum annealing of ultrathin bonded silicon-on-insulator structure.* Appl. Surf. Sci. **159-160** (2000) 121.

[38] R. Waser (ed.) *Nanoelectronics and Information Technology* (Wiley-VCH, Weinheim, 2003).

[39] C. J. Hawker & T. P. Russell. *Block Copolymer Lithography: Merging Bottom-Up with Top-Down Processes.* Mater. Res. Soc. Bull. **30** (2005) 952.

[40] Y. Ishikawa, Y. Imai, H. Ikeda & M. Tabe. *Pattern-induced alignment of silicon islands on buried oxide layer of silicon-on-insulator structure.* Appl. Phys. Lett. **83** (2003) 3162.

[41] C. Jahan, O. Faynot, L. Tosti & J. M. Hartmann. *Agglomeration control during the selective epitaxial growth of Si raised sources and drains on ultra-thin silicon-on-insulator substrates.* J. Cryst. Growth **280** (2005) 530.

[42] P. Bellon. *Nonequilibrium Roughening and Faceting of Interfaces in Driven Alloys.* Phys. Rev. Lett. **81** (1998) 4176.

[43] W. Schmitz (ed.) *Computersimulation in der Physik*, vol. 20 of *IFF-Ferienkurse* (FZ-Jülich, Jülich, 1989).

[44] D. Raabe. *Computational Materials Science: The Simulation of Materials, Microstructures and Properties* (Wiley-VCH, Weinheim, 1998).

[45] K. Ohno, K. Esfarjani & Y. Kawazoe. *Computational Materials Science*, vol. 129 of *Springer Series in Solid-State Science* (Springer, Berlin, 1999).

[46] S. Blügel (ed.) *Computational Condensed Matter Physics*, vol. 37 of *IFF-Ferienkurse* (FZ-Jülich, Jülich, 2006).

[47] D. P. Landau & K. Binder. *A Guide to Monte Carlo Simulations in Statistical Physics* (Cambridge University Press, Cambridge, 2000).

[48] J. R. Rodgers & D. Cebon. *Materials Informatics.* Mater. Res. Soc. Bull. **31** (2006) 975.

[49] V. Vitek & D. J. Srolovitz (eds.) *Atomistic Simulation of Materials Beyond Pair Potentials* (Plenum Press, New York, 1989).

[50] M. Griebel, S. Knapek, G. Zumbusch & A. Caglar. *Numerische Simulation in der Moleküldynamik* (Springer, Berlin, 2004).

[51] D. Frenkel & S. Berend. *Understanding Molecular Simulation*, vol. 1 of *Computational Science*

Series (Academic Press, San Diego, 2002), 2nd edn.

[52] M. Posselt, F. Gao & D. Zwicker. *Atomistic study of the migration of di- and tri-interstitials in silicon.* Phys. Rev. B **71** (2005) 245202.

[53] L. Koci, E. M. Bringa, D. S. Ivanov, J. Hawreliak, J. McNaney, A. Higginbotham, L. V. Zhigilei, A. B. Belonoshko, B. A. Remington & R. Ahuja. *Simulation of shock-induced melting of Ni using molecular dynamics coupled to a two-temperature model.* Phys. Rev. B **74** (2006) 012101.

[54] E. Bringa. Lawrence Livermore National Laboratory, Livermore, California.

[55] I. Mizushima, T. Sato, S. Taniguchi & Y. Tsunashima. *Empty-space-in-silicon technique for fabricating a silicon-on-nothing structure.* Appl. Phys. Lett. **77** (2000) 3290.

[56] N. Metropolis, A. W. Rosenbluth, M. N. Rosenbluth, A. H. Teller & E. Teller. *Equation of State Calculations by Fast Computing Machines.* J. Chem. Phys. **21** (1953) 1087.

[57] K. Kawasaki. *Kinetics of Ising models.* In C. Domb & J. L. Lebowitz (eds.) *Phase Transitions and Critical Phenomena*, vol. 2, chap. 11, p. 443 (Academic Press, London, 1972).

[58] T. Ala-Nissila, R. Ferrando & S. C. Ying. *Collective and single particle diffusion on surfaces.* Adv. Phys. **51** (2002) 949.

[59] M. E. J. Newman & G. T. Barkema. *Monte-Carlo Methods in Statistical Physics* (Clarendon Press, Oxford, 1999).

[60] D. A. Wolf-Gladrow. *Lattice-Gas Cellular Automata and Lattice Boltzmann Models*, vol. 1725 of *Lecture Notes in Mathematics* (Springer, Berlin, 2000).

[61] S. Wolfram. *A New Kind of Science* (Wolfram Media, Champaign, 2002).

[62] K. A. Brakke. *The Surface Evolver.* Exp. Math. **1** (1992) 141.

[63] R. Phillips. *The Modeling of Interfaces: Atoms or Continua?* JOM – J. Min. Met. Mater. Soc. **47(3)** (1995) 37.

[64] W. J. Boettinger, J. A. Warren, C. Beckermann & A. Karm. *Phase Field Simulation of Solidification.* Ann. Rev. Mater. Res. **32** (2002) 163.

[65] G. B. McFadden, A. A. Wheeler, R. J. Braun, S. R. Coriell & R. F. Sekerka. *Phase-field models for anisotropic interfaces.* Phys. Rev. E **48** (1993) 2016.

[66] R. F. Sekerka. *Equilibrium and growth shapes of crystals: how do they differ and why should we care?* Cryst. Res. Technol. **40** (2005) 291.

[67] W. Lu & Z. Suo. *Symmetry breaking in self-assembled monolayers on solid surfaces: Anisotropic surface stress.* Phys. Rev. B **65** (2002) 085401.

[68] A. Finel, D. Maziere & M. Veron (eds.) *Thermodynamics, Microstructures and Plasticity*, vol. 108 of *NATO Science Series II: Mathematics, Physics and Chemistry* (Kluwer, Dordrecht, 2003).

[69] R. A. Enrique, K. Nordlund, R. S. Averback & P. Bellon. *Nonequilibrium self-organization in alloys under irradiation leading to the formation of nanocomposites.* Nucl. Instrum. Methods B **202** (2003) 206.

[70] P. Bellon. *Kinetic Monte Carlo Simulations in Crystalline Alloys: Principles and Selected Applications.* In A. Finel, D. Maziere & M. Veron (eds.) *Thermodynamics, Microstructures and Plasticity*, vol. 108 of *NATO Science Series: II. Mathematics, Physics and Chemistry*, p. 395 (Kluwer Academic Publishers, Dordrecht, 2003).

[71] W. Ebeling. Humboldt University Berlin, Berlin, Germany. Private communication.

[72] J. E. Geguzin. *Lebender Kristall* (VEB Deutscher Verlag für Grundstoffindustrie, Leipzig, 1984).

[73] K. Binder & D. W. Herrmann. *Monte Carlo Simulation in Statistical Physics*, vol. 80 of *Solid-State Sciences* (Springer, Berlin, 2002), 4th edn.

[74] A. F. Voter. *Introduction to the kinetic Monte Carlo method.* In K. E. Sickafus, E. A. Kotomin & B. P. Uberuaga (eds.) *Radiation Effects in Solids*, vol. 235 of *NATO Science Series: II. Mathematics, Physics and Chemistry*, chap. 1, p. 1 (Springer, Dordrecht, 2007).

[75] S. J. Mitchell & D. P. Landau. *Phase Separation in a Compressible 2D Ising Model.* Phys. Rev. Lett. **97** (2006) 025701.

[76] T. A. Abinandanan, F. Haider & G. Martin. *Computer simulations of diffusional phase transformations: Monte Carlo algorithm and application to precipitation of ordered phases.* Acta Mater. **46** (1998) 4243.

[77] M. Athenes, P. Bellon & G. Martin. *Effects of atomic mobilities on phase separation kinetics: A Monte-Carlo study.* Acta Mater. **48** (2000) 2675.

[78] J.-M. Roussel & P. Bellon. *Vacancy-assisted phase separation with asymmetric atomic mobility:*

Coarsening rates, precipitate composition and morphology. Phys. Rev. B **63** (2001) 184114.

[79] F. Soisson & G. Martin. *Monte Carlo simulations of the decomposition of metastable solid solutions: Transient and steady-state nucleation kinetics.* Phys. Rev. B **62** (2000) 203.

[80] A. F. Voter, F. Montalenti & T. C. Germann. *Extending the Time Scale in Atomistic Simulation of Materials.* Ann. Rev. Mater. Res. **32** (2002) 321.

[81] R. Akis, D. K. Ferry & C. B. Musgrave. *Kinetic lattice Monte Carlo simulations of processes on the silicon (100) surface.* Physica E **19** (2003) 183.

[82] A. L. Magna, S. Coffa & L. Colombo. *A lattice kinetic Monte Carlo code for the description of vacancy diffusion and self-organization in Si.* Nucl. Instrum. Methods B **148** (1999) 262.

[83] R. A. Sutton & G. B. Schaffer. *An atomistic simulation of solid state sintering using Monte Carlo methods.* Mater. Sci. Eng. A **335** (2002) 253.

[84] C. C. Battaile & D. J. Srolovitz. *Kinetic Monte Carlo Simulation of Chemical Vapor Deposition.* Ann. Rev. Mater. Res. **32** (2002) 297.

[85] J. P. DeVita, L. M. Sander & P. Smereka. *Multiscale kinetic Monte Carlo algorithm for simulating epitaxial growth.* Phys. Rev. B **72** (2005) 205421.

[86] G. H. Gilmer, H. Huang, T. D. de la Rubia, J. D. Torre & F. Baumann. *Lattice Monte Carlo models of thin film deposition.* Thin Solid Films **365** (2000) 189.

[87] S. A. Barnett & A. Rockett. *Monte Carlo simulations of Si(001) growth and reconstruction during molecular beam epitaxy.* Surf. Sci. **198** (1988) 133.

[88] T. Michely & J. Krug. *Islands, Mounds and Atoms*, vol. 42 of *Springer Series in Surface Science* (Springer, Berlin, 2004).

[89] J. H. He, C. A. Carosella, G. K. Hubler, S. B. Qadri & J. A. Sprague. *Kinetic Monte Carlo simulations of nanoscale compositional patterning during film growth of phase-separated systems.* Phys. Rev. B **73** (2006) 235406.

[90] T. Kawamura. *Monte Carlo simulation of thin film growth on Si surfaces.* Prog. Surf. Sci. **44** (1993) 67.

[91] S. W. Levine, J. R. Engstrom & P. Clancy. *A kinetic Monte Carlo study of the growth of Si on Si(100) at varying angles of incident deposition.* Surf. Sci. **401** (1998) 112.

[92] J. M. Pomeroy, J. Jacobsen, C. C. Hill, B. H. Cooper & J. P. Sethna. *Kinetic Monte Carlo molecular dynamics investigations of hyperthermal copper deposition on Cu(111).* Phys. Rev. B **66** (2002) 235412.

[93] J. E. Rubio, M. Jaraiz, I. Martin-Bragado, J. M. Hernandez-Mangas, J. Barbolla & G. H. Gilmer. *Atomistic Monte Carlo simulations of three-dimensional polycrystalline thin films.* J. Appl. Phys. **94** (2003) 163.

[94] E. Chason, W. L. Chan & M. S. Bharathi. *Kinetic Monte Carlo simulations of ion-induced ripple formation: Dependence on flux, temperature, and defect concentration in the linear regime.* Phys. Rev. B **74** (2006) 224103.

[95] K. Binder. *Ordering of the Face-Centered-Cubic Lattice with Nearest-Neighbor Interaction.* Phys. Rev. Lett. **45** (1980) 811.

[96] W. Schweika. *Disordered Alloys*, vol. 141 of *Springer Tracts in Modern Physics* (Springer, Berlin, 1998).

[97] M. Müller & K. Albe. *Lattice Monte Carlo simulations of FePt nanoparticles: Influence of size, composition, and surface segregation on order-disorder phenomena.* Phys. Rev. B **72** (2005) 094203.

[98] H. Bernas, J.-P. Attané, K.-H. Heinig, D. Halley, D. Ravelosona, A. Marty, P. Auric, C. Chappert & Y. Samson. *Ordering Intermetallic Alloys by Ion Irradiation: A Way to Tailor Magnetic Media.* Phys. Rev. Lett. **91** (2003) 077203.

[99] C. Bichara, S. Crusius & G. Inden. *Monte Carlo analysis of order-disorder reactions in binary alloys with hexagonal structure.* Physica B **179** (1992) 221.

[100] A. Kerrache, H. Bouzara, M. Zemirli, V. Pierron-Bohnes, M. C. Cadeville & M. A. Khan. *Monte-Carlo simulation of order-disorder kinetics in 2D and fcc binary alloys.* Comp. Mater. Sci. **17** (2000) 324.

[101] M. Kozlowski, R. Kozubski, V. Pierron-Bohnes & W. Pfeiler. *$L1_0$-ordering kinetics in FePt nano-layers: Monte Carlo simulation.* Comp. Mater. Sci. **33** (2005) 287.

[102] R. Weinkamer, P. Fratzl, H. S. Gupta, O. Penrose & J. L. Lebowitz. *Using kinetic Monte Carlo*

simulations to study phase separation in alloys. Phase Transit. **77** (2004) 433.

[103] B. Yang, M. Asta, O. N. Mryasov, T. J. Klemmerb & R. W. Chantrell. *Equilibrium Monte Carlo simulations of A1-L1$_0$ ordering in FePt nanoparticles.* Scripta Mater. **53** (2005) 417.

[104] J.-M. Roussel & P. Bellon. *Self-diffusion and solute diffusion in alloys under irradiation: Influence of ballistic jumps.* Phys. Rev. B **65** (2002) 144107.

[105] J.-W. Liu & P. Bellon. *Patterning and ordering in driven alloys with coupled conserved and nonconserved order parameters.* Phys. Rev. B **66** (2002) 020303.

[106] G. Martin, P. Bellon & F. Soisson. *Modelling diffusion-controlled kinetics in equilibrium and driven alloys.* J. Comput. Aid. Mater. Des. **3** (1996) 187.

[107] F. Soisson. *Kinetic Monte Carlo simulations of radiation induced segregation and precipitation.* J. Nucl. Mater. **349** (2006) 235.

[108] K. Binder. *Monte Carlo Study of Entropy for Face-Centered Cubic Ising Antiferromagnets.* Z. Phys. B Con. Mat. **45** (1981) 61.

[109] M. K. Phani, J. L. Lebowitz & M. H. Kalos. *Monte Carlo studies of an fcc Ising antiferromagnet with nearest- and next-nearest-neighbor interactions.* Phys. Rev. B **21** (1980) 4027.

[110] T. R. Mattsson & H. Metiu. *Kinetic Monte Carlo simulations of nucleation on a surface with periodic strain: Spatial ordering and island-size distribution.* Appl. Phys. Lett. **75** (1999) 926.

[111] G. Russo & P. Smereka. *Computation of strained epitaxial growth in three dimensions by kinetic Monte Carlo.* J. Comp. Phys. **214** (2006) 809.

[112] J.-U. Sommer & G. Reiter. *The formation of ordered polymer structures at interfaces: A few intriguing aspects.* Adv. Polym. Sci. **200** (2006) 1.

[113] K.-H. Heinig. FZ Dresden-Rossendorf, Dresden, Germany. Private communication.

[114] M. Strobel, K.-H. Heinig & W. Möller. *A combination of atomic and continuum models describing the evolution of nanoclusters.* Comp. Mater. Sci. **10** (1998) 457.

[115] M. Strobel. *Modeling and Computer Simulation of Ion Beam Synthesis of Nanostructures.* Ph.D. thesis, TU Dresden (1999).

[116] T. Müller. *Low Energy Ion Beam Synthesis of Si Nanocrystals for Nonvolatile Memories - Modeling and Process Simulations.* Ph.D. thesis, TU Dresden (2005).

[117] J. v. Borany, K.-H. Heinig, R. Grötzschel, M. Klimenkov, M. Strobel, K.-H. Stegemann & H.-J. Thees. *Ion beam synthesis of narrow Ge nanocluster bands in thin SiO$_2$ films.* Microelectron. Eng. **48** (1999) 231.

[118] K.-H. Heinig, B. Schmidt, A. Markwitz, R. Grötzschel, M. Strobel & S. Oswald. *Precipitation, ripening and chemical effects during annealing of Ge$^+$ implanted SiO$_2$ layers.* Nucl. Instrum. Methods B **148** (1999) 969.

[119] T. Müller, K.-H. Heinig, W. Möller, C. Bonafos, H. Coffin, N. Cherkashin, G. B. Assayag, S. Schamm, G. Zanchi, A. Claverie, M. Tence & C. Colliex. *Multi-dot floating-gates for nonvolatile semiconductor memories: Their ion beam synthesis and morphology.* Appl. Phys. Lett. **85** (2004) 2373.

[120] T. Müller, K.-H. Heinig & W. Möller. *Size and location control of Si nanocrystals at ion beam synthesis in thin SiO$_2$ films.* Appl. Phys. Lett. **81** (2002) 3049.

[121] L. Röntzsch, K.-H. Heinig, B. Schmidt, A. Mücklich, W. Möller, J. Thomas & T. Gemming. *Direct evidence of self-aligned Si nanocrystals formed by ion irradiation of Si/SiO$_2$ interfaces.* Phys. Status Solidi A **202** (2005) R170.

[122] L. Röntzsch, K.-H. Heinig & B. Schmidt. *Experimental evidence of Si nanocluster δ-layer formation in buried and thin SiO$_2$ films induced by ion irradiation.* Mat. Sci. Semicon. Proc. **7** (2004) 357.

[123] P. Novikov, K.-H. Heinig, A. Larsen & A. Dvurechenskii. *Simulation of ion-irradiation stimulated Ge nanocluster formation in gate oxides containing GeO$_2$.* Nucl. Instrum. Methods B **191** (2002) 462.

[124] G. C. Rizza, M. Strobel, K.-H. Heinig & H. Bernas. *Ion irradiation of gold inclusions in SiO$_2$: Experimental evidence for inverse Ostwald ripening.* Nucl. Instrum. Methods B **178** (2001) 78.

[125] T. Müller, K.-H. Heinig & B. Schmidt. *Formation of Ge nanowires in oxidized silicon V-grooves by ion beam synthesis.* Nucl. Instrum. Methods B **175-177** (2001) 468.

[126] T. Müller, K.-H. Heinig & B. Schmidt. *Template-directed self-assembly of buried nanowires and the pearling instability.* Mater. Sci. Eng. C **19** (2002) 109.

[127] M. W. Finnis. *Interatomic Forces*, vol. 1 of *Oxford Series on Materials Modelling* (Oxford University Press, Oxford, 2003).

[128] R. W. Balluffi, S. M. Allen & W. C. Carter. *Kinetics of Materials* (John Wiley & Sons, Hoboken, 2005).

[129] S. Kobe. *Das Ising-Modell – gestern und heute.* Phys. Bl. **54** (1998) 917.

[130] K. Binder. *Applications of Monte Carlo methods to statistical physics.* Rep. Prog. Phys. **60** (1997) 487.

[131] E. Ising. *Beitrag zur Theorie des Ferromagnetismus.* Z. Phys. **31** (1925) 253.

[132] G. R. Carlow & R. F. Frindt. *Simulations of length-scale change for finger growth in intercalation compounds.* Phys. Rev. B **50** (1994) 11107.

[133] S. R. Bahn & K. W. Jacobsen. *Chain Formation of Metal Atoms.* Phys. Rev. Lett. **87** (2001) 266101.

[134] K. Huang. *Statistical Mechanics* (John Wiley & Sons, New York, 1987), 2nd edn.

[135] G. Bhanot. *The Metropolis algorithm.* Rep. Prog. Phys. **51** (1988) 429.

[136] C. Bichara & G. Inden. *Combined Monte Carlo and Cluster Variation Approach.* Prog. Theor. Phys. Supp. **115** (1994) 171.

[137] A. G. Schlijper & B. Smit. *Two-sided bounds on the free energy from local states in Monte Carlo simulations.* J. Stat. Phys. **56** (1989) 247.

[138] S. Weinketz. *Diffusion reordering kinetics in lattice-gas systems: Time evolution of configurational entropy and internal energy.* Phys. Rev. E **58** (1998) 159.

[139] S. Wolfram. *Statistical mechanics of cellular automata.* Rev. Mod. Phys. **55** (1983) 601.

[140] A. B. Bortz, M. H. Kalos & J. L. Lebowitz. *A new algorithm for Monte Carlo simulation of Ising spin systems.* J. Comp. Phys. **17** (1975) 10.

[141] A. F. Voter. *Classically exact overlayer dynamics: Diffusion of rhodium clusters on Rh(100).* Phys. Rev. B **34** (1986) 6819.

[142] E. Chason & B. W. Dodson. *Effect of step edge transition rates and anisotropy in simulations of epitaxial growth.* J. Vac. Sci. Technol. A **9** (1991) 1545.

[143] C. N. R. Rao & K. J. Rao. *Phase Transitions in Solids* (McGraw-Hill, New York, 1978).

[144] K. Binder & P. Fratzl. *Spinodal Decomposition.* In G. Kostorz (ed.) *Phase Transformations in Materials*, chap. 6, p. 409 (Wiley-VCH, Weinheim, 2001).

[145] J. M. Yeomans. *Statistical Mechanics of Phase Transition* (Clarendon Press, Oxford, 1992).

[146] J. Marro & R. Dickman. *Nonequilibrium Phase Transitions in Lattice Models* (Cambridge University Press, Cambridge, 1999).

[147] L. Onsager. *Crystal Statistics. I. A Two-Dimensional Model with an Order-Disorder Transition.* Phys. Rev. **65** (1944) 117.

[148] J. Philibert. *Atom Movements - Diffusion and Mass Transport in Solids* (Les Editions de Physique, Les Ulis, 1991).

[149] H. Bulou & C. Massobrio. *Mechanisms of exchange diffusion on fcc(111) transition metal surfaces.* Phys. Rev. B **72** (2005) 205427.

[150] G. Ehrlich. *Diffusion of individual adatoms.* Surf. Sci. **299-300** (1994) 628.

[151] R. L. Schwoebel. *Step Motion on Crystal Surfaces. II.* J. Appl. Phys. **40** (1969) 614.

[152] G. L. Kellogg. *Field ion microscope studies of single-atom surface diffusion and cluster nucleation on metal surfaces.* Surf. Sci. Rep. **21** (1994) 1.

[153] Y. W. Mo. *Direct determination of surface diffusion by displacement distribution measurement with scanning tunneling microscopy.* Phys. Rev. Lett. **71** (1993) 2923.

[154] I. Brihuega, O. Custance & J. M. Gomez-Rodriguez. *Surface diffusion of single vacancies on Ge(111)-c(2×8) studied by variable temperature scanning tunneling microscopy.* Phys. Rev. B **70** (2004) 165410.

[155] S. Arrhenius. *Über die Reaktionsgeschwindigkeit bei der Inversion von Rohrzucker durch Säuren.* Z. Phys. Chem. (Leipzig) **4** (1889) 226.

[156] P. Shewmon. *Diffusion in Solids* (The Minerals, Metals & Materials Society, Warregle, 1989), 2nd edn.

[157] G. Wulff. *Zur Frage der Geschwindigkeit des Wachsthums und der Auflösung der Krystallflächen.* Z. Kristallogr. **34** (1901) 449.

[158] C. A. Johnson & G. D. Chakerian. *On the proof and uniqueness of Wulff's construction of the shape of minimum surface free energy.* J. Math. Phys. **6** (1965) 1403.

[159] D. Margetis, P.-W. Fok, M. J. Aziz & H. A. Stone. *Continuum Theory of Nanostructure Decay Via a Microscale Condition.* Phys. Rev. Lett. **97** (2006) 096102.

[160] P. Müller & C. Mottet. *Equilibrium Nanoshapes: From Thermodynamics to Atomistic Simulations.* J. Comp. Theo. Nanosci. **4** (2007) 316.

[161] C. Rottman & M. Wortis. *Equilibrium crystal shapes for lattice models with nearest-and next-nearest-neighbor interactions.* Phys. Rev. B **29** (1984) 328.

[162] V. A. Shchukin & D. Bimberg. *Spontaneous ordering of nanostructures on crystal surfaces.* Rev. Mod. Phys. **71** (1999) 1125.

[163] M. Wortis. *Phases and Phase Transitions of Surfaces and Interfaces.* In E. G. D. Cohen (ed.) *Fundamental Problems in Statistical Physics VI*, p. 87 (North-Holland, Amsterdam, 1985).

[164] K. L. Murphy & C. Rottman. *Low-index interfaces in Ising models: Macroscopic faceting, roughening and phase diagrams.* Phys. Rev. B **42** (1990) 680.

[165] S. M. Foiles, M. I. Baskes & M. S. Daw. *Embedded-atom-method functions for the fcc metals Cu, Ag, Au, Ni, Pd, Pt, and their alloys.* Phys. Rev. B **33** (1986) 7983.

[166] B.-J. Lee, J.-H. Shim & M. I. Baskes. *Semiempirical atomic potentials for the fcc metals Cu, Ag, Au, Ni, Pd, Pt, Al, and Pb based on first and second nearest-neighbor modified embedded atom method.* Phys. Rev. B **68** (2003) 144112.

[167] D. P. Adams, S. M. Yalisove & D. J. Eaglesham. *Interfacial and surface energetics of CoSi$_2$.* J. Appl. Phys. **76** (1994) 5190.

[168] S. Mantl. *Ion beam synthesis of epitaxial silicides: fabrication, characterization and applications.* Mater. Sci. Rep. **8** (1992) 1.

[169] D. J. Eaglesham, A. E. White, L. C. Feldman, N. Moriya & D. C. Jacobson. *Equilibrium shape of Si.* Phys. Rev. Lett. **70** (1993) 1643.

[170] D. Kashchiev. *Nucleation: Basic Theory with Applications* (Butterworth-Heinemann, Oxford, 2000).

[171] W. T. Thomson. *On the Equilibrium of Vapour at a Curved Surface of Liquid.* Philos. Mag. **42** (1871) 448.

[172] L. D. Landau & E. M. Lifshitz. *Statistische Physik*, vol. 5 of *Lehrbuch der Theoretischen Physik* (Akademie-Verlag, Berlin, 1966).

[173] W. Ostwald. *Über die vermeintliche Isomerie des roten und gelben Quecksilberoxyds und die Oberflächenspannung fester Körper.* Z. Phys. Chem. **34** (1900) 495.

[174] L. R. Fisher & J. N. Israelachvili. *Direct experimental verification of the Kelvin equation for capillary condensation.* Nature **277** (1979) 548.

[175] J. G. Powles. *On the validity of the Kelvin equation.* J. Phys. A **18** (1985) 1551.

[176] G. W. Greenwood. *The growth of dispersed precipitates in solutions.* Acta Metall. **4** (1956) 243.

[177] I. M. Lifshitz & V. V. Slyozov. *The kinetics of precipitation from supersaturated solid solutions.* J. Phys. Chem. Solids **19** (1961) 35.

[178] C. Wagner. *Theorie der Alterung von Niederschlägen durch Umlösen.* Z. Electrochem. **65** (1961) 581.

[179] S. Reiss & K.-H. Heinig. *Ostwald ripening during ion beam synthesis - a computer simulation for inhomogeneous systems.* Nucl. Instrum. Methods B **84** (1994) 229.

[180] J. W. P. Schmelzer, G. Röpke & R. Mahnke. *Aggregation Phenomena in Complex Systems* (Wiley-VCH, Weinheim, 1999).

[181] D. Langbein. *Capillary Surfaces*, vol. 178 of *Springer Tracts in Modern Physics* (Springer, Berlin, 2002).

[182] K. N. Tu & U. Gösele. *Hollow nanostructures based on the Kirkendall effect: Design and stability considerations.* Appl. Phys. Lett. **86** (2005) 093111.

[183] B. J. Pines. *On sintering in the solid phase.* J. Tech. Phys. USSR **16** (1946) 737.

[184] G. Martin & P. Bellon. *Driven Alloys.* Solid State Phys. **50** (1997) 189.

[185] M.-O. Ruault, M. C. Ridgway, F. Fortuna, H. Bernas & J. S. Williams. *Shrinkage mechanism of nanocavities in amorphous Si under ion irradiation: An in situ study.* Nucl. Instrum. Methods B **206** (2003) 912.

[186] R. A. Enrique & P. Bellon. *Compositional Patterning in Systems Driven by Competing Dynamics*

Of Different Length Scale. Phys. Rev. Lett. **84** (2000) 2885.

[187] S. Matsumura, S. Müller & C. Abromeit. *Kinetics of irradiation-induced phase transformations in tricritical systems.* Phys. Rev. B **54** (1996) 6184.

[188] S. Rusponi, G. Costantini, C. Boragno & U. Valbusa. *Ripple Wave Vector Rotation in Anisotropic Crystal Sputtering.* Phys. Rev. Lett. **81** (1998) 2735.

[189] S. Rusponi, G. Costantini, C. Boragno & U. Valbusa. *Scaling Laws of the Ripple Morphology on Cu(110).* Phys. Rev. Lett. **81** (1998) 4184.

[190] W. L. Chan & E. Chason. *Making waves: Kinetic processes controlling surface evolution during low energy ion sputtering.* J. Appl. Phys. **101** (2007) 121301.

[191] M. Nastasi, J. W. Mayer & J. K. Hirvonen. *Ion-Solid-Interactions* (Cambridge University Press, Cambridge, 1996).

[192] R. W. Fathauer, A. Ksendzov, J. M. Iannelli & T. George. *Controllable surface-plasmon resonance in engineered nanometer epitaxial silicide particles embedded in silicon.* Phys. Rev. B **44** (1991) 1345.

[193] E. Rimini. *Ion Implantation* (Kluwer, Boston, 1995).

[194] R. Smith (ed.) *Atomic & Ion Collisions in Solids and at Surfaces* (Cambridge University Press, Cambridge, 1997).

[195] P. Sigmund. *Particle Penetration and Radiation Effects*, vol. 151 of *Springer Series in Solid-State Science* (Springer, Berlin, 2006).

[196] J. F. Ziegler (ed.) *Ion Implantation - Science and Technology* (Ion Implantation Technology, Edgewater, 2000).

[197] P. Sigmund. *Theory of Sputtering. I. Sputtering Yield of Amorphous and Polycrystalline Targets.* Phys. Rev. **184** (1969) 383.

[198] W. Möller & M. Posselt. *TRIDYN - FZR User Manual*, vol. 317 (FZR Publication, Dresden-Rossendorf, 2002).

[199] D. R. Lide (ed.) *CRC Handbook of Chemistry and Physics* (CRC Press, Boca Raton, 1994), 75$^{\text{th}}$ edn.

[200] A. M. Mazzone. *Defect Distribution in Ion-Implanted Silicon.* Prog. Surf. Sci. **95** (1986) 149.

[201] F. Harbsmeier & W. Bolse. *Ion beam induced amorphization in α quartz.* J. Appl. Phys. **83** (1998) 4049.

[202] K. Maex & M. v. Rossum (eds.) *Properties of Metal Silicides*, vol. 14 of *EMIS Datareviews Series* (INSPEC, London, 1995).

[203] P. D. Prewett & P. J. Heard. *Repair of opaque defects in photomasks using focused ion beams.* J. Phys. D **20** (1987) 1207.

[204] M. H. F. Overwijk, F. C. v. d. Heuvel & C. W. T. Bulle-Lieuwma. *Novel scheme for the preparation of transmission electron microscopy specimens with a focused ion beam.* J. Vac. Sci. Technol. B **11** (1994) 2021.

[205] J. Mayer, L. A. Giannuzzi, T. Kamino & J. Michael. *TEM Sample Preparation and FIB-Induced Damage.* Mater. Res. Soc. Bull. **32** (2007) 400.

[206] D. P. Adams, M. J. Vasile & T. M. Mayer. *Focused ion beam sculpting curved shape cavities in crystalline and amorphous targets.* J. Vac. Sci. Technol. B **24** (2006) 1766.

[207] M. D. Uchic, L. Holzer, B. J. Inkson, E. L. Principe & P. Munroe. *Three-Dimensional Microstructural Characterization Using Focused Ion Beam Tomography.* Mater. Res. Soc. Bull. **32** (2007) 408.

[208] P. D. Prewett & G. L. R. Mair. *Focused Ion Beams from Liquid Metal Ion Sources* (Research Studies Press, Taunton, 1991).

[209] L. Bischoff. *Alloy liquid metal ion sources and their application in mass separated focused ion beams.* Ultramicroscopy **103** (2005) 59.

[210] C. Akhmadaliev. FZ Dresden-Rossendorf, Dresden, Germany. Private communication.

[211] L. Bischoff, B. Schmidt, C. Akhmadaliev & A. Mücklich. *Investigation of FIB assisted $CoSi_2$ nanowire growth.* Microelectron. Eng. **83** (2006) 800.

[212] L. Bischoff. FZ Dresden-Rossendorf, Dresden, Germany. Private communication.

[213] J. Biersack & L. G. Haggmark. *A Monte Carlo computer program for the transport of energetic ions in amorphous targets.* Nucl. Instrum. Methods **174** (1980) 257.

[214] J. Biersack. *TRIM-DYNAMIC applied to marker broadening and SIMS depth profiling.* Nucl.

Instrum. Methods B **153** (1999) 398.

[215] W. Möller & W. Eckstein. *TRIDYN - a TRIM simulation code including dynamic composition changes*. Nucl. Instrum. Methods B **2** (1984) 814.

[216] M. Posselt. *Crystal-TRIM and its application to investigations on channeling effects during ion-implantation*. Radiat. Eff. Defects Solids **130** (1994) 87.

[217] W. Eckstein. *Computer Simulation of Ion-Solid Interactions*, vol. 10 of *Springer Series in Materials Science* (Springer, Berlin, 1991).

[218] J. P. Biersack & W. Eckstein. *Sputtering Studies with the Monte Carlo Program TRIM.SP*. Appl. Phys. A **34** (1984) 73.

[219] W. Boxleitner, G. Hobler & V. Kluppel. *Simulation of topography evolution and damage formation during TEM sample preparation using focused ion beams*. Nucl. Instrum. Methods B **175-177** (2001) 102.

[220] W. Boxleitner & G. Hobler. *FIBSIM - dynamic Monte Carlo simulation of compositional and topography changes caused by focused ion beam milling*. Nucl. Instrum. Methods B **180** (2001) 125.

[221] S. Hausmann. *Die Dynamik von Strahlenschäden durch fokussierte Ionenstrahlen am Beispiel der Ionenstrahlsynthese*. Ph.D. thesis, TU Dresden (2000).

[222] S. Hausmann, L. Bischoff, J. Teichert, M. Voelskow & W. Möller. *Dwell-time related effects in focused ion beam synthesis of cobalt disilicide*. J. Appl. Phys. **87** (2000) 57.

[223] S. Hausmann, L. Bischoff, J. Teichert, D. Grambole, F. Herrmann & W. Möller. *Investigation of Dwell-Time Effects in the Cobalt Disilicide Formation Using Focused Ion Beam Implantation*. Microelectron. Eng. **41-42** (1998) 233.

[224] B. Schmidt, D. Grambole & F. Herrmann. *Impact of ambient atmosphere on as-implanted amorphous insulating layers*. Nucl. Instrum. Methods B **191** (2002) 482.

[225] A. D. Brailsford. *Diffusion to a random array of identical spherical sinks*. J. Nucl. Mater. **60** (1976) 257.

[226] V. A. Borodin, K.-H. Heinig & S. Reiss. *Self-organization kinetics in finite precipitate ensembles during coarsening*. Phys. Rev. B **56** (1997) 5332.

[227] M. J. Anc (ed.) *SIMOX*, vol. 4 of *EMIS Processing Series* (Institution of Electrical Engineers, London, 2004).

[228] S. Reiss & K.-H. Heinig. *Computer simulation of mechanisms of the SIMOX process*. Nucl. Instrum. Methods B **102** (1995) 256.

[229] C. Akhmadaliev, L. Bischoff & B. Schmidt. FZ Dresden-Rossendorf, Dresden, Germany. Unpublished results.

[230] C. Akhmadaliev, B. Schmidt & L. Bischoff. *Defect induced formation of CoSi₂ nanowires by focused ion beam synthesis*. Appl. Phys. Lett. **89** (2006) 223129.

[231] A. Wellner, V. Paillard, C. Bonafos, M. Carrada, A. Claverie, B. Schmidt & K.-H. Heinig. *Stress measurements of germanium nanocrystals embedded in silicon oxide*. J. Appl. Phys. **94** (2003) 5639.

[232] A. Vantomme, M. F. Wu, G. Langouche, K. Maex, H. Vanderstraeten & Y. Bruynseraede. *Orientation and strain of single and double CoSi₂ epitaxial layers formed by ion implantation*. Nucl. Instrum. Methods B **59-60** (1991) 680.

[233] B. S. Bokstein, M. I. Mendelev & D. J. Srolovitz. *Thermodynamics and Kinetics in Materials Science* (Oxford University Press, Oxford, 2005).

[234] F. A. Nichols & W. W. Mullins. *Surface- (Interface-) and Volume-Diffusion Contributions to Morphological Changes Driven by Capillarity*. Trans. Metall. Soc. AIME **233** (1965) 1840.

[235] C. Weber. *Zum Zerfall eines Fluessigkeitsstrahls*. Z. Angew. Math. Mech. **11** (1931) 136.

[236] W. T. Pimbley & H. C. Lee. *Satellite Droplet Formation in a Liquid Jet*. IBM J. Res. Dev. **21** (1977) 21.

[237] S. Chandrasekhar. *Hydrodynamic and Hydromagnetic Stability* (Dover, New York, 1981).

[238] F. Savart. *Memoire sur la Constitution des Veines Liquides Lancees par des Orifices Circulaires en Mince Paroi*. Ann. Chem. Phys. **53** (1833) 337.

[239] M. C. Yuen. *Non-linear capillary instability of a liquid jet*. J. Fluid Mech. **33** (1968) 151.

[240] J. W. S. Rayleigh. *The Theory of Sound*, vol. 2 (Dover, New York, 1945), 2nd edn.

[241] E. F. Goedde & M. C. Yuen. *Experiments on liquid jet instability*. J. Fluid Mech. **40** (1970)

495.

[242] J. W. Cahn. *Stability of rods with anisotropic surface energy.* Scripta Metall. **13** (1979) 1069.

[243] A. M. Glaeser. *Model Studies of Rayleigh Instabilities via Microdesigned Interfaces.* Interface Sci. **9** (2001) 65.

[244] J. S. Stölken & A. M. Glaeser. *The morphological evolution of cylindrical rods with anisotropic surface free energy via surface diffusion.* Scripta Metall. Mater. **27** (1992) 449.

[245] K. F. Gurski & G. B. McFadden. *The effect of surface tension anisotropy on the Rayleigh instability.* Proc. R. Soc. London A **459** (2003) 2575.

[246] M. K. Santala & A. M. Glaeser. *Surface-energy-anisotropy-induced orientation effects on Rayleigh instabilities in sapphire.* Surf. Sci. **600** (2006) 782.

[247] F. Kassubek, C. A. Stafford, H. Grabert & R. E. Goldstein. *Quantum suppression of the Rayleigh instability in nanowires.* Nonlinearity **14** (2001) 167.

[248] C.-H. Zhang, J. Bürki & C. A. Stafford. *Stability of metal nanowires at ultrahigh current densities.* Phys. Rev. B **71** (2005) 235404.

[249] Y. Chen, D. A. A. Ohlberg, G. Medeiros-Ribeiro, Y. A. Chang & R. S. Williams. *Self-assembled growth of epitaxial erbium disilicide nanowires on silicon (001).* Appl. Phys. Lett. **76** (2000) 4004.

[250] M. S. McCallum, P. W. Voorhees, M. J. Miksis, S. H. Davis & H. Wong. *Capillary instabilities in solid thin films: Lines.* J. Appl. Phys. **79** (1996) 7604.

[251] G. B. McFadden, S. R. Coriell & B. T. Murray. *The Rayleigh instability for a cylindrical crystal-melt interface.* In A. Friedman & J. Spruck (eds.) *Variational and Free Boundary Problems,* vol. 53 of *The IMA Volumes in Mathematics and its Applications,* p. 159 (Springer, New York, 1993).

[252] E. D. Williams. *Nanoscale Structures: Lability, Length Scales, and Fluctuations.* Mater. Res. Soc. Bull. **29** (2004) 621.

[253] F. M. Kolb, H. Hofmeister, M. Zacharias & U. Gösele. *On the morphological instability of silicon/silicon dioxide nanowires.* Appl. Phys. A **80** (2005) 1405.

[254] V. Schmidt, S. Senz & U. Gösele. *The shape of epitaxially grown silicon nanowires and the influence of line tension.* Appl. Phys. A **80** (2005) 445.

[255] B. M. Reinhard, M. Siu, H. Agarwala, A. P. Alivisatos & J. Liphardt. *Calibration of Dynamic Molecular Rulers Based on Plasmon Coupling between Gold Nanoparticles.* Nano Lett. **5** (2005) 2246.

[256] P. K. Jain, W. Huang & M. A. El-Sayed. *On the Universal Scaling Behavior of the Distance Decay of Plasmon Coupling in Metal Nanoparticle Pairs: A Plasmon Ruler Equation.* Nano Lett. **7** (2007) 2080.

[257] S. Prasad & A. Paul. *Theoretical consideration on the formation of nanotube following the Kirkendall effect.* Appl. Phys. Lett. **90** (2007) 233114.

[258] M. E. Toimil-Molares & C. Trautmann. GSI Darmstadt. Private communication, results to be published.

[259] M. E. Toimil-Molares, V. Buschmann, D. Dobrev, R. Neumann, R. Scholz, I. U. Schuchert & J. Vetter. *Single-Crystalline Copper Nanowires Produced by Electrochemical Deposition in Polymeric Ion Track Membranes.* Adv. Mater. **13** (2001) 62.

[260] J. Lian, L. Wang, X. Sun, Q. Yu & R. C. Ewing. *Patterning Metallic Nanostructures by Ion-Beam-Induced Dewetting and Rayleigh Instability.* Nano Lett. **6** (2006) 1047.

[261] I. N. Bronstein, K. A. Semendjajew, G. Musiol & H. Mühlig. *Taschenbuch der Mathematik* (Harri Deutsch, Frankfurt am Main, 1999), 4th edn.

[262] W. Greiner & H. Stock. *Hydrodynamik*, vol. 2A of *Theoretische Physik* (Verlag Harri Deutsch, 1984), 2nd edn.

[263] J. Zhou, T. Koschny, M. Kafesaki, E. N. Economou, J. B. Pendry & C. M. Soukoulis. *Saturation of the Magnetic Response of Split-Ring Resonators at Optical Frequencies.* Phys. Rev. Lett. **95** (2005) 223902.

[264] M. W. Klein, C. Enrich, M. Wegener, C. M. Soukoulis & S. Linden. *Single-slit split-ring resonators at optical frequencies: limits of size scaling.* Opt. Lett. **31** (2006) 1259.

[265] P. J. A. Kenis & A. D. Stroock. *Materials for Micro- and Nanofluidics.* Mater. Res. Soc. Bull. **31** (2006) 87.

[266] X. Zhang & S. J. Haswell. *Materials Matter in Microfluidic Devices.* Mater. Res. Soc. Bull. **31** (2006) 95.

[267] T. Sato, K. Mitsutake, I. Mizushima & Y. Tsunashima. *Micro-structure Transformation of Silicon: A Newly Developed Transformation Technology for Patterning Silicon Surfaces using the Surface Migration of Silicon Atoms by Hydrogen Annealing.* Jpn. J. Appl. Phys. **39** (2000) 5033.

[268] K. F. Jensen. *Silicon-Based Microchemical Systems: Characteristics and Applications.* Mater. Res. Soc. Bull. **31** (2006) 101.

[269] O. D. Sagazan, M. Denoual, P. Guil, D. Gaudin & O. Bonnaud. *Horizontal buried channels in monocrystalline silicon.* Microsyst. Technol. **12** (2006) 959.

[270] N. Blow. *Microfluidics: in search of a killer application.* Nature Methods **4** (2007) 665.

[271] J. Virbulis. Talk at the E-MRS Spring Meeting, May 30, 2006, Nice, France. Symp. V 02/04.

[272] Z. L. Wang (ed.) *Nanowires and Nanobelts I - Metal and Semiconductor Nanowires* (Kluwer, Boston, 2003).

[273] Z. L. Wang (ed.) *Nanowires and Nanobelts II - Nanowires and Nanobelts of Functional Materials* (Kluwer, Boston, 2003).

[274] S. V. N. T. Kuchibhatla, A. S. Karakoti, D. Bera & S. Seal. *One dimensional nanostructured materials.* Prog. Mater. Sci. **52** (2007) 699.

[275] B. Legrand, V. Agache, T. Melin, J. P. Nys, V. Senez & D. Stievenard. *Thermally assisted formation of silicon islands on a silicon-on-insulator substrate.* J. Appl. Phys. **91** (2002) 106.

[276] S. M. Reimann & M. Manninen. *Electronic structure of quantum dots.* Rev. Mod. Phys. **74** (2002) 1283.

[277] S. Maier. *Guiding of electromagnetic energy in subwavelength periodic metal structures.* Ph.D. thesis, CIT Pasadena (2003).

[278] L. Pavesi & G. Guillot (eds.) *Optical Interconnects: The Silicon Approach*, vol. 119 of *Springer Series in Optical Sciences* (Springer, Berlin, 2006).

[279] A. M. Cazabat, F. Heslot, S. M. Troian & P. Carles. *Fingering instability of thin spreading films driven by temperature gradients.* Nature **346** (1990) 824.

[280] H. C. Kuhlmann. *Thermocapillary Convection in Models of Crystal Growth*, vol. 152 of *Springer Tracts in Modern Physics* (Springer, Berlin, 1999).

[281] T. M. Squires & S. R. Quake. *Microfluidics: Fluid physics at the nanoliter scale.* Rev. Mod. Phys. **77** (2005) 977.

[282] V. G. Levich & V. S. Krylov. *Surface-Tension-Driven Phenomena.* Annu. Rev. Fluid. Mech. **1** (1969) 293.

[283] A. Oron, S. H. Davis & S. G. Bankoff. *Long-scale evolution of thin liquid films.* Rev. Mod. Phys. **69** (1997) 931.

[284] F. Korte, J. Koch & B. N. Chichkov. *Formation of microbumps and nanojets on gold targets by femtosecond laser pulses.* Appl. Phys. A **79** (2004) 879.

[285] Y. F. Guan, A. J. Pedraza, J. D. Fowlkes & D. A. Joy. *Nanostructures produced by ultraviolet laser irradiation of silicon. II. Nanoprotrusions and nanoparticles.* J. Vac. Sci. Technol. B **22** (2004) 2836.

[286] B. R. Tull, J. E. Carey, E. Mazur, J. P. McDonald & S. M. Yalisove. *Silicon Surface Morphologies after Femtosecond Laser Irradiation.* Mater. Res. Soc. Bull. **31** (2006) 626.

[287] A. S. Basu & Y. B. Gianchandani. *Shaping high-speed Marangoni flow in liquid films by micro-scale perturbations in surface temperature.* Appl. Phys. Lett. **90** (2007) 034102.

[288] P. S. Ho & T. Kwok. *Electromigration in metals.* Rep. Prog. Phys. **52** (1989) 301.

[289] X. Chu, L. Bauer & W. W. Mullins. *Spreading of a void along a singular surface during electromigration: A failure mode.* Appl. Phys. Lett. **70** (1997) 194.

[290] C. Q. Ru. *Thermomigration as a driving force for instability of electromigration induced mass transport in interconnect lines.* J. Mater. Sci. **35** (2000) 5575.

[291] H. Yasunaga & A. Natori. *Electromigration on semiconductor surfaces.* Surf. Sci. Rep. **15** (1992) 205.

[292] T. Y. Tan. *Mass transport equations unifying descriptions of isothermal diffusion, thermomigration, segregation, and position-dependent diffusivity.* Appl. Phys. Lett. **73** (1998) 2678.

[293] T. Ichinokawa, C. Haginoya, D. Inoue, H. Itoh & J. Kirschner. *Electro- and Thermomigration*

of Metallic Islands on Si(100) Surface. Jpn. J. Appl. Phys. **32** (1993) 1379.

[294] B. Stahlmecke, F.-J. M. zu Heringdorf, L. I. Chelaru, M. H. von Hoegen, G. Dumpich & K. R. Roos. *Electromigration in self-organized single-crystalline silver nanowires.* Appl. Phys. Lett. **88** (2006) 053122.

[295] F. Mücklich, A. Lasagni & C. Daniel. *Laser interference metallurgy-periodic surface patterning and formation of intermetallics.* Intermetallics **13** (2005) 437.

[296] B. Rothenhäusler, J. Rabe, P. Korpiun & W. Knoll. *On the Decay of Plasmon Surface Polaritons at Smooth and Rough Ag-Air Interfaces: A Reflectance and Photo-Acoustic Study.* Surf. Sci. **137** (1984) 373.

[297] V. Vlasko-Vlasov, A. Rydh, J. Pearson & U. Welp. *Spectroscopy of surface plasmons in metal films with nanostructures.* Appl. Phys. Lett. **88** (2006) 173112.

[298] F. Keilmann, K. W. Kussmaul & Z. Szentirmay. *Imaging of optical wavetrains.* Appl. Phys. B **47** (1988) 169.

[299] E. Anemogiannis, E. N. Glytsis & T. K. Gaylord. *Determination of guided and leaky modes in lossless and lossy planar multilayer optical waveguides: reflection pole method and wavevector density method.* J. Lightwave Technol. **17** (1999) 929.

[300] J. D. Jackson. *Classical Electrodynamics* (John Wiley & Sons, New York, 1999), 3rd edn.

[301] F. Keilmann, B. Knoll & A. Kramer. *Long-Wave-Infrared Near-Field Microscopy.* Phys. Status Solidi B **215** (1999) 849.

[302] D. R. Lide (ed.) *CRC Handbook of Chemistry and Physics* (CRC Press, Boca Raton, 2004), 85th edn.

[303] www.surface-tension.de/solid-surface-energy.htm.

[304] Z.-W. Liu, Q.-H. Wei & X. Zhang. *Surface Plasmon Interference Nanolithography.* Nano Lett. **5** (2005) 957.

[305] W. S. amd N. Fang, S. Durant, M. Ambati, C. Sun & X. Zhang. *Sub-100 nm lithography using ultrashort wavelength of surface plasmons.* J. Vac. Sci. Technol. B **22** (2004) 3475.

[306] M. M. Ovsyanko. *Ion sculpting of Cu(001).* Ph.D. thesis, U Twente (2006).

[307] R. Friedberg & J. E. Cameron. *Test of the Monte Carlo Method: Fast Simulation of a Small Ising Lattice.* J. Chem. Phys. **52** (1970) 6049.

[308] M. Creutz, L. Jacobs & C. Rebbi. *Experiments with a Gauge-Invariant Ising System.* Phys. Rev. Lett. **42** (1979) 1390.

[309] J. Hardy, O. Pazzis & Y. Pomeau. *Molecular dynamics of a classical lattice gas: Transport properties and time correlation functions.* Phys. Rev. A **13** (1976) 1949.

[310] D. Stauffer. *Computer simulations of cellular automata.* J. Phys. A **24** (1991) 909.

[311] Platon. *Der Staat: Über das Gerechte*, vol. 80 of *Philosophische Bibliothek* (Meiner, Hamburg, 1989), 11th edn.

[312] G. Odor. Research Institute for Technical Physics and Materials Science, Budapest, Hungary. Private communication.

[313] V. Cardoso & O. J. C. Dias. *Rayleigh-Plateau and Gregory-Laflamme Instabilities of Black Strings.* Phys. Rev. Lett. **96** (2006) 181601.

[314] D. M. Y. Sommerville. *An introduction to the geometry of n dimensions* (Dover, New York, 1958).

[315] T. F. Banchoff. *Beyond the Third Dimension* (Scientific American Library, New York, 1990).

[316] J. M. Bardeen, B. Carter & S. W. Hawking. *The Four Laws of Black Hole Mechanics.* Commun. Math. Phys. **31** (1973) 161.

[317] R. F. Brooks, I. Egry, S. Seetharaman & D. Grant. *Reliable data for high-temperature viscosity and surface tension: results from a European project.* High Temp. - High Press. **33** (2001) 631.

List of Figures

List of Tables

Acknowledgements

This dissertation would not have come into being without support, encouragement, understanding, and patience of many persons. I am deeply grateful to all of them, in particular, I would like to thank

- Professor Dr. Wolfhard Möller for the continuous and benevolent support throughout my course of studies at TU Dresden, particularly in view of the field of ion-solid interactions and related research areas: *Hauptseminar*, *Laborpraktikum*, *Mitarbeit in der Forschergruppe*, diploma thesis, and finally this dissertation all of which I conducted under his kind patronage at the Institute for Ion Beam Physics and Materials Research (FWI);

- Professor Dr. Harry Bernas for insightful discussions about ion implantation and ion irradiation effects on various occasions (conferences, Erice summer school, visits at FWI) and for examining this work;

- Professor Dr. Thomas Michely for his kind willingness to examine this work;

- Dr. Karl-Heinz Heinig, my direct advisor, for introducing me into the virtual reality of lattice KMC simulations, for teaching me to think in the binary realm of bytes and bits, for countless discussions during morning and afternoon coffee breaks which have brought me atomistic insight and enduring scientific as well as technological stimulation, for providing considerable project and travel funds over the last years, and for the critical and careful reading of this and many other manuscripts;

- Dr. Matthias Posselt and all present as well as former members of the theory division at FWI for various scientific discussions and for the enjoyable company over the last years;

- Dr. Bernd Schmidt, Dr. Lothar Bischoff, and Dr. Chavkat Akhmadaliev from the FIB group at FWIP for a close collaboration on FIB-based NW synthesis; Dr. Bernd Schmidt in particular for the critical reading of the manuscript;

- Dr. Johannes von Borany for the kind supply of additional funds;

- the external colleagues:

    - Professor Dr. Mark L. Brongersma and Mr. Jon A. Schuler (Geballe Laboratory for Advanced Materials, Stanford University, USA) for the joint venture on SPP-induced thermocapillarity phenomena in thin films;

    - Dr. Christina Trautmann, Dr. Maria Eugenia Toimil Molares, and Dr. Thomas W. Cornelius (Materials Research Department at GSI, Darmstadt, Germany) for the collaboration on draining of metal-filled tubes and for insight-

ful discussions on the Plateau-Rayleigh instability of single-crystalline metal NWs;

- Mr. Erwan Dornel (CEA-LETI, Grenoble, France) for fruitful discussions and exchange of views on dewetting of ultra-thin SOI layers;

- Dr. Geza Odor (Academy of Sciences, Budapest, Hungary) for a very stimulating debate on cellular automata and lattice-based simulations in higher dimensions;

• the Rossendorf Information Technology staff for their omnipresent help and support and for solving manifold hardware and software problems with the virtual laboratories *Hades* and *Hydra* (in alphabetical order): Mr. Uwe Eisold, Mr. Andreas Geyer, Mr. Torsten Hantzsche, Dr. Uwe Konrad, Mr. Achim Kreher, Dr. Manfred Kunicke, Mrs. Katrin Paul, Dr. Matthias Schlett, Mr. Nils Schmeißer, Mr. Henrik Schulz, and Mrs. Kirstin Wandelt;

• the Rossendorf Library staff for their omnipresent help and support, in particular for the supply of countless inter-library loans over the last years (in alphabetical order): Mrs. Ramona Brückner, Mrs. Elke Hänel, Mrs. Kerstin Henrion, Mrs. Hannelore Müller, Mrs. Sabine Pförtner, Mrs. Edith Reschke, Mrs. Isabell Richter, Mrs. Romy Schindler, and Mr. Milan Scholze;

• Dr. Christine Bohnet and Mrs. Annett Weissig from the Rossendorf Public Relations staff for providing the platform to teach ion-solid interactions to groups of high school and college students as well as for the chance of becoming a cunning "ion billiardist" – I enjoyed these moments of publicity immensely;

• all scientific, technical and administrative members of FWI for the friendly and solidary atmosphere at work;

• all my friends, relatives in spirit, and fellow students who do not want to be mentioned by name out of modesty;

• my parents Christine and Hansgeorg Röntzsch for their love, for their belief in me and my abilities, and for their enduring spiritual and material support.

Peace and Solidarity!

Curriculum Vitae

Personal Information

name	Lars Röntzsch
born	September 9, 1977, Dresden
e-mail	lars@roentzsch.org
website	www.roentzsch.org

Employment History

09/2007 onward	Scientific staff at the Fraunhofer Institute for Manufacturing Technology and Applied Materials Research (IFAM) in Dresden; group manager "Hydrogen Storage"
05/2007 – 08/2007	Scientific staff at the Institute of Materials Science at TU Dresden

Awards

05/2004	E-MRS Young Scientist Award, Strasbourg, France
09/2004	IBMM Poster Award, Monterey, USA
09/2000 – 05/2001	Scholarship of the *Kulturstiftung Dresden der Dresdner Bank*

Education

12/2007	Graduation: *doctor rerum naturalium*
11/2003 – 04/2007	Doctoral thesis at FZ Dresden-Rossendorf (Institute for Ion Beam Physics and Materials Research) within the DFG project "Theoretical studies of growth, stability and functionality of nanowires" (project no. HE 2137/2-1)
09/2003	Graduation: *Diplom-Physiker*
10/2002 – 09/2003	Diploma thesis at FZ Rossendorf (Institute for Ion Beam Physics and Materials Research) within the EU project "NEON" on semiconductor nanocrystal non-volatile memories; title: Self-Organization of Si Nanocluster δ-Layers at Ion-Beam-Mixed Si-SiO_2 Interfaces (ISSN1437-322)
09/2000 – 05/2001	Study of Physics, Philosophy of Science, and International Relations at Boston University (exchange student)
10/1997 – 09/2003	Study of Physics at TU Dresden
06/1996	*Abitur* at the Ferdinand-Sauerbruch-Gymnasium Großröhrsdorf
09/1984 – 06/1996	School attendance

Practical Experience

09/2001 – 09/2002	Student employee with AMD Saxony LLC (Material Analysis Department under Dr. Ehrenfried Zschech): Investigations on the soft-error sensitivity of SOI devices
08/1998 – 09/1999	Student employee at the Fraunhofer Institute for Electron Beam and Plasma Technology under Professor Dr. Volker Kirchhoff and Dr. Matthias Schulze: DC sputtering of zinc oxide; Optical plasma emissions in the reactive bipolar pulse magnetron sputtering process of titanium oxide
08/1997 – 10/1997	Internship at the Institute for Applied Physics and Didactics at TU Dresden under Professor Dr. Michael Loewenhaupt and Dr. Mathias Dörr: DC conductivity of oxides, intermetallic and rare-earth transition-metal compounds

Further Skills

computer	C/C++, Kinetic Monte Carlo, Basic, Latex, PovRay, RasMol, TRIM, TRIDYN, FlexPDE, Maple, Corel Draw, Origin, MS-Office, Windows/Linux
experiment	ion beam techniques, ellipsometry, thin film deposition techniques, thermoanalytical techniques
languages	English (fluent); Spanish (basic); Latin, Classical Greek, Russian (school level)
hobbies	strawberry breeding**, tennis, architecture

**Further information can be found at: `http://www.roentzsch.org/Fragaria/index.html`

List of Publications

Articles

- **L. Röntzsch**, K.-H. Heinig, J. A. Schuller & M. L. Brongersma, *Thin film patterning by surface-plasmon-induced thermocapillarity.* Appl. Phys. Lett. **90** (2007) 044105.

- B. Schmidt, A. Mücklich, **L. Röntzsch** & K.-H. Heinig. *How do high energy heavy ions shape Ge nanoparticles embedded in SiO_2?* Nucl. Instr. Meth. B **257** (2007) 30.

- **L. Röntzsch**, K.-H. Heinig, B. Schmidt & A. Mücklich. *Experimental evidence of Si nanocluster δ-layer formation in the vicinity of ion-irradiated SiO_2-Si interfaces.* Nucl. Instr. Meth. B **242** (2006) 149.

- B. Schmidt, K.-H. Heinig, **L. Röntzsch**, T. Müller, K.-H. Stegemann & E. Votintseva. *Ion irradiation through SiO_2/Si interfaces: Non-conventional fabrication of Si nanocrystals for memory applications.* Nucl. Instr. Meth. B **242** (2006) 146.

- **L. Röntzsch**, K.-H. Heinig, B. Schmidt, A. Mücklich, W. Möller, J. Thomas & T. Gemming. *Direct evidence of self-aligned Si nanocrystals formed by ion irradiation of Si/SiO_2 interfaces.* physica status solidi A **202** (2005) R170.

- **L. Röntzsch** & K.-H. Heinig. *Reaction pathways of ion beam synthesis and stability of monocrystalline nanowires.* Proceedings of the 1st International Workshop on Semiconductor Nanocrystals, Budapest, Hungary, Sept. 10-12, 2005, eds. Pödör *et al.*, ISBN 963-7371-18-4, Vol. 1, p. 165-169.

- **L. Röntzsch**, K.-H. Heinig & B. Schmidt. *Experimental Evidence of Si Nanocluster δ-Layer Formation in Buried and Thin SiO_2 Films Induced by Ion Irradiation.* Mater. Sci. Semicond. Proc. **7** (2004) 357.

Conferences

Invited Talk:

- MRS-J, Tokyo, Japan, 2006: *Synthesis of Nanowire Structures using Focused Ion Beams.*

Contributed Talks:

- IBMM, Taormina, Italy, 2006: *Modeling of Focused-Ion-Beam-Based Synthesis of Nanowire Structures.*

- MRS, San Francisco, USA, 2006: *Size and Position Control of Chains or Arrays of Nanoparticles by Surface-Plasmon-Polariton-Induced Thermocapillarity.*

- DPG, Berlin, Germany, 2005: *Theoretical Study on Reaction Paths of Formation and Decay of 1D Nanostructures.*

- EURESCO, Giens, France, 2004: *Evidence of Self-Aligned Si Nanocluster δ-Layers in Buried SiO_2 Films Induced by Ion Irradiation.*

- E-MRS, Strasbourg, France, 2004: *Experimental Evidence of Si Nanocluster δ-Layer Formation in Buried and Thin SiO_2 Films Induced by Ion Irradiation.*

- DPG, Regensburg, Germany, 2004: *Self-Organization of Nanocluster δ-Layers at Ion-Beam-Mixed Si-SiO_2 Interfaces.*

Posters (selection):

- E-MRS, Nice, France, 2006: *Nanowire Transformation into Long-Range-Ordered Nanocluster Chains Controlled by Thermocapillarity.*

- E-MRS, Nice, France, 2006: *Nanowire Synthesis with Focused Ion Beams: Predictive Atomistic Simulations on the Fabrication of Functional Nanowire Structures.*

- MRS, San Francisco, USA, 2006: *Predictive Process Simulation of the FIB-Based Fabrication of Metallic Nanoparticle Waveguides.*

- MRS, San Francisco, USA, 2006: *Focused-Ion-Beam-Based Synthesis of Semiconductor Nanowires and Functional Structures.*

- MRS, San Francisco, USA, 2006: *Search for Reaction Pathways of a CMOS-Compatible Fabrication of Nanofluidic Channels by means of Atomistic Computer Simulations.*

- DPG, Dresden, Germany, 2006: *Reaction Pathways of a Regular Disintegration of Nanowires by Thermocapillarity.*

- SEMINANO, Budapest, Hungary, 2005: *Reaction Pathways of Ion Beam Synthesis and Stability of Monocrystalline Nanowires.*

- 25th GIF Meeting, Dresden, Germany, 2005: *Ion Beam Synthesis of $CoSi_2$ Nanowires in Si and their Stability - Predictions of Atomistic Computer Simulations.*

- E-MRS, Strasbourg, France, 2005: *Ion Beam Synthesis of $CoSi_2$ Nanowires in Si and Their Stability - Predictions of Atomistic Computer Simulations.*

- DPG, Berlin, Germany, 2005: *Atomistic Computer Simulations on Ion Beam Synthesis and Decay of $CoSi_2$ Nanowires.*

- 342nd Wilhelm & Else Heraeus Seminar, Bad Honnef, Germany, 2005: *Predictive Atomistic Computer Simulations on Synthesis and Stability of Single-crystalline Nanowires.*

- IBMM, Monterey, USA, 2004: *Experimental Evidence of Si Nanocluster δ-Layer Formation in the Vicinity of Ion-Irradiated SiO_2-Si Interfaces.*

Declaration / Versicherung

Hereby, I do solemnly and sincerely declare that this dissertation was done by me, personally. Due acknowledgement has been made in the text to all other sources and material used. The material has not been accepted in whole, or in part, for any other degree. This dissertation has been prepared at the Institute of Ion Beam Physics and Materials Research of the Research Center Dresden-Rossendorf under the guidance of Professor Dr. Wolfhard Möller and Dr. Karl-Heinz Heinig.

Hiermit versichere ich, dass ich die vorliegende Arbeit ohne unzulässige Hilfe Dritter und ohne Benutzung anderer als der angegebenen Hilfsmittel angefertigt habe; die aus fremden Quellen direkt oder indirekt übernommenen Gedanken sind als solche kenntlich gemacht. Die Arbeit wurde bisher weder im Inland noch im Ausland in gleicher oder ähnlicher Form einer anderen Prüfungsbehörde vorgelegt. Diese Dissertation wurde am Institut für Ionenstrahlphysik und Materialforschung des Forschungszentrums Dresden-Rossendorf unter der wissenschaftlichen Betreuung von Professor Dr. Wolfhard Möller sowie Dr. Karl-Heinz Heinig angefertigt.

Dresden, August 14, 2007